
Super-Resolution Fluorescence Microscopy Based on Physical Models

François Aguet

Thèse N° 4418 (May 2009)

*Thèse présentée à la faculté des sciences et techniques de l'ingénieur
pour l'obtention du grade de docteur ès sciences
et acceptée sur proposition du jury*

Prof. René-Paul Salathé, *président*
Prof. Michael Unser, *directeur de thèse*
Prof. Theo Lasser, *rapporteur*
Dr. Suliana Manley, *rapporteur*
Prof. Jean-Christophe Olivo-Marin, *rapporteur*

École polytechnique fédérale de Lausanne—2009

Cover design by Annette Unser
Printing and binding by Repro-EPFL
Typeset with L^AT_EX
Copyright © 2009 by François Aguet
Available at <http://bigwww.epfl.ch/>

Abstract

This thesis introduces a collection of physics-based methods for super-resolution in optical microscopy. The core of these methods constitute a framework for 3-D localization of single fluorescent molecules. Localization is formulated as a parameter estimation problem relying on a physically accurate model of the system's point spread function (PSF). In a similar approach, methods for fitting PSF models to experimental observations and for extended-depth-of-field imaging are proposed.

Imaging of individual fluorophores within densely labeled samples has become possible with the discovery of dyes that can be photo-activated or switched between fluorescent and dark states. A fluorophore can be localized from its image with nanometer-scale accuracy, through fitting with an appropriate image function. This concept forms the basis of fluorescence localization microscopy (FLM) techniques such as photo-activated localization microscopy (PALM) and stochastic optical reconstruction microscopy (STORM), which rely on Gaussian fitting to perform the localization. Whereas the image generated by a single fluorophore corresponds to a section of the microscope's point spread function, only the in-focus section of the latter is well approximated by a Gaussian. Consequently, applications of FLM have for the most part been limited to 2-D imaging of thin specimen layers.

In the first section of the thesis, it is shown that localization can be extended to 3-D without loss in accuracy by relying on a physically accurate image formation model in place of a Gaussian approximation. A key aspect of physically realistic models lies in their incorporation of aberrations that arise either as a consequence of mismatched refractive indices between the layers of the sample setup, or as an effect of experimental settings that deviate from the design conditions of the system. Under typical experimental conditions, these aberrations change as a function of sample depth, inducing axial shift-variance in the PSF. This property is exploited in a maximum-likelihood framework for 3-D localization of single fluorophores. Due to the shift-variance of the PSF, the axial position of a fluorophore is uniquely encoded in its diffraction pattern, and can be estimated from a single acquisi-

tion with nanometer-scale accuracy.

Fluorescent molecules that remain fixed during image acquisition produce a diffraction pattern that is highly characteristic of the orientation of the fluorophore's underlying electromagnetic dipole. The localization is thus extended to incorporate the estimation of this 3-D orientation. It is shown that image formation for dipoles can be represented through a combination of six functions, based on which a 3-D steerable filter for orientation estimation and localization is derived. Experimental results demonstrate the feasibility of joint position and orientation estimation with accuracies of the order of one nanometer and one degree, respectively. Theoretical limits on localization accuracy for these methods are established in a statistical analysis based on Cramér-Rao bounds. A noise model for fluorescence microscopy based on a shifted Poisson distribution is proposed.

In these localization methods, the aberration parameters of the PSF are assumed to be known. However, state-of-the-art PSF models depend on a large number of parameters that are generally difficult to determine experimentally with sufficient accuracy, which may limit their use in localization and deconvolution applications. A fitting algorithm analogous to localization is proposed; it is based on a simplified PSF model and shown to accurately reproduce the behavior of shift-variant experimental PSFs.

Finally, it is shown that these algorithms can be adapted to more complex experiments, such as imaging of thick samples in brightfield microscopy. An extended-depth-of-field algorithm for the fusion of in-focus information from frames acquired at different focal positions is presented; it relies on a spline representation of the sample surface, and as a result yields a continuous and super-resolved topography of the specimen.

Keywords

3-D Imaging, Deconvolution, Extended Depth of Field, Fluorescence, Localization, Microscopy, Orientation, Point Spread Function, Single Molecules, Steerable Filters, Super-resolution

Résumé

Cette thèse présente un ensemble de méthodes de super-résolution pour la microscopie optique, basées sur des modèles physiques. L'essentiel de ces méthodes est appliqué à la localisation tridimensionnelle de molécules fluorescentes. La localisation est formulée à travers un problème d'estimation de paramètres reposant sur un modèle physiquement précis de la réponse impulsionnelle (PSF) du système. Avec une approche semblable, des méthodes sont proposées pour l'ajustement du modèle aux mesures expérimentales, ainsi que pour l'imagerie à profondeur de champs étendue.

L'observation de molécules individuelles au sein d'un ensemble dense de fluorophores a été rendue possible par la découverte de molécules pouvant être activés ou commutés entre un état fluorescent et un état sombre. Une molécule fluorescente peut être localisée à partir de son image avec une précision nanométrique, par ajustement avec un modèle adéquat. Ce concept est à la base des techniques de microscopie à localisation de fluorescence (FLM) telles que la microscopie à localisation par photo-activation (PALM) et la microscopie optique à reconstruction stochastique (STORM), basées sur un modèle Gaussien de la PSF. Tandis que l'image générée par un fluorophore isolé correspond à une section de la PSF du microscope, seule la section dans le plan focal est correctement approximée par une Gaussienne. En conséquence, les applications de FLM ont, pour la plupart, été limitées à l'imagerie 2-D d'échantillons fins.

Dans la première partie de la thèse, il est démontré que la localisation peut être étendue à trois dimensions sans perte de précision en s'appuyant sur un modèle précis de la formation d'image au lieu de l'approximation Gaussienne. La prise en compte d'aberrations provenant à la fois de l'inégalité entre les indices de réfraction du milieu d'immersion et de l'échantillon, ainsi que de déviations potentielles des autres paramètres du système optique par rapport à leur valeur nominale, constitue un aspect déterminant pour les modèles physiquement réalistes. Dans des conditions expérimentales typiques, ces aberrations varient en fonction de la profondeur dans l'échantillon, ce qui induit une dépendance par translation axiale dans la PSF. Cette propriété est exploitée dans une approche à maximum

de vraisemblance pour la localisation tridimensionnelle de fluorophores individuels à travers leur figure de diffraction. La variance axiale de la PSF encode de manière unique sa position, qui peut ainsi être estimée à partir d'une seule image avec une précision nanométrique.

Les molécules fluorescentes immobiles lors de l'acquisition d'image produisent une figure de diffraction qui est hautement caractéristique de l'orientation du dipôle électromagnétique constitué par le fluorophore. La localisation est alors étendue à l'estimation additionnelle de cette orientation tridimensionnelle. Il est démontré que la formation d'image pour les dipôles peut être représentée à travers la combinaison de six fonctions, à partir desquelles un filtre orientable 3-D est dérivé pour l'estimation conjointe de l'orientation et de la position. Une validation expérimentale démontre la faisabilité de cette approche, avec des résultats d'une précision de l'ordre du nanomètre pour la position et de l'ordre du degré pour l'orientation. Des limites théoriques pour la précision de localisation sont établies dans le cadre d'une analyse statistique basée sur des bornes de Cramér-Rao. Un modèle de bruit pour la microscopie à fluorescence basé sur une distribution de Poisson décalée est proposé.

Dans le cadre de ces méthodes de localisation, les paramètres d'aberration dans la PSF sont supposés connus. Cependant, les modèles de PSF physiquement exacts dépendent d'un nombre élevé de paramètres qui ne peuvent généralement pas être déterminés avec une précision suffisante, ce qui peut limiter leur application pour la localisation ou la déconvolution. Un algorithme d'estimation analogue à la localisation est proposé pour le calibrage d'un modèle par rapport à des mesures expérimentales; basé sur une expression légèrement simplifiée, le modèle résultant reproduit correctement le comportement variant par décalage des PSFs expérimentales.

Enfin, il est démontré que ces méthodes peuvent être adaptées à des expériences plus complexes, telles que l'imagerie d'échantillons épais en microscopie à champ large. Un algorithme de profondeur de champ étendue pour la fusion d'information focalisée extraite d'images acquises à différentes positions focales est présenté. Il est basé sur une représentation de la surface de l'échantillon en fonctions spline, et produit une version continue et super-résolue de la topographie de l'échantillon.

Mots-clés

Déconvolution, Extension de profondeur de champs, Filtres orientables, Fluorescence, Imagerie 3-D, Microscopie, Molécules individuelles, Orientation, Réponse impulsionnelle, Super-résolution

To Eva, Michel & Julien

Contents

Abstract	i
Résumé	iii
List of notations	xiii
1 Introduction	1
1.1 Super-resolution in optical microscopy	2
1.1.1 Super-resolution through localization	2
1.2 Fluorescence localization microscopy	4
1.3 Contributions of the thesis	7
1.4 Organization of the thesis	8
2 Fluorescence microscopy	9
2.1 Introduction	9
2.2 Fluorescence	11
2.2.1 The physical principles of fluorescence	11
2.2.2 The green revolution	12
2.3 Microscopes	17
2.3.1 The widefield microscope	17
2.3.2 The confocal scanning microscope	20
2.3.3 Sample setup and aberrations	21
2.4 Detectors	22
2.4.1 Characteristic parameters of detection systems	22
2.4.2 Detection technologies	23
2.5 Limitations	25
2.5.1 Noise sources	26
2.5.2 Sample-dependent limitations	26
2.6 Fluorescence Techniques	27
2.6.1 FRET	28
2.6.2 FRAP	28
2.6.3 FLIM	29

2.7	Signal Processing	30
2.7.1	Data size and dimensionality	30
2.7.2	Image preparation	31
2.7.3	Restoration	32
2.7.4	Registration	33
2.7.5	Segmentation	34
2.7.6	Quantitative analysis	35
2.8	Trends	36
2.8.1	Fluorescent labels	36
2.8.2	Advanced microscopy systems	37
2.9	Conclusion	39
3	Image formation in optical microscopy	41
3.1	Imaging modalities	42
3.1.1	Fresnel-Kirchhoff diffraction	44
3.1.2	Diffraction in the microscope: Born & Wolf model . .	46
3.1.3	Defocus model	48
3.1.4	Resolution and depth of field	49
3.2	Gibson & Lanni Model	51
3.2.1	Original analysis	52
3.2.2	Alternative formulation	54
3.3	Vectorial Models	56
3.4	PSF characteristics	57
3.5	Implementation	60
3.6	Conclusion	62
4	2-D Localization: PSF- vs. Gaussian-based approaches	63
4.1	Image formation	64
4.1.1	Discretization and pixelation	65
4.2	Signal-to-noise ratio	65
4.2.1	Simulations	66
4.3	Localization accuracy	66
4.3.1	Fisher information and the Cramér-Rao bound	67
4.4	Results and discussion	69
5	Axial localization of fluorescent nanoparticles	71
5.1	Introduction	71
5.1.1	Review of computational approaches	72
5.1.2	Organization of the chapter	73
5.2	Materials and methods	74
5.2.1	Notations and conventions	74
5.2.2	Simulation parameters and experimental setup . . .	74

5.2.3	Image formation model	75
5.2.4	Theoretical Bounds	78
5.2.5	A maximum likelihood estimator for axial localization	80
5.2.6	Localization in three dimensions	82
5.3	Results	82
5.3.1	Calibration and experimental setup	84
5.3.2	Extension of the statistical noise model	85
5.3.3	Validation with real data	86
5.3.4	Optimal acquisition settings	88
5.4	Discussion	89
5.4.1	Influence of the PSF model	91
5.4.2	Shortcomings and possible extensions of the method	92
6	3-D localization of fluorescent nanoparticles	95
6.1	Introduction	95
6.2	Theoretical bounds	95
6.3	Maximum-likelihood estimator	96
6.4	Results	97
6.4.1	Properties of the CRB	97
6.4.2	Estimation results	100
7	Steerable filter-based localization of fluorescent dipoles	103
7.1	Introduction	103
7.1.1	Localization of fluorescent dipoles	104
7.1.2	New approach based on 3-D steerable filters	105
7.1.3	Organization of the paper	106
7.2	Image formation	106
7.2.1	Noise model	110
7.2.2	Pixelation	111
7.3	Dipole localization using steerable filters	111
7.3.1	Orientation estimation	113
7.3.2	Sub-pixel position estimation	114
7.3.3	Joint estimation algorithm	114
7.4	Dipole localization accuracy	115
7.4.1	Performance of the algorithm	116
7.5	Results	116
7.5.1	Experimental setup	116
7.5.2	Evaluation	118
7.6	Discussion	120
7.7	Conclusion	122

8	Experimental calibration of an axially shift-variant PSF	123
8.1	Introduction	123
8.2	Image formation model	125
8.2.1	PSF model	125
8.3	Maximum-likelihood estimation framework	127
8.4	Estimation of the model parameters	127
8.5	Simplified OPD model	128
8.6	Estimation algorithm	129
8.6.1	Focal shift compensation	129
8.6.2	Iterative approach based on two measurements	130
8.7	Results	131
8.7.1	Experimental setup	131
8.7.2	Calibration results	132
8.7.3	Validity of the method for arbitrary measurements	135
8.8	Discussion	135
9	Model-based 2.5-D deconvolution for extended depth of field	137
9.1	Introduction	137
9.1.1	Review of previous work	138
9.1.2	Towards a new model-based approach	139
9.1.3	Organization of the chapter	140
9.2	Image formation in brightfield microscopy	140
9.3	Joint texture and topography estimation	142
9.3.1	Texture estimation	142
9.3.2	Topography estimation	144
9.3.3	Coarse-to-fine optimization	145
9.3.4	Implementation	146
9.3.5	Refinements for processing color data	147
9.4	Theoretical PSF model	148
9.5	Results	149
9.5.1	Performance comparison in simulation	150
9.5.2	Results on experimental data	151
9.6	Discussion	155
9.6.1	Sensitivity to the PSF model parameters	156
9.6.2	Computational aspects	157
9.7	Conclusion	157
10	Conclusion	159
10.1	Summary of results	159
10.2	Outlook for future research	160

A	Derivatives of the PSF models	163
A.1	Scalar model	163
A.2	Vectorial model	166
B	Bessel functions	167
C	Dipole model	169
C.1	Quartic equations for orientation estimation	169
C.2	Derivatives of the dipole model	172
D	Dipole imaging setup	173
	Acknowledgements	175
	Bibliography	177
	Curriculum Vitæ	189

List of notations

Symbols

A	Amplitude
a	Aperture radius
α	Angular aperture
b	Mean value of the background signal
$\beta^n(x)$	B-spline of degree n
c	Photon count conversion coefficient
$\delta(x)$	Dirac delta
δz	Defocus
\mathcal{E}	Electric field vector
ε_0	Permittivity of free space
f	Focal length
\mathcal{H}	Magnetic field vector
h	Intensity point spread function
h_λ	Amplitude point spread function
θ_p	Zenith angle of a dipole
i	$\sqrt{-1}$
J	Cost function
$J_n(z)$	Bessel function of the first kind of degree n
$\mathbf{k} = (k_x, k_y, k_z)$	Wavevector
$k = 2\pi/\lambda$	Wavenumber
Λ	Optical path difference
λ	Wavelength
λ_{em}	Emission wavelength
λ_{ex}	Excitation wavelength
M	Magnification
μ_0	Permeability of free space
n	Refractive index
\mathbf{p}	Dipole moment
$\phi = \tan^{-1}(y/x)$	Azimuth angle in the detector plane
ϕ_p	Azimuth angle of a dipole
q	Photon count

\bar{q}	Average photon count
r	Radius in the detector plane
ρ	Normalized radius in the exit pupil
σ	Standard deviation
\mathcal{S}	Support, $\mathcal{S} \subset \mathbb{Z}^2$ or $\mathcal{S} \subset \mathbb{Z}^3$
t_p	Parallel Fresnel transmission coefficient
t_s	Orthogonal Fresnel transmission coefficient
τ	PSF parameters
$U(\mathbf{x})$	Complex wave
$\mathbf{x} = (x, y, z)$	Object space coordinates
ξ, η, ζ	Image space coordinates
Ω	Domain, $\Omega \subset \mathbb{R}^2$ or $\Omega \subset \mathbb{R}^3$

Operators

$*$	Convolution operator
v^*	Complex conjugate of v
v^T	Hermitian transpose of v
\Im	Imaginary part
\Re	Real part

Acronyms

CRB	Cramér-Rao Bound
EDF	Extended Depth of Field
FLM	Fluorescence Localization Microscopy
FIONA	Fluorescence Imaging with One Nanometer Accuracy
GFP	Green Fluorescent Protein
MLE	Maximum-Likelihood Estimator
NA	Numerical Aperture
OPD	Optical Path Difference
PALM	Photo-Activated Localization Microscopy
PSF	Point Spread Function
PSNR	Peak Signal to Noise Ratio
SNR	Signal to Noise Ratio
SPT	Single Particle Tracking
STORM	Stochastic Optical Reconstruction Microscopy
TIRF(M)	Total Internal Reflection Fluorescence (Microscopy)

Chapter 1

Introduction

The discovery of the green fluorescent protein (GFP) in a jellyfish species by Osamu Shimomura in 1961 is at the origin of a series of breakthroughs that enabled the labeling of single proteins in living cells. In 1993, Martin Chalfie used newly developed gene cloning techniques to express GFP in *C. elegans*, which demonstrated fluorescence labeling in a living organism for the first time. Subsequently, Roger Tsien showed that GFP and similar naturally occurring proteins can be engineered to fluoresce at different wavelengths, leading to a wide variety of alternative fluorescent markers. As a result of these innovations, which were awarded the 2008 Nobel prize in Chemistry, it has become feasible to study *in vivo* protein dynamics and interactions using fluorescence microscopy. Resolution limits restricted these studies to processes occurring at the scale of sub-cellular structures, however. This motivated the development of optical imaging techniques that could circumvent or break the diffraction barrier of classical optics, and played a key role in fostering the development of modern fluorescence microscopy.

The diffraction limit was defined by Abbe as

$$d = \frac{\lambda}{2n \sin \alpha}, \quad (1.1)$$

where λ is the imaging wavelength, n is the refractive index of the medium, and α is the angular aperture of the system [1]. For a typical high-end system using an oil-immersion objective with a high numerical aperture ($\text{NA} = n \sin \alpha$), the limit is approximately 200 nanometers. Objects that are closer than this distance can therefore not be resolved. A system capable of discerning individual molecules would require a resolving power greater by at least an order of magnitude.

High-resolution imaging can be achieved with electron microscopy, where the wavelength of the electron beam is sufficiently small to resolve

molecular and even atomic structures. Unfortunately, the energies associated with these wavelengths are destructive for biological samples, and preclude electron microscopy from imaging living specimens. Furthermore, electron microscopy lacks highly specific markers analogous to fluorescent proteins.

In recent years, several optical imaging approaches succeeded in bypassing the diffraction barrier. They can be broadly categorized into two complementary classes: purely physics-based methods where resolution is improved through minimization of the excitation volume, and hybrid methods that combine novel illumination schemes with image processing in order to produce super-resolved images. Approaches from both categories take advantage of the fact that light emission in fluorescent samples can be precisely controlled through excitation, and their application is thus intrinsically limited to fluorescence microscopy.

1.1 Super-resolution in optical microscopy

Physics-based methods comprise some well established techniques, including confocal microscopy [2], 2-photon microscopy [3], and 4-Pi microscopy [4]. These are primarily designed to improve axial resolution, in order to achieve better optical sectioning of thick specimens. A breakthrough was reached with the invention of stimulated emission depletion (STED) microscopy [5], which exploits the quantum properties of fluorescence to generate highly confined excitation volumes that are considerably smaller than a diffraction-limited spot. Recent refinements of STED have led to isotropic resolutions slightly below 50 nanometers [6]. Despite the improvement in resolution over conventional optics, however, resolutions at the single-molecule scale are still beyond the scope of these techniques. Deconvolution can be applied to further improve image quality [7], but due to noise and the lack of high frequency information, the potential gain in resolution is not sufficient to resolve individual fluorophores.

Structured illumination is one of the first hybrid techniques to rely on signal processing to produce an image; by fusing frequency information from a set of images acquired through modulated excitation [8, 9], recent incarnations of the technique achieve resolutions down to 100 nm, both in the lateral and axial directions [10, 11].

1.1.1 Super-resolution through localization

The image of a single fluorescent molecule corresponds to a section of the three-dimensional (3-D) point spread function (PSF) of the microscope. As-

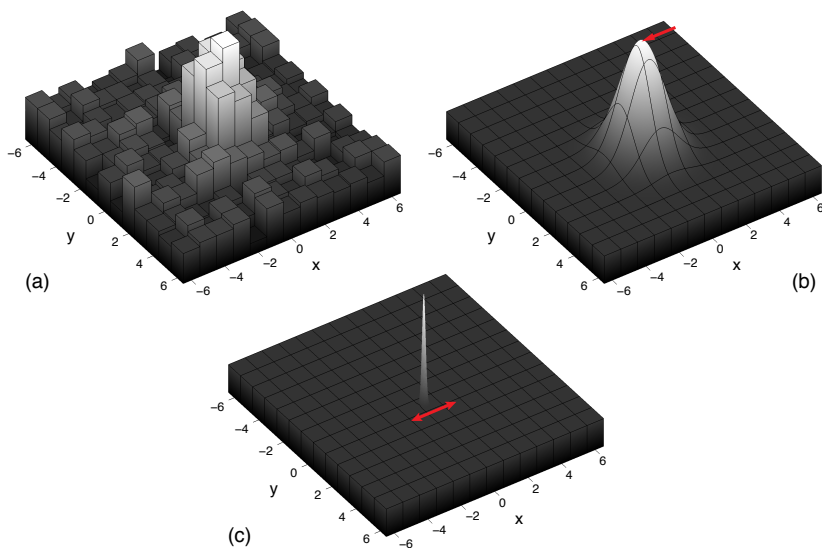


Figure 1.1 Illustration of model-based super-resolution localization. (a) Simulated acquisition of a single fluorescent molecule. The image corresponds to a noisy section of the PSF. (b) A Gaussian fit to the acquisition yields a precise sub-pixel position. The shape of the Gaussian is determined by the PSF. (c) The super-resolved Gaussian peak. Its standard deviation corresponds to the localization accuracy, which essentially depends on the detected number of photons (and thus by on the SNR of the image) and on the validity of the Gaussian approximation of the PSF. Pixel size: 100 nm.

suming that it is possible to formulate a model of the PSF, the position of the fluorophore can be computed by fitting this model to an image of the molecule. If the model is correct, this results in a localization accuracy that is well beyond the size of the original diffraction-limited spot [12]. In the case of 2-D imaging, the in-focus section of the PSF is well approximated by a Gaussian function, which renders the localization of individual molecules straightforward and computationally efficient. The general principle behind the ensuing gain in resolution is illustrated in Fig. 1.1. For localization-based techniques, resolution is generally defined in terms of localization accuracy, which essentially depends on the number of photons emitted by the fluorophore, and, consequently, on the signal-to-noise ratio (SNR).

Single molecule localization techniques were initially applied in the context of single particle tracking (SPT), where the gain in resolution enabled the study of single protein dynamics [13–15]. In particular, it rendered imaging-based studies of molecular motors moving at nanometer and sub-nanometer scales possible. Yildiz et al. used Gaussian-based localization to precisely analyze the motion of actin molecules and to deduce their displacement mechanism in an investigation of the progression of actin molecules on myosin V [16]. Localization accuracies of 1.5 nm were reported

in that study, and are among the best localization accuracies obtained to date in an experimental investigation of a biological process. The localization technique was termed fluorescence imaging with one nanometer accuracy (FIONA). The success of these methods led to rigorous investigations of the limits on localization accuracy in SPT [13, 17, 18].

Most SPT experiments are carried out in total internal reflection fluorescence microscopy (TIRFM), which combines the advantage of good optical sectioning properties (100-200 nm depth below the coverslip) with a weak background excitation. Relatively high SNRs for single molecules can be achieved in TIRFM, but studies are essentially limited to 2-D processes. The PSF varies little over the imaging range and is assumed to be well approximated by a Gaussian.

1.2 Fluorescence localization microscopy

Imaging of individual fluorophores within densely labeled samples became possible with the discovery of fluorophores that can be photo-activated (e.g., photo-activatable GFP [19]) or switched between a fluorescent and a dark, non-fluorescent state (e.g., Cy3-Cy5 pairs [20]). Upon excitation at a specific wavelength, these molecules become fluorescent at a (usually) different wavelength. The switching/activation process is stochastic, with its rate depending on the energy of the excitation pulse. By appropriately tuning this energy, the activation of a sparse subset of fluorophores in the sample can be triggered. Individual molecules then appear as isolated spots, and can be imaged until they bleach or switch back to their dark state. Subsequently, the Gaussian localization techniques developed for SPT can be applied to estimate the position of each molecule with super-resolution accuracy. By repeating this process for a sufficiently large amount of fluorophore subsets and by combining the resulting positions into a single frame, a super-resolved image of the sample can be generated. This process forms the basis of fluorescence localization microscopy (FLM).

The first experimental demonstrations of FLM were the result of simultaneously developed approaches called photo-activated localization microscopy (PALM) [21], fluorescence photoactivation localization microscopy (FPALM) [22], and stochastic optical reconstruction microscopy (STORM) [23]. These methods are based on standard TIRF excitation, which, combined with the high acquisition times required to record the fluorophore subsets, initially limited their application to imaging 2-D sections of fixed cells.

Many recent developments have improved on these initial limitations, rendering FLM much more versatile. Advances in chemistry are yielding

Resolution		Method	Excitation	Modality	Year
Lateral	Axial				
1.5 nm	N/A	FIONA [16]	TIRF	Localization	2003
20 nm	N/A	PALM [21]	TIRF	Localization	2006
20 nm	N/A	STORM [23]	TIRF	Localization	2006
20 nm	N/A	Pointillism [24]	Widefield	Localization	2005
20 nm	20 nm	iPALM [25]	4-Pi	Hybrid	2009
25 nm	—	STED [5]	STED	Optical	1994
30 nm	60 nm	3D STORM [26]	TIRF	Hybrid	2008
30 nm	75 nm	BP FPALM [27]	Widefield	Localization	2008
50 nm	50 nm	isoSTED [6]	STED	Optical	2008
50 nm	N/A	PALMIRA [28]	Widefield	Localization	2007
65 nm	N/A	live PALM [29]	TIRF	Localization	2008
80 nm	N/A	FPALM [22]	Widefield	Localization	2006
100 nm	100 nm	I ⁵ S [10]	Widefield	Struct. illum.	2008
100 nm	350 nm	2-photon [3]	2-photon	Optical	1990
200 nm	100 nm	4-Pi [30]	4-Pi confocal	Optical	1990
200 nm	100 nm	I ⁵ M [9]	Widefield	Struct. illum.	1999
200 nm	500 nm	Confocal [2]	Confocal	Optical	1957
200 nm	700 nm	Diff. limit. [1, 31]	Widefield	Optical	1848

Table 1.1 Resolution across imaging modalities. For the localization methods, resolution is based on localization accuracy. The diffraction limited resolution criterion is given for $\lambda = 450$ nm. N/A for axial resolution signifies that the method as published is limited to 2-D imaging. A dash indicates absence of published information. Hybrid methods combine a specific optical setup with localization. The widefield denomination stands for standard epifluorescence microscopy.

a wider range of switchable fluorophores compatible with FLM [32, 33]. Notably, FLM approaches relying on photo-switching of a single dye have been reported: PALMIRA based on rs-FastLime molecules [28] and dSTORM based on Cy5 [34]. Combinations of different photo-switchable fluorophores have enabled extensions of FLM to multispectral imaging [33, 35–37].

Extensions to 3-D based on astigmatic imaging have been suggested [26, 38]. Inclusion of a cylindrical lens in the optical train of the microscope results in an elliptically distorted PSF, whose shape and orientation depend on the molecule’s axial position. Axial localization is then performed through a combination of bivariate Gaussian fitting and empirical calibration. Although these approaches demonstrate the feasibility of axial localization based on the PSF, they are limited in range and subject to bias due to their reliance on an empirical reference. FPALM based on polarization imag-

ing was developed in order to recover the orientation of single fluorophores in addition to their position [39].

Long acquisition times are another intrinsic limitation of FLM. The initial results obtained with PALM required imaging over several hours to generate a single image. Significant accelerations of the switching/activation/bleaching cycles have now reduced acquisition times by an order of magnitude. Further pushing acquisition times will eventually result in the activation of denser sets of fluorophores, with a higher probability of overlap between their images. While essentially all implementations of FLM rely on Gaussian fitting, other alternatives that prove more effective in isolating individual molecules have been suggested. An approach based on independent component analysis that exploits the blinking nature of quantum dots to segment and localize individual sources in dense groups yields resolutions of the same order as Gaussian localization-based methods [24].

With the acquisition time reduced to the scale of minutes, recent proof-of-concept experiments have demonstrated live-cell imaging in the context of slowly evolving cellular processes [29, 40, 41]. Adapting FLM and especially STORM-based techniques to *in vivo* imaging remains a challenge due to the toxicity of sample preparation.

The resolutions achieved by the various imaging approaches presented in this overview are summarized in Table 1.1. For most of the localization-based methods, resolution was assessed in terms of structures with known dimensions, and is not necessarily equivalent to localization accuracy.

To date, the highest resolutions are achieved by methods that are essentially limited to 2-D imaging. This can be attributed to the difficulty of extending Gaussian-based localization techniques to 3-D; the principal obstacle is the lack of a similarly simple model which approximates the PSF.

Due to the relative complexity of the PSF of modern microscopes, few PSF-based methods for 3-D localization have been proposed. However, axial localization based on the radius of the outermost diffraction ring observed in defocused images of single fluorescent particles was experimentally shown to reach accuracies at the nanometer scale [42]. Although this approach makes some simplifying assumptions that limit its applicability, it demonstrated the possibility of axial localization based on a more sophisticated model.

Furthermore, as will be discussed in Chapter 7, the Gaussian approximation of the PSF is not necessarily valid for fluorophores that lie in the focal plane of the microscope. If the molecule is immobile during image acquisition, the observed diffraction spot may be shifted by as much as several tens of nanometers with respect to the fluorophore's position, inducing a severe bias in Gaussian-based localization results [43].

1.3 Contributions of the thesis

The research presented in this thesis was instigated by an investigation of the feasibility of super-resolved axial tracking (that is, localization in the depth dimension) based on an accurate PSF model. Various results demonstrate the potential of this philosophy to outperform instrumentation-based FLM techniques for both 3-D and orientation-based imaging. The contributions of the thesis fall into the following categories:

- **Single molecule localization** A framework for super-resolution localization of single fluorescent molecules based on a physically accurate image formation model is described. It contains two central results: a maximum-likelihood method for 3-D localization [44] and a method for the joint orientation and position estimation of fluorescent dipoles [45]. Orientation estimation in the latter is described as the optimization of a 3-D steerable filter. Both methods are based on off-focus imaging; the second relies on fluorophores that are immobile during image acquisition. Theoretical limits on localization accuracy are formulated using Cramér-Rao bounds. These bounds show that nanometer-scale accuracies are possible, and help establish the experimental conditions under which these accuracies can be reached. Experimental results that corroborate these theoretical limits are presented; accuracies of the order of one nanometer for lateral localization, ten nanometers for axial localization, and one degree for orientation estimation are reported.

These results demonstrate the feasibility of super-resolved 3-D single molecule position and orientation estimation based on a physically realistic PSF model for the first time. The reported estimation accuracies suggest that this type of localization approach has the potential to outperform currently existing super-resolution fluorescence microscopy techniques.

- **Image formation in optical microscopy** A physically realistic depth-dependent PSF model is formulated in such a way that it can be applied to super-resolution axial localization, as well as shift-variant deconvolution. The model is extended for fluorescent dipoles and shown to decompose into six basis functions that decouple from the dipole's orientation, which renders the calculation of dipole diffraction patterns highly efficient [45]. An algorithm for the estimation of unknown parameters in these PSFs is proposed; it relies on a maximum-likelihood framework analogous to the one introduced for localization [46]. A fast numerical implementation of these models is

described; it accelerates computations by at least an order of magnitude with respect to competing approaches.

- **Extended depth of field imaging** Due to the shallow depth of field of high-NA objectives, high-resolution brightfield imaging of thick samples usually requires multiple acquisitions that each capture a different section of the sample in focus. Analysis of the resulting image stack is cumbersome, and topographical information reduced to discrete positions in the stack. The fusion of in-focus information and generation of a continuous topography is formulated as a 2.5-D deconvolution problem in a setting that extends the previously introduced localization methods to more complex object models [47]. This is the first extended-depth-of-field method designed to estimate a continuous and super-resolved topography of specimens, enabling their 3-D visualization and facilitating their analysis.

1.4 Organization of the thesis

In Chapter 2, we present a general introduction to fluorescence microscopy that includes a historical overview and a discussion of present and future challenges for the development of hybrid signal processing and optics-based imaging techniques. The various microscopy modalities discussed in this introduction are also described in greater detail. Chapter 3 is a comprehensive review of image formation in optical microscopes, where we show how state-of-the-art PSF models are derived from Maxwell's equations and expanded to accurately reproduce the axially shift-variant behavior of experimentally observed PSFs. In Chapter 4, we compare Gaussian- and PSF-based localization techniques, and show that the latter present advantages over the former under most conditions, except when fluorophores are imaged perfectly in focus, where both approaches lead to statistically equivalent results. Based on the PSF model presented in Chapter 3, we describe a method for super-resolved axial localization of single fluorophores in Chapter 5. We discuss extensions of this method to 3-D localization in Chapter 6, and expand localization to incorporate orientation estimation for fluorescent dipoles in Chapter 7. In Chapter 8, we present an algorithm for matching an axially shift-variant PSF model to experimental measurements. Finally, in Chapter 9, we propose an algorithm for extended-depth-of-field imaging based on z-stack acquisitions. We conclude the thesis with a summary of results and a discussion of potential directions for future research.

Chapter 2

Fluorescence microscopy

2.1 Introduction

The discovery of fluorescent labels suitable for *in vivo* use and the development of high-resolution microscopes have transformed the fluorescence microscope into a mainstream tool, bringing about a revolution for biological imaging, and having a profound impact on the way research is being conducted in the life sciences. Among a myriad of new imaging possibilities, sub-cellular components and processes can now be visualized *in vivo*, both structurally and functionally. Observations can be made in two or three dimensions, at different wavelengths (spectroscopy), and, for the investigation of dynamic processes, using time-lapse imaging.

The observation of many biological processes relies on the ability to identify and locate specific proteins within their cellular environment. Cells are mostly transparent in their natural state, and the immense number of molecules that constitute them are optically indistinguishable from one another. This makes the identification of a particular protein a very complex task—akin to finding a needle in a haystack. However, if a bright marker were attached to the protein of interest, it could very precisely indicate its position. Much effort has gone into finding suitable markers for this purpose, but it is only over the course of the past decade, with the advent of fluorescent proteins, that this concept has been revolutionized. These biological markers have the crucial properties necessary for dynamic observations of living cells: they are essentially harmless to the organism, and can be attached to other proteins without impacting their function.

This chapter is based on: F. Aguet et al., “An introduction to fluorescence microscopy: basic principles, challenges, and opportunities,” in *Microscopic Image Analysis for Life Science Applications*, J. Rittscher, R. Machiraju, and S. T. C. Wong, Eds. Artech House, 2008, ch. 4, pp. 85–114, [48, 49].

Fluorescence microscopy was invented almost a century ago, when microscopists were experimenting with ultraviolet light to achieve higher resolutions. In the very beginning, observations were limited to specimens that naturally fluoresce¹. Rapidly, fluorescent dyes for staining tissues and cells were investigated. But it was not until the 1940s that fluorescence microscopy became popular, when A. Coons and M. Kaplan introduced a technique to label antibodies with a fluorescent dye to study antibody-antigen interactions, which profoundly changed the field of immunohistochemistry [50]. The discovery that really brought fluorescence microscopy to the forefront came in 1994, when M. Chalfie et al. succeeded in expressing a naturally fluorescent protein, the now famous green fluorescent protein (GFP), in living organisms [51]. This was a landmark evolution in the field, fostering a whole new class of tagging methods.

While genetic engineering is at the origin of this new methodology, a number of innovations from the fields of physics, optics, mechanical and electrical engineering have been combined to provide the necessary instrumentation. Impressive enhancements in classical microscopy have been achieved, and new imaging systems are actively being developed. A key element for the evolution of microscopy in general was the shift to digital imaging in the 1990s, with the availability of affordable high-sensitivity acquisition devices and powerful computer hardware.

The capabilities of today's systems often lead to enormous data sets that, in most cases, require post-processing for their interpretation. Signal processing methods for biological research are only at their prelude; the needs are considerable and most probably not even clearly formulated yet. It is thus predictable that signal processing will be one of the main challenges of fluorescence microscopy in the forthcoming years.

The ambition of this chapter is to provide the reader with an introduction covering the key aspects of modern fluorescence microscopy. We begin by recalling the principles of fluorescence, and review the history of discoveries that led to the instruments and techniques in use today. Next, we present the optics and examine various types of detectors used in fluorescence microscopy. A further section is devoted to a discussion of signal and image processing challenges in fluorescence microscopy, and finally, we highlight some current developments and future perspectives in the field.

¹This property is called autofluorescence or primary fluorescence.

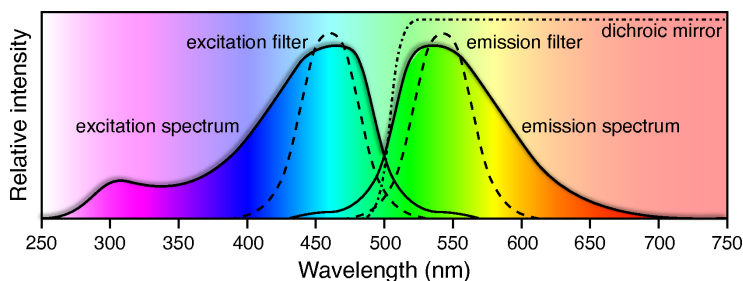


Figure 2.1 Representation of typical excitation/emission spectra of a fluorophore (in relative intensities). The excitation spectrum shows the emission intensity as a function of excitation wavelength, and the emission spectrum shows the relative emission intensities as a function of emission wavelengths for an excitation at the peak absorption wavelength. Explanations on the filters are given in Section 2.3.

2.2 Fluorescence

2.2.1 The physical principles of fluorescence

Definition

Fluorescence is a phenomenon by which a molecule, upon illumination at a specific wavelength, reemits light at another (typically longer) wavelength. A molecule that has the ability to fluoresce is called a fluorophore or fluorochrome². It has distinctive excitation and emission spectra (see Fig. 2.1), although in practice, it is often characterized by the two wavelengths corresponding to the respective peak intensities of these spectra.

A molecule can exist in a variety of energetic states, which, for the most part, are determined by the configuration of its electrons and the vibrational agitation of its atomic nuclei. If a photon with sufficient energy is absorbed by a fluorophore, the latter moves from its ground state to an excited electronic state (see Fig. 2.2a). Fluorescence occurs when the excited molecule returns to the ground state by releasing energy through emission of a photon. Because some of the energy gained during excitation is converted to heat, the emitted photon has a lower energy than the absorbed one. This explains the difference in wavelength mentioned earlier (since $E = h\nu = hc/\lambda$), which is also known as the Stokes shift. Fluorophores whose spectra present a large Stokes shift are usually preferred since their emitted light can be separated from the excitation light more easily by the means of optical filters (see Fig. 2.1).

²Specifically, the former describes an atomic compound responsible for fluorescence, while the latter is a more general term for a dye that renders a body fluorescent.

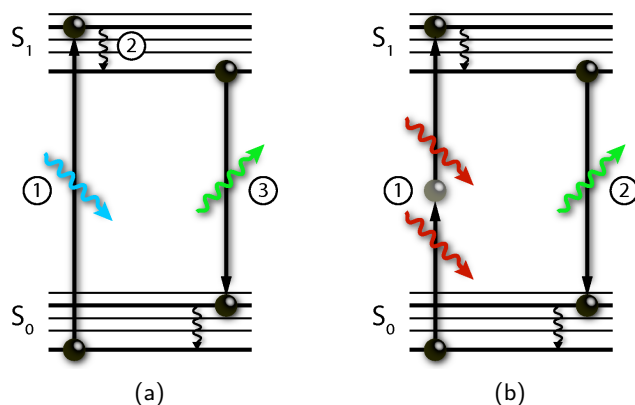


Figure 2.2 Jablonski diagrams representing the energy-level transitions involved in fluorescence. Thick lines represent electronic energy levels; thin ones are associated vibrational energy levels. (a) Upon absorption of a photon at a specific wavelength (blue), the molecule moves from the ground state S_0 to the excited state S_1 (1). Vibrational energies are immediately converted into heat in a process called vibrational relaxation (2). When the molecule returns to the ground state, the remaining energy is released via emission of a new photon at a longer wavelength (green). (b) In two-photon excitation, the simultaneous absorption of two photons at twice the excitation wavelength (1) leads to the same excited state and thus to emission at the same wavelength (2) as in single photon excitation.

Related phenomena

When in an excited state, a fluorophore can be forced to the ground state in a process called stimulated emission. Upon absorption of a second photon at the excitation wavelength, the molecule returns to the ground state by emitting two photons that are in phase and whose wavelengths are identical to the second photon's wavelength. This phenomenon is relevant to some of the concepts discussed later, but is best known as the light-amplification principle behind lasers.

Another important concept is that of multiphoton excitation. A fluorophore can also be excited by the simultaneous absorption of two or more photons, given that the combined energy of the photons corresponds to the energy required for single-photon excitation (see Fig. 2.2b). In this particular situation the excitation wavelength is longer — in the case of two-photon excitation, twice as long as the single-photon excitation wavelength.

2.2.2 The green revolution

The developments that had the biggest impact on biological research and made fluorescence microscopy ubiquitous took place during the past two decades. Consequently, we shall focus on this period for the remainder of

this section. However, these recent developments could not have occurred without previous discoveries and inventions in a variety of fields, starting in the 16th century. An overview of events that played an essential role in contributing to the development of modern fluorescence microscopy is given in the form of a timeline in Tables 2.1 and 2.2.

In the early 1990s, fluorescence labeling techniques such as immunofluorescence³ and covalent marking⁴ were already widely in use for imaging. However, a straightforward means for selectively labeling a given protein with a non-perturbing fluorescent marker was not yet available. Only such a tag would make the *in vivo* observation of interactions between a specific protein with other proteins and the environment feasible.

The breakthrough came in 1994, when Chalfie et al. [51] succeeded in expressing a fluorescent protein that naturally occurs in a jellyfish species in other organisms by modifying their genome to code for this protein. At the origin of this innovation, accordingly dubbed “the green revolution” [63], was the discovery of GFP by Shimomura et al. in 1961 [64]. During their studies of the jellyfish *aequorea victoria*, whose fluorescing nature was described for the first time in 1955, they discovered that the source of the fluorescence was a naturally produced protein. Its chemical structure was reported by Shimomura in 1979, and in 1992, Prasher et al. cloned and determined its genetic sequence [65], paving the way for the work of Chalfie et al.

Since the first experiments with GFP, many variants have been engineered and discovered. From the naturally occurring GFP, called wtGFP for wild-type GFP, and from similar fluorescent proteins occurring in other marine organisms, new, more powerful mutants have been derived. Their properties range from different excitation and emission spectra⁵ to stronger fluorescence and higher resistance to photobleaching [66]. Two widespread examples are cyan fluorescent protein (CFP) and yellow fluorescent protein (YFP), named for their characteristic emission spectra.

Biologists can label virtually any desired protein with a fluorescent protein by means of straightforward procedures. The first step leading to the creation of a labeled protein is to append the marker protein’s sequence to that of the target. The resulting sequence is then introduced into cells, where its transcription results in the synthesis of a fusion protein. A common means

³A technique (also called immunostaining) for detecting an antigen (protein) with a fluorochrome-labeled antibody.

⁴Proteins are purified, covalently labeled with a fluorescent molecule, and then introduced into cells.

⁵The currently available fluorescent protein tags offer a wide choice of wavelengths within the visible spectrum.

1565	Nicolás Monardes observes luminescence in the extract of the wood <i>lignum nephriticum</i> , a substance then used for treating kidney ailments.
1609	Galileo Galilei develops the compound microscope.
1646	Athanasius Kircher relates that an infusion of <i>lignum nephriticum</i> reflects blue and transmits yellow light.
1800	Frederick William Herschel discovers infrared radiation.
1801	Johann Wilhelm Ritter discovers the ultraviolet region of the spectrum.
1833	David Brewster observes red radiation in a solution containing chlorophyll upon illuminating it with white light.
1845	John F. W. Herschel (the son of F. W. Herschel) discovers the phenomenon of fluorescence in a quinine solution.
1852	George Gabriel Stokes describes the luminescence observed in the fluorspar mineral as fluorescence, and formulates the Stokes law.
1871	Adolf von Baeyer discovers and synthesizes fluorescein, still widely used as a dye.
1873	Ernst Abbe formulates the theory that links resolution to the wavelength of light, and proposes the use of ultraviolet light to increase the resolution of microscopes [1].
1904	August Köhler and Moritz von Rohr develop the ultraviolet microscope. Autofluorescence observed in the visible domain starts the era of fluorescence microscopy.
1905	Albert Einstein describes the photoelectric effect [52].
1908	August Köhler and Henry Friedrich Wilhelm Siedentopf build and demonstrate the first fluorescence microscope.
1911	Max Haitinger coins the term fluorochrome to describe dyes that render non-fluorescent objects fluorescent. Numerous investigations into fluorescent dyes begin.
1911	The first commercialized fluorescence microscopes, using carbon arc lamps, are produced by Reichert (Otto Heimstädt and Carl F. W. Reichert, 1911) and Carl Zeiss (Heinrich Lehmann, 1913). Observations are limited to specimens that present autofluorescence.
1929	Philipp Ellinger and August Hirt propose a fluorescence microscope with epi-illumination for the observation of living organisms. They use the fluorochromes fryptaflavine, which stains cell nuclei, and fluorescein, to study kidney function [53].
1935	Alexander Jablonski presents his model to explain fluorescence.

Table 2.1 History of fluorescence microscopy, Part I.

1935	The first photomultiplier tube is built by Harley E. Iams and Bernard Salzberg [54].
1941	Albert Coons and Melvin Kaplan introduce immunofluorescence, a labeling method still in use today [50].
1946	Theodor Förster discovers fluorescence resonance energy transfer [55].
1957	Marvin Minsky submits his patent for the confocal microscope [2].
1958	Arthur L. Schawlow and Charles H. Townes invent the laser [56]
1960	The first functioning laser is built by Theodore Maiman [57].
1961	Osamu Shimomura et al. discover aequorin and GFP in the jellyfish <i>Aequorea</i> [58].
1969	George Smith and Willard Boyle invent the CCD.
1978	Colin J. R. Sheppard and Rudolf K. Kompfner propose the concept of two-photon fluorescence microscopy [59].
1980	John G. J. Bauman et al. introduce fluorescence <i>in situ</i> hybridization (FISH), a method for localizing specific genetic sequences by labeling RNA molecules with a fluorochrome [60].

Modern Era

1983	David A. Agard and John W. Sedat reconstruct chromosomes from <i>Drosophila</i> larvae using computer deconvolution [7].
1990s	Affordable digital imaging hardware becomes available, launching a new era in microscopy.
1990	Winfried Denk, James H. Strickler, and Watt W. Webb experimentally demonstrate two-photon microscopy [3].
1991	Joseph R. Lakowicz et al. describe fluorescence lifetime imaging (FLIM) [61].
1994	Martin Chalfie et al., and Satoshi Inouye and Frederick Tsuji express GFP in living organisms (<i>E. coli</i> and <i>C. elegans</i>) [51] [62].
1994	Stefan Hell and Jan Wichmann invent STED microscopy [5].
2006	Localization-based fluorescence microscopy [21–23] is made possible by the discoveries of photoactivatable [19] and photoswitchable [20] fluorophores. The resolutions achievable by these techniques rival electron microscopy. Current developments include extensions to 3-D imaging [26, 27], molecular orientation imaging, and time-lapse imaging [40, 41].

Table 2.2 History of fluorescence microscopy, Part II.

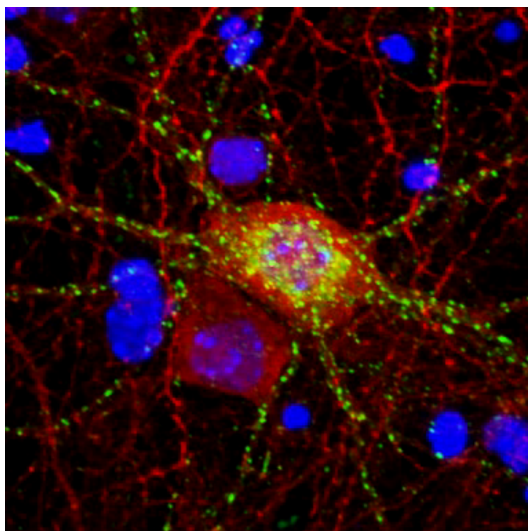


Figure 2.3 Image of a neuron where specific receptor proteins (delta opioid) have been fused with eGFP and appear in green. The red dots (GABA immunostaining) correspond to intracellular proteins located inside the neuron and its extensions. The nuclei of surrounding cells are stained in blue with DAPI, a fluorochrome that specifically binds to DNA. Courtesy of G. Scherrer, P. Tryoen-Toth and B. L. Kieffer, IGBMC, Illkirch, France.

for doing this is by placing the gene onto a plasmid⁶, which can then be taken up by a cell. Such plasmids exist for a wide range of fluorescent proteins and are available from specialized companies.

The fusion protein (Fig. 2.3) is expressed throughout the lifetime of the cell, as long as its sequence is present in the cell's nucleus. Note that this procedure typically results in the expression of both the fusion and natural versions of the protein, since the genetic sequence of the former does not replace that of the latter. Although the function and localization of the two variants are in most cases identical, it is necessary to verify that the label has no influence on cellular functions. For further details, we refer to [67, 68].

The availability of fluorescent protein tagging techniques led to a fundamental change in the way biological research is conducted and to an explosion of experimental possibilities (see also Section 2.6). For instance, within the past 10 years, the relative number of experiments dealing with live samples at the IGBMC imaging center (Illkirch, France) increased almost a hundred-fold.

⁶Plasmids are small, circular, double-stranded sequences of DNA that naturally occur in bacteria and are part of their genome. They can easily be introduced into cells, where they are expressed in the same fashion as chromosomal DNA. Plasmids are not replicated upon cellular division; however, in some cases they are integrated into the cell's chromosomal DNA.

2.3 Microscopes

We now turn our attention to the instrumentation for fluorescence imaging. This section provides a brief description of the two main types of image forming systems: widefield and confocal microscopes. While the former are usually less expensive than the latter (depending on the configuration), their optical resolution is intrinsically more limited, especially in the axial (i.e., z) direction. Both systems can yield volume images of the sample under inspection, possibly with the help of deconvolution. However, in widefield microscopes the volume is acquired plane by plane (as opposed to point by point in standard confocal systems), which allows for faster acquisitions.

2.3.1 The widefield microscope

Principle

Widefield microscopy is based on the paradigm of Köhler illumination, according to which the sample is observed under a uniform light beam. Fig. 2.4a shows how this is obtained in a simplified epi-illumination microscope: the light source (an arc or filament lamp) is magnified by the collector lens and projected onto the iris diaphragm. This aperture is located in a conjugate plane of the objective's back focal plane. Therefore the latter acts as a condenser lens and the intensity from the iris is uniformly distributed onto the sample.

Let us now consider a single point of the sample. It will reemit light by reflection and possibly by fluorescence. If located in the focal plane, this will generate a beam of parallel light rays through the microscope tube. The image is formed by integrating the effect of all secondary point sources within the specimen; it can be observed through the eyepiece, or recorded by placing a CCD sensor in the image plane.

One of the critical parameters in this setting is the numerical aperture (NA); that is, the angular opening of the light cone emerging from the object and collected by the objective. The magnification effect results from the combination of the objective, tube and ocular lenses.

Components for fluorescence imaging

Fluorescence imaging requires specific additional components for controlling the spectrum of the light (see also Fig. 2.1). While usual lamps produce “white light” (covering the whole visible spectra, with some peaks at characteristic wavelengths), the fluorescent sample has to be illuminated with a specific excitation wavelength. This is ensured by inserting an excitation

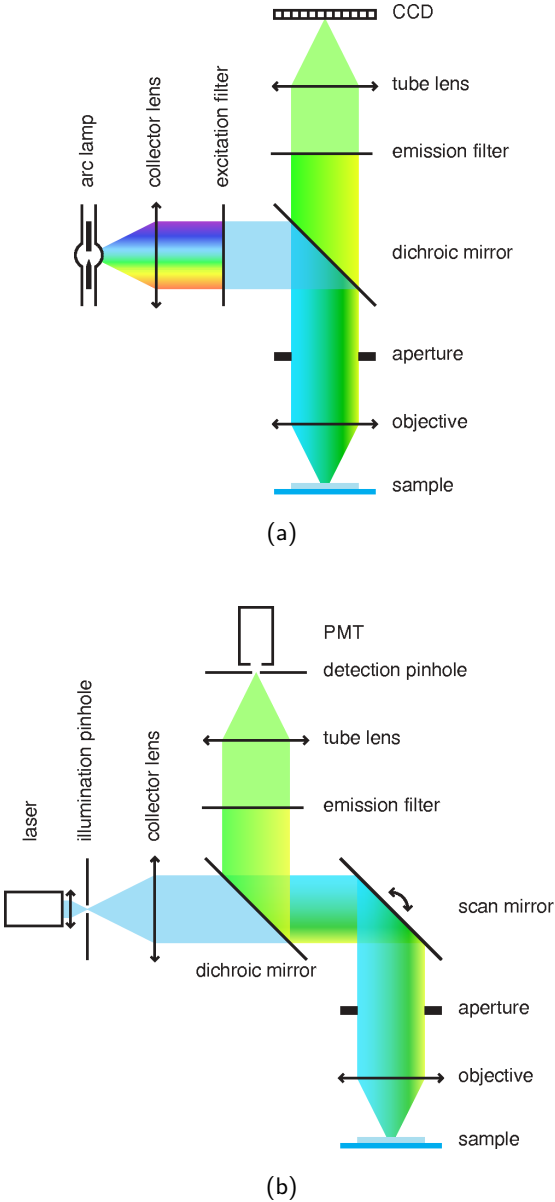


Figure 2.4 Schematics of widefield (a) and confocal (b) fluorescence microscopes, showing their main components. The illumination path is shown in blue (excitation at 395 nm) and the image-forming path in green (emission at 509 nm), to suggest the spectral composition of the different light beams in the case of a GFP-tagged sample.

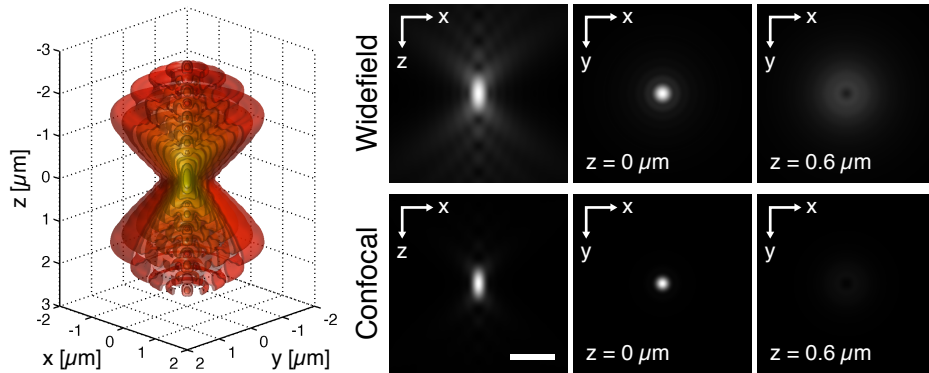


Figure 2.5 Cross-sections of the image of a fluorescent point source with a 1.4 NA objective (ideal 3-D intensity PSF). An isosurface representation of the 3-D PSF is shown on the left. The upper row corresponds to a widefield microscope ($|h_{\lambda_{\text{em}}}|^2$), and the lower row to a confocal system ($|h_{\lambda_{\text{ex}}}|^2|h_{\lambda_{\text{em}}}|^2$). Here $\lambda_{\text{ex}} = 395 \text{ nm}$ and $\lambda_{\text{em}} = 509 \text{ nm}$, which are the excitation and emission wavelengths of GFP. Scale bar: $1 \mu\text{m}$; units are given in object space.

filter in the illumination path. The emission filter, on the other hand, ensures that only the wavelength corresponding to fluorescence emission gets transmitted to the sensor or to the eyepiece, whereas reflected light (at the excitation wavelength) is discarded. A dichroic mirror helps to achieve this by reflecting light below a certain transition wavelength (which is chosen to be between the excitation and emission wavelengths of the fluorophore) and transmitting light above that wavelength.

Incoherent point spread function

Because of the random nature of photon emission, fluorescence microscopy is an incoherent imaging process. This means that each point of the sample contributes independently (without interference) to the light intensity distribution in the image space. Moreover, in the paraxial approximation, moving the object does not influence its image, except for a shift. From a signal-processing standpoint, a widefield microscope can thus be modeled as a linear space-invariant system in intensity. In other words, the light intensity (which is the physical value measured by a photodetector) in the neighborhood of the primary imaging plane ($z = 0$) is given by a convolutive expression:

$$I(x, y, z) \propto \int_{\mathbb{R}^3} \left| h_{\lambda_{\text{em}}} \left(\frac{x}{M} - u, \frac{y}{M} - v, \frac{z}{M^2} - w \right) \right|^2 \chi(u, v, w) \, du \, dv \, dw \quad (2.1)$$

where M is the magnification of the objective (note that the axial magnification is M^2). Here, χ is the characteristic function of the object; it describes

its ability to convert incident light into fluorescence intensity at the emission wavelength λ_{em} and is thus mostly related to the fluorophore concentration. The impulse response $|h_{\lambda_{\text{em}}}|^2$ is called the incoherent (or intensity) point spread function (PSF), since it defines the image of an ideal point object ($\chi(x, y, z) = \delta(x, y, z)$). For a given wavelength λ it is defined by a 2-D Fourier transform:

$$h_{\lambda}(x, y, z) = \int_{\mathbb{R}^2} P(\xi, \eta) \exp\left(\frac{-jkz(\xi^2 + \eta^2)}{2f^2}\right) \exp\left(\frac{-jk(x\xi + y\eta)}{f}\right) d\xi d\eta. \quad (2.2)$$

In this expression, f is the focal length of the objective and $k = \frac{2\pi}{\lambda}$ is the wavenumber. P represents the pupil function, which is an indicator function that corresponds to the circular aperture of the objective. Its radius r is related to the focal length by $\text{NA} \simeq r/f$. Note the presence of the depth coordinate z in the phase factor — it accounts for the defocusing effect illustrated in Fig. 2.5. A complete development of this expression is provided in the next chapter.

2.3.2 The confocal scanning microscope

Principle

In a confocal microscope (Fig. 2.4b and [69]) the illuminating point source is usually obtained from a laser. The latter illuminates a pinhole located in a plane conjugate to the sample. In this way, the light is focused onto a very small volume in the sample, and the returning fluorescence radiation is collected by a photomultiplier tube (PMT [70]). The essential difference with a widefield microscope is the detection pinhole, which drastically reduces the proportion of light coming from out-of-focus points, especially in the axial direction.

Since only one point is observed at a time, the object has to be scanned. In the x and y dimensions, this is achieved by using a scan mirror, which deflects the illumination beam, hence moving the illumination spot in the same plane. In the z direction, the sample is usually moved mechanically by means of a motorized stage. The ability to resolve different planes within the object is called optical sectioning and leads to a complete volumetric representation (a stack of 2-D images).

A critical parameter in this setting is the pinhole diameter, which is usually expressed in Airy units (AU)⁷. One Airy unit corresponds to the size of the central disc of the PSF of the system (Fig. 2.5, second image in the bot-

⁷After back-projection into object space, i.e. dividing the effective diameter by the magnification factor.

tom row). The smaller the pinhole, the better the resolution; however, this also means that less light is collected, implying a higher noise level.

Incoherent point spread function

The imaging process of fluorescent material can be modeled as follows: first, we have to take into account the effect of illumination, which consists in multiplying the fluorescence strength of the object by the PSF of the objective (taking into account the scan coordinate (x_0, y_0, z_0)). The reemitted light intensity is then given by

$$|h_{\lambda_{\text{ex}}}(x - x_0, y - y_0, z)|^2 \chi(x, y, z - z_0) \quad (2.3)$$

where λ_{ex} denotes the excitation wavelength. The intensity at the detector is the convolution of this expression with the objective PSF, evaluated at the origin (the position of the detection pinhole):

$$\int_{\mathbb{R}^3} |h_{\lambda_{\text{em}}}(x_0 - x, y_0 - y, -z)|^2 |h_{\lambda_{\text{ex}}}(x - x_0, y - y_0, z)|^2 \chi(x, y, z - z_0) dx dy dz \quad (2.4)$$

where λ_{em} denotes the emission wavelength. Note that we did not indicate the magnification factors here, which is equivalent to back-projecting the image into object space; also, the returning light beams are descanned when they hit back on the scanning mirror. Since $h_{\lambda_{\text{ex}}}$ is symmetric in x and y , the final intensity PSF of the system is $|h_{\lambda_{\text{ex}}} h_{\lambda_{\text{em}}}|^2$, illustrated in the lower part of Fig. 2.5. It shows that a confocal microscope has a PSF that is more concentrated in space than a widefield one; i.e., a better resolution, especially in the axial direction.

2.3.3 Sample setup and aberrations

In an ideal optical system, wavefronts propagate without undergoing phase distortions, also called aberrations. Modern microscope optics are highly sophisticated and are corrected to high levels of precision to avoid such distortions. The optical properties of the sample play an important role in the formation and correction of aberrations. Samples are usually placed onto a glass slide and need to be covered with a glass coverslip for use with most objectives. As shown in Fig. 2.6, there is an immersion layer between the objective and the sample (to increase resolution, an immersion medium with a high refractive index, such as oil, is used). To minimize aberrations, each objective is designed for a specific setup, corresponding to parameters such as the refractive index of the immersion medium, the coverslip thickness, and the imaging depth. Small deviations from these optimal values (e.g.,

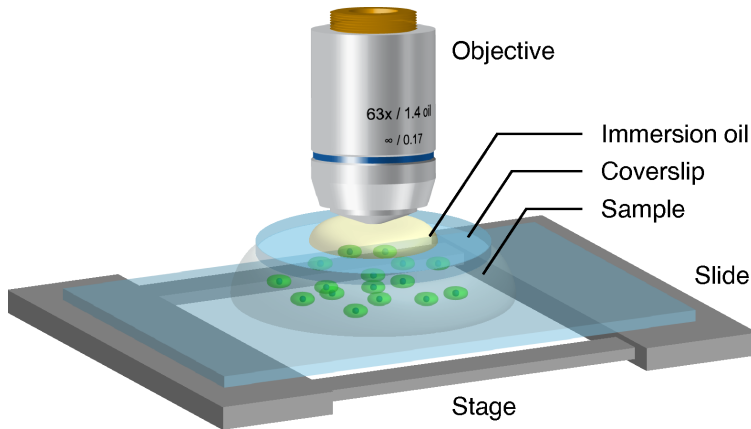


Figure 2.6 Schematic representation of a typical sample setup.

due to temperature changes or incorrect sample preparation) can introduce aberrations. A common and often unavoidable source of aberrations is the imaging depth in situations where the refractive indices of the specimen and immersion layers are mismatched. In the case where this mismatch is significant, it may result in the PSF becoming shift-variant, especially along the axial direction z [71].

2.4 Detectors

Fluorescence imaging can sometimes be a real challenge due to very low light conditions. Especially for live samples undergoing fast biological changes, it may not be possible to integrate more than a few tens of photons at each sampling position. Such conditions call for very sensitive detection devices with very accurate synchronization and control.

2.4.1 Characteristic parameters of detection systems

Most detectors are actually designed for specific applications and provide increased accuracy along the corresponding dimensions. In what follows, we briefly review the main characteristics of a detection device with respect to different parameters.

Wavelength

One of the critical parameters of a detector is its quantum efficiency; i.e., the average rate of incoming photons that are converted into an electronic

charge. This rate strongly depends on the wavelength, and is therefore also called spectral sensitivity.

Intensity

Some detectors operate by internal amplification of the light signal they receive, which leads to the notion of gain. Detectors with gain adjustment offer increased interscene dynamic range, that is, the range of intensity levels that they can adapt to, for different imaging situations. The intrascene dynamic range characterizes the range of intensities to which the sensor can respond linearly, for a given imaging situation. The maximum value, divided by the noise level, defines the peak signal-to-noise ratio (PSNR). The quantization precision (number of bits per sample) must be chosen accordingly.

Spatial resolution

For array/line (resp. point) detectors, the pixel size (resp. detection aperture) represents a tradeoff between resolution and noise level. Another parameter is the effective photosensitive area, which may not cover the whole detector.

Temporal resolution

Long integration times will reduce noise but slow down the acquisition process. High readout speeds will allow faster frame rates/scan frequencies. For fluorescence lifetime measurements, one needs to precisely know when a given event occurred, which requires high synchronization and timing accuracy.

Operating temperature

Cooling is often mandatory to reduce electronic noise.

2.4.2 Detection technologies

We can distinguish between two main types of detectors for fluorescence microscopy:

Semiconductor detectors

They are based on an internal photoelectric effect and are most often encountered as 2-D or 1-D array detectors. Typical examples are CCD (Charge Coupled Device, [72]) cameras for widefield microscopy.

Fig. 2.7a presents the structure of a CCD sensor. Its elementary building block (pixel) is a MOS (Metal-Oxide-Semiconductor) photocapacitor, whose role is to convert photons into electric charge. While the internal conversion process can achieve rates close to 100 %, the transmission coefficients of the electrodes and the insulating layer limit the overall quantum efficiency of the detection to 40 % at most. To improve upon this value, the photocapacitor can be illuminated from the silicon substrate side, or back-illuminated. However, this requires a complex (and expensive) etching process to reduce the substrate thickness.

The accumulated charge is essentially a linear function of the number of incoming photons, until a saturation level is reached. Above that level, additional charges may diffuse to neighboring pixels, an effect known as blooming. The maximum number of electrons, divided by the average number of electrons generated by noise (see below), gives the peak SNR. High sensitivity cameras can reach ratios of 30000:1 or better.

In CCD detectors, the charges are read-out using an analog shift-register⁸. In the full-frame transfer scheme illustrated in Fig. 2.7a, the charges of each pixel row are sequentially moved towards the shift register by adjusting the gate voltages P_1 , P_2 and P_3 in a periodic pattern. At the register, each row is again sequentially “emptied” and the charges are converted to voltages which are amplified and digitized.

Photomultiplier tubes

PMTs [70, 73] are based on the photoemissive effect. They have no intrinsic spatial resolving power and are thus mostly used in combination with a scanning system and a detection aperture, typically in confocal microscopes. Fig. 2.7b shows the schematic diagram of a PMT.

When photons with sufficient energy hit the photocathode, they may excite electrons and induce their release inside the tube. These are directed towards the first dynode by means of a focusing electrode. There, some are reflected, while others are absorbed and can excite secondary electrons. The number of reflected and secondary electrons divided by the incoming electrons defines a single dynode gain g . In total, a series of n dynode stages (typically a dozen or more) is traversed before the anode finally collects the electrons that have been produced. This principle can lead to very high gains, g^n being of the order of 10^6 to 10^8 .

The photocathode is a key element as it determines the quantum efficiency of the system (for the most part). Typically, less than 30 % of the in-

⁸As opposed to digital shift-registers used in CMOS detectors, which allow each pixel to be accessed individually, at the expense of a reduced photosensitive area.

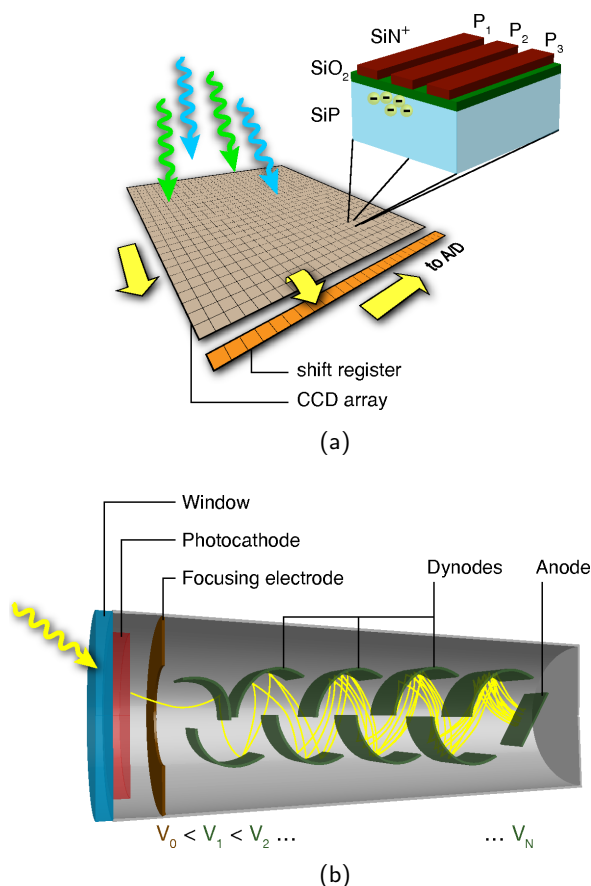


Figure 2.7 Examples of detectors for fluorescence imaging. (a) MOS photocapacitor in a full-frame-transfer CCD array. Two layers of a semiconductor silicon crystal with (P-type or N-type) impurities are separated by insulating silicon dioxide (SiO₂). When a photon penetrates into the substrate, it can excite electrons that are part of the crystalline structure. By applying suitable voltages at the electrodes (or gates) P_1 , P_2 and P_3 , these are “trapped” under the SiO₂ layer. (b) Transmission-mode PMT, composed of a vacuum tube and several electrodes that are submitted to a voltage gradient. The first one is protected from outside oxidation by a window that is transparent to light.

coming photons are effectively “converted” into electrons, depending on the wavelength.

2.5 Limitations

Two sources act as the principal limiting factors in fluorescence imaging: 1) the instrumentation, which, apart from its inherent resolution limitation, introduces measurement noise, and 2) the sample itself, whose optical prop-

erties and emission characteristics are often non-ideal.

2.5.1 Noise sources

Photon shot noise

The fundamental limitation of any photodetector resides in the random nature of photon emission. The arrival of photons at the detector is well described by a Poisson process whose (statistical) intensity is proportional to the (physical) intensity of the fluorescence signal.

Background noise

The ambient radiation, especially in the infrared domain, can also be a significant source of noise; it often requires the use of additional filters at the detection stage.

Dark current

Among the numerous internal noise sources in a detector, thermal agitation is the most important. The higher the temperature, the higher the kinetic energy of the electrons. For semiconductor detectors, this results in so-called dark currents (that exist even in the absence of light), which tend to charge the photocapacitors when the integration time and/or the temperature are too high. For point detectors such as PMTs, thermal energy can trigger spontaneous electron emissions. Consequently, high-sensitivity detectors are very often cooled down to reduce thermal noise.

Auxiliary noise sources

For semiconductor devices, additional noise is generated at read-out time. In particular, the charge transfer in CMOS sensors is less efficient than in CCD chips. Both technologies are subject to amplifier noise. For PMTs, there can be fluctuations in the internal gain of the unit, which also result in noise. Finally, any detector with digital output produces quantization noise.

2.5.2 Sample-dependent limitations

Photobleaching

An important property of fluorophores is that they are more chemically reactive in their excited state. Depending on the environment, they can undergo reactions that lead to permanent changes, by which the molecule loses its capability to fluoresce altogether, or becomes non-absorbent for the specified

excitation wavelength. This effect, called photobleaching, limits the total intensity of light, and accordingly, the exposure time, until loss of fluorescence occurs. As a result, the observation time of a fluorescence-tagged specimen is limited. Photobleaching is a cumulative effect; this means that reducing the exposure time or excitation intensity will not prevent it, but merely reduce the rate at which it occurs.

Autofluorescence

Many organic molecules are naturally fluorescent, and thus even unstained biological samples can emit fluorescence in the visible domain. This autofluorescence is an important source of noise when it overlaps with the emission of a selected fluorophore, especially when the latter is sparsely expressed or exhibits weak fluorescence. This interference can render the detection of a signal very difficult.

Absorption and scattering of the medium

In a biological specimen, the intensity of the fluorescence signal decreases as the fluorophore's depth within the specimen increases. This attenuation is due to the absorption and scattering⁹ of light; it strongly limits both the depth at which a fluorophore can be excited and the depth at which a fluorescence signal can be detected¹⁰. These effects are not always negligible. Therefore, to obtain truly quantitative measurements, it may be necessary to develop reconstruction algorithms that take into account the space-varying and complex nature of the refractive index.

2.6 Fluorescence Techniques

Besides standard imaging that involves the quantitative analysis of local fluorophore concentrations, there exist more sophisticated experimental techniques for studying protein-protein interactions and for investigating biological processes at the molecular scale. Among the techniques presented below, FLIM and FRET can be performed on both widefield and confocal microscopes. The photobleaching techniques, however, are usually performed with lasers and often require the ability to precisely define the region to be bleached; they are therefore mostly implemented on confocal microscopes.

⁹Scattering is the phenomenon by which particles with a refractive index different from the medium's index partially diffuse electromagnetic radiation in all directions. It commonly occurs when the particle sizes are comparable to the wavelength.

¹⁰Typically in the 100 μm range for one-photon confocal microscopy.

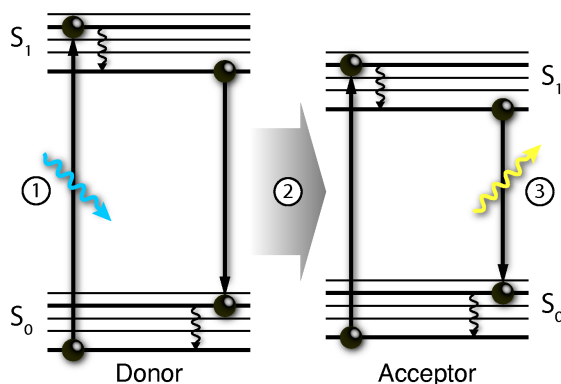


Figure 2.8 The principle of FRET between a suitable donor-acceptor pair: the energy of the excited donor molecule is transferred (without emission of a photon) to the acceptor after vibrational relaxation (1). For FRET to occur, the distance between the two molecules must typically be in the range of 1-10 nm [66].

2.6.1 FRET

Protein-protein interactions take place at scales that are too small to be resolved by optical microscopy; however, they can be detected by exploiting a mechanism called fluorescence resonance energy transfer (FRET). This process is a direct transfer of energy (i.e., it does not involve the emission or absorption of a photon) between a suitable donor and an acceptor, as illustrated in Fig. 2.8. FRET is only possible between two fluorophores if the emission spectrum of the donor overlaps with the excitation spectrum of the acceptor. An example of a suitable pair of fluorescent proteins is the aforementioned CFP/YFP couple.

The efficiency of FRET strongly depends on the distance that separates the two molecules (the rate is inversely proportional to the 6th power of the distance) and on the relative orientation of their dipole moments. This means that FRET can be used to study the optical subresolution colocalization of a labeled protein pair of interest. FRET can also serve as an indicator of conformational changes in a protein: if complementary markers are placed at the extremities of the protein, then an energy transfer can occur when the protein folds [74]. Fig. 2.9 illustrates a FRET experiment.

2.6.2 FRAP

Although photobleaching has already been mentioned as a limitation, it can be exploited to study the intracellular dynamics of proteins. FRAP (fluorescence recovery after photobleaching) consists in intentionally bleaching a small region of a cell using high-intensity light, thereby rendering it non-

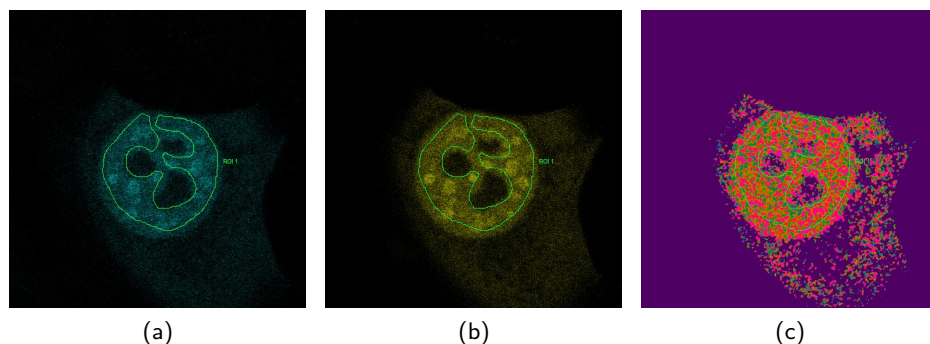


Figure 2.9 Images from a FRET experiment, showing the (normalized) donor (a) and acceptor (b) channels. From these images, a computer-generated FRET-efficiency image is obtained (c). In this case, the scientists were interested in the average FRET efficiency inside a region of interest corresponding to the cell nucleus. Courtesy of M. C. Rio, A. Baguet, and P. Kessler, IGBMC, Illkirch, France.

fluorescent. The region then regains its fluorescence as fluorophores from the surroundings enter and pass through it, which yields information about the diffusion and mobility of the labeled protein [75].

2.6.3 FLIM

All of the techniques discussed up to this point rely on intensity-based measurements. In the presence of autofluorescence, or when multiple fluorophores with similar emission spectra are used, it can be difficult to discriminate among the different signals. Intensity-based imaging is also highly dependent on fluorophore concentration.

In fluorescence lifetime imaging microscopy (FLIM), image contrast is generated based on the lifetime of fluorophores, which is the average time a fluorophore remains in the excited electronic state. The key point is that every fluorophore has a unique lifetime. A common method for measuring fluorescence lifetimes consists in exciting fluorophores with a picosecond pulsed laser source and recording the arrival times of the emitted photons with a high speed photodetector.

The lifetime of a fluorophore is sensitive to many environmental factors such as oxygen concentration, pH, and calcium ion concentration. Thus, FLIM can be used to obtain information about the local environment of a particular fluorophore. FLIM can also serve as an experimental verification that FRET occurs (see Fig. 2.10).

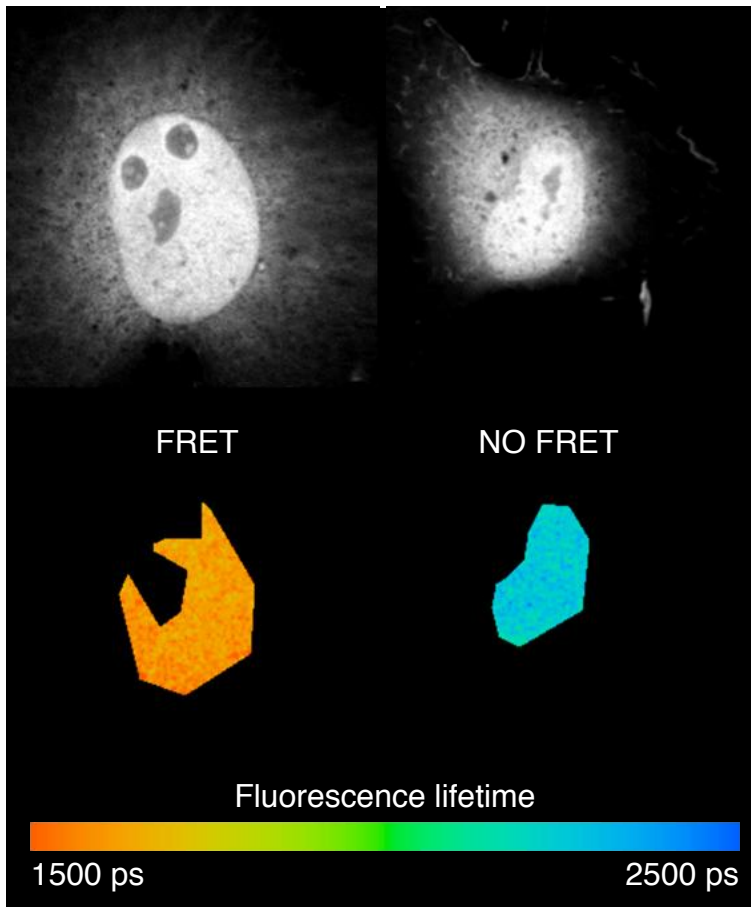


Figure 2.10 FLIM experiment for confirming the occurrence of FRET. The images show the fluorescence lifetime of the donor over two regions of interest corresponding to different cell nuclei. In the presence of FRET (left-hand side), the fluorescence lifetime is significantly reduced, due to the energy transfer to the acceptor. Courtesy of C. Rochette-Egly, S. Lalevée and P. Kessler, IGBMC, Illkirch, France.

2.7 Signal Processing

2.7.1 Data size and dimensionality

Modern research in biology requires quantitative experimental data. As a consequence, microscopes have developed into sophisticated digital image acquisition workstations that are capable of acquiring very large data sets of high dimensionality.

To get a better feeling of what is involved, consider an experiment monitored with a confocal microscope that requires the periodic (time-lapse) 3-D acquisition of a sample labeled with two fluorophores. This yields a

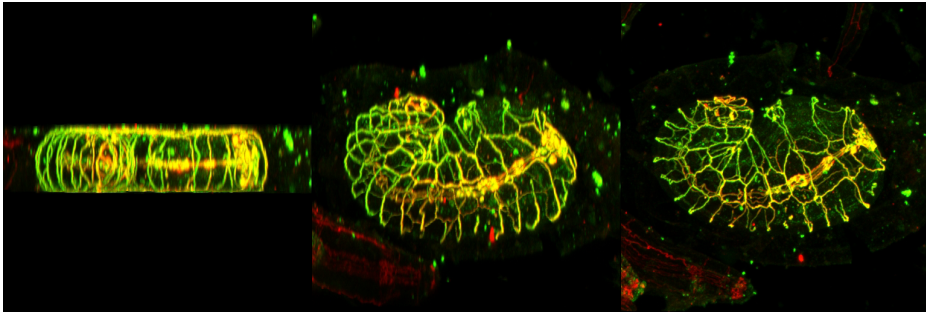


Figure 2.11 3-D projections of a nematode worm embryo (*C. elegans*) [76]. Courtesy of L. McMahon, J.-L. Vonesch and M. Labouesse, IGBMC, Illkirch, France.

5-D data set indexed by the space coordinates x , y and z , the time t , and the wavelength parameter λ . Assuming that each image has a resolution of 1024×1024 and that 32 slices are acquired per volume every 20 minutes over 24 hours with a 12-bit quantizer, the whole experiment results in nearly 7 gigabytes of data. If a comparative analysis is performed, this figure must be multiplied by the total number of samples.

Studies involving comparable or even larger amounts of data are becoming commonplace. Even with today's performance levels of computer hardware, the storage, extraction, manipulation and representation of such data sets remain complex. One major challenge lies in the design of database systems and compression formats allowing for efficient retrieval and visualization (projections, 3-D rendering — see the example in Fig. 2.11).

But most importantly, signal processing is becoming increasingly indispensable for the analysis and understanding of quantitative biological experiments; in fact, it is increasingly considered part of the experimental protocol itself, as a way to infer the validity of a biological model.

Without claiming exhaustiveness, we give examples of current image processing problems in biology among five main categories: image preparation, image restoration, image registration, image segmentation, and quantitative image analysis.

2.7.2 Image preparation

Image calibration

Calibration is an important step both for image analysis and visualization. It can involve various preprocessing tasks such as histogram equalization, inhomogeneous illumination compensation, background correction, or image rescaling. While these tasks may appear relatively simple, some of them can rely on advanced signal processing.

Image simplification

In some cases, biological structures are too complex to be processed directly and an image simplification step is required. To preserve the objects of interest, the operator can choose among the wide range of available tools (morphological operations, filtering, multiresolution structures, diffusion equations, etc.); application-specific solutions can also be envisaged.

Feature detection

Biological images often present characteristic elements such as particles and filaments. The detection of these features may require the development of optimized filters [77, 78], as well as multiresolution methods [79]. Here, a challenging aspect is the shape variability observed in live-cell imaging.

Experimentalists should at least be aware of the aforementioned preparation operations; otherwise, they run the risk of a significant loss of information, thereby leading to questionable results. Algorithm designers, on the other hand, should put more efforts into education and the development of user-friendly imaging software.

2.7.3 Restoration

Restoration encompasses the classical problems of denoising and deconvolution.

Denoising

Simple methods such as median filtering often need adaptation; for example, a 3-D stack may exhibit lower SNR levels as deeper portions of the object are imaged, due to absorption and/or autofluorescence. More generally, restoration methods should be based on physically realistic noise models (e.g., Poisson statistics) and take into account various noise sources (see Section 2.5). Advanced algorithms, relying on wavelet-domain thresholding strategies [80], PDE and variational formulations, or statistical frameworks, are just starting to be used in the field of bioimaging, and deserve more exploration.

Deconvolution

This operation requires an adequate characterization of the underlying imaging system, which can be either theoretical (involving a PSF model) or, frequently, experimental. In the latter case, the PSF is obtained by imaging subresolution fluorescent beads, under conditions as close as possible

to the actual biological preparation. By averaging, possibly with simplifying assumptions (e.g., symmetry), a relatively noise-free PSF can be obtained. For further details concerning algorithmic deconvolution methods, we refer to [81, 82].

One of the main challenges is the design of computationally tractable methods that take into account the nonstationarity of the PSF, especially in the axial direction (see Section 2.3.3). A recent attempt is the EM-algorithm proposed by Preza and Conchello [83]. In their image-formation model, the object is divided into several layers that are associated with a series of (depth-dependent) PSFs. The image of each layer is then obtained from classical (stationary) convolutions.

Other inverse problems

Restoration can also be considered in the wider framework of inverse problems.

One example concerns relatively thick objects with surface labeling, observed under a widefield microscope. Because of the 3-D conical extension of its PSF (Fig. 2.5, top row on the left), such a system has a limited depth of field; that is, only a small slice of the object around the focal plane appears sharp. To compensate for this, images at different focal depths can be taken and fused together so as to obtain a single, entirely sharp image¹¹. State-of-the-art (so-called extended-depth-of-field) algorithms are described in [84] and in Chapter 9. Such methods can also be used to extract 3-D maps of the object's surface.

Another problem of interest is related to the detection and localization of subresolution particles [85]. New methods take into account the 3-D shift-variance of the PSF to achieve precision in the nanometer range (see Chapter 5).

2.7.4 Registration

Registration is a frequently-needed post-acquisition step. Here, researchers can take advantage of the availability of high-quality registration algorithms that were initially developed for medical imaging [86].

Mosaicing

Because of the limited field of view of high-magnification objectives, it can be necessary to acquire multiple images of a sample; for example, in a mo-

¹¹This process should not be confused with deconvolution, which yields a 3-D stack instead of a single image.

saic scheme. Despite the high accuracy that sample stages can achieve, perfect alignment is never possible. Rigid-body registration algorithms can correct this, provided that the acquired images or volumes overlap slightly [87]. Within a given stack, it might also be necessary to compensate for pixel shifts between successive images. In addition, refractive indices — and thus focusing depths — are wavelength-dependent, which can necessitate the realignment of the different fluorescence channels.

Imaging live samples

During time-lapse acquisitions, spatial drifts can occur due to thermal processes; the sample itself might also be subject to motion. Therefore, even if the parts of interest lie in a relatively thin slice, they may not be observable in a unique focal plane over the whole experiment. This implies that either a stack of neighboring planes must be acquired and the planes of interest must be extracted (or fused); or a real-time focusing algorithm must be used to control the stage.

More sophisticated elastic registration may be required for compensating the deformation of living tissues, or for matching specimens of comparable shape [88].

If a periodic biological process is too fast to be imaged with sufficient time-resolution (such as the repetitive 3-D flow of blood cells in the heart), a registration approach may also be applied: in [89], images over several periods are recorded and reassembled so as to obtain a single period at a high frame-rate.

2.7.5 Segmentation

Segmentation is a mandatory step for image analysis. User interaction for the manual delineation of regions of interest is time-consuming and lacks reproducibility. The need for automated segmentation methods is therefore important, e.g., for local intensity measures, object and event counting, as well as tracking.

While simple approaches such as prefiltering and thresholding are available in commercial software packages, advanced techniques — for instance active contours [90] — have not yet been much exploited in the context of biological image analysis.

The most accurate segmentation methods are often application-dependent and typically require specific developments. For example, the tracing of neuronal dendrites can be improved using graph-optimization techniques [91].

In the context of live microscopy, it also makes good sense to adapt the segmentation methods so that they exploit temporal coherence, e.g., for the labeling of cells.

2.7.6 Quantitative analysis

Data preprocessing

In multispectral imaging, each pixel consists of (possibly a large number of) intensity measures at different wavelengths (obtained using different filter sets, an interferometer, or a diffractive system). If several fluorophores are used, their spectra are likely to overlap, and channel-crosstalk must be expected. This gives rise to unmixing problems [92] that can be solved by taking separate reference images of each fluorophore (to measure its contribution to each channel) and using, for example, a singular-value decomposition [93]. Blind separation methods may also be applicable. As a general observation, the correct normalization of spectral data is critical for the interpretation of fluorescence images. Quantitative assessments using FRET or ratio imaging (comparing the relative intensities of different wavelengths) require careful preprocessing based on physical parameters such as spectrum overlap or fluorophore concentration.

Model fitting

Other advanced fluorescence techniques are based on the fitting of parametric models: in FLIM, the fluorescence lifetimes are obtained by fitting (possibly multiple) exponential trends to the photon arrival densities; in FRAP, the diffusion coefficients characterize fluorescence recovery curves [94]. Generally speaking, quantitative research often relies on the mapping of physical or biochemical models in the image and/or time domains, especially for dynamic processes.

Motion assessment and tracking

The diffusion of fluorescent proteins can be characterized by estimating motion fields. In many instances, it is interesting to track individual objects, which can also be a challenging task. We refer the reader to other sources that cover the broad field of movement analysis [15, 95].

Pattern recognition and classification; screening

Screening experiments consist in a systematic, automated study of a large number of samples (up to several hundreds of thousands), e.g., for the study

of gene function or for drug discovery. This can involve terabytes of data and several weeks of computerized analysis. Pattern recognition and classification algorithms play a major role in this analysis. In particular, one must identify how the biological characteristics of interest translate into measurable image features. Computational complexity is a strong limiting factor, while the reliability of the methods must be thoroughly validated [96].

2.8 Trends

In addition to the signal processing tools that have been discussed in the previous section, both the probes [66] and the instrumentation are being refined constantly. We therefore close our discussion with a description of current trends and future directions in the field.

2.8.1 Fluorescent labels

Quantum dots

Among the most recent developments are quantum dots [97], labels composed of a core nanometer-sized semiconductor crystal and an external protective shell. Their main advantages with respect to earlier fluorophores are their broader absorption and narrower emission spectra, resulting in brighter fluorescence. Also, they are more stable chemically and thus less subject to bleaching. These inorganic structures can be used for *in vivo* imaging, although they cannot be expressed by cells [98].

Labeling of recombinant proteins

The principle of this technique is to create fusion proteins that are not fluorescent by themselves, but which express a receptor to which a specific label can be added at a later time [99]. The label can be chosen from a wide range of fluorophores, with properties that GFP-type proteins may not be able to provide (such as higher resistance to photobleaching and stronger fluorescence). The receptor continues to be expressed in newly synthesized proteins, but only the stained proteins exhibit fluorescence, which allows for the selective labeling of a protein population at a given point in time.

Enhanced fluorescent proteins

New fluorescent proteins are being developed that provide increased quantum efficiency (e.g., enhanced GFP, or eGFP, with a 35-fold increase in brightness with respect to the original GFP) or whose emission spectra are

closer to infra-red wavelengths (700 nm and above). These wavelengths are generally less absorbed by biological samples, hence allowing deeper observation. They are also less masked by cell autofluorescence occurring in the visible spectrum.

Photocontrollable proteins

Recent research has also been devoted to the design of photoactivatable [19] and photoswitchable [100, 101] proteins. The former exhibit little fluorescence in their initial, quiescent state. When exposed to a strong irradiation at a specific wavelength (usually lower than the fluorescence excitation wavelength), a 100-fold or higher increase in fluorescence brightness can be observed. For switchable proteins, strong irradiation changes both the excitation and emission spectrum. For example PS-CFP [102] is sensitive to irradiation at 405 nm, which produces a 1500-fold increase in its green-to-cyan ratio. Both types of labels can be used to activate and observe proteins in a specific region of a cell, without the interference of newly synthesized proteins or proteins outside of the selected region. This property is useful for protein lifetime and tracking as well as cell lineage studies.

2.8.2 Advanced microscopy systems

We conclude this section with some of the more advanced developments in the field of optics.

Faster scanning – slit detectors and Nipkow-disks

To cope with the high speed of some biological processes, the traditional confocal scanning microscope equipped with a point detector is often not sufficient. To accelerate the scanning process, a whole line can be imaged simultaneously by replacing the pinholes and the PMT by slit apertures and a linear camera. More generally, using e.g., a Nipkow-disk system [103], a 2-D illumination pattern can be shifted across the sample, allowing time lapse imaging at up to 120 frames per second. This comes with a significant tradeoff in terms of resolution, due to crosstalk between the different detection apertures.

Deeper imaging – multiphoton microscopy

In a multiphoton microscope [3], optical sectioning is achieved by properties of the illumination; as a consequence, there is no need for a detection pinhole in such a system. Very short laser pulses (in the pico- to femtosecond range) are sent to the sample in brief intervals (of the order of nanoseconds).

The probability that two photons encounter the same molecule, hence bringing it to its excited state and making it fluoresce, is significant only in the very central region of the illumination spot. A key advantage is that the corresponding infrared wavelengths are less absorbed by biological tissues so that samples can be imaged much deeper than with traditional confocal systems (at a comparable resolution). Photobleaching and toxicity are also reduced because the excitation intensity is effectively concentrated at the focal spot.

Improved optical sectioning – TIRF microscopy

Background excitation due to the axial extent of the PSF is especially problematic in single molecule imaging experiments, where it further reduces the intrinsically low SNR. Total internal reflection fluorescence (TIRF) microscopy exploits the evanescent wave generated by total internal reflection to achieve significantly improved optical sectioning [104]. Due to the exponential decay of this wave, only fluorophores within approximately 100 nm of the interface are excited. Initial implementations of TIRF microscopy relied on mounting the sample between the coverslip and a prism; high-NA (1.45 or greater) objectives have enabled a more practical approach through objective illumination [105].

Increased axial resolution – 4Pi microscopy

Since the numerical aperture has such a fundamental influence on resolution, Hell et al. proposed to insert the sample between two objectives, so as to send and collect light from both sides; accordingly, they called the method 4Pi microscopy [4]. Using computational methods, an improvement in axial resolution by a factor of six can be achieved. Such systems are commercially available, but they suffer from limitations on the sample thickness and sensitivity to differences in the length of the two optical paths. More recently, these ideas have been applied to widefield microscopy (I⁵M, [9]).

Super-resolution – STED microscopy

One of the most advanced microscopy techniques to emerge from the quest for increased resolution is called STED, which stands for stimulated emission depletion [5] (see also Section 2.2.1). The principle is to prevent fluorescent molecules outside the very central region of the illumination spot from emitting light by forcing them back to their fundamental state. This is achieved by dividing the excitation into two brief successive laser pulses, where the second pulse is red-shifted and doughnut-shaped, having zero intensity at its center. Superimposed on the focal spot of the initial pulse, it

induces stimulated emission, dramatically reducing the excitation volume, hence augmenting the resolution.

Super-resolution – localization-based techniques

Fluorescence localization microscopy, which comprises PALM, FPALM, and STORM, is a novel approach to super-resolution microscopy based on imaging and localizing sparse subsets of photo-activatable or photo-switchable fluorophores (see Section 2.8.1). An in-depth overview of these techniques is presented in Chapter 1.

Other developments

Another promising technique to improve the resolution of widefield systems is structured illumination. Illuminating the object with sinusoidal patterns, combined with adequate processing, can result in a two-fold or higher [106] improvement of the microscope's spatial bandwidth. It also yields optical sectioning properties and the processing can be done on specific hardware for real-time observation [107].

Another approach proposed by Stelzer et al. (selective plane illumination microscopy (SPIM) [108]) consists in projecting the light onto the object perpendicularly to the optical axis, in a diffraction-limited plane; then only fluorescence from molecules within this excitation plane is collected using a traditional CCD sensor. This system provides true optical sectioning for widefield systems.

2.9 Conclusion

Although this panorama is necessarily incomplete, we hope to have convinced the reader of the invaluable role of fluorescence microscopy in modern biology. It owes its current popularity to the GFP-like fluorescent proteins that are the key ingredient for *in vivo* studies of molecular processes in cells. These are currently opening up a plethora of experimental possibilities that have only begun to be explored.

This colored revolution could clearly not have happened without numerous technological advances. In particular, progress in optics and instrumentation has been considerable in recent years; there is now a consistent trend towards non-linear techniques, such as multiphoton and saturated illumination imaging, which, with the help of computational methods, are contributing to overcoming Abbe's resolution barrier.

Signal processing is also at the heart of these developments and is expected to play an ever-increasing role in the field. It is already an integral

part of optics and is becoming an essential tool for biologists, who rely more and more on imaging software to quantitate their data.

Therefore, a crucial aspect of the research lies in the successful collaboration between signal processing engineers and biologists. In modern research institutes, imaging core facilities are expected to play an important mediating role in this interaction. Our advice to colleagues that want to be part of this effort is that they try to understand the physics and, to some extent, the biology in order to design better and more useful algorithms. We believe that it is truly worth the effort.

Chapter 3

Image formation in optical microscopy

An accurate theoretical description of the point spread function (PSF) of optical microscopes is a crucial aspect of most of the methods presented in this thesis. The literature on PSF modeling is extensive, and characterized by a large number of approximations with varying degrees of accuracy. One particular challenge in representing the PSF of a microscope is the lack of detailed information about the exact design of the objectives. Indeed, the only parameters that are usually known are the overall optical characteristics of the objective (i.e., magnification, numerical aperture, etc.) and the experimental conditions for which it is designed (i.e., refractive index of the immersion medium, working distance). It is therefore desirable to obtain a formulation of the PSF that relies only on these known parameters, accordingly treating the objective as a black box. A significant contribution in this direction was made by Gibson and Lanni [71], who proposed a scalar model based on a calculation of the optical path difference (OPD) between experimental conditions and the design conditions of the objective. The residual aberrations arising as a result of a mismatch between these conditions are a central aspect of image formation, and even though some applications require a more accurate, vectorial expression of the PSF, the calculation proposed in [71] is equivalent to those found in these more advanced models [109]. The vectorial theory was established by Wolf and Richards [110, 111] on the basis of Maxwell's and Debye's [112] results, and later expanded by Török et al. [113] and Hell et al. [114]. In this chapter, we provide a review of the theoretical developments behind the aforementioned methods. First, we discuss the characteristics of the PSF for the principal imaging modalities in optical microscopy. Following that, we derive the expressions of scalar and vectorial image formation, starting from the fundamentals of diffraction theory.

Our discussion here is centered on the scalar PSF model proposed by Gibson and Lanni; in Chapter 7, we formulate a state-of-the-art vectorial image formation model to compute the diffraction patterns observed when imaging single fluorescent dipoles.

3.1 Imaging modalities

The formation of an image in an incoherent optical system (see Chapter 2) can be mathematically expressed as

$$I(\mathbf{x}) = \int_{\mathbb{R}^3} o(\mathbf{t})h(\mathbf{x}; \mathbf{t}) d\mathbf{t}, \quad (3.1)$$

where the object $o(\mathbf{x})$, the system's PSF $h(\mathbf{x})$, and the observed image $I(\mathbf{x})$ are positive, real-valued functions representing intensities. Under appropriate hypotheses, the system can be assumed to be shift-invariant, such that

$$I(\mathbf{x}) = \int_{\mathbb{R}^3} o(\mathbf{t})h(\mathbf{x} - \mathbf{t}) d\mathbf{t} = (o * h)(\mathbf{x}), \quad (3.2)$$

although this assumption is sometimes limited¹ to the x and y dimensions. Due to the intrinsically incoherent process (at a wavelength scale) of photon emission in fluorophores, any form of fluorescence microscopy can be represented by one of these models, and thus, the system's imaging properties are reflected by the PSF alone. Specific examples of the PSF for widefield, confocal, and 2-photon excitation are

$$\begin{aligned} \text{Widefield: } h(\mathbf{x}) &= |h_{\lambda_{\text{em}}}(\mathbf{x})|^2 \\ \text{Confocal: } h(\mathbf{x}) &= |h_{\lambda_{\text{ex}}}(\mathbf{x})|^2 (|h_{\lambda_{\text{em}}}(\mathbf{x})|^2 * p_r(x, y)) \\ \text{2-photon: } h(\mathbf{x}) &= |h_{\lambda_{\text{ex}}}(\mathbf{x})|^4, \end{aligned} \quad (3.3)$$

where λ_{ex} and λ_{em} denote the excitation and emission wavelength, respectively, and where $p_r(x, y)$ is the pinhole function, i.e.,

$$p_r(x, y) = \begin{cases} 1 & \text{if } \sqrt{x^2 + y^2} \leq r, \\ 0 & \text{otherwise,} \end{cases} \quad (3.4)$$

where r is of the order of $1.22\lambda/\text{NA}$, which is also called an Airy Unit. For larger values of r , the PSF tends towards the widefield model. Note that, in this notation, $h_\lambda(\mathbf{x})$ is the coherent model of the impulse response at wavelength λ .

¹The reasons behind the axially shift-variant behavior of the PSF are detailed in the discussion of the Gibson and Lanni model, in Section 3.2.

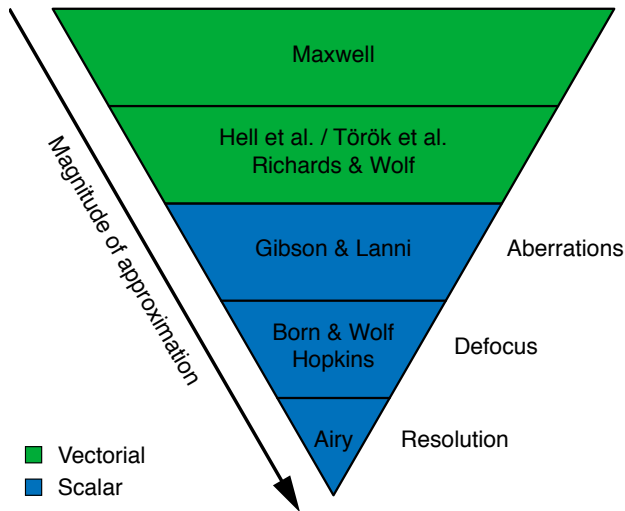


Figure 3.1 Hierarchy of the most significant PSF models in terms of contributions and accuracy. Derived from Maxwell’s equations, vectorial models provide a rigorous treatment of diffraction in microscopes. Their scalar counterpart was used to formulate an accurate model of the aberrations arising during image formation. The most common type of aberration is due to defocus, which forms the basis of the simplest and most widely used model (Born and Wolf [115], Hopkins [116]).

By contrast, for coherent or partially coherent systems, image formation is expressed as

$$I(\mathbf{x}) = \left| \int_{\mathbb{R}^3} o(\mathbf{t}) h_{\lambda}(\mathbf{x}; \mathbf{t}) d\mathbf{t} \right|^2,$$

where both $h(\mathbf{x})$ and $o(\mathbf{x})$ are described in amplitude and phase. Brightfield microscopy, where image formation is a partially coherent process [117], employs light sources designed for uniform emission over the visible spectrum. This can be modeled by integrating the PSF over the domain of visible wavelengths:

$$h(\mathbf{x}) = \int h_{\lambda}(\mathbf{x}) d\lambda. \quad (3.5)$$

The amplitude PSF $h_{\lambda}(\mathbf{x})$ is identical across the different imaging modalities discussed above, irrespective of image formation being coherent or not. This is simply due to the fact that the key optical components of these systems are the same. In the next section, we review the foundations of diffraction theory, starting from Maxwell’s equations, after which we derive several expressions with various degrees of accuracy for the amplitude PSF; the hierarchy of these models is illustrated in Fig. 3.1.

3.1.1 Fresnel-Kirchhoff diffraction

In the absence of free charge — specifically, for a linear, nondispersive, homogeneous, and isotropic medium — Maxwell's equations are given by

$$\begin{aligned}\nabla \times \mathcal{E} &= -\mu \frac{\partial \mathcal{H}}{\partial t} & \nabla \cdot \varepsilon \mathcal{E} &= 0 \\ \nabla \times \mathcal{H} &= \varepsilon \frac{\partial \mathcal{E}}{\partial t} & \nabla \cdot \mu \mathcal{H} &= 0,\end{aligned}\tag{3.6}$$

where \mathcal{E} is the electric field, \mathcal{H} is the magnetic field, μ is the permeability of the medium, and ε is the permittivity of the medium. By combining the equations in \mathcal{E} , one obtains the wave vector equation

$$\nabla^2 \mathcal{E} - \frac{n^2}{c^2} \frac{\partial^2 \mathcal{E}}{\partial t^2} = 0,\tag{3.7}$$

where $c = 1/\sqrt{\varepsilon_0 \mu_0}$ is the vacuum speed of light and $n = \sqrt{(\varepsilon \mu)/(\varepsilon_0 \mu_0)}$ is the refractive index of the medium (an analogous expression exists for \mathcal{H}). Each component of the electric field \mathcal{E} and the magnetic field \mathcal{H} can then be shown to satisfy the scalar wave equation

$$\nabla^2 u - \frac{n^2}{c^2} \frac{\partial^2 u}{\partial t^2} = 0.\tag{3.8}$$

By further assuming that this scalar field is a monochromatic wave, i.e.,

$$u(\mathbf{x}, t) = \Re\{U(\mathbf{x})e^{-i\omega t}\} \quad \text{where } U(\mathbf{x}) = A(\mathbf{x})e^{-i\phi(\mathbf{x})}\tag{3.9}$$

and substituting this expression into (3.8), one finds that $U(\mathbf{x})$ must satisfy the Helmholtz equation

$$\nabla^2 U + k^2 U = 0,\tag{3.10}$$

where $k = 2\pi/\lambda = 2\pi\nu n/c = \omega n/c$.

The essence of the diffraction problem consists in expressing the value of $U(\mathbf{x}_d)$ at a point of observation \mathbf{x}_d behind an aperture (see Fig. 3.2) as a function of the value of $U(\mathbf{x})$ within that aperture. Its solution is given by the integral theorem of Kirchhoff and Helmholtz [118], which states that

$$U(\mathbf{x}_d) = \frac{1}{4\pi} \iint_{\Sigma} \left(\frac{\partial U}{\partial n} \frac{e^{iks}}{s} - U \frac{\partial}{\partial n} \frac{e^{iks}}{s} \right) dS,\tag{3.11}$$

where $\partial/\partial n$ is the directional derivative in the direction of the normal \mathbf{n} to the aperture Σ , i.e., $\frac{\partial U}{\partial n} = \mathbf{n} \cdot \nabla U$, and where $k = 2\pi n_i/\lambda$ is the wavenumber for a medium of refractive index n_i . Since

$$\frac{\partial}{\partial n} \frac{e^{iks}}{s} = \cos(\mathbf{n}, \mathbf{s}) e^{iks} \left(ik - \frac{1}{s} \right),\tag{3.12}$$

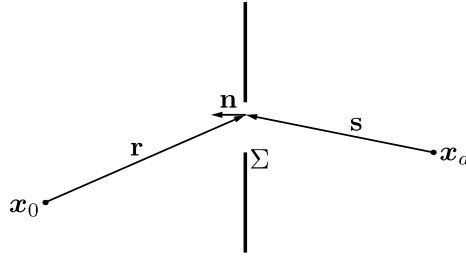


Figure 3.2 Diffraction by a planar aperture. Kirchhoff's theorem expresses the field at the point x_d as a function of the field in the aperture Σ ; the Fresnel-Kirchhoff diffraction formula is based on the further assumption that the aperture is illuminated by a point source located in x_0 .

and provided that the distance from the x_d to the aperture is large compared to the wavelength (i.e., $s \gg \lambda$), the approximation

$$\frac{\partial}{\partial n} \frac{e^{iks}}{s} \approx ik \cos(\mathbf{n}, \mathbf{s}) e^{iks} \quad (3.13)$$

is valid, and consequently

$$U(x_d) = \frac{1}{4\pi} \iint_{\Sigma} \left(\frac{\partial U}{\partial n} \frac{e^{iks}}{s} - ikU \cos(\mathbf{n}, \mathbf{s}) \frac{e^{iks}}{s} \right) dS. \quad (3.14)$$

Considering now that the aperture is illuminated by a point source situated in x_0 (see Fig. 3.2), the value of the field at a point x_a in the aperture is

$$U(x_a) = A \frac{e^{ikr}}{r}. \quad (3.15)$$

Substituting this into the preceding equation, we obtain the Fresnel-Kirchhoff diffraction formula

$$U(x_d) = -\frac{A}{2i\lambda} \iint_{\Sigma} \frac{e^{ik(r+s)}}{rs} (\cos(\mathbf{n}, \mathbf{r}) - \cos(\mathbf{n}, \mathbf{s})) dS. \quad (3.16)$$

If we further assume that both the source and detector points are distant from the aperture, i.e., that $\cos(\mathbf{n}, \mathbf{r}) \approx 1$ and $\cos(\mathbf{n}, \mathbf{s}) \approx 1$, the previous expression reduces to

$$U(x_d) = \frac{A}{i\lambda} \iint_{\Sigma} \frac{e^{ik(r+s)}}{rs} dS. \quad (3.17)$$

This result can now be generalized for an arbitrary source, such that

$$U(x_d) = \frac{1}{i\lambda} \iint_{\Sigma} U(\xi, \eta, 0) \frac{e^{iks}}{s} d\xi d\eta. \quad (3.18)$$

where we introduce the aperture coordinates ξ and η . This result is the expression of the Huygens-Fresnel principle, which considers the field in $U(\mathbf{x}_d)$ as the superposition of spherical waves generated by point sources in the aperture.

Before continuing with the development of a diffraction formula that applies to microscopes, we briefly recall the well-known approximations to the Fresnel-Kirchoff integral by Fresnel and Fraunhofer. Specifically, with the approximations

$$s \approx z + \frac{(x - \xi)^2 + (y - \eta)^2}{2z} \quad (3.19)$$

and $1/r \approx 1/z$, introduced by Fresnel, we obtain the Huygens-Fresnel integral

$$U(\mathbf{x}_d) = \frac{-i}{z\lambda} e^{ikz} \iint_{\Sigma} U(\xi, \eta, 0) e^{i\frac{k}{2z}((x-\xi)^2 + (y-\eta)^2)} d\xi d\eta. \quad (3.20)$$

If, furthermore, it can be assumed that the screen is at a very large distance from the aperture, i.e.,

$$z \gg \frac{k(\xi^2 + \eta^2)_{\max}}{2}, \quad (3.21)$$

the quadratic terms in aperture coordinates can be neglected (Fraunhofer approximation), and the integral further reduces to

$$U(\mathbf{x}_d) = \frac{-i}{z\lambda} e^{ikz} e^{i\frac{k}{2z}(x^2 + y^2)} \iint_{\Sigma} U(\xi, \eta, 0) e^{-i\frac{k}{z}(x\xi + y\eta)} d\xi d\eta, \quad (3.22)$$

which, up to a multiplicative phase factor, is the Fourier transform of the wavefront in the aperture.

3.1.2 Diffraction in the microscope: Born & Wolf model

In order to construct a model of the microscope's PSF, we consider an adapted version of the Fresnel-Kirchoff integral (3.16), where, instead of a point source illuminating the aperture, a spherical wave with focal point \mathbf{x}_f is converging onto the aperture, while keeping the observation point \mathbf{x}_d unchanged (see Fig. 3.3):

$$U(\mathbf{x}_d) = \frac{1}{2i\lambda} \iint_{\Sigma} U(\xi, \eta, 0) \frac{e^{-ik(r-s)}}{rs} (\cos(\mathbf{n}, \mathbf{s}) - \cos(\mathbf{n}, \mathbf{r})) dS. \quad (3.23)$$

Using the same approximations as above, we thus obtain

$$U(\mathbf{x}_d) = \frac{1}{i\lambda} \iint_{\Sigma} U(\xi, \eta, 0) \frac{e^{-ik(r-s)}}{rs} dS. \quad (3.24)$$

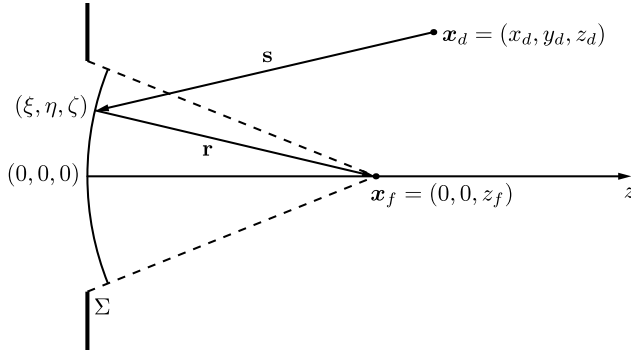


Figure 3.3 Kirchhoff diffraction for a converging spherical wave viewed through an aperture. This representation corresponds to the configuration in a microscope.

If, furthermore, the amplitude is assumed to vary slowly over the aperture with respect to r [119], i.e., $U(\xi, \eta, 0)/r \approx A$, then

$$U(\mathbf{x}_d) = \frac{A}{i\lambda} \iint_{\Sigma} \frac{e^{-ik(r-s)}}{s} dS. \quad (3.25)$$

The next step consists in expressing the distances

$$\begin{aligned} s &= \sqrt{(x_d - \xi)^2 + (y_d - \eta)^2 + (z_d - \zeta)^2} \\ r &= \sqrt{\xi^2 + \eta^2 + (z_f - \zeta)^2} \end{aligned} \quad (3.26)$$

as a function of the focal distance z_f and defocus $\delta z = z_d - z_f$. This is only possible through approximations, and has led to the development of a variety of models (a review can be found in [119]).

The first rigorous scalar model of diffraction in the microscope was proposed by Born and Wolf [71, 115]. This model is still often cited as a reference, and is frequently resorted to when the PSF is assumed to be 3-D shift-invariant. It is based on the approximations

$$s \approx z_f + (z_d - z_f) - \frac{x_d \xi + y_d \eta}{z_f} - \frac{(\xi^2 + \eta^2)(z_d - z_f)}{2z_f^2} \quad (3.27)$$

$$r \approx z_f$$

as well as the assumption that $1/s \approx 1/z_f$, such that

$$U(\mathbf{x}_d) = \frac{A}{i\lambda z_f} e^{ik\delta z} \iint_{\Sigma} \exp \left[\frac{-ik(\xi x_d + \eta y_d)}{z_f} \right] \exp \left[\frac{-ik(\xi^2 + \eta^2)\delta z}{2z_f^2} \right] d\xi d\eta. \quad (3.28)$$

Since the aperture in a microscope is circular, the above model can then be simplified using the cylindrical coordinates $\xi = a\rho \cos \theta$, $\eta = a\rho \sin \theta$, $x_d = r \cos \phi$, $y_d = r \sin \phi$, where a is the radius of the aperture:

$$\begin{aligned} U(\mathbf{x}_d) &= \frac{A}{i\lambda z_f} e^{ik\delta z} \int_0^1 \int_0^{2\pi} \exp\left[\frac{-ika\rho r \cos(\theta - \phi)}{z_f}\right] \exp\left[\frac{-ika^2\rho^2\delta z}{2z_f^2}\right] d\theta \rho d\rho \\ &= \frac{2\pi A}{i\lambda z_f} e^{ik\delta z} \int_0^1 J_0\left(\frac{ka\rho r}{z_f}\right) \exp\left[\frac{-ika^2\rho^2\delta z}{2z_f^2}\right] \rho d\rho, \end{aligned} \quad (3.29)$$

where $J_0(z)$ is the Bessel function of the first kind of order 0. If, in addition, the aperture is small with respect to the focal distance, i.e., $a \ll z_f$, then $\frac{a}{z_f} = \sin \alpha = \frac{NA}{n_i}$, and

$$U(\mathbf{x}_d) = \frac{2\pi A}{i\lambda z_f} e^{ik\delta z} \int_0^1 J_0(k_0 r NA \rho) \exp\left[\frac{-ik_0\delta z NA^2 \rho^2}{2n_i}\right] \rho d\rho, \quad (3.30)$$

which is the classical defocus model established by Born and Wolf. In the last development, note the distinction between k and k_0 , the wavenumber in vacuum, where $k = n_i k_0$. Finally, the intensity PSF for the Born and Wolf model is given by

$$h(\mathbf{x}_d; \delta z) = \left| \frac{k_0 A}{z_f} \int_0^1 J_0(k_0 r NA \rho) \exp\left[\frac{-ik_0\delta z NA^2 \rho^2}{2n_i}\right] \rho d\rho \right|^2. \quad (3.31)$$

3.1.3 Defocus model

The phase term in the Born and Wolf model arises from the approximations of the distances r and s as a function of defocus. Alternatively, it can also be derived by considering the aberration in a defocused system with respect to a perfectly focused one. Specifically, the aberration at an arbitrary point in the exit pupil of a system is defined as the optical path difference between the aberrated wavefront and the spherical reference wavefront at that point, i.e.,

$$\Lambda = n\delta, \quad (3.32)$$

where n is the refractive index of the medium², and δ is the distance travelled. Using the geometric construction in Fig. 3.4, an approximation of the optical path difference as a function of the defocus distance can be found, using the same assumptions on the angles as in the development of the Born and Wolf model, such that $R + \delta z = z$ and $\delta + R \approx z - \delta z \cos \theta$. Thus $\delta = \delta z(1 - \cos \theta)$,

²In a continuous medium, Fermat's principle implies $\Lambda = \int n(s) ds$.

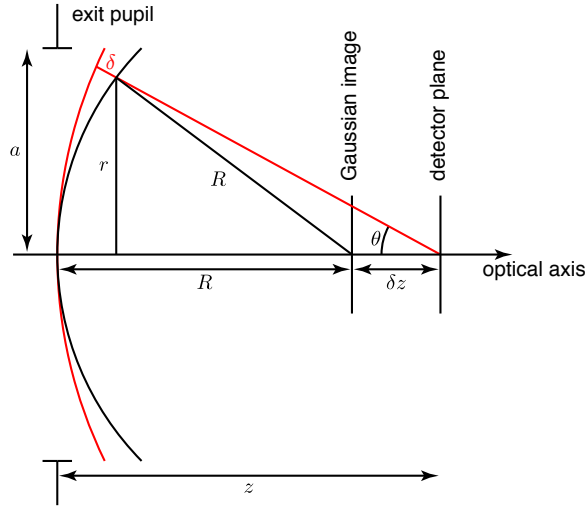


Figure 3.4 Geometric construction for the computation of the optical path difference in a simple defocus model. The red curve represents the defocused wavefront.

and using the approximation $\cos \theta \approx 1 - \frac{r^2}{2z^2}$, we obtain $\delta = \delta z \frac{r^2}{2z^2}$. Finally, substituting the normalized radius $\rho = r/a$, and $\frac{a}{z} \approx \frac{\text{NA}}{n}$, we obtain

$$\Lambda(\rho, \delta z) = \frac{\delta z \text{NA}^2 \rho^2}{2n_i}, \quad (3.33)$$

which corresponds to the phase term of the Born and Wolf model (since $\Phi(\rho, \delta z) = k_0 \Lambda(\rho, \delta z)$).

3.1.4 Resolution and depth of field

Evaluated at the in-focus position, the Born and Wolf model is equivalent to the Airy disc function

$$\begin{aligned} h(x, y, 0; 0) &= \left| A \int_0^1 J_0(k_0 r \text{NA} \rho) \rho \, d\rho \right|^2 \\ &= |A|^2 \left(\frac{J_1(k_0 r \text{NA})}{k_0 r \text{NA}} \right)^2, \end{aligned} \quad (3.34)$$

which also corresponds to Fraunhofer diffraction at a circular aperture [120]. This model was used by Rayleigh to establish his well-known resolution criterion, defined as

$$d_r = \frac{0.61\lambda}{\text{NA}}. \quad (3.35)$$

This distance corresponds to the location of the first zero in the Airy function (i.e., two overlapping Airy functions are not resolvable if they are closer than

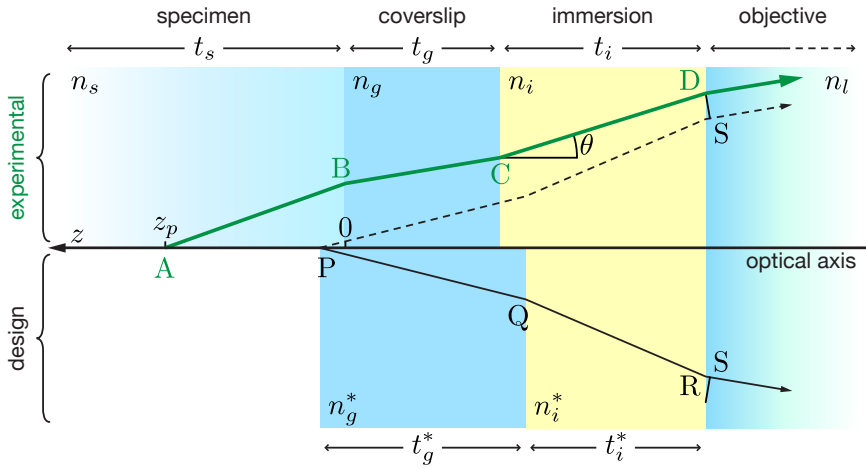


Figure 3.5 Geometric construction for the computation of the optical path difference between experimental and design conditions in an optical microscope.

d_r). Similarly, under the Born and Wolf model, the axial intensity profile is described by

$$\begin{aligned}
 h(0, 0, z; \tau) &= \left| A \int_0^1 e^{-ik_0 z \frac{NA^2}{2n_i} \rho^2} \rho d\rho \right|^2 \\
 &= \frac{2n_i^2}{k_0^2 z^2 NA^4} \left(1 - \cos \left(\frac{k_0 z NA^2}{2n_i} \right) \right).
 \end{aligned} \tag{3.36}$$

The criterion for axial resolution analogous to Rayleigh's is therefore

$$d_z = \frac{2\lambda n_i}{NA^2}. \tag{3.37}$$

Depth of field is often defined as half of this value, i.e.,

$$d_f = \frac{\lambda n_i}{NA^2}. \tag{3.38}$$

Another approach is to define depth of field as the axial region within which the PSF's diameter is smaller than the Rayleigh criterion, which, by modeling the PSF envelope as a double cone, is given by

$$d_f = \frac{0.61\lambda}{n \sin \alpha \tan \alpha} = \frac{0.61\lambda \sqrt{n_i^2 - NA^2}}{NA^2}. \tag{3.39}$$

3.2 Gibson & Lanni Model

The Born and Wolf model is accurate for a perfect system, where the only aberrations are due to defocus. Modern microscope objectives are designed to provide optimal imaging conditions for sources located directly on the coverslip, in which case the Born and Wold model holds. By contrast, these conditions are not necessarily met for fluorescent sources that are located at an arbitrary distance from the coverslip, which may give rise to spherical and higher order aberrations [115, 121]. The assumption made by Gibson and Lanni is that all observed aberrations are generated by factors external to the objective, and therefore originate in the sample/coverslip/immersion medium combination. By analogy to the defocus model, these aberrations can be characterized by the optical path difference between a ray in a perfect system and a ray under experimental conditions, as illustrated in Fig. 3.5. In addition to source depth-dependent mismatches/aberrations, typical factors that induce aberrations are the coverslip thickness, which may deviate up to 10% from design values, and the refractive index of the immersion medium (especially for oil), which can be sensitive to temperature. For the reference conditions, the optical path length is given by

$$\overline{\text{PQRS}} = n_g^* \frac{t_g^*}{\cos \theta_g^*} + n_i^* \frac{t_i^*}{\cos \theta_i^*} + n_l \gamma, \quad (3.40)$$

where

$$\gamma = \overline{\text{RS}} = \sin \theta \left(t_s \tan \theta_s + t_g \tan \theta_g + t_i \tan \theta_i - t_g^* \tan \theta_g^* - t_i^* \tan \theta_i^* \right), \quad (3.41)$$

and for a source located at an arbitrary depth z_p that corresponds to a sample layer thickness t_s , it is equal to

$$\overline{\text{ABCD}} = n_s \frac{z_p}{\cos \theta_s} + n_g \frac{t_g}{\cos \theta_g} + n_i \frac{t_i}{\cos \theta_i}. \quad (3.42)$$

The optical path difference Λ is then equal to

$$\begin{aligned} \Lambda(\theta, z; z_p, \tau) = & n_s \frac{z_p}{\cos \theta_s} + n_g \frac{t_g}{\cos \theta_g} + n_i \frac{t_i}{\cos \theta_i} - n_g^* \frac{t_g^*}{\cos \theta_g^*} - n_i^* \frac{t_i^*}{\cos \theta_i^*} \\ & - n_l \sin \theta_l \left(z_p \tan \theta_s + t_g \tan \theta_g + t_i \tan \theta_i - t_g^* \tan \theta_g^* - t_i^* \tan \theta_i^* \right), \end{aligned} \quad (3.43)$$

where the thickness and refractive index of each layer are labeled as illustrated in Fig. 3.5. An angle θ with subscript indicates the angle between the ray and the optical axis in the corresponding layer, and an asterisk denotes

an index or layer thickness in the design configuration; n_l is the refractive index of the front lens of the objective. By applying the Snell-Descartes law for each layer with respect to the immersion layer — i.e., for the sample layer, where $n_i \sin \theta_i = n_s \sin \theta_s$ and

$$\frac{n_s z_p}{\cos \theta_s} - n_l t_s \tan \theta_s \sin \theta_l = z_p \sqrt{n_s^2 - n_i^2 \sin^2 \theta_i} \quad (3.44)$$

— we rewrite the OPD as

$$\begin{aligned} \Lambda(\theta, z; z_p, \tau) = & z_p \sqrt{n_s^2 - n_i^2 \sin^2 \theta_i} \\ & + t_i \sqrt{n_i^2 - n_i^2 \sin^2 \theta_i} - t_i^* \sqrt{n_{i^*}^2 - n_i^2 \sin^2 \theta_i} \\ & + t_g \sqrt{n_g^2 - n_i^2 \sin^2 \theta_i} - t_g^* \sqrt{n_{g^*}^2 - n_i^2 \sin^2 \theta_i}. \end{aligned} \quad (3.45)$$

3.2.1 Original analysis

In their paper, Gibson and Lanni proceed to expand the optical path difference as a function of the normalized radius in the exit pupil, which is the standard approach to characterize aberrations [122, 123]. To this end, the OPD is expressed in terms of exit pupil coordinates using

$$n_i \sin \theta_i = M \sin \phi, \quad (3.46)$$

where ϕ is the angle between the converging ray and the optical axis in image space, and M is the magnification of the objective. Furthermore,

$$\sin \phi = \frac{r}{\sqrt{r^2 + z_d^2}}, \quad (3.47)$$

where r is the radius at which the ray intersects the exit pupil, and z_d is the distance of the detector plane from the exit pupil. When r is equal to the aperture radius a ,

$$\sin \phi_{\max} = \frac{a}{\sqrt{a^2 + z_d^2}} = \frac{\text{NA}}{M}, \quad (3.48)$$

where NA is the numerical aperture of the objective. Then,

$$z_d^2 = \frac{a^2 (M^2 - \text{NA}^2)}{\text{NA}^2} \quad (3.49)$$

and

$$M^2 \sin^2 \phi = \frac{\text{NA}^2 \rho^2}{\frac{\text{NA}^2}{M^2} (\rho^2 - 1) + 1}, \quad (3.50)$$

where $\rho = r/a$. Since $\frac{NA^2}{M^2}(1 - \rho^2) \ll 1$, the approximation

$$\frac{NA^2 \rho^2}{\frac{NA^2}{M^2}(\rho^2 - 1) + 1} \approx NA^2 \rho^2 \quad (3.51)$$

is always valid. According to these changes, the OPD becomes

$$\begin{aligned} \Lambda(\rho; z_p, \tau) = & z_p \sqrt{n_s^2 - NA^2 \rho^2} + t_g \sqrt{n_g^2 - NA^2 \rho^2} + t_i \sqrt{n_i^2 - NA^2 \rho^2} \\ & - t_g^* \sqrt{n_g^{*2} - NA^2 \rho^2} - t_i^* \sqrt{n_i^{*2} - NA^2 \rho^2}. \end{aligned} \quad (3.52)$$

The reference value for the immersion layer thickness, t_i^* , corresponds to the working distance of the objective, which is known. The actual value t_i is variable, however, and depends on the focal setting of the system. Therefore, it is desirable to express this parameter as a function of defocus. To this end, consider the Taylor expansion of the optical path difference around $\rho = 0$:

$$\begin{aligned} \Lambda(\rho; z_p, \tau) = & n_s z_p + n_g t_g + n_i t_i - n_g^* t_g^* - n_i^* t_i^* \\ & - \frac{NA^2 \rho^2}{2} \left(\frac{z_p}{n_s} + \frac{t_g}{n_g} + \frac{t_i}{n_i} - \frac{t_g^*}{n_g^*} - \frac{t_i^*}{n_i^*} \right) \\ & - \frac{NA^4 \rho^4}{8} \left(\frac{z_p}{n_s^3} + \frac{t_g}{n_g^3} + \frac{t_i}{n_i^3} - \frac{t_g^*}{n_g^{*3}} - \frac{t_i^*}{n_i^{*3}} \right) \\ & - \frac{NA^6 \rho^6}{16} \left(\frac{z_p}{n_s^5} + \frac{t_g}{n_g^5} + \frac{t_i}{n_i^5} - \frac{t_g^*}{n_g^{*5}} - \frac{t_i^*}{n_i^{*5}} \right) \\ & - \dots \end{aligned} \quad (3.53)$$

In the above, the second order term in ρ corresponds to the phase difference generated by defocus [71, 124], i.e.,

$$\Lambda_{\delta z}(\rho, \tau) = -\frac{\delta z NA^2 \rho^2}{2n_i}. \quad (3.54)$$

By identification, Gibson and Lanni define

$$\frac{\delta z}{n_i} \equiv \frac{z_p}{n_s} + \frac{t_g}{n_g} + \frac{t_i}{n_i} - \frac{t_g^*}{n_g^*} - \frac{t_i^*}{n_i^*}, \quad (3.55)$$

and consequently

$$t_i = n_i \left(\frac{\delta z}{n_i} + \frac{t_g^*}{n_g^*} - \frac{t_g}{n_g} + \frac{t_i^*}{n_i^*} - \frac{z_p}{n_s} \right). \quad (3.56)$$

The final expression for the optical path difference is then given by

$$\begin{aligned} \Lambda(\rho, z; z_p, \boldsymbol{\tau}) = & \left(z_p - z + n_i \left(-\frac{z_p}{n_s} - \frac{t_g}{n_g} + \frac{t_g^*}{n_g^*} + \frac{t_i^*}{n_i^*} \right) \right) \sqrt{n_i^2 - \text{NA}^2 \rho^2} \\ & + z_p \sqrt{n_s^2 - \text{NA}^2 \rho^2} + t_g \sqrt{n_g^2 - \text{NA}^2 \rho^2} \\ & - t_g^* \sqrt{n_{g^*}^2 - \text{NA}^2 \rho^2} - t_i^* \sqrt{n_{i^*}^2 - \text{NA}^2 \rho^2}, \end{aligned} \quad (3.57)$$

where we substituted $\delta z = z - z_p$, z being the axial coordinate of the focal plane. With the phase $\Phi(\rho, z; z_p, \boldsymbol{\tau}) = k_0 \Lambda(\rho, z; z_p, \boldsymbol{\tau})$ the PSF becomes

$$h(\mathbf{x}; \mathbf{x}_p, \boldsymbol{\tau}) = \left| A \int_0^1 e^{i\Phi(\rho, z; z_p, \boldsymbol{\tau})} J_0(k_0 r \text{NA} \rho) \rho \, d\rho \right|^2. \quad (3.58)$$

3.2.2 Alternative formulation

The aim of the development used by Gibson and Lanni was to enforce the defocus constraint in order to eliminate the dependency on the unknown parameter t_i . Their final result uses an approximation of (3.45), which can be avoided by substituting (3.56) directly. Then, instead of integrating over the radius of the exit pupil, the domain is changed to the angular aperture in the immersion medium, i.e.,

$$h(\mathbf{x}; \mathbf{x}_p, \boldsymbol{\tau}) = \left| A \frac{n_i^2}{\text{NA}^2} \int_0^\alpha e^{ik_0 \Lambda(\theta, z; z_p, \boldsymbol{\tau})} J_0(k_0 r n_i \sin \theta) \sin \theta \cos \theta \, d\theta \right|^2, \quad (3.59)$$

where $\alpha = \sin^{-1} \frac{\text{NA}}{n_i}$, and where we dropped the index i from the angle θ_i for ease of notation. Accordingly, the OPD becomes

$$\begin{aligned} \Lambda(\theta, z; z_p, \boldsymbol{\tau}) = & \left(z_p - z + n_i \left(-\frac{z_p}{n_s} - \frac{t_g}{n_g} + \frac{t_g^*}{n_g^*} + \frac{t_i^*}{n_i^*} \right) \right) n_i \cos \theta \\ & + z_p \sqrt{n_s^2 - n_i^2 \sin^2 \theta} + t_g \sqrt{n_g^2 - n_i^2 \sin^2 \theta} \\ & - t_g^* \sqrt{n_{g^*}^2 - n_i^2 \sin^2 \theta} - t_i^* \sqrt{n_{i^*}^2 - n_i^2 \sin^2 \theta}. \end{aligned} \quad (3.60)$$

The two expressions for the PSF in (3.58) and (3.59) are approximately equivalent through the relation $\rho \text{NA} \approx n_i \sin \theta_i$, where ρ is the radius in the exit pupil. If, however, ρ is instead defined as the normalized radius in the entrance pupil, the previous relation becomes an equality. In that setting, the defocus constraint remains an approximation, having been derived for the exit pupil. Nevertheless, it can easily be transposed to entrance pupil coordinates, yielding the same result. The exit pupil conventions need not be

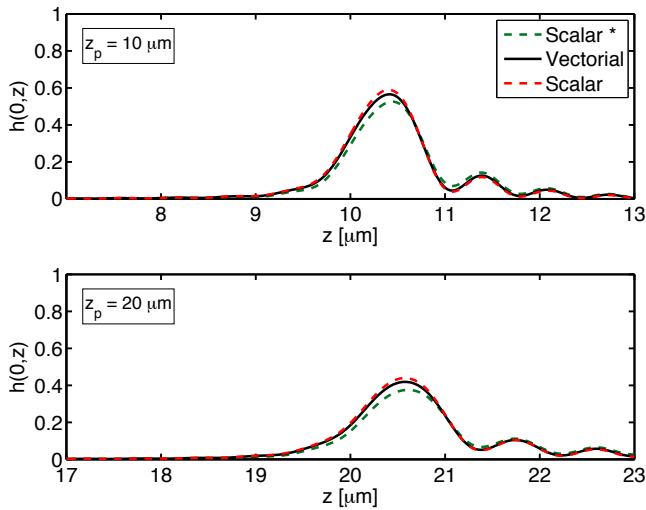


Figure 3.6 Axial intensity profiles corresponding to scalar and vectorial PSF calculations with different apodizations, for a $63\times$, 1.4 NA oil immersion objective. The scalar model with $\cos \theta$ (red dashed line) is much closer to the vectorial result than the model using $\sqrt{\cos \theta}$ (green dashed line).

enforced here, since simply an expression of t_i as a function of defocus is sought, rather than a characterization of the system's aberrations. Consequently, under the hypothesis of an analogous expansion of aberration orders in entrance pupil coordinates, the formulation in (3.59) is exact. Furthermore, it enables us to comment on the link between this model and the vectorial analysis by Richards [111] whose formulation based on conservation of energy between object and image space resulted in the appearance of the apodization function $\sqrt{\cos \theta}$ in place of the $\cos \theta$ term in (3.59). It has been suggested to correct this in the Gibson and Lanni model [109]; a closer inspection of the effect of this correction reveals that the original formulation is a closer approximation of the vectorial model, however. The effect of the apodization terms on the axial intensity profile of the PSF is illustrated in Fig. 3.6.

Until the introduction of a vectorial approach in Chapter 7, or unless mentioned otherwise, all results presented in this thesis are based on the angular version of the Gibson and Lanni model (3.59). In the next section, we briefly introduce a state-of-the-art vectorial PSF model based on the analysis of Richards and Wolf, after which we conclude by discussing some relevant characteristics and comparisons between scalar and vectorial PSF models.

3.3 Vectorial Models

The reliance on small angle approximations in the development of a scalar PSF model limits its validity for high numerical apertures. For many applications, including super-resolved localization, the Gibson and Lanni model is sufficiently precise, but in other cases, it is necessary to incorporate the vectorial nature of the electric field into the PSF calculation. In Chapter 7, we present a method for the localization of individual fluorescent dipoles, whose diffraction patterns can only be predicted using vectorial calculations, for which we introduce an appropriate model. In this section we briefly recall the model introduced by Wolf and Richards, which laid the foundations for PSF calculations based on the propagation of the electric field vector in an optical system. The following three integrals are defined according to our formulation in Chapter 7, and rely on the same parameters as the Gibson and Lanni model:

$$\begin{aligned}
 I_0(\mathbf{x}; \mathbf{x}_p, \tau) &= \int_0^\alpha B_0(\theta, \mathbf{x}; \mathbf{x}_p, \tau) (t_s^{(1)} t_s^{(2)} + t_p^{(1)} t_p^{(2)} \frac{1}{n_s} \sqrt{n_s^2 - n_i^2 \sin^2 \theta}) d\theta \\
 I_1(\mathbf{x}; \mathbf{x}_p, \tau) &= \int_0^\alpha B_1(\theta, \mathbf{x}; \mathbf{x}_p, \tau) (t_p^{(1)} t_p^{(2)} \frac{n_i}{n_s} \sin \theta) d\theta \\
 I_2(\mathbf{x}; \mathbf{x}_p, \tau) &= \int_0^\alpha B_2(\theta, \mathbf{x}; \mathbf{x}_p, \tau) (t_s^{(1)} t_s^{(2)} - t_p^{(1)} t_p^{(2)} \frac{1}{n_s} \sqrt{n_s^2 - n_i^2 \sin^2 \theta}) d\theta,
 \end{aligned} \tag{3.61}$$

where

$$B_m(\theta, \mathbf{x}; \mathbf{x}_p, \tau) = \sqrt{\cos \theta} \sin \theta J_m(kr n_i \sin \theta) e^{ik\Lambda(\theta, \mathbf{z}; \mathbf{z}_p, \tau)}. \tag{3.62}$$

The Fresnel coefficients

$$\begin{aligned}
 t_s^{(l)} &= \frac{2n_l \cos \theta_l}{n_l \cos \theta_l + n_{l+1} \cos \theta_{l+1}} \\
 t_p^{(l)} &= \frac{2n_l \cos \theta_l}{n_{l+1} \cos \theta_l + n_l \cos \theta_{l+1}}
 \end{aligned} \tag{3.63}$$

are the transmission coefficients for orthogonal and parallel polarization between the different layers in object space. The electric field in the detector plane is

$$\mathcal{E} = \begin{bmatrix} -iA(I_0 + I_2 \cos(2\phi_d)) \\ -iAI_2 \sin(2\phi_d) \\ -2AI_1 \cos(\phi_d) \end{bmatrix} \tag{3.64}$$

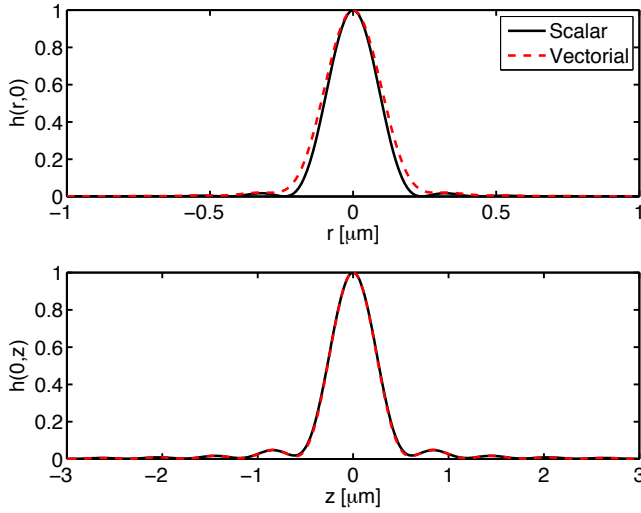


Figure 3.7 Radial (top) and axial (bottom) intensity profiles of the ideal PSF for a $63\times$, 1.4 NA oil immersion objective, resulting from scalar and vectorial calculations. The radial profile illustrates the principal difference between the two models: with the vectorial approach the intensity does not reach zero after the central peak.

where ϕ_d is the azimuth angle in the detector plane. The corresponding observed intensity for linearly polarized light in the x direction is thus given by

$$\begin{aligned}
 h(\mathbf{x}; \mathbf{x}_p, \tau) &= \frac{1}{16\pi} |\mathcal{E}|^2 \\
 &= \frac{|A|^2}{16\pi} \left(|I_0|^2 + |I_2|^2 + 2\Re\{I_0 I_2^*\} \cos(2\phi_d) + 4|I_1|^2 \cos^2 \phi_d \right)
 \end{aligned} \tag{3.65}$$

The image intensity for unpolarized light is obtained by integrating over ϕ_d , i.e.,

$$\begin{aligned}
 \bar{h}(\mathbf{x}; \mathbf{x}_p, \tau) &= \frac{1}{2\pi} \int_0^{2\pi} h(\mathbf{x}; \mathbf{x}_p, \tau) d\phi_d \\
 &= \frac{|A|^2}{16\pi} (|I_0|^2 + 2|I_1|^2 + |I_2|^2).
 \end{aligned} \tag{3.66}$$

3.4 PSF characteristics

As the developments in the previous sections have shown, the aberration in the PSF is strongly influenced by the axial position z_p of the point source, and thus results in an axially shift-variant behavior. Its importance in localization problems will be discussed in later chapters, but in order to provide

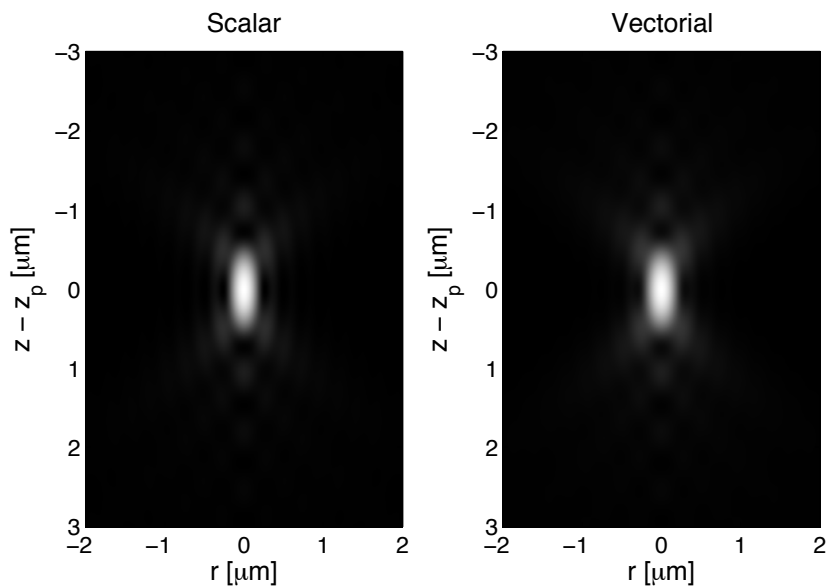


Figure 3.8 x - z cross section of the PSF for a $63\times$, 1.2 NA water immersion objective generated by a source located in $z_p = 0 \mu m$ in a medium of index $n_s = 1.46$.

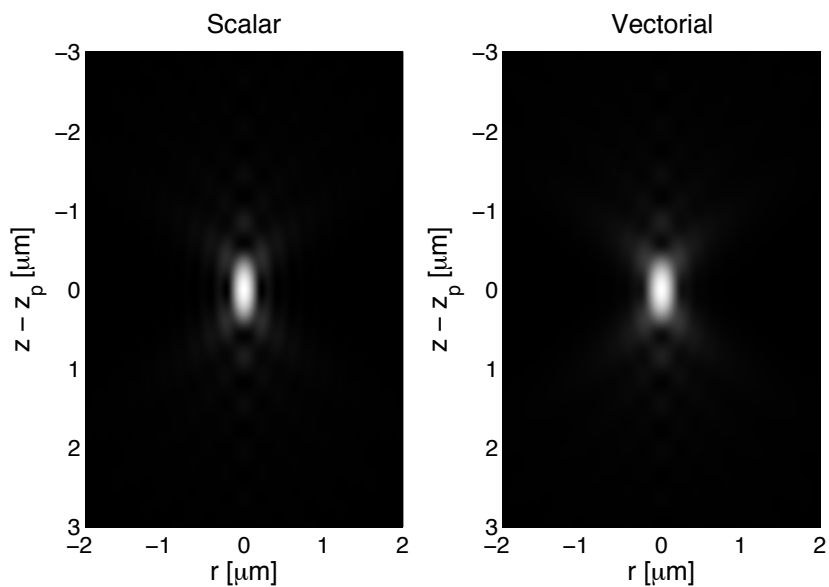


Figure 3.9 x - z cross section of the PSF for a $63\times$, 1.4 NA oil immersion objective generated by a source located in $z_p = 0 \mu m$ in a medium of index $n_s = 1.46$.

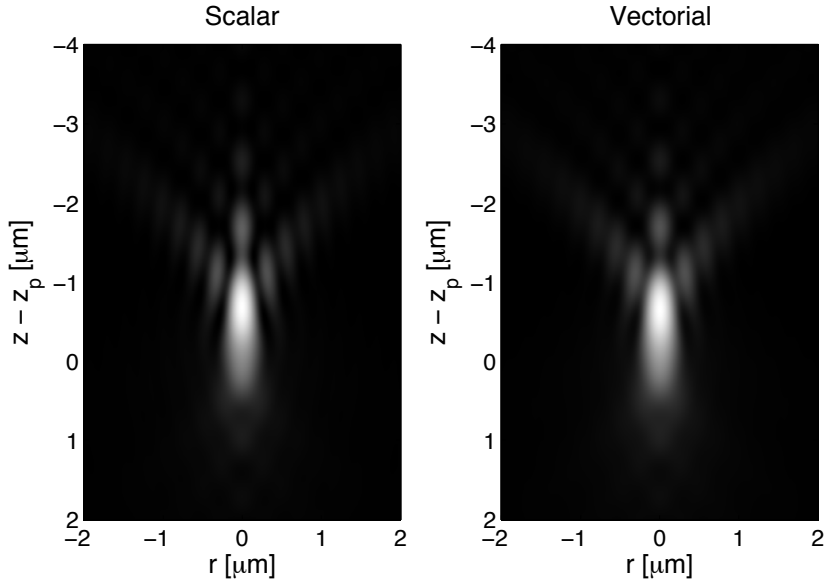


Figure 3.10 x - z cross section of the PSF for a $63\times$, 1.2 NA water immersion objective generated by a source located in $z_p = 10\ \mu\text{m}$ in a medium of index $n_s = 1.46$.

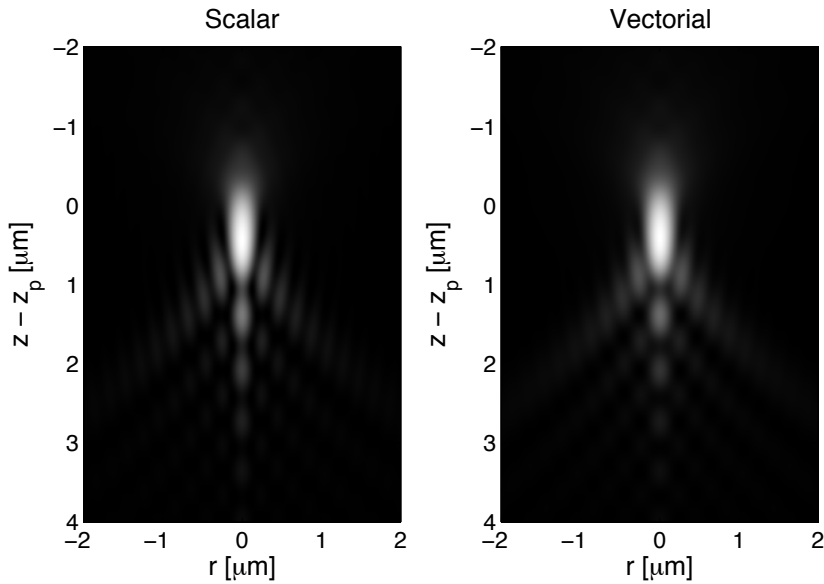


Figure 3.11 x - z cross section of the PSF for a $63\times$, 1.4 NA oil immersion objective generated by a source located in $z_p = 10\ \mu\text{m}$ in a medium of index $n_s = 1.46$.

the reader with some intuition of the PSF's appearance, some examples are provided here. For the sake of completeness, the results for both scalar and vectorial calculations are shown. Given a source located in $z_p = 0$, and in the absence of any refractive index or thickness mismatches, the Gibson and Lanni formulation is equivalent to a standard defocus model. In Fig. 3.7, the corresponding radial and axial intensity profiles are shown. The axial profiles from the scalar and vectorial calculations match perfectly, however, for the radial case the vectorial model does not correspond to the Airy disc function.

A more complete picture is given, for the same configuration, in Fig. 3.8 for a Leica HCX PL APO 63×1.2 NA water immersion objective, and in Fig. 3.9 for a Zeiss Plan-Apochromat $63\times, 1.4$ NA oil immersion objective. Under the same assumptions concerning mismatched indexes or thicknesses, but for a source located away from the coverslip-specimen interface in a medium whose refractive index differs from the index of the immersion medium, depth-dependent aberrations are observed in the PSF. This is illustrated in Fig. 3.10 for a water immersion objective and in Fig. 3.11 for an oil immersion objective, assuming a source located at $z_p = 10\text{ nm}$. In both cases, a shift of the order of several hundred nanometers of the observed intensity maximum with respect to the source position occurs; the magnitude of this shift is related to the mismatch between n_s and n_i , albeit in nonlinear fashion. It is also nonlinearly linked to other PSF parameters, such as the source's axial position z_p and the wavelength, as illustrated in Fig. 3.12. Due to the magnitude of this intensity maximum shift, it is crucial to use a model that correctly reproduces this behavior when axial localization accuracies at nanometer or 10-nm scales are desired.

3.5 Implementation

The evaluation of the expressions for the PSF models discussed in this chapter is rather involved due to numerical integration. However, by taking advantage of the radial symmetry in the integrals, and by judiciously choosing the integration step size, highly efficient implementations can be achieved. Via Simpson's rule, the integral in $h(\mathbf{x}; \mathbf{x}_p, \boldsymbol{\tau})$ is approximated by evaluating

$$\int_0^\alpha f(\theta) d\theta \approx \frac{\alpha}{3n} \left[f(0) + 2 \sum_{j=1}^{n/2-1} f(\theta_{2j}) + 4 \sum_{j=1}^{n/2} f(\theta_{2j-1}) + f(\alpha) \right], \quad (3.67)$$

where $f(\theta)$ is the integrand of $h(\mathbf{x}; \mathbf{x}_p, \boldsymbol{\tau})$. The key to an efficient evaluation of $h(\mathbf{x}; \mathbf{x}_p, \boldsymbol{\tau})$ lies in determining the minimum number of samples n required to accurately approximate the integration. Both the optical path

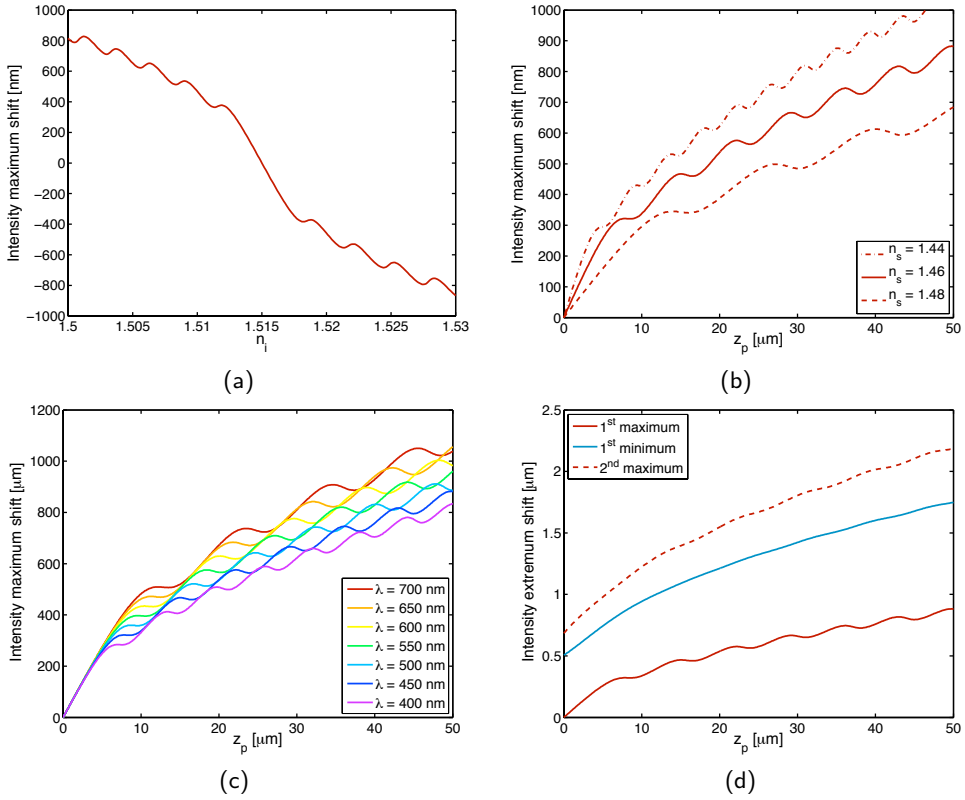


Figure 3.12 Influence of several parameters on the shift of the PSF's intensity maximum. (a) Mismatch of the refractive index n_i with respect to the design value n_i^* . (b) Combined effect of particle depth z_p and refractive index n_s of the specimen. (c) Effect of the wavelength. (d) Shift of the first intensity minimum and secondary maximum.

difference $\Lambda(\theta, \mathbf{x}; \mathbf{x}_p, \boldsymbol{\tau})$ and the Bessel function can be highly oscillatory; for the latter, the oscillation frequency is determined by its argument (i.e., $\omega_J = k_0 r n_i$), and for the former, it can be determined by considering the $\cos(ik_0 \Lambda(\theta, \mathbf{z}; z_p, \boldsymbol{\tau}))$ component of the complex exponential in $h(\mathbf{x}; \mathbf{x}_p, \boldsymbol{\tau})$. By taking a first order Taylor expansion of Λ around the angle θ_0 (chosen at or close to α , where the exponential term presents the strongest oscillations), i.e.,

$$\cos(k_0 \Lambda(\theta, \mathbf{z}; z_p, \boldsymbol{\tau})) \approx \cos\left(k_0 \left(\Lambda(\theta_0, \mathbf{z}; z_p, \boldsymbol{\tau}) + \Lambda'(\theta_0, \mathbf{z}; z_p, \boldsymbol{\tau})(\theta - \theta_0)\right)\right), \quad (3.68)$$

the corresponding frequency $\omega_{\text{exp}} = k_0 \Lambda'(\theta_0, \mathbf{z}; z_p, \boldsymbol{\tau})$ is obtained. Accordingly, the required number of samples is $N = c_0 \alpha \omega_{\text{max}} / \pi$, where $\omega_{\text{max}} = \max(\omega_{\text{exp}}, \omega_J)$, and c_0 is the number of samples needed to integrate \cos over

	Computation time [s]
Gaussian model	0.085
Reference method [125]	20.87
Scalar model	0.22
Vectorial model	0.61

Table 3.1 Performance comparison between a state-of-the-art PSF implementation and the proposed implementation of the scalar and vectorial formulations described in this chapter. The reported computation times are averages for the evaluation of 3-D PSF volumes comprising 10^6 samples each. Timings were measured on a 2.66 GHz Intel Xeon dual-core CPU.

a period; in practice, $c_0 = 8$ yields sufficiently accurate results. The sampling step is $s = \alpha/N$. A performance comparison between this approach and a state-of-the-art implementation [125] is given in Table 3.1; an approximately 100-fold acceleration is achieved. Fast computation times are the principal reason behind the reliance of FLM techniques on Gaussian fitting. These results show that it is possible to achieve comparable speeds in the evaluation of accurate PSF models, rendering their use in FLM algorithms feasible.

3.6 Conclusion

In this chapter, we reviewed image formation models for optical microscopy and showed how they are derived from Maxwell's equations. The final scalar and vectorial formulations are equivalent to state-of-the-art models in the literature. An efficient implementation of these models was proposed, which enables their use in iterative localization algorithms. In the next chapter, we compare Gaussian- and PSF-based approaches in terms of localization accuracy.

Chapter 4

Localization accuracy in the plane—A comparison between PSF- and Gaussian-based approaches

To date, most FLM techniques have relied on 2-D Gaussian fitting (see, e.g. the supplement of [21]). Indeed, due to the close resemblance of the in-focus PSF of a microscope to a Gaussian, this assumption works well for imaging fluorophores that are in or very close to the focus. The principal advantage of using a Gaussian (matched to the in-focus section of the PSF) for performing the localization is mainly computational, since the calculation of a 2-D Gaussian function is less costly than the evaluation of a PSF model, which involves numerical integration (see Chapter 3). In order to retain the advantages of Gaussian-based localization, 3-D extensions of FLM based on astigmatic imaging have been proposed¹, where axial localization is performed by fitting an elongated Gaussian to the elliptically distorted image of the PSF [26, 38]. However, these approaches are limited to samples (or thin sections) in which the PSF is axially shift-invariant, and require experimental calibration of the Gaussian covariance matrix.

A more general method for axial localization that relies on standard microscope optics and an accurate PSF model will be introduced in the next chapter. Here, we present a brief discussion of localization in 2-D, highlighting a comparison between PSF- and Gaussian-based approaches. In the pro-

¹This achieved by introducing a cylindrical lens in the microscope optics. The resulting distortion depends on the direction of defocus, i.e., the direction for positive defocus values is orthogonal to the distortion for negative values. This provides a straightforward means of identifying the axial location of the source relative to the focal plane.

cess, we identify the conditions under which the Gaussian model is a valid approximation; i.e., when the localization accuracy reaches the theoretical limits predicted using the appropriate PSF model. In a review of several basic localization methods aimed at particle tracking, Cheezum et al. [13] discussed the limitations of Gaussian-based localization in terms of signal-to-noise ratio (SNR), based on simulations. These results confirmed earlier observations by Kubitschek et al. [126] in experiments involving the localization of single GFP molecules; they will be used as a reference in the comparison between PSF- and Gaussian-based approaches.

This chapter is organized as follows: in the next section, we briefly introduce a measurement noise model that will be developed in greater detail in subsequent chapters. Following this, we discuss SNR measures to assess image quality. In Section 4.3, we present the statistical tools based on which the theoretical bounds on localization accuracy are established. Following this, we compare the localization accuracies obtained through Gaussian- and PSF-based fitting against these bounds, and conclude with a discussion of the results.

4.1 Image formation

For the sake of simplicity, a shift-variant PSF as well as ideal experimental conditions are assumed. Here, we use the notation $h(\mathbf{x}; \mathbf{x}_p, \boldsymbol{\tau})$ for the defocus model described in the previous chapter. For a single molecule, the intensity $s(\mathbf{x})$ at the detector, formulated in object space, can be written as

$$s(\mathbf{x}) = h(\mathbf{x}; \mathbf{x}_p, \boldsymbol{\tau}) + b. \quad (4.1)$$

The PSF h comprises an amplitude factor A , and b accounts for a background signal due to, i.e., autofluorescence of the sample (a more detailed description of potential background contributions will be discussed in the next chapter).

The average number of photons \bar{q} corresponding to this intensity is expressed as

$$\bar{q}(\mathbf{x}) = c \cdot s(\mathbf{x}), \quad (4.2)$$

where c is an appropriate conversion factor that accounts for the system's detection efficiency. A detailed noise model for fluorescence microscopy will be presented in the next chapter; for the present analysis, we assume a photon-limited noise scenario, where the probability of observing q photons at a point \mathbf{x} in the detector plane is given by

$$P_{q(\mathbf{x}; \mathbf{x}_p, \boldsymbol{\tau})}(q) = \frac{e^{-\bar{q}(\mathbf{x}; \mathbf{x}_p, \boldsymbol{\tau})} \bar{q}(\mathbf{x}; \mathbf{x}_p, \boldsymbol{\tau})^q}{q!}. \quad (4.3)$$

4.1.1 Discretization and pixelation

Discretization of the PSF needs to take the pixelation of the detector into account. Due to the physical size of a pixel compared to the oscillations in the PSF model, a sampled version of the PSF can be significantly different from a model that takes integration over the pixel area into account. This is notably the case around the focus, where the intensity is concentrated in a small number of pixels. Ideally, the discretization of $h(x; x_p, \tau)$ thus amounts to computing

$$s[\mathbf{k}] = c \int_{\Omega} s(\mathbf{x}) d\mathbf{x}, \quad (4.4)$$

where $\Omega \subset \mathbb{R}^2$ is the neighborhood of a pixel centered on the detector coordinate \mathbf{k} . To make the computation tractable, several simplifying assumptions are made, however. The assumption of contiguous pixels can be made without a notable loss in accuracy; incorporating the fill rate does not significantly alter the numerical evaluation of the PSF model. Furthermore, the integration can be efficiently approximated by oversampling and averaging the PSF model.

4.2 Signal-to-noise ratio

Image quality depends on the energy of the fluorophores (which is reflected in the amplitude A of the PSF), the background value b , the factor c , and on possible extraneous noise sources. The SNR is a convenient measure for quantifying quality when the underlying signal is known. Due to the usually dominant contribution of the background, such a criterion should only be applied to the signal above the mean background level; i.e., to h , which for the standard definition of SNR yields

$$\text{SNR} = 10 \log_{10} \frac{c^2 \|h\|^2}{c^2 \|h - (\tilde{s} - b)\|^2} = 10 \log_{10} \frac{\|h\|^2}{\|s - \tilde{s}\|^2}. \quad (4.5)$$

In our notation, \tilde{s} represents the measured image and $\|\cdot\|$ stands for the ℓ_2 -norm; the discrete versions of signals are pixelated versions of their continuous counterparts. A notable problem with this definition lies in the influence of the support of h (the constant component of the support is generally much larger than the support of the fluorescent signal). It is therefore preferable to rely on the peak signal-to-noise ratio (PSNR), where this influence is reduced. It is defined as

$$\text{PSNR} = 10 \log_{10} \frac{\max(h)^2}{\frac{1}{N} \|s - \tilde{s}\|^2}, \quad (4.6)$$

where N is the number of pixels in s .

An alternative definition of SNR used in the localization literature [126] is given by

$$\text{SNR} = \frac{\max(\tilde{s})}{\sqrt{\sigma_b^2 + \text{Var}(\tilde{s} - b)}}, \quad (4.7)$$

where σ_b^2 is the variance of background-induced noise. The equivalent logarithmic expression

$$\text{SNR} = 10 \log_{10} \frac{\max(\tilde{s})^2}{\sigma_b^2 + \text{Var}(\tilde{s} - b)} \quad (4.8)$$

closely resembles the definition of the PSNR given above, up to the background variance term. Since the latter can be assumed to be constant for the duration of an experiment, the two definitions yield the same information. Another similar criterion is given in [13], where the mean value above background is used for the signal term, and the mean square error (MSE) is used to compute the noise term.

4.2.1 Simulations

For the purpose of simulations, it is more convenient to define image quality in terms of the PSNR than in terms of photon counts. This can be achieved by expressing c as a function of the PSNR, whose expectation is equal to

$$\mathbb{E}\{\text{PSNR}\} = 10 \log_{10} \frac{c \sum \max(h)^2}{\frac{1}{N} \sum s}. \quad (4.9)$$

Solving for c yields

$$c = 10^{\frac{\text{PSNR}}{10}} \frac{\frac{1}{N} \sum s}{\max(h)^2}. \quad (4.10)$$

Simulated acquisitions of a single fluorophore for a range of PSNR values are shown in Fig. 4.1. Contrary to the values obtained on natural images in the image processing literature, PSNRs up to 35 dB correspond to strong noise levels.

4.3 Localization accuracy

Localization accuracy is generally defined in terms of the standard deviation of the position estimator \hat{x}_p [12]. The Cramér-Rao bound (CRB) establishes a limit on the variance of any unbiased estimator, and can be used to define a theoretical limit on localization accuracy [127]. For a multivariate estimator, these bounds are calculated using the Fisher information matrix.

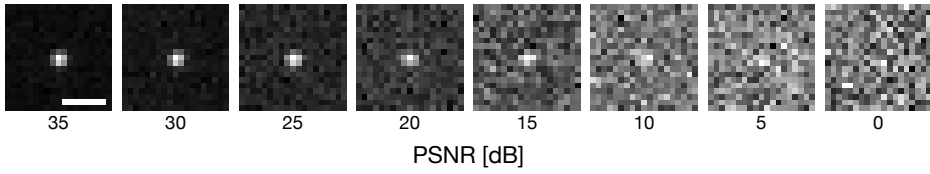


Figure 4.1 Image of a point source at different levels of PSNR, for a $63\times$, 1.4 NA objective under ideal conditions, recorded with a $6.45\times 6.45\ \mu\text{m}^2$ pixel CCD at 100 nm defocus. Scale bar: 500 nm.

4.3.1 Fisher information and the Cramér-Rao bound

For a parameter estimation problem involving a set of N_p unknown parameters $\vartheta = \{\vartheta_1, \dots, \vartheta_{N_p}\}$, the Fisher information matrix is defined as

$$\mathbf{F}_{ij} = \mathbb{E} \left\{ \frac{\partial}{\partial \vartheta_i} \ln f_{\vartheta}(X) \frac{\partial}{\partial \vartheta_j} \ln f_{\vartheta}(X) \right\}, \quad (4.11)$$

where f_{ϑ} is the probability density function of the underlying process. For the Poisson noise model described in (4.3), this expression reduces to

$$\mathbf{F}_{ij} = \mathbb{E} \left\{ \frac{\partial}{\partial \vartheta_i} (-\bar{q} + q \ln \bar{q}) \frac{\partial}{\partial \vartheta_j} (-\bar{q} + q \ln \bar{q}) \right\}. \quad (4.12)$$

Evaluating the expectation in this result finally leads to [128]

$$\mathbf{F}_{ij} = \int_{\mathbb{R}^2} \frac{1}{\bar{q}} \frac{\partial \bar{q}}{\partial \vartheta_i} \frac{\partial \bar{q}}{\partial \vartheta_j} d\mathbf{x}. \quad (4.13)$$

There exists no closed-form solution for the integral (due to the form of the PSF model in \bar{q}), and the following discretization is used:

$$\mathbf{F}_{ij} = \sum_{\mathbf{k} \in S} \frac{1}{\bar{q}} \frac{\partial \bar{q}}{\partial \vartheta_i} \frac{\partial \bar{q}}{\partial \vartheta_j}, \quad (4.14)$$

where the model and derivatives take pixelation into account. The Cramér-Rao bound on the estimators of the elements of ϑ_i are then given by the diagonal of the inverse of the Fisher information matrix, i.e.,

$$\text{Var}(\hat{\vartheta}_i) \geq [\mathbf{F}^{-1}]_{ii}. \quad (4.15)$$

For the scalar case, the CRB is given directly by

$$\text{Var}(\hat{\vartheta}) \geq 1 / \int_{\mathbb{R}^2} \frac{1}{\bar{q}} \left(\frac{\partial \bar{q}}{\partial \vartheta} \right)^2 d\mathbf{x}. \quad (4.16)$$

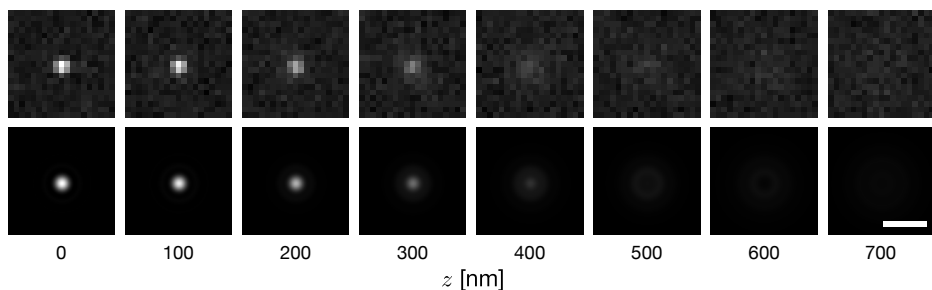


Figure 4.2 Top row: image of a point source at different levels of defocus, for a $63\times$, 1.4 NA objective under ideal conditions, recorded with a $6.45\times 6.45\ \mu\text{m}^2$ pixel CCD. The corresponding PSNR levels are 30.01, 29.23, 26.86, 22.58, 19.96, 7.90, 5.03, 1.27 dB. Bottom row: underlying continuous intensity distribution. Scale bar: 500 nm.

Bounds for 2-D localization

In the 2-D localization problem, the parameter set reduces to $\vartheta = (x_p, y_p, A)$. Due to the circular symmetry of the PSF, the non-diagonal elements of the Fisher information matrix for this parameter set are equal to zero, and the CRBs are accordingly given by

$$\text{Var}(\hat{x}_p) \geq 1 \left/ \int_{\mathbb{R}^2} \frac{1}{\bar{q}} \left(\frac{\partial \bar{q}}{\partial x_p} \right)^2 dx \right. \quad (4.17)$$

$$\text{Var}(\hat{y}_p) \geq 1 \left/ \int_{\mathbb{R}^2} \frac{1}{\bar{q}} \left(\frac{\partial \bar{q}}{\partial y_p} \right)^2 dx \right. \quad (4.18)$$

$$\text{Var}(\hat{A}) \geq 1 \left/ \int_{\mathbb{R}^2} \frac{1}{\bar{q}} \left(\frac{\partial \bar{q}}{\partial A} \right)^2 dx \right. \quad (4.19)$$

An in-depth analysis of these bounds was carried out by Ober et al. [18]. These authors established the conditions under which the CRBs are minimal for 2-D localization, and discussed the influence of the imaging system's properties on the bounds. In their approach, they relied on an ideal PSF defined by the Airy function to perform the fitting. Here, we take defocus into account, which allows for small variations in the images of fluorophores that are within the depth of field, as illustrated in Fig. 4.2. With a $63\times$, 1.4 NA oil immersion objective, fluorophores within a focal range of approximately 600 nm appear as highly similar spots. The focus of the remainder of this chapter is to assess the effect on localization accuracy when the exact model is replaced by a Gaussian.

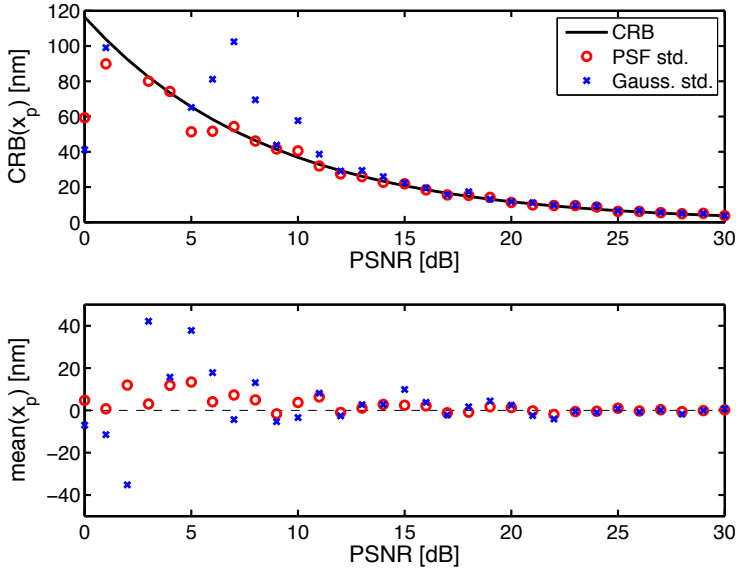


Figure 4.3 Comparison of PSF- and Gaussian-based localization accuracies as a function of PSNR. Results are shown for 100 realizations of noise at each PSNR level.

4.4 Results and discussion

In this section, we rely on the optimization of a least-squares criterion to perform the localization, i.e.,

$$(\hat{x}_p, \hat{y}_p) = \arg \max_{(x_p, y_p)} \|s - \tilde{s}\|^2, \quad (4.20)$$

which is the approach commonly used in FLM. A more accurate (with respect to the Poisson-based noise model) maximum-likelihood criterion is presented in the next chapter. The model term s is adjusted depending on whether the exact PSF model or a Gaussian approximation thereof is used for the localization.

In Fig. 4.3, we compare the localization accuracy for these approaches in terms of the PSNR. Both begin to break down at PSNR values around 12 dB, although the PSF-based approach remains significantly more accurate at lower PSNRs (which is expected since the model is exact in this case). In the results by Cheezum et al. [13] and Kubitscheck et al. [126], the reported threshold values were $\text{SNR} = 4$, which corresponds to 12 dB (see (4.8)).

In Fig. 4.4, we compare the localization accuracy between Gaussian- and PSF-based approaches for particles at different focal positions. Up to defocus values of 400 nm, which corresponds to particles that are within the depth of field of the objective, there is no significant difference between the

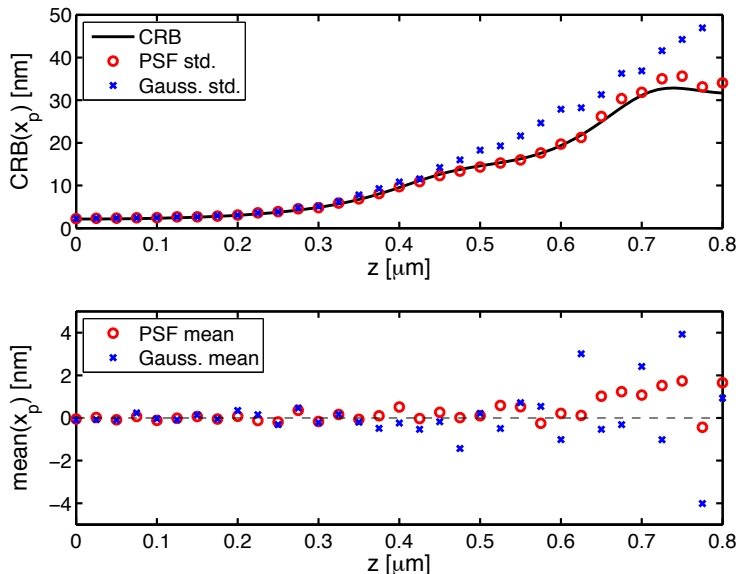


Figure 4.4 Comparison of PSF- and Gaussian-based localization accuracies as a function of defocus. Results are shown for 100 realizations of noise at each PSNR level.

two approaches; both are near-optimal and reach the CRB. For larger values of defocus, Gaussian localization accuracy decreases due to the presence of diffraction rings in the PSF. While this result confirms the validity of a Gaussian approximation for 2-D localization, it also illustrates the resulting discrepancy between axial and lateral resolution in 2-D localization, which can reach two orders of magnitude compared to a factor of approximately 3.5 for a widefield system.

In the next chapter, we will show how the depth of field ambiguity can be circumvented through off-focus imaging.

Chapter 5

A maximum-likelihood formalism for subresolution localization of fluorescent nanoparticles

5.1 Introduction

Luminescent markers such as fluorescent proteins and quantum dots have become an invaluable tool in biology, where they enable studies of molecular dynamics and interactions in living cells and organisms. Such studies are usually performed with a fluorescence microscope configured to acquire a time-series of two or three-dimensional data, the latter generally in the form of a stack of images taken at different focal distances. These are then processed using particle tracking techniques, which aim to establish the particles' trajectories from their position in individual acquisitions. Determining these positions with a high level of precision is essential for obtaining biologically significant results; the typical sizes of the commonly employed fluorophores are of the order of 10 nm, which is significantly smaller than the optical resolution of the system.

This implies that a fluorescent particle can be assimilated to a point source, and thus, that its image corresponds to a section of the microscope's three-dimensional point spread function (PSF), degraded by various types of noise. In essence, the localization task then amounts to determining the position of the particle by fitting a model of the PSF to such an image.

This chapter is based on: F. Aguet et al., "A maximum-likelihood formalism for subresolution axial localization of fluorescent nanoparticles," *Opt. Express*, vol. 13, pp. 10503–10522, 2005, [44].

In the lateral directions, for particles that are in focus, this is a relatively straightforward task for which several methods have been proposed. Axial localization is more challenging, however, since even when the specimen can be optically sectioned with an arbitrarily fine step¹, localization is made difficult by the poor axial optical resolution, the fact that the PSF of a microscope is non-stationary along the optical axis [114], and the presence of noise [129].

These factors are not only limiting in the case of particle localization, but in any 3D imaging application in microscopy. Consequently, various approaches for improving the resolution of optical microscopes, such as I⁵M [9], 4-Pi Microscopy [4], and STED [5], have been proposed in recent years, showing that Abbe's resolution limit can be broken. Alternatively, a system specifically destined for particle tracking localization was introduced by Kao et al., who proposed the use of cylindrical optics to encode a particle's axial position [38], and reached axial resolutions down to 12 nm. The downside of these methods is that they require customized hardware, which currently still limits their widespread applicability. In this chapter, we show that via computational means, particles can be localized with a precision that is clearly beyond the limit traditionally imposed by optical resolution. The method is destined for widefield fluorescence microscopy, which makes it widely applicable.

5.1.1 Review of computational approaches

The model-based methods proposed for lateral localization typically rely on a simplified diffraction model, or some Gaussian approximation of the PSF (see, e.g. [12, 13]). Notably, Thompson et al. proposed an iterative method based on the minimization of the least-squares difference between an image of a particle and a Gaussian model of the PSF [17], and Ober et al. studied the theoretical limits of lateral localization [18]. By computing the Cramér-Rao bound (CRB) for the lateral position, they confirmed that, although the images of single particles are limited by the microscope's resolution, it is possible to estimate the lateral position with sub-resolution accuracy. In some cases, nanometer-scale localization can be achieved.

To date, only few studies have dealt explicitly with the issue of sub-resolution localization in the axial direction. This can be partly attributed to the scarcity of simple but accurate PSF models for optical microscopes. Several attempts to circumvent the use of a PSF model have been made. Van Oijen et al. [130] proposed a method involving a high-resolution z-stack acqui-

¹In practice, the number of possible optical sections is constrained by the exposure time, the dynamics of the biological process under study, and photobleaching of the fluorescent labels.

sition of the particle (i.e. a series of images taken at different focal distances with regular intervals). It is based on identifying the slice for which the radial size of a Gaussian fit to the diffraction-limited spot is minimal within the z-stack. There are several limitations to this approach, however. It can only work properly if the movement of the particle during the acquisition process is sufficiently slow, and localization is limited by the size and resolution of the z-stack. Additionally, the section of the PSF whose radial size is minimal does not necessarily correspond to the situation where the particle is in the focal plane (we will emphasize this in the following section). Also, for the estimation algorithm to be as fast as possible, it is desirable to localize particles from only one or few acquisitions, without needing to process entire high-resolution z-stacks.

Speidel et al. demonstrated the feasibility of sub-resolution localization by experimentally showing that the axial position of a particle can be determined from a single defocused image of the particle [42]. When the particle is sufficiently out of focus, it gives rise to diffraction rings. These authors empirically established a linear relation between the radius of the outermost diffraction ring and the axial position of the particle, which allows them to estimate its position with nanometer precision. This is especially attractive since the estimation becomes possible from a single acquisition. The downside of the approach is again related to the non-stationarity of the PSF, meaning that the linear relationship may vary as a function of the particle's depth within the specimen. It is also constrained to the localization of particles that are sufficiently out-of-focus such that rings are present in their diffraction patterns.

In principle, it is possible to obtain an analytical solution to axial localization by using a theoretical PSF model to estimate a particle's position from one or few out-of-focus acquisitions (the diffraction pattern increases in complexity as a function of defocus, thus containing more "information", but also less signal). In a preliminary report, we have investigated the viability of such an approach by establishing the fundamental theoretical limits with respect to the precision that can be expected in the estimation [131].

5.1.2 Organization of the chapter

In this chapter we present a refined particle localization method, built upon a non-stationary theoretical PSF model. We first introduce an image formation model, which also includes the effect of noise. Next we establish the Cramér-Rao bound on axial localization, which gives us the fundamental precision that can be achieved with such an image formation model, independently of the estimator used. We hereby extend the methodology presented by Ober et al. [18] to three dimensions. Subsequently, we derive a

maximum-likelihood estimator for the axial position, and show that, under ideal circumstances, it reaches the precision predicted by the theoretical bound. In the final part of the chapter, we incorporate lateral localization into the maximum-likelihood estimator, and show the validity of our approach by demonstrating the axial localization with sub-resolution precision of fluorescent beads. We also discuss the possibility of optimizing acquisition parameters based on the CRB.

5.2 Materials and methods

5.2.1 Notations and conventions

To formulate the mathematical expressions throughout this chapter, we use an absolute coordinate system placed in the object space of the microscope. We make the hypothesis that a standard microscope setup is used, meaning that the sample consists of a specimen mounted between a microscope slide and a coverslip. We define the origin of our system at the interface between the coverslip and specimen layer (see Fig. 5.1). The optical axis (z -axis) points from the objective towards the sample, such that distances into the specimen are positive. We denote the position of a particle by (x_p, y_p, z_p) , and a point of observation (corresponding to a point on the focal plane) by (x, y, z) . When multiple acquisitions at different focal positions are considered, (x, y, z_n) corresponds to a point on the n th acquisition. In the first part, where we concentrate on axial localization, we assume that the particle is located in $(0, 0, z_p)$ for the sole purpose of making expressions as simple as possible. For the sake of consistency, we also express the pixel coordinates of acquisitions in object space (imagine acquisitions being demagnified and projected onto the focal plane). This results in a direct link between the PSF and the image generated on the CCD. Finally, all figures showing xz -sections of PSFs are logarithmically adjusted for intensity in order to emphasize details in the diffraction pattern.

5.2.2 Simulation parameters and experimental setup

The implementation and simulation of the algorithms were performed using the Matlab programming environment (The Mathworks, Natick, MA). Experimental measurements were carried out on a Zeiss Axioplan 2 microscope system. Both theoretical and experimental results were computed for a $63\times$ magnification, 1.4 NA Zeiss Plan-Apochromat oil-immersion objective. For experimental validation, we prepared samples using fluorescent nanobeads by drying dilutions of TetraSpeck fluorescent microspheres (Molecular Probes, Eugene, OR) onto a slide, and subsequently embedding

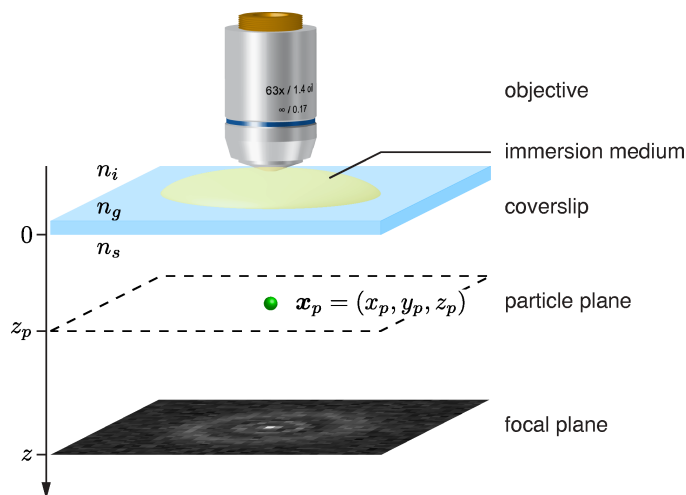


Figure 5.1 Coordinate system and notational conventions used in this chapter.

them under a coverslip using a solid mounting medium of refractive index 1.46. The excitation and emission peaks of these beads are 365 nm and 430 nm, respectively. In conjunction with this, we used a DAPI beamsplitter corresponding to an excitation wavelength of 365 nm and an emission wavelength of 450 nm. The physical pixel width of the AxioCam CCD mounted on the microscope is $6.45 \mu\text{m}$.

In order to verify the estimated position of the particles in our sample during experimental validation, we used a Leica TCS SP2 AOBS confocal microscope, configured to record 50% of the light reflected by the specimen. In this way, the beads along with the coverslip-specimen and specimen-slide interfaces are visible in acquisitions. The microscope has the capability of scanning a single line through the sample, which results in an xz-acquisition. The latter confirmed that all beads were adjacent to the microscope slide. Distance measures on such acquisitions are accurate within 100 nm, which is sufficient to indicate the validity of our experimental results.

5.2.3 Image formation model

We now briefly describe the theoretical PSF model, and put forward an image formation model that incorporates noise.

PSF model

The dominant source of aberrations in modern optical microscopes originates from a mismatch between the refractive index of the specimen and those of the immersion and coverslip layers. Objectives are designed for use with a specific immersion medium and coverslip, but cannot compensate for the wide variety of specimen types occurring in practice. In fact, they only produce aberration-free images for sources that are positioned at the coverslip-specimen layer interface. For sources at an arbitrary depth within the specimen, the optical path of light rays differs from the path for a source located at the aforementioned interface. This optical path difference (OPD) then generates spherical aberrations in the images produced by the system. Most importantly, the amount of aberration depends on the distance between the source and the coverslip, implying that the PSF is non-stationary along the optical axis.

In practice, most biological samples feature refractive indices closer to that of water than that of immersion oil (which is required for high NA objectives). Even for objects that are located only a few micrometers below the coverslip, the aberrations induced by the mismatch of refractive indices become non-negligible. Much effort has gone into establishing suitable theoretical models that account for these aberrations. The most accurate ones use vectorial computations based on either the Huygens-Fresnel principle [114] or the Debye approximation [132]. It was recently shown that these two approaches are equivalent in the case of an infinitely high Fresnel number [133], which is a reasonable assumption in biological microscopy. However, when evaluated at the resolutions provided by the sensor grid of currently available CCDs, these models do not yield significant improvements over scalar formulations of the OPD, especially when considering the computational advantages of the latter. This aspect will be further justified in the discussion section.

Gibson and Lanni [71] proposed a scalar PSF model that is reasonably simple and has the advantage of depending only on the standard parameters of the objective and the optical properties of the specimen, both of which can be determined with adequate accuracy. According to this model (formulated in object space), the response to a point source located in $\mathbf{x}_p = (x_p, y_p, z_p)$ is given by

$$h(\mathbf{x}; \mathbf{x}_p, \boldsymbol{\tau}) = \left| A \int_0^\alpha e^{ik\Lambda(\theta, z; z_p, \boldsymbol{\tau})} J_0(kr n_i \sin \theta) \sin \theta \cos \theta d\theta \right|^2, \quad (5.1)$$

where $\Lambda(\theta, z; z_p, \boldsymbol{\tau})$ is the OPD, k is the wavenumber of the emitted light, α is the angular aperture of the microscope objective, n_i is the refractive index of the immersion medium, and A is a constant complex amplitude. Due

to the hypothesis of spatial invariance in planes orthogonal to the optical axis, the PSF is radially symmetric and expressed as a function of the radius $r = \sqrt{(x - x_p)^2 + (y - y_p)^2}$. The detailed expression for the OPD is derived in Chapter 3. Note that when imaging a source located at the interface between the coverslip and specimen layers, the PSF corresponds to the standard defocus model [134], where $\Lambda(\theta, z; 0, \tau)$ is proportional to $-z$. When, in addition to this, the system is in focus, $W(\Lambda, 0; 0, \tau) = 0$, and $h(\mathbf{x}; \mathbf{x}_p, \tau)$ becomes the familiar Airy function.

Noise model

In fluorescence microscopy, noise from a variety of sources contributes to the recorded images of a specimen, depending on the nature of the specimen and the type of image acquisition setup used. The three main sources of noise occurring in CCD devices are photon noise (also called shot noise), dark noise, and read-out noise. For high-performance cameras the latter two can be considered negligible. Photon noise results from statistical variation in the arrival rate of photons incident on the CCD. As a result of the nature of this variation, the recorded signal at a given pixel on the CCD follows a Poisson distribution. Note that the effect of photon noise is particularly important when the energy of the photon-emitting source is low, implying a lower photon flux. We thus define an image formation model where the photon count at a given pixel on the CCD follows a Poisson distribution whose mean is proportional to the intensity predicted by the PSF model. We characterize the ratio between the expected photon count and the predicted intensity by introducing the conversion factor c , defined as the amount of photons corresponding to a unitary increase in measured intensity. This factor, along with the constant amplitude $|A|^2$, depends on various properties of the experimental setup used, such as the energy of the fluorescent particle, the sensitivity of the CCD sensor (a fixed property of the camera), and the exposure time. Let \bar{q} denote the expected number of photons corresponding to the measured intensity due to a point source located at $(0, 0, z_p)$. Clearly

$$\bar{q}(\mathbf{x}; \mathbf{x}_p, \tau) = c (Ah(\mathbf{x}; \mathbf{x}_p, \tau) + b) \quad (5.2)$$

where the PSF is given by (5.1). The probability of observing q photons emitted by a particle located in $(0, 0, z_p)$ at a point (x, y) in the focal plane positioned at z_n is then given by

$$P_{\bar{q}(\mathbf{k}; \mathbf{x}_p, \tau)}(q) = \frac{e^{-\bar{q}(\mathbf{x}; \mathbf{x}_p, \tau)} \bar{q}(\mathbf{x}; \mathbf{x}_p, \tau)^q}{q!}, \quad (5.3)$$

which constitutes the basis for our image acquisition model. Thus, the probability of observing a given spatial distribution $q(x, y, z_n)$ of photons due to

a particle located in x_p is then given by the joint probability

$$\prod_{n=1}^N \prod_{x,y \in S} P_{q(x; x_p, \tau)}(q(x, y, z_n)), \quad (5.4)$$

where S is the set of points in object space corresponding to pixels in the CCD array, and N corresponds to the number of acquisitions of the particle. In order to simplify the notation, we shall refer to the photon counts q and \bar{q} without explicitly writing their arguments $(x; x_p, \tau)$.

Pixelation

The effects of pixelation of the detector have been extensively covered by Ober et al. [18]. In our notation, it is assumed hereinafter that a point of observation x represents a pixel on the CCD, and thus that, when appropriate, functions of x incorporate integration over the pixel's area (pixels are assumed to be contiguous and non-overlapping).

Model-based particle localization

Localization consists of estimating the particle's position (x_p, y_p, z_p) from the aforementioned distribution of photons. The estimation is done by fitting a theoretical model to the acquisition(s) of a particle. As opposed to conventional approaches where a generic model such as a Gaussian is used, we perform the localization by fitting our image formation model to the acquisitions.

5.2.4 Theoretical Bounds

Having formulated the image formation model for a single fluorescent particle, we now proceed with an investigation of the feasibility of axial localization. The aim is to establish the maximal theoretical precision that axial localization can achieve. To determine this maximal precision, we compute the Cramér-Rao bound, which is the theoretical lower bound on the variance of any unbiased estimator. Based on the image formation model, it yields a lower bound on the precision that can be reached in estimating the particle's axial position z_p . Mathematically, the bound states that

$$\text{Var}(\hat{z}_p) \geq 1 / \left(-E \left\{ \frac{\partial^2}{\partial z_p^2} \ln \prod_{n=1}^N \prod_{x,y \in S} P_{\bar{q}(x; x_p, \tau)}(q(x, y, z_n)) \right\} \right), \quad (5.5)$$

where \hat{z}_p is an unbiased estimator of the particle's position z_p . By substituting (5.3) into this result and simplifying, we obtain

$$\text{Var}(\hat{z}_p) \geq 1 \left/ \sum_{n=1}^N \sum_{x,y \in \mathcal{S}} \bar{q}(\mathbf{x}; \mathbf{x}_p, \boldsymbol{\tau})^{-1} \left(\frac{\partial}{\partial z_p} \bar{q}(\mathbf{x}; \mathbf{x}_p, \boldsymbol{\tau}) \right)^2 \right., \quad (5.6)$$

where the expression for $\frac{\partial \bar{q}}{\partial z_p}$ is given in Appendix A.1. The practical relevance of this fundamental result becomes more readily apparent when applying the bound to particular cases, and studying its relationship with the PSF. A simple example is given in Fig. 5.2, for a source located at the interface between the coverslip and specimen layers. Note the singular behavior of the CRB around the origin, which is related to the depth of field of the microscope. The PSF varies little within the center of that region, and localization becomes less precise. Mathematically speaking, the singularity at the origin is due to the derivative of the PSF, which in this particular case is zero at the in-focus position (since $z_p = 0$).

As indicated by (5.6), the shape of the CRB is solely determined by the PSF model, whereas the scale depends on the amount of noise present in the acquisitions. In fact, the amplitude of the CRB is proportional to $(c|A|^2)^{-1}$. As mentioned above, besides exposure time, the energy of the particle is the determining factor for the signal-to-noise ratio. A low-energy particle emits fewer photons, which results in a higher variability in the photon counting process on the CCD. The recorded image will thus be noisier than for a higher energy particle; consequently the CRB will be proportionally higher (meaning that the precision of any estimator will be lower). In our model, the energy of the particle is implicitly related to the amplitude A . Another parameter that influences the CRB—but to a lesser extent—is the size of the support within which the particle is observed. At high defocus distances, the support needs to be sufficiently large in order to include the outermost rings of the diffraction pattern.

A more complete illustration of the CRB's behavior in relation to the PSF and the particle's depth is given in Fig. 5.3. For very small changes of z_p (not shown, i.e., in our ongoing example, up to approximately 100 nm), the PSF can be assumed to be locally stationary. However, as the change of z_p increases (up to approximately 1 μm), although the shape of the PSF remains essentially the same, a non-negligible axial shift of the PSF with respect to the particle's position occurs. This phenomenon is accentuated for larger changes of z_p , where the “focal shift” increases as a function of the particle's depth. Incidentally, while the CRB also reflects this shift, it depends much more on the complexity of the diffraction pattern. For sources deeper within the specimen, the diffraction patterns become more complex and the CRB gets lower accordingly. Thus, the bound is much higher for sections of the

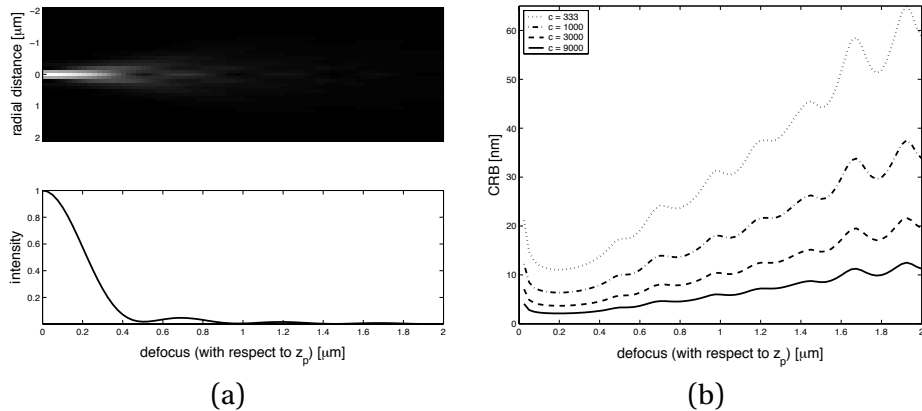


Figure 5.2 (a) xz-section (top) and axial intensity profile (bottom) for a source located at the interface between the coverslip and specimen layer, in which case the PSF is symmetric. (b) Corresponding CRB for different values of the quantization factor c (where c is given in units of $1/|A|^2$). The decrease of the bound is proportional to this factor. At a defocus distance of $0.5 \mu\text{m}$, these values of c correspond to the following SNRs: 7.4, 18.0, 28.4, and 38.8 dB.

PSF that resemble a blurred spot, which is not surprising. For a given configuration (i.e., set of acquisition parameters), the value of the CRB changes as a function of the amount of defocus alone. It is minimal only for a specific interval situated approximately between the in-focus position and the positions where the first diffraction rings appear. From this, it is readily apparent that taking out-of-focus acquisitions will lead to a better precision in the estimation.

Having established the fundamental limits on sub-resolution particle localization we now proceed with the development of an estimator whose precision reaches this lower bound.

5.2.5 A maximum likelihood estimator for axial localization

An optimal maximum-likelihood (ML) estimator for the axial position of a particle is obtained by maximizing the likelihood of our image formation model—in other words of (5.4)—with respect to the particle's position z_p :

$$\frac{\partial}{\partial z_p} \ln \prod_{n=1}^N \prod_{x,y \in S} P_{\bar{q}(x; \mathbf{x}_p, \boldsymbol{\tau})}(q(x, y, z_n)) = \sum_{n=1}^N \sum_{x,y \in S} \frac{\partial \bar{q}}{\partial z_p} \left(\frac{q}{\bar{q}} - 1 \right) = 0. \quad (5.7)$$

The ML estimator for the axial position is then obtained by solving for z_p in the above expression. Since it is not possible to obtain a closed form solution, we deploy a Newton optimization scheme by linearizing the maximum-likelihood around an estimate of the position. Using the Taylor expansion of

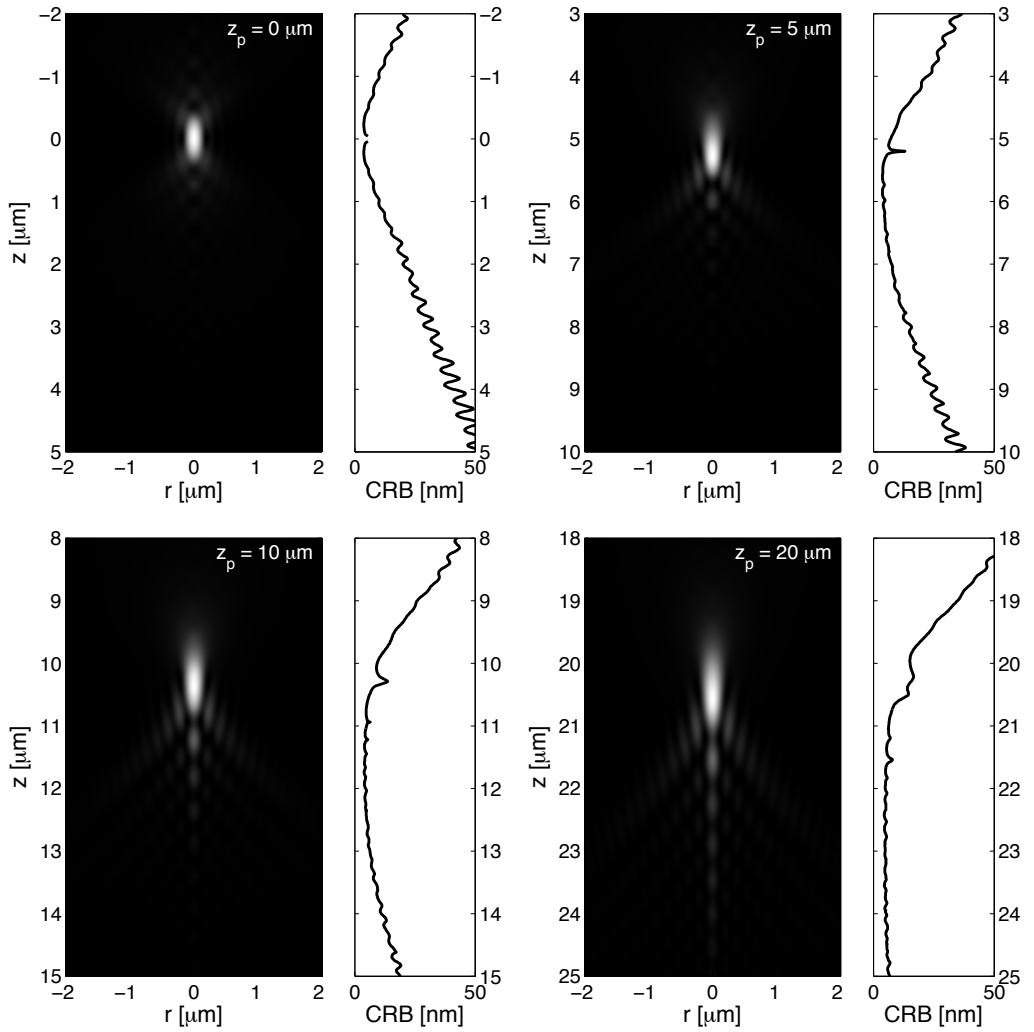


Figure 5.3 CRBs and xz-sections of the theoretical PSF corresponding to point sources located at different depths z_p of the specimen. $c = 3000$ (in units of $1/|A|^2$).

the model, we obtain the following first order approximation of (5.7):

$$\begin{aligned}
 \frac{\partial}{\partial z_p} \ln \prod_{n=1}^N \prod_{x,y \in S} P(q) &\approx \sum_{n=1}^N \sum_{x,y \in S} \frac{\partial \bar{q}}{\partial z_p} \left(\frac{q}{\bar{q}} - 1 \right) \\
 &+ \sum_{n=1}^N \sum_{x,y \in S} \left(\frac{\partial^2 \bar{q}}{\partial z_p^2} \left(\frac{q}{\bar{q}} - 1 \right) - \left(\frac{\partial \bar{q}}{\partial z_p} \right)^2 \frac{q}{\bar{q}^2} \right) (z_p - \hat{z}_p) \equiv 0,
 \end{aligned}
 \tag{5.8}$$

where \hat{z}_p is an initial estimate of the axial position. It is then obvious that the linearization can be performed around the new estimate z_p , which implicitly leads to the following iterative expression:

$$\hat{z}_p^{(m+1)} = \hat{z}_p^{(m)} - \frac{\sum_{n=1}^N \sum_{x,y \in \mathcal{S}} \left(\frac{\partial \bar{q}}{\partial z_p} \left(\frac{q}{\bar{q}} - 1 \right) \right)}{\sum_{n=1}^N \sum_{x,y \in \mathcal{S}} \left(\frac{\partial^2 \bar{q}}{\partial z_p^2} \left(\frac{q}{\bar{q}} - 1 \right) - \left(\frac{\partial \bar{q}}{\partial z_p} \right)^2 \frac{q}{\bar{q}^2} \right)}, \quad (5.9)$$

where m denotes the m th iteration. An adequate initialization for the algorithm is crucial, since the linearization of the likelihood holds only locally. If the initial estimate is too remote from the correct position, convergence of the algorithm is not guaranteed. An efficient way of obtaining an adequate initial estimate $\hat{z}_p^{(0)}$ is to evaluate the normalized cross-correlation between the acquisitions and a number of sections pre-computed from the 3D PSFs corresponding to a range of possible particle positions:

$$\hat{z}_p^{(0)} = \arg \max_{z_p} \frac{\sum_{n=1}^N \sum_{x,y \in \mathcal{S}} (q - \mu_q)(\bar{q} - \mu_{\bar{q}})}{\sqrt{\sum_{n=1}^N \sum_{x,y \in \mathcal{S}} (q - \mu_q)^2 \sum_{n=1}^N \sum_{x,y \in \mathcal{S}} (\bar{q} - \mu_{\bar{q}})^2}}, \quad (5.10)$$

where μ_q and $\mu_{\bar{q}}$ are the mean values of pixels in the acquisitions and model, respectively. An appropriate stopping criterion for the algorithm can be defined based on the absolute value of the update step. If the latter is smaller than the CRB by an order of magnitude, further refining the estimation is statistically meaningless and the algorithm can thus be stopped.

5.2.6 Localization in three dimensions

In practice, localizing a particle along the optical axis is not possible without determining its position in the acquisition plane. To this end, an ML estimator for the xy-position can be obtained by making the same developments as for the axial estimator. Since the aim of this chapter is to demonstrate a new approach for axial localization, we do not state the resulting expressions here. Note, however, that the experimental results presented below were obtained by using an ML estimator for all three dimensions.

5.3 Results

Prior to testing our estimation algorithm on experimental data, we verified its performance in simulation. We generated phantom data by applying

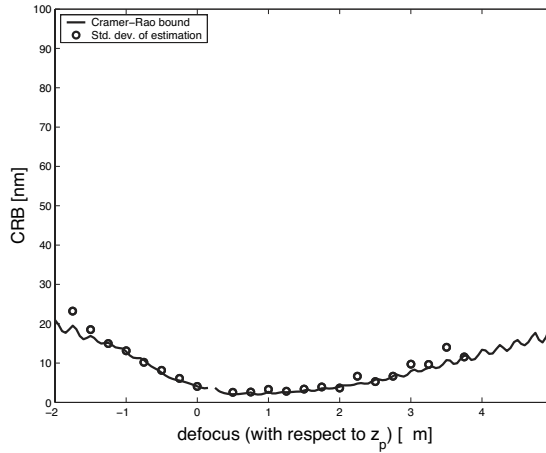


Figure 5.4 Result of the ML estimation from simulated acquisitions. For every point, the estimation was performed 50 times with a single acquisition (using different realizations of the noise). The standard deviation of the estimates matches the CRB well, showing that our ML estimator is optimal. The singularity around $0.25 \mu\text{m}$ is due to the mathematical properties of the first derivative of the PSF, which is close to zero when the focus is near to the particle’s position.

Poisson noise to computed sections of the PSF corresponding to a particle at an arbitrary depth within the specimen. The estimation algorithm was then run with these simulated acquisitions, generated for a particle situated at $z_p = 5 \mu\text{m}$, using an initial estimate that differed by $0.1 \mu\text{m}$ from the actual value. The process was repeated for various focal distances, using different realizations of the Poisson noise. We then compared the standard deviation of these estimations with the CRB. Fig. 5.4 shows this result for one particular set of parameters; from other simulations, we have strong evidence that our algorithm achieves the theoretical precision for any configuration.

In their analysis of lateral localization, Ober et al. [18] discussed the theoretical limits on estimation precision and used a maximum-likelihood estimator based on their approximative two-dimensional image formation model to show that these limits can be reached. Here, we have presented an analytical expression for a maximum-likelihood estimator based on a complete, three-dimensional formulation of the image formation process, and shown that it reaches the theoretical limits in axial localization. Although they have not been specifically shown here, theoretical bounds on lateral localization can be established for our model as well, and the estimator can be shown to reach these bounds.

5.3.1 Calibration and experimental setup

Before presenting the results obtained with our localization method, it is necessary to mention how the constant complex amplitude A (cf. (5.1)) and the photon quantization factor c can be estimated in practice. The former can be easily approximated by fitting the model to the data after an initial estimate for the particle's position has been determined using normalized cross-correlation (which is used precisely because it is independent of A). Using a least-squares fit, a sufficiently precise value of A is obtained. While an approximation of c is not required by the estimation algorithm, it is needed when computing the CRB for experimental data. Assuming that the measures follow a Poisson distribution, the mean is equal to the variance in every point. Since we only have a single realization per point, the mean can be computed using the PSF model (with the estimate of A), and the standard deviation approximated with the difference between the model and measure. We obtain an estimate of c by computing the sum of pointwise ratios of standard deviation over mean.

Because our method relies on a non-stationary PSF, it requires the knowledge of the focal positions z_n in order to estimate z_p . In practice, there are two possibilities to obtain these values. The first is to prepare samples in a way such that the focus can be calibrated to the coverslip-specimen interface. This is possible, for example, by drying reference beads onto the coverslip, in order to mark the interface. Since focusing is done using a piezo actuator, the position of the acquisition plane with respect to the interface is then known. The other approach is to include reference beads that are visible over a large axial range in the specimen. By acquiring z-stacks with known relative displacements, and performing a global fit of the PSF model to these stacks, we can determine the position of the acquisition planes together with the locations of the calibration beads. The precision of this calibration increases with the number of views used in the fit (cf. discussion on CRB). In our case, we used the latter approach with 30 views. The initialization step also gave us very precise estimates of the position of the reference beads, which could then be used as gold standards for our experiments.

Experimental data were obtained by acquiring z-stacks with an axial step of 100 nm of the fluorescent nano-bead preparations described in the materials and methods section. An xz-section of such a stack is shown in Fig. 5.5(a). The corresponding section of the theoretical PSF (Fig. 5.5(b)) shows that the model fits the data well, even for relatively difficult conditions (high NA, depth of the particle). As apparent in the xz-section, but more evidently so in the slices of the z-stack shown in Fig. 5.6, a non-negligible amount of background noise is present in the acquisitions. This needs to be taken into account for the estimation algorithm and thus requires an exten-

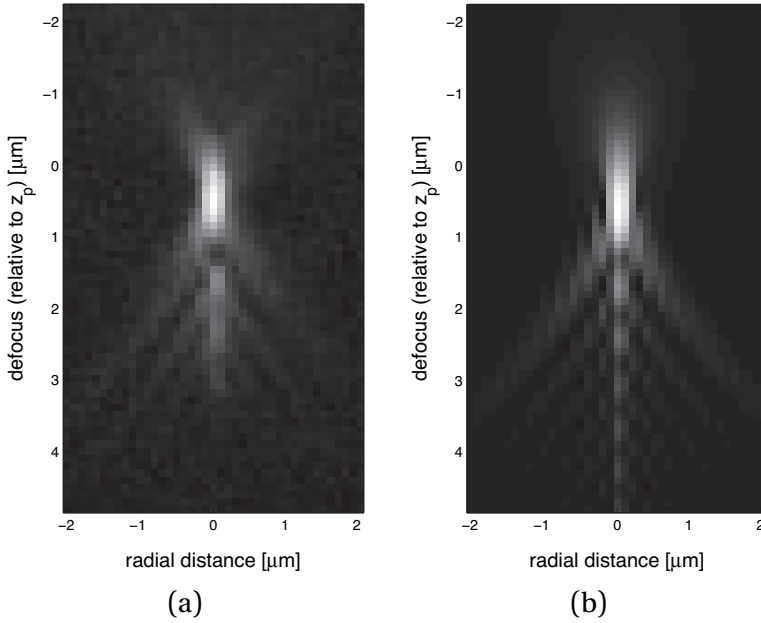


Figure 5.5 (a) xz-section of a z-stack of a bead located at $z_p = 22.1 \mu\text{m}$. (b) xz-section of the PSF model corresponding to the parameters from (a).

sion of our image formation model.

5.3.2 Extension of the statistical noise model

The mean and variance of the background noise can be estimated to reasonable accuracy from sections of acquisitions that are exempt of fluorescent sources. For the sample discussed at the end of this section, the estimated values for the mean and variance are, respectively, $\mu_b = 514.74$ and $\sigma_b^2 = 177.82$. From these measures it is obvious that the background noise does not follow a Poisson distribution, which suggests that the background in our experiment is due to read-out noise (especially since a cooled camera was used). In principle, it is possible to extend our statistical model (5.3) such as to incorporate background noise, which is typically described as white Gaussian in the literature. To facilitate this extension, we investigate the possibility of approximating background noise with Poisson statistics.

A fundamental property of the Poisson distribution is that it rapidly converges towards a Gaussian with equal mean and variance, given that the latter is large enough, which is usually considered the case when $\mu > 10$. Since the variance of the background noise is significantly higher than this value, we make the approximation by splitting the Gaussian distribution into a Poisson distribution and a fixed offset (equal to $\mu_b - \sigma_b^2$), which leaves us

with the convolution between two Poisson distributions. The convolution of two Poisson distributions yields another Poisson distribution, whose mean is equal to the sum of means from the original distributions. We thus obtain the following extension of our image formation model:

$$P(q) = \frac{e^{-(\bar{q} + \sigma_b^2)} (\bar{q} + \sigma_b^2)^q}{q!}. \quad (5.11)$$

Consequently, the expression for the CRB becomes

$$\text{Var}(\hat{z}_p) \geq 1 / \left(\sum_{n=1}^N \sum_{x,y \in \mathcal{S}} \frac{\left(\frac{\partial}{\partial z_p} \bar{q}(\mathbf{x}; \mathbf{x}_p, \boldsymbol{\tau}) \right)^2}{\bar{q}(\mathbf{x}; \mathbf{x}_p, \boldsymbol{\tau}) + \sigma_b^2} \right), \quad (5.12)$$

with the iterative estimator given by:

$$\hat{z}_p^{(m+1)} = \hat{z}_p^{(m)} - \frac{\sum_{n=1}^N \sum_{x,y \in \mathcal{S}} \left(\frac{\partial \bar{q}}{\partial z_p} \left(\frac{q}{\bar{q} + \sigma_b^2} - 1 \right) \right)}{\sum_{n=1}^N \sum_{x,y \in \mathcal{S}} \left(\frac{\partial^2 \bar{q}}{\partial z_p^2} \left(\frac{q}{\bar{q} + \sigma_b^2} - 1 \right) - \left(\frac{\partial \bar{q}}{\partial z_p} \right)^2 \frac{q}{(\bar{q} + \sigma_b^2)^2} \right)}. \quad (5.13)$$

To illustrate the appropriateness of this model, we compare in Fig. 5.6 a few slices of a measured z-stack with the simulated acquisitions obtained using the extended model. When rings are present in the diffraction model, there is an intensity peak at the center of the pattern. If the source is aligned with the xy-grid, this peak is recorded by a single pixel on the CCD. If, however, the source is slightly shifted, the peak's intensity is distributed across four pixels, like it appears in these examples. Localization in three dimensions was used to determine the particle's position in the measured z-stack. This estimated position was then used to generate the phantom data.

5.3.3 Validation with real data

In our acquisitions of the nano-bead sample described in the materials and methods section, several dozen beads were visible. Among these, we chose five beads whose diffraction patterns were well separated, such that estimation errors due to overlap from the patterns of different beads were not possible.

For our setup, the CRB shown in Fig. 5.3 indicates that localization is much more precise when positioning the focus below the bead, such that diffraction rings appear in the acquisition. The xz-section of the bead confirms this; it is indeed much harder to differentiate two acquisitions that depict a blurred spot of light than two acquisitions that present clearly disparate

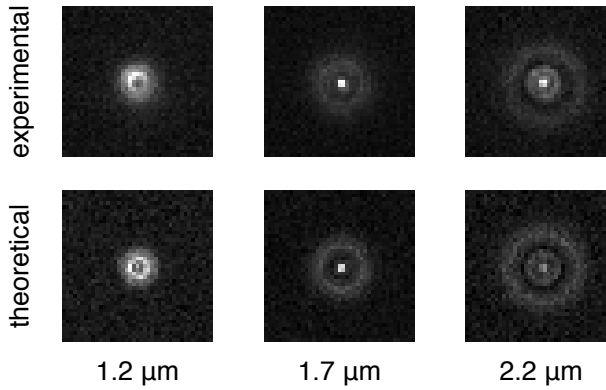


Figure 5.6 Comparison of acquisitions of a bead located at $z_p = 22.1 \mu\text{m}$ with their counterparts generated from the theoretical model. The distances indicate the amount by which the acquisitions are defocused.

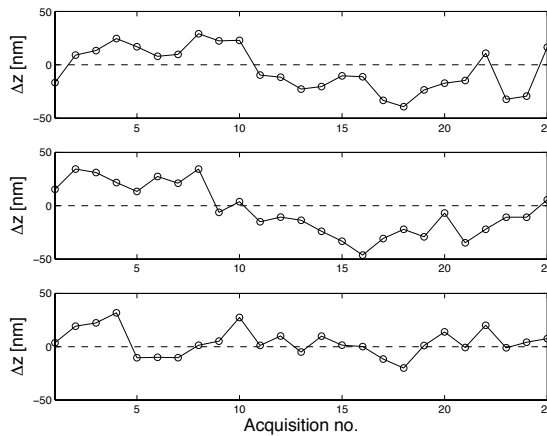


Figure 5.7 Localization results for three different beads. The values plotted are the deviation $\Delta z = \hat{z}_p - z_{\text{ref}}$, where z_{ref} is the reference position estimated using all acquisitions. The respective reference values are, from top to bottom: $22.050 \mu\text{m}$, $22.073 \mu\text{m}$, and $22.081 \mu\text{m}$, with the corresponding averages of the estimations: $22.046 \mu\text{m}$, $22.069 \mu\text{m}$, and $22.085 \mu\text{m}$.

diffraction patterns. In order to illustrate the performance of our estimator, we thus apply it to acquisitions that feature diffraction rings. Initial values for the particle's position were obtained using normalized cross-correlation with a series of slices of the PSF model computed with the same axial spacing (100 nm) as the experimental acquisitions.

To demonstrate the localization for acquisitions taken at various defocus distances, the estimation was performed using pairs of acquisitions spaced by 200 nm, for all such pairs within the acquired z-stacks. Independently of

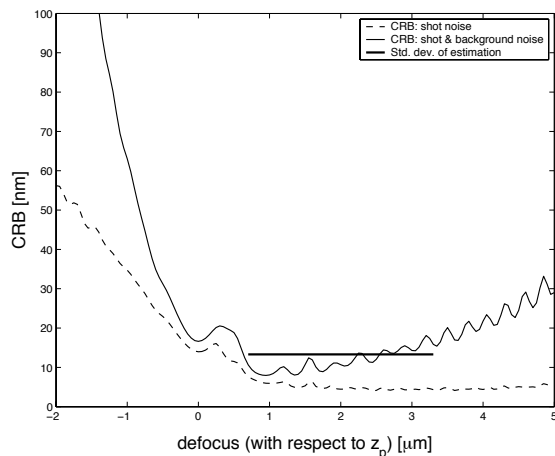


Figure 5.8 Standard deviation of the localization results with respect to the CRB, displayed over the range in which the estimations were performed.

the amount of defocus, the algorithm converges rapidly, requiring 5 iterations on average. Fig. 5.7 demonstrates the result of the estimation for three beads over a range of $2.5 \mu\text{m}$. In the best case, localization precision (i.e., standard deviation of the estimation with respect to the reference) of 12.8 nm is achieved. The worst result obtained with the selected beads was a precision of 23.8 nm . The averages of the estimated positions for the three beads shown in Fig. 5.7 are $22.046 \mu\text{m}$, $22.069 \mu\text{m}$, and $22.085 \mu\text{m}$, respectively. These values are also in perfect agreement with the reference positions of the beads ($22.050 \mu\text{m}$, $22.073 \mu\text{m}$, and $22.081 \mu\text{m}$, respectively), which are obtained using a global fit where all measurements are included. To further confirm our results, we compared our estimates with those obtained using the Leica TCS SP2 AOBS confocal microscope. This acquisition showed that the beads were located approximately between $22.0 \mu\text{m}$ and $22.1 \mu\text{m}$ within the specimen, which is strong evidence for the soundness of our estimations. In Fig. 5.8 we show the CRB for the shot noise-only image formation model, the CRB for the extended image formation model and the average value of the precision estimation achieved with the beads.

5.3.4 Optimal acquisition settings

Beyond its theoretical applications, the CRB can also be used to determine optimal acquisition settings that may serve as guidelines to experimentalists. As the evaluation of the CRB showed, it is advantageous to take acquisitions slightly defocused with respect to the particle's actual position. In practice, however, particles can be situated anywhere within the specimen, and it is

therefore not possible to adequately position the focus with respect to an individual particle. Still, the study of particles is usually confined to a predetermined section of the specimen. In such cases, under the hypothesis that the particle's axial position follows a uniform distribution within the section, optimal focal positions leading to the lowest average CRB can be determined. This optimization is non-trivial, but can be performed by solving the following cost function:

$$\arg \min_{z_1, \dots, z_N} \int_a^b \left(1 / \sum_{n=1}^N \sum_{x,y \in \mathcal{S}} \frac{1}{\bar{q}} \left(\frac{\partial \bar{q}}{\partial z_p} \right)^2 \right) dz_p, \quad (5.14)$$

where a and b are the bounds of the region of interest. In Fig. 5.9, we show the results of this optimization for a variety of settings. It is immediately clear that the optimal settings are non-trivial. The estimation precision is significantly higher when acquisitions are taken with an optimal focus, especially for particles that are deeper within the specimen. At the same time, these results also show the effect on the CRB of increasing the number of acquisitions. Notice how the CRB decreases as the number of acquisitions is augmented. This is expected, since increasing the amount of “information” on the particle should implicitly lead to a better estimation precision. This property is especially useful in highly noisy acquisition conditions.

5.4 Discussion

By investigating the fundamental theoretical limits of axial localization from defocused acquisitions of sub-resolution fluorescent particles, we have shown that nanometer precision can be achieved. The maximum-likelihood estimator proposed in this chapter reaches the theoretical limit provided that the image formation model is accurate, which we have experimentally shown to be the case. The use of a non-stationary PSF model makes the localization applicable to any configuration of microscope objectives and specimen preparation; it is especially powerful for localizing particles at any depth within the specimen. Usually, the non-stationary nature of the PSF along the optical axis requires approximative models that suppose stationarity to hold for small layers of the specimen (see, e.g., [83]). Here, we developed an approach based directly on the analytical expression of the PSF, thus guaranteeing convergence within the precision of the theoretical limits.

In our experimental tests we have shown that an axial localization precision below 15 nm can be reached. These results confirm the practical applicability of the proposed approach, and demonstrate sub-resolution localization. They also confirm the findings of Speidel et al. [42], who were the first

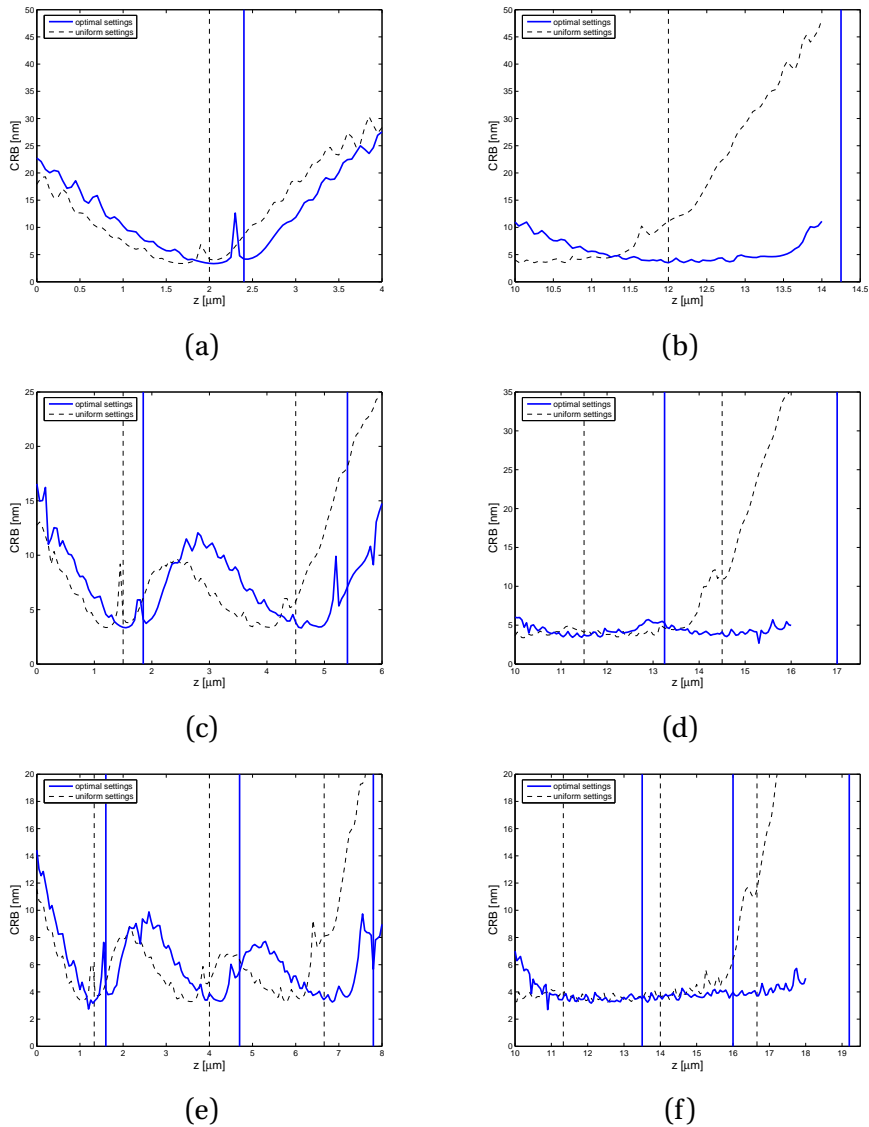


Figure 5.9 Optimal focal positions for a variety of acquisition settings. For a single acquisition, (a) and (b) clearly show the influence of the particle's depth on the optimal position; this is notably due to the focal shift that occurs as a particle moves deeper into the specimen (here a $4\ \mu\text{m}$ thick section is considered). The optimal position is indicated by the vertical bars. (c), (d) Optimal focal positions when two acquisitions are used for two different sections of the sample. (e), (f) Scenario with three acquisitions. The optimal acquisition settings are considerably different from the uniform ones, and their effect on the CRB is substantial.

to show that nanometer-precision axial localization from defocused acquisitions is possible in widefield fluorescence microscopy. While most localization and tracking approaches that claim such a precision along the optical axis are limited to one or two particles (see, e.g., [135]), the method proposed here can be applied to any number of particles detected within a z-stack. For such a multiple-particle scenario, our model could be extended to account for overlap between the diffraction patterns of particles.

An efficient method to model the combined effect of various sources of noise was introduced, rendering the estimation possible for a wide range of configurations. In particular, incorporating additional sources does not increase the complexity of the model.

An important observation is that the localization algorithm performs significantly better for acquisitions that are taken by placing the focus on the side of the particle where the diffraction pattern is more detailed (in cases where $n_s < n_i$, such as in our example, this corresponds to $z_n > z_p$). The lesser performance of the estimation on the other side is consistent with the higher value of the CRB (see Fig. 5.3); we also suspect that it may be partly due to slight discordances between the PSF model and the experimental observations (see Fig. 5.5 in the range of -2 to $0 \mu\text{m}$).

5.4.1 Influence of the PSF model

We briefly justify our choice of a scalar PSF model for the proposed localization method. Our experiments with the vectorial model proposed by Török et al. [132] and Hell et al. [114, 133] indicate that the differences with respect to the results obtained using the scalar model are not significant in the context of our work. Studies of the CRB for the vectorial formulation show that in some cases, it is slightly lower than its scalar equivalent (see Fig. 5.10). However, this is only apparent for strongly out-of-focus acquisitions where the signal intensity is weak and generally undetectable, mainly due to background noise. Also, this effect is most noticeable for less aberrated cases; as one penetrates deeper into the specimen, the CRBs for the two models become virtually equivalent.

Moreover, the scalar model has a clear computational advantage. A vectorial model requires three integrals instead of one for the scalar case, not to mention the fact that the integrands are much more involved. Since the localization algorithm also requires the second derivative of the PSF, the difference in computational cost is considerable.

We note that our methodology is generic enough to accommodate for other theoretical models as further progress is made in this field (see, e.g., [113, 136]).

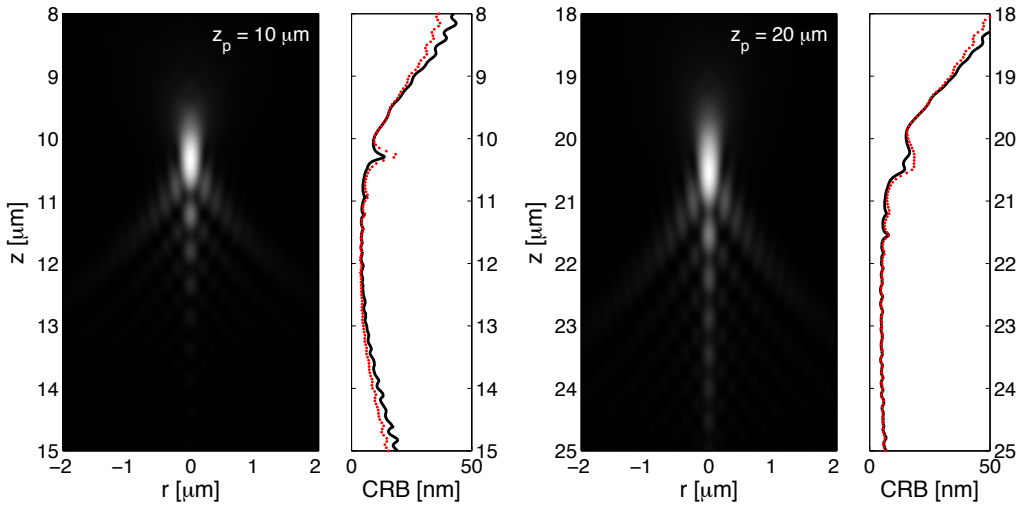


Figure 5.10 Comparison of the Cramér-Rao bounds for the scalar and vectorial formulations of the PSF. The xz -sections of the PSF and the dotted line in the CRB plots were obtained using the vectorial model. As the source moves deeper into the specimen, the difference between the two models becomes increasingly negligible.

5.4.2 Shortcomings and possible extensions of the method

In practice, when a thick section of specimen is considered, a z -stack with sufficient axial resolution (i.e., low spacing between acquisitions) is required to guarantee that all particles present in the specimen are recorded. As a consequence, each particle is visible in multiple slices, which can then be used in the localization. The analytical expression for the CRB can be used to derive the optimal acquisition positions with respect to a particular experiment, in order to maximize the performance of the localization.

A parameter not explicitly taken into account is the temporal resolution of the acquisitions; its determining factor is the movement of the particle during the acquisition of the z -stack. For fast-moving particles, it is still possible to perform the localization, however, by limiting the number of acquisitions. The volume (i.e., depth) of observation is then reduced, and as a consequence localization becomes less precise. Another element that can hinder the efficiency of localization is the diffusion of light occurring within the specimen. Although our approach permits the localization of particles at any depth, it is in this respect limited by a factor that affects any localization method.

The first-order approximation made in the development of the ML estimator holds only locally, meaning that the estimator is very sensitive to

the initial estimate. Precision in the latter can be increased, if necessary, by computing the normalized cross-correlation with a finer sampling step (see (5.10)). Another possible improvement in this direction might be obtained by using a higher order (e.g. quadratic) approximation of the likelihood function.

These limitations aside, the methodology presented in this chapter is promising, showing that with a standard widefield fluorescence microscope, particles can be localized with nanometer-scale precision. Our experimental results confirm that the localization precision is comparable to that of specialized hardware such as the setup proposed by Kao et al. [38].

Chapter 6

Super-resolved maximum-likelihood localization of fluorescent nanoparticles in three dimensions

6.1 Introduction

In this chapter, we extend our previous analysis on axial localization to a complete framework for the localization of fluorophores in 3-D. In particular, we focus on the influence of the shift-variant PSF on the localization bounds and propose a maximum-likelihood estimator that reaches these bounds.

6.2 Theoretical bounds

We begin with an analysis of the localization accuracy attainable with an estimator based on the scalar image formation model described in Chapter 3. A limit on the 3-D localization accuracy is obtained by means of the Cramér-Rao bound (CRB), similarly to the limit derived for axial localization. As mentioned in Chapter 4, this bound is given by the diagonal of the inverse of the Fisher information matrix in the case of multiple parameters. Under the assumption that the PSF is radially symmetric, the Fisher information

This chapter is based on: F. Aguet et al., “Sub-resolution maximum-likelihood based localization of fluorescent nanoparticles in three dimensions,” in *Proc. 4th IEEE Int. Symp. Biomedical Imaging*, 2007, pp. 932–935, [137].

matrix is diagonal and the CRBs for the coordinates of the particle's position \mathbf{x}_p are given by

$$\text{Var}(\hat{x}_p) \geq 1 \left/ -\mathbb{E} \left\{ \frac{\partial^2}{\partial x_p^2} \ln \prod_{\mathbf{x} \in \mathcal{S}} P_{\bar{q}(\mathbf{x}; \mathbf{x}_p, \boldsymbol{\tau})}(q(\mathbf{x})) \right\} \right., \quad (6.1)$$

where \mathcal{S} is the set of pixels in the acquisition, and where \hat{x}_p is an unbiased estimator of the particle's x -coordinate, with homologous expressions for the bounds on y and z . Evaluating the bounds for our image formation model yields

$$\text{Var}(\hat{x}_p) \geq 1 \left/ \sum_{\mathbf{x} \in \mathcal{S}} \frac{\left(\frac{\partial}{\partial x_p} \bar{q}(\mathbf{x}; \mathbf{x}_p, \boldsymbol{\tau}) \right)^2}{\bar{q}(\mathbf{x}; \mathbf{x}_p, \boldsymbol{\tau})} \right., \quad (6.2)$$

again with homologous expressions for $\text{Var}(\hat{y}_p)$ and $\text{Var}(\hat{z}_p)$. The partial derivatives of the PSF with respect to the position coordinates are given in Appendix A.1.

6.3 Maximum-likelihood estimator

We now introduce an estimator for a particle's position that is optimal in the sense that it reaches the theoretical bounds stated above. The probability of observing a given spatial distribution $q(\mathbf{x}; \mathbf{x}_p, \boldsymbol{\tau})$ of photons emitted by a source located at \mathbf{x}_p is given by

$$\prod_{\mathbf{x} \in \mathcal{S}} P(q(\mathbf{x}; \mathbf{x}_p, \boldsymbol{\tau})). \quad (6.3)$$

By maximizing the likelihood of (6.3) with respect to x_p , we obtain the basis for our estimator:

$$\frac{\partial}{\partial x_p} \ln \prod_{\mathbf{x} \in \mathcal{S}} P(q) = \sum_{\mathbf{x} \in \mathcal{S}} \frac{\partial \bar{q}}{\partial x_p} \left(\frac{q}{\bar{q}} - 1 \right) = 0. \quad (6.4)$$

Since there is no closed-form solution for x_p in the above expression, we take the first-order Taylor approximation of the maximum-likelihood function around an estimate \hat{x}_p of x_p , which gives us the following iterative expression:

$$\hat{x}_p^{(m+1)} = \hat{x}_p^{(m)} - \frac{\sum_{\mathbf{x} \in \mathcal{S}} \left(\frac{\partial \bar{q}}{\partial x_p} \left(\frac{q}{\bar{q}} - 1 \right) \right)}{\sum_{\mathbf{x} \in \mathcal{S}} \left(\frac{\partial^2 \bar{q}}{\partial x_p^2} \left(\frac{q}{\bar{q}} - 1 \right) - \left(\frac{\partial \bar{q}}{\partial x_p} \right)^2 \frac{q}{(\bar{q})^2} \right)}, \quad (6.5)$$

where m denotes the iteration. The second partial derivative of the PSF with respect to x_p is given in Appendix A.1.

The proposed linearization holds only locally and thus requires an adequate initialization. This can be obtained by evaluating the normalized cross-correlation between the acquisition and a precomputed set of 3-D PSFs corresponding to the range of possible particle positions:

$$\hat{x}_p = \arg \max_{x_p \in \mathcal{S}} \frac{\sum_{x \in \mathcal{S}} (q - \mu_q)(\bar{q} - \mu_{\bar{q}})}{\sqrt{\sum_{x \in \mathcal{S}} (q - \mu_q)^2 \sum_{x \in \mathcal{S}} (\bar{q} - \mu_{\bar{q}})^2}}, \quad (6.6)$$

where μ_q and $\mu_{\bar{q}}$ are the mean pixel values in acquisitions and model, respectively. The estimation can be stopped when the absolute value of the update step becomes smaller than the CRB by an order of magnitude, after which further refining the estimate becomes irrelevant.

6.4 Results

We now provide some examples of our estimator and its performance relative to the CRB for some specific situations: first in simulation and then on experimental data. The acquisition parameters are the same for all examples provided, and are taken from the experiments, which were carried out on a Zeiss AxioPlan 2 microscope equipped with an AxioCam CCD with $6.45 \times 6.45 \mu\text{m}^2$ pixels. The objective used is a Zeiss Plan-Apochromat 1.4 NA oil-immersion objective. The test sample consisted of 100 nm-diameter beads fluorescing at 430 nm, deposited onto a microscope slide and embedded in a solid mounting medium of refractive index 1.46. The immersion oil has a refractive index of 1.515.

6.4.1 Properties of the CRB

Analyzing the behavior of the CRBs for specific experimental parameters gives some important insights into the imaging conditions required to maximize the localization accuracy.

The axial accuracy significantly improves when performed on out-of-focus acquisitions of particles that are located deeper within the specimen (see Fig. 6.1 for the photon-limited case without any background signal, and Fig. 6.2 for a more realistic scenario with a 10% background level). In comparison, the localization accuracy in the acquisition plane evolves similarly, but is optimal where the intensity of the PSF is maximal, in which case the

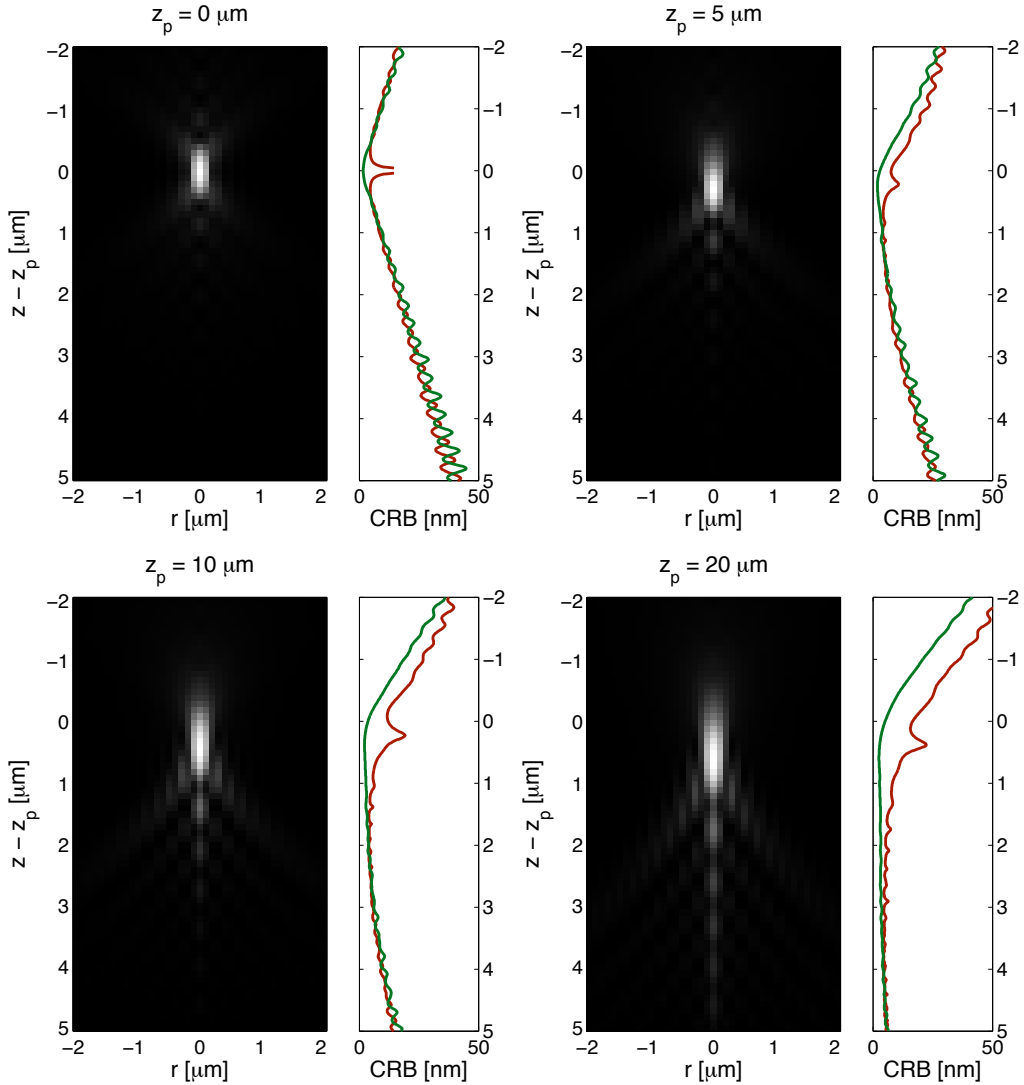


Figure 6.1 xz-sections of the PSF shown together with the CRBs for z_p (red line) and x_p (green line) for different axial positions z_p of the particle (with x_p centered on a pixel). The CRBs are shown as a function of defocus, for shot noise with $c = 5$, $A = 100$, and $b = 0$.

axial localization is usually poor. As the different plots show, the loss in accuracy for xy-localization under imaging conditions that are optimal for axial localization is small, and thus offers an easy compromise.

As Ober et al. have investigated, the xy-localization accuracy also varies as a function of the particle's position with respect to the CCD grid [18]. For

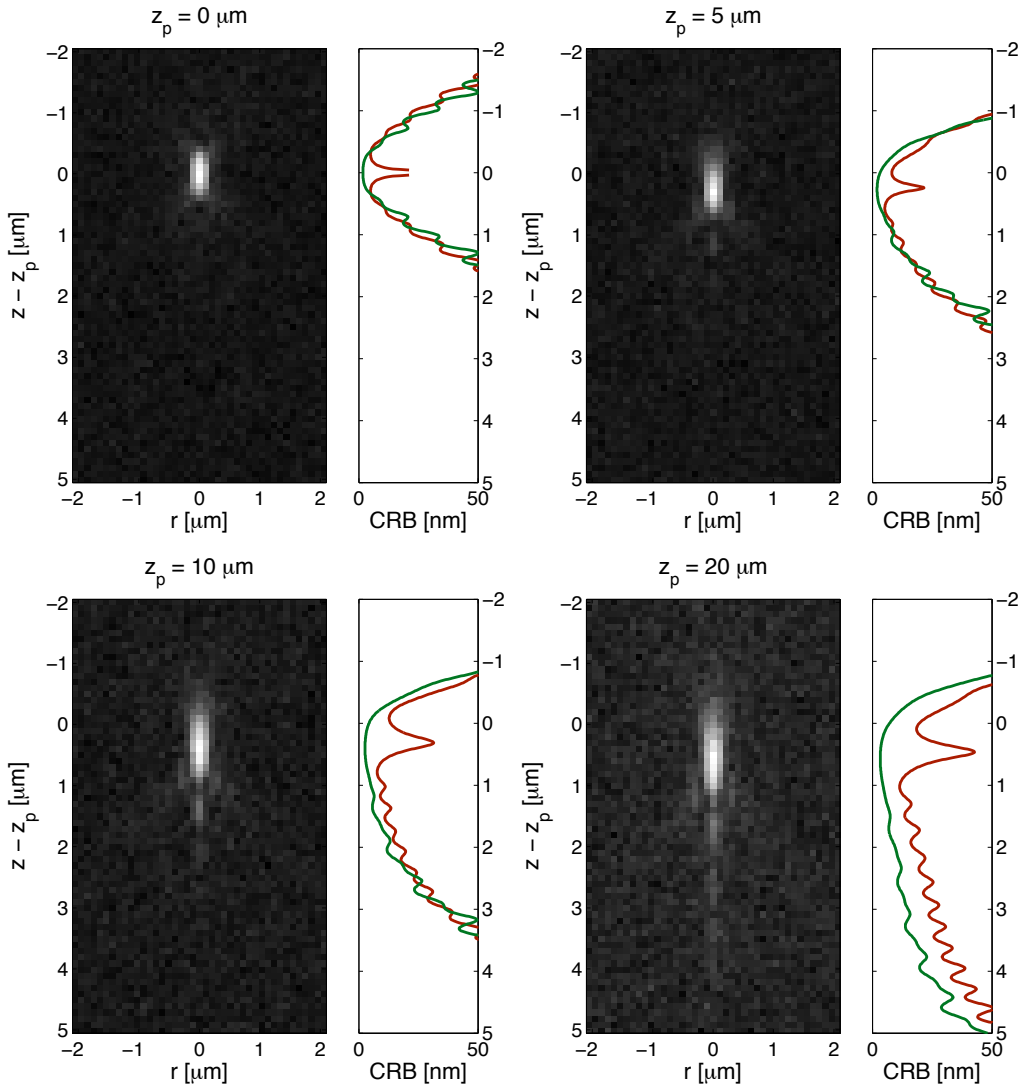


Figure 6.2 xz-sections of the PSF shown together with the CRBs for z_p (red line) and x_p (green line) for different axial positions z_p of the particle (with x_p centered on a pixel). The CRBs are shown as a function of defocus, for shot noise with $c = 10$, $A = 90$, and $b = 10$.

3-D localization experiments, our results show that the amount of defocus and the position of the particle within the specimen can be at least as important in determining the localization accuracy. Nevertheless, they can be optimized to some degree — especially when multiple particles are involved — using prior knowledge of the particles' distribution within the specimen

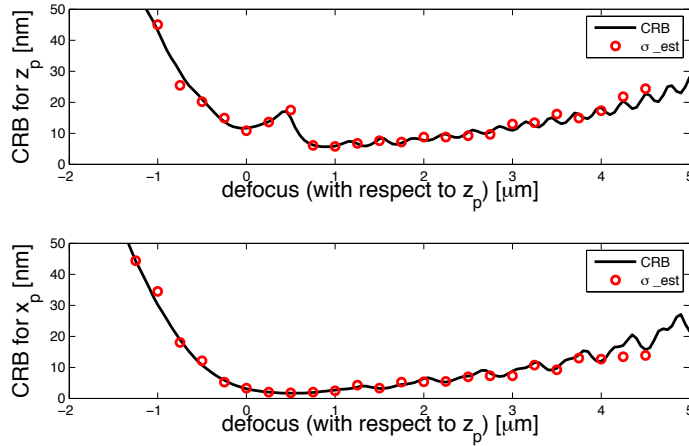


Figure 6.3 Estimation results and CRBs for z_p and x_p as a function of defocus ($z - z_p$), for a particle located at $x_p = (0.035, 0.0, 5.0) \mu m$. The estimator reaches the theoretical limit; for each focal position (z), the estimation was performed on 50 different realizations of noise with $c = 20$, $A = 450$, and $\sigma_b^2 = 3$, yielding a 18.3 dB average SNR.

(see previous chapter).

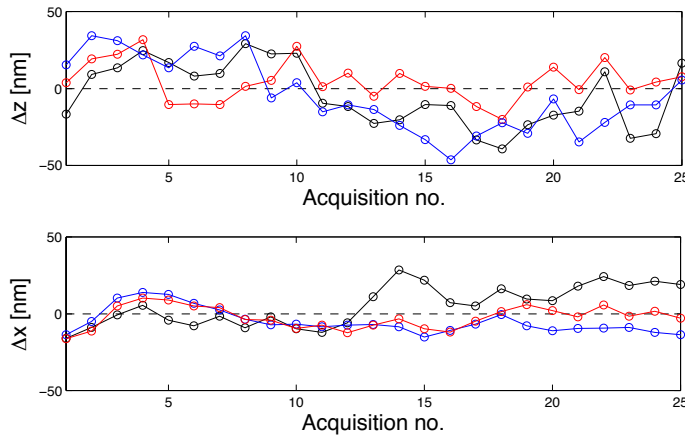


Figure 6.4 Experimental localization results for three beads. The plots show the deviations $\Delta z = \hat{z}_p - z_{\text{ref}}$ and $\Delta x = \hat{x}_p - x_{\text{ref}}$, respectively, where z_{ref} and x_{ref} are the reference positions estimated using all acquisitions.

6.4.2 Estimation results

In Fig. 6.3 we compare the standard deviation of the localization results using our estimator with the CRBs for x_p and z_p . As the plots indicate, the es-

timator is optimal in the sense that it reaches the CRB. Its performance on experimental data is shown in Fig. 6.4. A stack with a z -step of 100 nm was acquired over the entire visible range of each fluorescent microsphere. To derive a ground truth for each particle's position, we performed a global fit of the unknown parameters using all available acquisitions, which also provided us with the acquisition positions z required by the estimator, due to its reliance on a shift-variant PSF. The details of this calibration are discussed in the previous chapter. In the best cases, localization accuracies of 12.8 nm axially and 7.15 nm in the acquisition plane were achieved.

A important — and to a degree surprising — aspect of these results comes from the comparison of the lateral and axial localization accuracies, where, contrary to the differences expected in terms of resolution, the theoretical limits are very close. In the photon-limited case, the magnitude of the limits is identical in the axial range of the PSF where diffraction rings are clearly visible. In the presence of a background signal or read-out noise, the bound for axial localization increases slightly over the bound for lateral localization. These results demonstrate the potential of 3-D FLM techniques based on an accurate PSF model. Specifically, they show that 3-D localization based on off-focus imaging can achieve accuracies that surpass those obtained with Gaussian-based FLM techniques (see Chapter 1).

Chapter 7

Super-resolution orientation estimation and localization of fluorescent dipoles using 3-D steerable filters

7.1 Introduction

Fluorescence localization microscopy (FLM) has emerged as a powerful family of techniques for optically imaging biological samples at molecular resolutions, down to the nanometer scale [138]. This is achieved by employing specific fluorescent labels that can be activated [19], switched on [20], or that intrinsically blink [24], which make it possible to image sparse subsets of the fluorophores contained within the specimen in sequence. Fluorophores appear as spatially isolated spots in the resulting image frames; their center can then be computationally localized with an accuracy that far surpasses the resolution limit formulated by Abbe. A super-resolved image of the specimen is generated by imaging a large number of such fluorophore subsets, localizing every molecule within each frame, and combining the resulting positions to render a composite image at a finer scale. The resolution achieved by these techniques is thus directly dependent upon the achievable localization accuracy. This accuracy in turn depends on the number of photons collected [17] and on the image formation model used in the localization algorithm.

The primary implementations of FLM proposed to date include photoac-

This chapter is based on: F. Aguet et al., "Super-resolution orientation estimation and localization of fluorescent dipoles using 3-D steerable filters," *Opt. Express*, vol. 17, pp. 6829–6848, 2009, [45].

tivated localization microscopy (PALM) [21], fluorescence photoactivation localization microscopy (FPALM) [22], and stochastic optical reconstruction microscopy (STORM) [23]. Developed contemporaneously, these methods demonstrated resolutions at the 10 nm scale experimentally. Due to the long acquisition times required for the collection of a sufficient amount of frames, these methods were initially designed to image 2-D sections of thin, fixed specimens. For such samples, it is generally assumed that the image of a single molecule corresponds to the in-focus section of the system's 3-D point spread function (PSF), which can be approximated by a 2-D Gaussian function. Under the latter assumption, it has been shown that Gaussian-based fitting algorithms do not result in a significant loss in localization accuracy [13].

Prior to the introduction and practical feasibility (due to a lack of suitable fluorophores) of FLM, localization-based approaches were generally limited to single molecule tracking applications, with inherent isolation of individual fluorophores. In a study of the progression of the molecular motor Myosin V on actin fibers, Yildiz et al. achieved a Gaussian localization-based resolution of 1.5 nm, and accordingly named their technique fluorescence imaging with one-nanometer accuracy (FIONA) [16]. In the framework of single particle tracking, theoretical limits on the achievable localization accuracy have been formulated for lateral (i.e. x - y) localization [18] and axial localization [44]; these limits translate into a measure of resolution when extended to incorporate multiple sources.

In all of the previously cited methods, it is assumed that individual fluorophores act as isotropically emitting point sources (which also implies that their image corresponds to a section of the system's PSF). Whereas this is valid for molecules that freely rotate during image acquisition, it does not hold when imaging fixed fluorophores. Their corresponding diffraction patterns differ significantly from the PSF, and are highly specific of the orientation of the fluorophore's underlying electromagnetic dipole [139, 140].

7.1.1 Localization of fluorescent dipoles

Dipole diffraction patterns are generally not radially symmetric, and as a consequence, their point of maximum intensity in the image plane is shifted with respect to the position of the fluorophore. Applying Gaussian-based localization to such patterns can lead to a bias in the range of 5-20 nm, even for dipoles that are imaged in focus [43]. This is especially significant in the context of FLM, where resolutions of the same order are striven for. Due to the complexity of the dipole patterns, avoiding this bias requires localization methods based on a more accurate image formation model than a simple Gaussian.

Moreover, localization based on a physically realistic model makes it possible to estimate the dipole's orientation in addition to its position. So far, this has been exploited in an extension of the FIONA technique named dipole orientation and position imaging (DOPI) [141]. In the study of Myosin V, the estimation of the fluorescent labels' orientation made it possible to characterize its progression on actin much more precisely than with FIONA. A shortcoming of the current implementation of DOPI is its reliance on two separate procedures for orientation and position estimation.

The current state of the art in dipole orientation and position estimation is based on matched filtering of defocused images. Using an advanced image formation model for dipoles [142], Patra et al. proposed to estimate the orientation based on a finite number of precomputed templates corresponding to rotated versions of a dipole diffraction pattern for a given amount of defocus [143]. The accuracy of this approach is inherently limited by the angular sampling stemming from the finite number of templates, which is usually restricted due to computational cost. As a further consequence, the matched filtering approach limits position estimates to pixel-level accuracy. In DOPI, super-resolved position information is recovered by taking two images of every fluorophore: a defocused image for orientation estimation, and an in-focus image for position estimation, which uses the Gaussian-based localization method proposed in FIONA.

Other methods for estimating the orientation of fluorescent dipoles have been proposed in the literature. Often relying on specific instrumentation, most of these methods are incompatible with a joint position and orientation approach over a reasonably large field of view. Notable techniques are based on direct imaging of the emission pattern in the back focal plane of the objective lens (see, e.g., [144–146]), and on annular illumination [147].

7.1.2 New approach based on 3-D steerable filters

In this work, we introduce an efficient method for the joint estimation of position and orientation for fluorescent dipoles from a single (defocused) image. We show that image formation for dipoles can be expressed as a linear combination of six templates weighted by trigonometric functions of the dipole angles. As a consequence, the estimation problem can be formulated as the optimization of a 3-D steerable filter [148]. The resulting algorithm serves both as an initial detection of dipoles with localization accuracy at the pixel level, and as an efficient means for iteratively updating the orientation estimates when performing the subsequent sub-pixel localization to achieve super-resolution. We formulate the theoretical limits on estimation accuracy for position and orientation using Cramér-Rao bounds (CRB), and show that our method reaches these bounds. Notably, these limits make it possible to

establish the acquisition settings (e.g., defocus) that will lead to the highest estimation accuracy. Our experimental results indicate that dipoles can be localized with a position accuracy of at least 5 nm and an orientation accuracy of at least 2 degrees, at a peak signal-to-noise ratio (PSNR) of approximately 25 dB.

7.1.3 Organization of the paper

In the next section, we introduce an image formation model for fluorescent dipoles and show how it decomposes into six non-orthogonal templates. Subsequently, in Section 7.3, we use this steerable decomposition to formulate a localization algorithm for the estimation of both the position and orientation of fluorescent dipoles. In Section 7.4, we establish the theoretical limits on the accuracy of these estimators, using Fisher information. Finally, in Section 7.5, we demonstrate our method on simulated and experimental data. We conclude with a discussion of potential applications and extensions of the proposed technique.

7.2 Image formation

A single fluorescent molecule can be characterized as a harmonically oscillating dipole with moment $\mathbf{p} = (\sin \theta_p \cos \phi_p, \sin \theta_p \sin \phi_p, \cos \theta_p)$ and position $\mathbf{x}_p = (x_p, y_p, z_p)$, where the angles θ_p and ϕ_p are the zenith (i.e., between the dipole and the optical axis) and azimuth angle of the dipole, respectively. In our notation, the subscript p indicates a dipole parameter. The intensity radiated by such a dipole is modeled by propagating the emitted electric field through the optical system. We begin by expressing the amplitude of the electric field in object space as

$$\mathcal{E}_s = \langle \mathbf{p}, \mathbf{e}_p^s \rangle \mathbf{e}_p^s + \langle \mathbf{p}, \mathbf{e}_s \rangle \mathbf{e}_s, \quad (7.1)$$

where the vectors \mathbf{e}_p^s and \mathbf{e}_s are the p - and s -polarized components of \mathcal{E}_s in the sample layer [149], as illustrated in Fig. 7.1 (the superscript s on the \mathbf{e}_p vector denotes the sample medium; \mathbf{e}_s remains constant throughout the system). A constant factor representing the magnitude (see, e.g., [149, 150]) has been neglected in this expression and will be reintroduced later. We assume a standard model for the object space, consisting of a sample layer (refractive index n_s), a glass layer (corresponding to the coverslip, index n_g), and an immersion layer (index n_i) [71]. After propagating through these layers and the objective, the field is given by

$$\mathcal{E}_a = \langle \mathbf{p}, \mathbf{e}_p^s \rangle t_p^{(1)} t_p^{(2)} \mathbf{e}_p^a + \langle \mathbf{p}, \mathbf{e}_s \rangle t_s^{(1)} t_s^{(2)} \mathbf{e}_s, \quad (7.2)$$

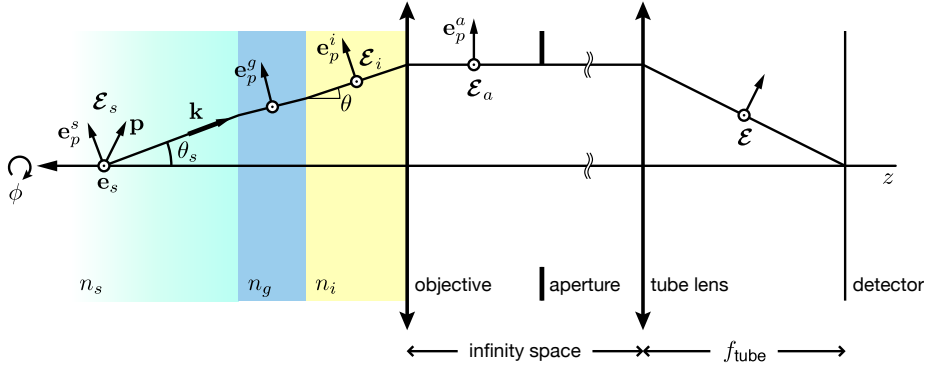


Figure 7.1 Electric field propagation in a microscope. The illustrated path is in direction of the azimuth angle ϕ .

where $t_p^{(l)}$ and $t_s^{(l)}$ are the Fresnel transmission coefficients for p -polarized and s -polarized light from layer l to layer $l + 1$, i.e.,

$$\begin{aligned} t_p^{(l)} &= \frac{2n_l \cos \theta_l}{n_{l+1} \cos \theta_l + n_l \cos \theta_{l+1}} \\ t_s^{(l)} &= \frac{2n_l \cos \theta_l}{n_l \cos \theta_l + n_{l+1} \cos \theta_{l+1}}, \end{aligned} \quad (7.3)$$

where $(n_1, n_2, n_3) = (n_s, n_g, n_i)$ for the configuration considered here. Note that Eq. (7.2) can easily be generalized to an arbitrary number of strata. The unit vectors of the relevant polarization directions, expressed in spherical coordinates, are

$$\begin{aligned} \mathbf{e}_p^s &= (\cos \theta_s \cos \phi, \cos \theta_s \sin \phi, -\sin \theta_s) \\ &= \left(\frac{1}{n_s} \sqrt{n_s^2 - n_i^2 \sin^2 \theta} \cos \phi, \frac{1}{n_s} \sqrt{n_s^2 - n_i^2 \sin^2 \theta} \sin \phi, -\frac{n_i}{n_s} \sin \theta \right) \\ \mathbf{e}_p^a &= (\cos \phi, \sin \phi, 0) \\ \mathbf{e}_s &= (-\sin \phi, \cos \phi, 0), \end{aligned} \quad (7.4)$$

where θ_s is the zenith angle between the wavevector \mathbf{k} and the optical axis in the sample layer, θ is the corresponding angle in the immersion layer, and ϕ is the azimuth angle (see Fig. 7.1). The wavevector is thus parameterized as

$$\mathbf{k} = -kn_i(\cos \phi \sin \theta, \sin \phi \sin \theta, \cos \theta), \quad (7.5)$$

where $k = \frac{2\pi}{\lambda}$ is the wavenumber. The field in the detector plane, expressed

in object space coordinates, is given by the Richards-Wolf integral [110, 111]:

$$\begin{aligned}\mathcal{E} &= \frac{-iA_0}{\lambda} \int_0^{2\pi} \int_0^\alpha \mathcal{E}_a e^{i\langle \mathbf{k}, \mathbf{x} \rangle} e^{ik\Lambda(\theta; \boldsymbol{\tau})} \sqrt{\cos \theta} \sin \theta \, d\theta \, d\phi \\ &= \frac{-iA_0}{\lambda} \int_0^{2\pi} \int_0^\alpha \mathcal{E}_a e^{ikr n_i \sin \theta \cos(\phi - \phi_d)} e^{-ikn_i z \cos \theta} e^{ik\Lambda(\theta; \boldsymbol{\tau})} \sqrt{\cos \theta} \sin \theta \, d\theta \, d\phi,\end{aligned}\tag{7.6}$$

where A_0 is the scalar amplitude of the field, λ its wavelength, and α is the maximal angular aperture of the objective (i.e., $\alpha = \sin^{-1}(\text{NA}/n_i)$). The phase component $\Lambda(\theta; \boldsymbol{\tau})$ describes the system's aberrations. Its argument

$$\boldsymbol{\tau} = (n_i, n_i^*, n_g, n_g^*, n_s, t_i^*, t_g, t_g^*)\tag{7.7}$$

is a vector containing the optical parameters of the setup; the subscripts on the refractive indices n and thicknesses t indicate the respective layer for each parameter (see Fig. 7.1), and an asterisk signals a design value (i.e., n_i is the refractive index of the immersion medium under experimental conditions, and n_i^* its corresponding design value). The field \mathcal{E} is a function of the point of observation $\mathbf{x} = (-r \cos \phi_d, -r \sin \phi_d, z)$ on the detector, where $r = \sqrt{(x - x_p)^2 + (y - y_p)^2}$ and $\phi_d = \tan^{-1}((y - y_p)/(x - x_p))$; z denotes defocus. All units are expressed in object space coordinates, which allows us to place the origin of the coordinate system at the interface between the sample layer and the coverslip in order to facilitate the expression of the phase term $\Lambda(\theta; \boldsymbol{\tau})$.

We describe the system's aberrations based on the optical path difference (OPD) between actual (experimental) imaging conditions and the corresponding design values of the system, as proposed in [71]. Aberrations are assumed to arise exclusively as the result of a mismatch between the refractive indices and/or the thicknesses of the different layers in the sample setup. State-of-the-art vectorial PSF calculations all incorporate this phase term (see, e.g., [113, 114]), and although the formalism employed differs from [71], these approaches lead to the same result for the phase and are considered equivalent [109, 133]. We thus replace the aberration term $\Lambda(\theta; \boldsymbol{\tau})$ with the OPD $\Lambda(\theta, z; z_p, \boldsymbol{\tau})$, defined as

$$\begin{aligned}\Lambda(\theta, z; z_p, \boldsymbol{\tau}) &= \left(z_p - z + n_i \left(-\frac{z_p}{n_s} - \frac{t_g}{n_g} + \frac{t_g^*}{n_g^*} + \frac{t_i^*}{n_i^*} \right) \right) n_i \cos \theta \\ &\quad + z_p \sqrt{n_s^2 - n_i^2 \sin^2 \theta} + t_g \sqrt{n_g^2 - n_i^2 \sin^2 \theta} \\ &\quad - t_g^* \sqrt{n_{g^*}^2 - n_i^2 \sin^2 \theta} - t_i^* \sqrt{n_{i^*}^2 - n_i^2 \sin^2 \theta}.\end{aligned}\tag{7.8}$$

Note that $\Lambda(\theta, z; 0, \boldsymbol{\tau})$ is the phase term corresponding to the standard defocus model [115].

By substituting Eq. (7.2) into Eq. (7.6) and simplifying the result, we can rewrite the vector \mathcal{E} as

$$\mathcal{E} = -i \begin{bmatrix} I_0 + I_2 \cos(2\phi_d) & I_2 \sin(2\phi_d) & -2iI_1 \cos(\phi_d) \\ I_2 \sin(2\phi_d) & I_0 - I_2 \cos(2\phi_d) & -2iI_1 \sin(\phi_d) \end{bmatrix} \mathbf{p}, \quad (7.9)$$

where

$$\begin{aligned} I_0(\mathbf{x}; \mathbf{x}_p, \tau) &= \int_0^\alpha B_0(\theta) \left(t_s^{(1)} t_s^{(2)} + t_p^{(1)} t_p^{(2)} \frac{1}{n_s} \sqrt{n_s^2 - n_i^2 \sin^2 \theta} \right) d\theta \\ I_1(\mathbf{x}; \mathbf{x}_p, \tau) &= \int_0^\alpha B_1(\theta) t_p^{(1)} t_p^{(2)} \frac{n_i}{n_s} \sin \theta d\theta \\ I_2(\mathbf{x}; \mathbf{x}_p, \tau) &= \int_0^\alpha B_2(\theta) \left(t_s^{(1)} t_s^{(2)} - t_p^{(1)} t_p^{(2)} \frac{1}{n_s} \sqrt{n_s^2 - n_i^2 \sin^2 \theta} \right) d\theta \end{aligned} \quad (7.10)$$

with

$$B_m(\theta) = \sqrt{\cos \theta} \sin \theta J_m(kr n_i \sin \theta) e^{ik\Lambda(\theta, z; z_p, \tau)}. \quad (7.11)$$

It should be noted that these integrals are standard for vectorial PSF calculations (for equivalent expressions see, e.g. [113, 133]). The amplitude factor A_0 was dropped from this formulation and will again be reintroduced later. Due to an already involved notation, we choose to omit the argument $(\mathbf{x}; \mathbf{x}_p, \tau)$ from functions such as $|I_0|^2$ from this point on.

The orientation-dependent intensity in the detector plane is accordingly given by

$$\begin{aligned} h_{\theta_p, \phi_p}(\mathbf{x}; \mathbf{x}_p, \tau) &= |\mathcal{E}|^2 \\ &= \sin^2 \theta_p \left(|I_0|^2 + |I_2|^2 + 2 \cos(2\phi_p - 2\phi_d) \Re\{I_0^* I_2\} \right) \\ &\quad - 2 \sin(2\theta_p) \cos(\phi_p - \phi_d) \Im\{I_1^* (I_0 + I_2)\} + 4 |I_1|^2 \cos^2 \theta_p \\ &= \mathbf{p}^\top \mathbf{M} \mathbf{p}. \end{aligned} \quad (7.12)$$

An asterisk denotes complex conjugation, and \mathbf{v}^\top stands for the Hermitian transpose of the vector \mathbf{v} ; $\Re\{v\}$ and $\Im\{v\}$ represent the real and imaginary components of v , respectively. The symmetric matrix $\mathbf{M} = (m_{ij})_{1 \leq i, j \leq 3}$ is specified by

$$\begin{aligned} m_{11} &= |I_0|^2 + |I_2|^2 + 2 \Re\{I_0^* I_2\} \cos 2\phi_d \\ m_{12} &= 2 \Re\{I_0^* I_2\} \sin 2\phi_d \\ m_{13} &= -2 \cos \phi_d \Im\{I_1^* (I_0 + I_2)\} \\ m_{22} &= |I_0|^2 + |I_2|^2 - 2 \Re\{I_0^* I_2\} \cos 2\phi_d \\ m_{23} &= -2 \sin \phi_d \Im\{I_1^* (I_0 + I_2)\} \\ m_{33} &= 4 |I_1|^2. \end{aligned} \quad (7.13)$$

The quadratic form in Eq. (7.12) is of particular interest, since it decouples the dipole orientation from the calculation of the field propagation. The dipole diffraction pattern can thus be modeled as the linear combination of six non-orthogonal templates, which forms the basis of the steerable filter-based algorithm presented in this work.

The result of Eq. (7.12) is consistent with the other vectorial PSF models cited earlier [109, 111, 113, 114, 133]: for a fluorophore that is freely rotating during exposure, the resulting intensity is obtained by integrating the above result over all possible orientations, i.e.,

$$\begin{aligned} h(\mathbf{x}; \mathbf{x}_p, \boldsymbol{\tau}) &= \int_0^{2\pi} \int_0^\pi h_{\theta_p, \phi_p}(\mathbf{x}; \mathbf{x}_p, \boldsymbol{\tau}) \sin \theta_p \, d\theta_p \, d\phi_p \\ &= \frac{8\pi}{3} \left(|I_0|^2 + 2|I_1|^2 + |I_2|^2 \right). \end{aligned} \quad (7.14)$$

Illustrations of the different diffraction patterns observed for different orientation and defocus values are provided in Fig. C.1 and Fig. C.2 in Appendix C.

7.2.1 Noise model

In single molecule fluorescence microscopy, shot noise is the dominant source of noise. Further potential sources include a background term due to autofluorescence, as well as residual signals from other fluorophores in the sample. Read-out noise in the detector may also contribute to observations. Whereas the former sources obey Poisson statistics, read-out noise is Gaussian distributed, which presumes an additive noise model. However, given that the Poisson distribution rapidly converges towards a Gaussian with equal mean and variance when the variance is large enough (this is usually considered the case when $\sigma^2 > 10$), we propose a general noise model consisting of a shifted Poisson formulation that incorporates a term accounting for the read-out noise factor and the background. Consequently, we formulate the expected photon count $\bar{q}(\mathbf{x}; \mathbf{x}_p, \boldsymbol{\tau})$ corresponding to a point \mathbf{x} on the detector (in object-space coordinates) as

$$\bar{q}(\mathbf{x}; \mathbf{x}_p, \boldsymbol{\tau}) = c \cdot (A h_{\theta_p, \phi_p}(\mathbf{x}; \mathbf{x}_p, \boldsymbol{\tau}) + b), \quad (7.15)$$

where A is the amplitude, c is a conversion factor, and b is the sum of the background fluorescence signal and the variance σ_r^2 (in intensity) of the read-out noise. The probability of detecting q photons at \mathbf{x} is then given by

$$P_{q(\mathbf{x}; \mathbf{x}_p, \boldsymbol{\tau})}(q) = \frac{e^{-\bar{q}(\mathbf{x}; \mathbf{x}_p, \boldsymbol{\tau})} \bar{q}(\mathbf{x}; \mathbf{x}_p, \boldsymbol{\tau})^q}{q!}. \quad (7.16)$$

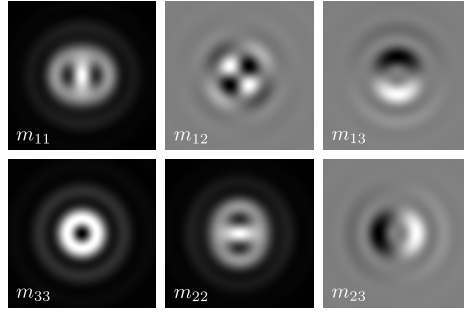


Figure 7.2 High-resolution versions of the templates involved in the steerable decomposition of a dipole diffraction pattern. The example corresponds to a Cy5 dipole ($\lambda = 660$ nm) at an air/glass interface, imaged with a $100\times$, 1.45 NA oil immersion objective at 500 nm defocus. The template labels match the definitions given in Eq. (7.13).

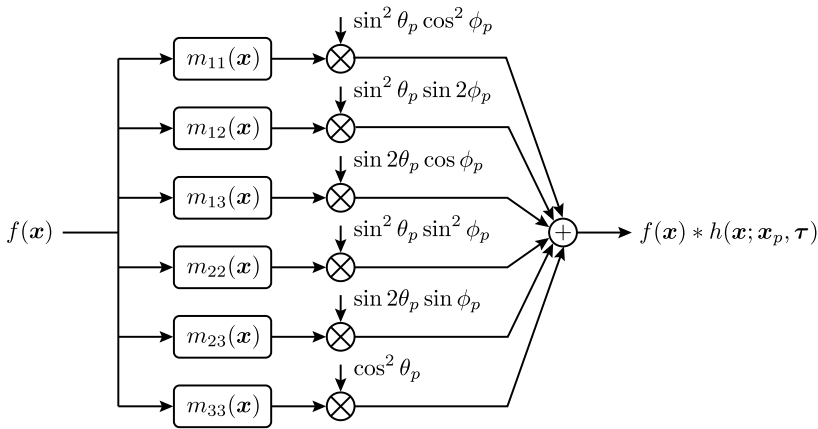


Figure 7.3 Filterbank implementation of the steerable dipole filters.

7.2.2 Pixelation

The pixelation of the detector has a non-negligible effect on the measured intensity distribution corresponding to a dipole, and must therefore be taken into account in the implementation of the model. Hereinafter, we assume that whenever a point of observation \mathbf{x} represents a pixel on the CCD, functions of \mathbf{x} incorporate integration over the pixel's area (pixels are assumed to be contiguous and non-overlapping).

7.3 Dipole localization using steerable filters

A standard solution to estimating the position and orientation of arbitrarily rotated image features consists in correlating the input data with a set of

filters corresponding to rotated versions of the feature template. This is the approach currently used in joint dipole orientation and position estimation methods [141, 143]. Mathematically, it is formulated as

$$(\theta_p^*(\mathbf{x}), \phi_p^*(\mathbf{x})) = \arg \max_{(\theta_p, \phi_p)} f(\mathbf{x}) * g_{\theta_p, \phi_p}(\mathbf{x}), \quad (7.17)$$

where $\theta_p^*(\mathbf{x})$ and $\phi_p^*(\mathbf{x})$ are the optimal orientations in every point \mathbf{x} , $f(\mathbf{x})$ is the measured data, $*$ is the convolution operator, and $g_{\theta_p, \phi_p}(\mathbf{x}) = h_{\theta_p, \phi_p}(\mathbf{x}; (0, 0, z_p), \boldsymbol{\tau})$ is a feature template corresponding to the dipole diffraction pattern for the orientation (θ_p, ϕ_p) . The accuracy on $\theta_p^*(\mathbf{x})$ and $\phi_p^*(\mathbf{x})$ depends on the sampling of θ_p and ϕ_p chosen for the optimization—for accuracies of a few degrees, this requires convolution with hundreds of templates, rendering the process very costly.

For specific feature template functions, rotation of the templates can be decoupled from the convolution by decomposing the template into a small number of basis templates that are interpolated by functions of the orientation. These functions, called steerable filters, were introduced by Freeman and Adelson [148]. The best known class of steerable filters are Gaussian derivatives, due to their applicability to edge and ridge detection in image processing [77].

The quadratic form of Eq. (7.12) shows that the 3-D rotation of a dipole can be decoupled from filtering; i.e., that the orientation and position estimation can be expressed through a 3-D steerable filter. Specifically, the dipole diffraction pattern is decomposed into six non-orthogonal templates, as illustrated in Fig. 7.2. Orientation estimation then amounts to filtering measured dipole patterns with these templates, followed by optimizing the trigonometric weighting functions that interpolate the dipole model. This process is illustrated in the filterbank representation of Fig. 7.3.

For each spatial location \mathbf{x} , the dipole model is fitted to the data by minimizing the least-squares criterion

$$\begin{aligned} J_{\text{LS}}(\mathbf{x}; \theta_p, \phi_p) &= \int_{\Omega} (Ah_{\theta_p, \phi_p}(\mathbf{v}; \mathbf{x}_p, \boldsymbol{\tau}) - f(\mathbf{x} - \mathbf{v}))^2 d\mathbf{v} \\ &= \|Ah_{\theta_p, \phi_p}(\mathbf{x}; \mathbf{x}_p, \boldsymbol{\tau})\|^2 + \int_{\Omega} f(\mathbf{x} - \mathbf{v})^2 d\mathbf{v} \\ &\quad - 2Ah_{\theta_p, \phi_p}(\mathbf{x}; \mathbf{x}_p, \boldsymbol{\tau}) * f(\mathbf{x}), \end{aligned} \quad (7.18)$$

where $f(\mathbf{x})$ is the observed signal from which the average background value has been subtracted, and where $\Omega \subset \mathbb{R}^2$ is the support of h_{θ_p, ϕ_p} . The correlation term is steerable and can be expressed as

$$\begin{aligned} (h_{\theta_p, \phi_p} * f)(\mathbf{x}) &= \sum_{ij} a_{ij}(\theta_p, \phi_p) (m_{ij} * f)(\mathbf{x}) \\ &= \mathbf{p}^T \mathbf{M}_f \mathbf{p}, \end{aligned} \quad (7.19)$$

where $a_{ij}(\theta_p, \phi_p)$ are the weighting functions given in Fig. 7.3, and where $[\mathbf{M}_f]_{ij} = m_{ij} * f$. Concretely, this means that we can compute Eq. (7.19) for each location \mathbf{x} very efficiently by first convolving the image f with the six templates m_{ij} —which yields \mathbf{M}_f —followed by applying the trigonometric weights $a_{ij}(\theta_p, \phi_p)$, which amounts to computing the quadratic form $\mathbf{p}^\top \mathbf{M}_f \mathbf{p}$. Due to the symmetry of \mathbf{M} , only six basis templates are involved in the process.

In order to simplify the expression for the optimization of Eq. (7.18), we rewrite the model energy term, which is independent of ϕ_p , as

$$\|Ah_{\theta_p, \phi_p}(\mathbf{x}; \mathbf{x}_p, \boldsymbol{\tau})\|^2 = A^2 \mathbf{u}_{\theta_p}^\top \mathbf{E} \mathbf{u}_{\theta_p}, \quad (7.20)$$

where $\mathbf{u}_{\theta_p} = (\sin^2 \theta_p, \sin 2\theta_p, \cos^2 \theta_p)^\top$, and where \mathbf{E} is defined as

$$\mathbf{E} = \begin{bmatrix} \langle m_{11}^2 \rangle & \langle m_{11}m_{13} \rangle & \langle m_{11}m_{33} \rangle \\ \langle m_{11}m_{13} \rangle & \langle m_{13}^2 \rangle & \langle m_{13}m_{33} \rangle \\ \langle m_{11}m_{33} \rangle & \langle m_{13}m_{33} \rangle & \langle m_{33}^2 \rangle \end{bmatrix}. \quad (7.21)$$

The notation $\langle m_{ij} \rangle$ stands for integration over the support Ω of $m_{ij}(\mathbf{x})$. We can then rewrite the cost criterion as

$$J(\mathbf{x}; \theta_p, \phi_p) = A^2 \mathbf{u}_{\theta_p}^\top \mathbf{E} \mathbf{u}_{\theta_p} - 2A \mathbf{p}^\top \mathbf{M}_f \mathbf{p}. \quad (7.22)$$

The data term $\int_{\Omega} f(\mathbf{x} - \mathbf{v})^2 d\mathbf{v}$ in Eq. (7.18) has no effect on the optimization and was eliminated from the criterion.

7.3.1 Orientation estimation

The criterion in Eq. (7.22) cannot be solved in closed form for θ_p , ϕ_p , and A . However, for a given set of templates corresponding to a position estimate, an iterative algorithm is obtained by setting the partial derivatives

$$\begin{aligned} \frac{\partial}{\partial \theta_p} J(\mathbf{x}; \theta_p, \phi_p) &= 2A \left(A \mathbf{u}_{\theta_p}^\top \mathbf{E} \frac{\partial}{\partial \theta_p} \mathbf{u}_{\theta_p} - 2 \mathbf{p}^\top \mathbf{M}_f \frac{\partial}{\partial \theta_p} \mathbf{p} \right) \\ \frac{\partial}{\partial \phi_p} J(\mathbf{x}; \theta_p, \phi_p) &= -4A \mathbf{p}^\top \mathbf{M}_f \frac{\partial}{\partial \phi_p} \mathbf{p} \end{aligned} \quad (7.23)$$

to zero, and alternately solving for θ_p and ϕ_p ; we found this to be more efficient than a standard gradient-descent based approach. The quartic equations whose solution yields the optimal values for both angles are given in Appendix C. The notation $\frac{\partial}{\partial t} \mathbf{v}$ stands for the component-wise derivative of the vector \mathbf{v} with respect to t . Between these iterations, the amplitude is updated using the least-squares estimator

$$\hat{A} = \frac{\mathbf{p}^\top \mathbf{M}_f \mathbf{p}}{\mathbf{u}_{\theta_p}^\top \mathbf{E} \mathbf{u}_{\theta_p}}. \quad (7.24)$$

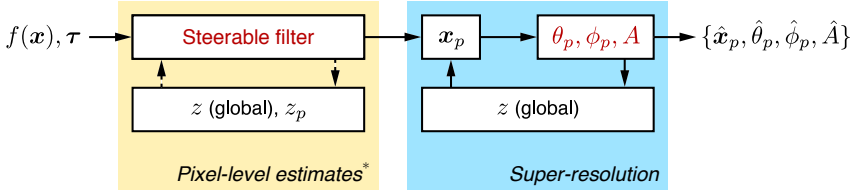


Figure 7.4 Schematic outline of the proposed detection algorithm. The steerable filter-based component yields results that are accurate at the pixel level (*finer scale results can be obtained by applying shifted versions of the feature templates). Every update of the position estimates generates a new set of appropriately shifted templates, from which the orientation is estimated at little cost by making use of the steerable decomposition.

For fixed values of x_p and z , the angles can be estimated to sufficient accuracy in a small number of iterations (usually less than five).

7.3.2 Sub-pixel position estimation

Discretization of Eq. (7.22) yields a filter-based algorithm that returns position estimates with pixel-level accuracy. In order to recover super-resolved position estimates, an iterative fitting algorithm analogous to the Gaussian-based fitting algorithms employed by FLM can be applied to the dipole model in Eq. (7.12). In this work, this was achieved with the Levenberg-Marquardt algorithm. An alternative would be to use a maximum-likelihood-based cost criterion, which is optimal with respect to the Poisson-based noise model [44]. However, the localization accuracy achieved using the proposed least-squares criterion is near-optimal in the sense that it reaches the theoretical limits (see Section 7.4).

7.3.3 Joint estimation algorithm

In addition to the lateral position (x_p, y_p) , amplitude A , and orientation (θ_p, ϕ_p) of dipoles, which can be estimated using the proposed steerable filter in the minimization of Eq. (7.22), the axial position z_p of the dipole and the position of the focus z are further degrees of freedom in the model. Estimation of these two parameters can be challenging due to their mutual influence in the phase term of Eq. (7.8); possible solutions for resolving this ambiguity were discussed in [44], in the framework of 3-D localization of isotropic point sources.

However, for the distances z_p from the coverslip that are observable under TIRF (total internal reflection fluorescence) excitation, which is currently the method of choice for FLM due to its thin depth excitation (around 100 nm), the axial shift variance in the PSF is essentially negligible. This means that a dipole with axial position z_p that is observed at the focal distance z is

virtually undistinguishable from an identical dipole at the origin that is observed at $z - z_p$. Consequently, we set $z_p = 0$ for our experiments.

For a given value of defocus z , the minimization of Eq. (7.22) is achieved in two steps. The input image is first filtered with the six templates corresponding to z , which yields orientation and position estimates that are accurate at the pixel level. This is followed by an iterative optimization that refines the position estimates to sub-pixel accuracy. At each iteration, a new set of templates corresponding to the sub-pixel position estimates is evaluated; the corresponding orientation is computed with the method described in Section 7.3.1. If required, the estimation of z can be included between steps of this iterative procedure, both at the pixel level and the super-resolution level. A simplified flowchart representation of the algorithm is given in Fig. 7.4.

7.4 Dipole localization accuracy

Resolution in FLM is defined as a function of localization accuracy. Theoretical limits on localization accuracy can be established based on the Cramér-Rao bounds for the parameters of interest (see [18, 127] for an analysis of lateral localization accuracy, and [44] for axial localization accuracy). The CRB yields a lower bound on the variance of an estimator, provided that the latter is unbiased. For multi-parameter estimation, this bound is obtained by computing the inverse of the Fisher information matrix [128]. For our image formation model, this matrix is defined through

$$\mathbf{F}_{ij} = \int_{\Omega} \frac{1}{\bar{q}} \frac{\partial \bar{q}}{\partial \vartheta_i} \frac{\partial \bar{q}}{\partial \vartheta_j} d\mathbf{x} \quad (7.25)$$

where the parameters to be estimated are $\vartheta = (x_p, y_p, \theta_p, \phi_p, z, A)$. In the matrix \mathbf{F} , the cross-terms between ϕ_p and the other parameters are zero, which slightly simplifies the inversion. The CRBs for $\vartheta = (x_p, y_p, \theta_p, z, A)$ are thus given by

$$\text{Var}(\hat{\vartheta}_i) \geq [\mathbf{F}^{-1}]_{ii}, \quad (7.26)$$

and the bound for ϕ_p by

$$\text{Var}(\hat{\phi}_p) \geq 1 \left/ \int_{\Omega} \frac{1}{\bar{q}} \left(\frac{\partial \bar{q}}{\partial \phi_p} \right)^2 d\mathbf{x} \right. \quad (7.27)$$

The partial derivatives of Eq. (7.12) relevant to the computation of the CRBs are given in Appendix C.

An example of the CRBs for all parameters is shown in Fig. 7.5, as a function of z and θ_p . As the different plots illustrate, the bounds are relatively flat

for a large range of values. In-focus imaging leads to lower accuracy for orientation and defocus estimation. Off-focus imaging, on the other hand, preserves excellent localization accuracy in the plane, while leading to higher accuracies for orientation and defocus estimation. Note that these observations hold true for the general case; changing the system and acquisition parameters essentially amounts to a scaling of the bounds.

7.4.1 Performance of the algorithm

The localization accuracy of the proposed algorithm was evaluated by performing the fit on simulated acquisitions generated using the image formation model in Eq. (7.15). In Fig. 7.6, we show standard deviations of the estimation results for each parameter compared to the associated CRB. The standard deviations consistently match the value of the CRB, which indicates that the performance of the algorithm is near-optimal. A fully optimal solution for the proposed Poisson-based noise model would consist in a maximum-likelihood formulation. However, this would lead to a computationally less efficient solution compared to the filter-based approach obtained through the proposed least-squares formulation.

7.5 Results

7.5.1 Experimental setup

To demonstrate the performance of our algorithm experimentally, we imaged single Cy5 dipoles at an air/glass interface. Samples were prepared by drying a solution of Cy5 molecules bound to single-stranded DNA (ssDNA) fragments onto a coverslip (isolated Cy5 binds to the glass surface at a specific orientation, leading to limited diversity in the observed diffraction patterns). These were then imaged using TIRF excitation at a wavelength of $\lambda = 635$ nm. Imaging was performed on the microscope setup described in [151] (α Plan-Fluar 100×1.45 NA objective with ImmersolTM 518F (Carl Zeiss Jena, Jena, Germany)), where we added a highly sensitive CCD camera (Luca^{EM} S 658M (Andor, Belfast, Northern Ireland), $10\times 10\ \mu\text{m}^2$ pixels) in the image plane (a schematic of the setup is provided in Appendix D). Images were acquired with an EM gain setting of 100 (the shot noise variance distortion resulting from the electron multiplying process [152] can be compensated in the background term of Eq. (7.15) in order to conserve the Poisson statistics). Despite weak photostability in air, individual molecules could be imaged for several tens of seconds before bleaching.

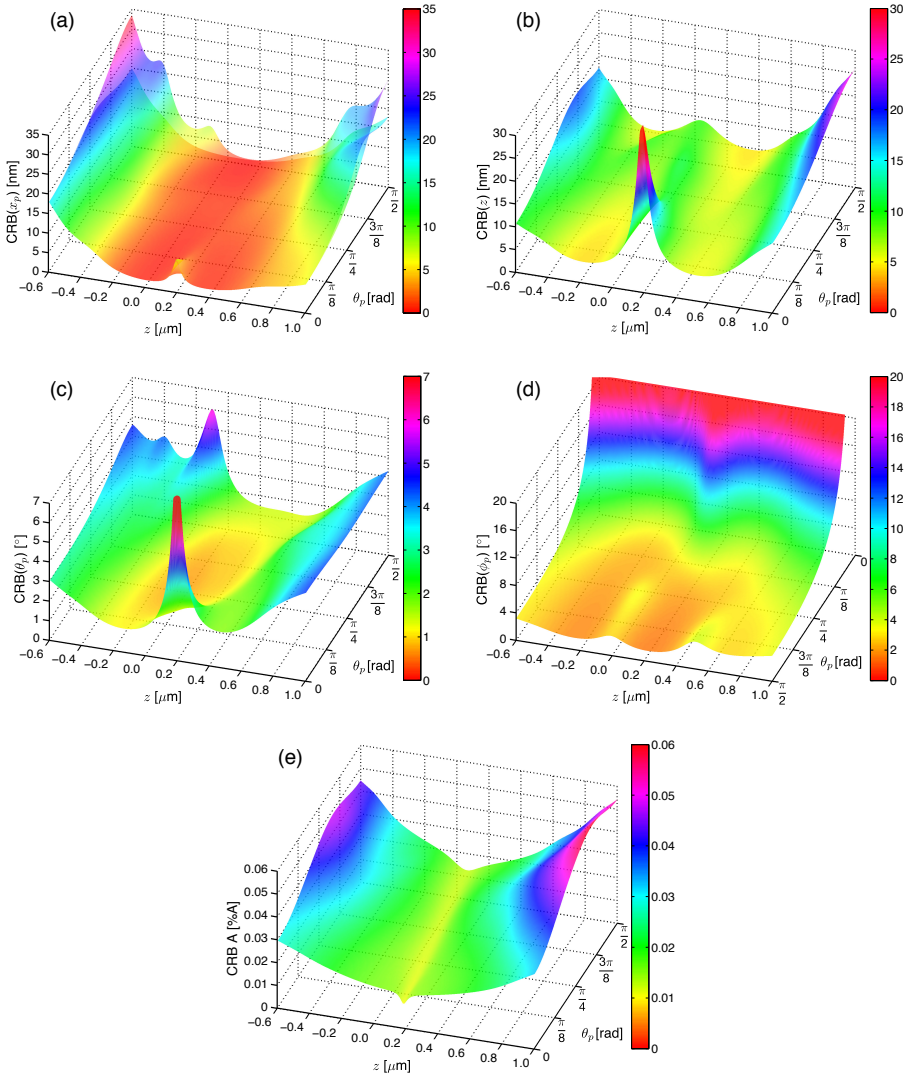


Figure 7.5 Cramér-Rao bounds for (a) x_p and y_p , (b) z , (c) θ_p , (d) ϕ_p , and (e) A . The two surfaces in (a) are the maximum and minimum values of the bound for x_p , and vice-versa for y_p ; the localization accuracy for these parameters varies as a function of ϕ_p . System parameters: $n_i = 1.515$, $n_s = 1.00$, $\lambda = 565$ nm. Average PSNR = 35 dB, background intensity level 20%.

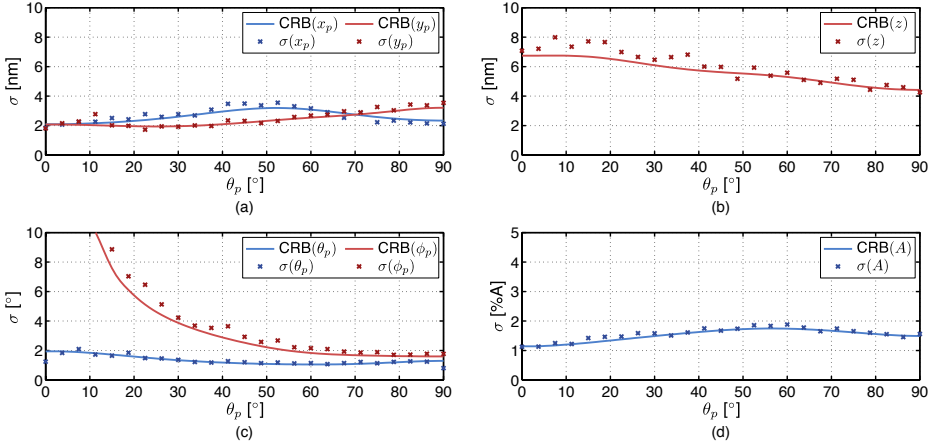


Figure 7.6 Performance of the 3-D steerable filter-based estimation of (a) x_p and y_p , (b) z , (c) θ_p and ϕ_p , and (d) A . The solid lines show the CRB for each parameter, and the markers correspond to the standard deviation of the estimation over 250 realizations of noise for each point. Parameters: $\text{NA} = 1.45$, $n_i = 1.515$, $n_s = 1.00$, $z = 400$ nm, average PSNR = 34 dB, background intensity level 10%.

7.5.2 Evaluation

For an experimental assessment of the accuracy of our algorithm, we applied the estimation to image sequences of individual molecules taken under identical acquisition conditions. Standard deviations on position, orientation, and defocus for such an experiment are given in Table 7.1; some frames from the sequence used are shown in Fig. 7.7. The results are in good agreement with the values predicted by the CRB. Specifically, it is the relative magnitude between the different standard deviations that precisely matches the behavior predicted by the CRB (for comparison, see Fig. 7.6). Although the average PSNR was relatively high for these acquisitions (26.43 dB, computed with respect to the average of all acquisitions), they provide an indication of experimentally achievable accuracy.

In a similar experiment, we compared the estimation accuracy over a series of frames of the same dipole taken at different levels of defocus. The resulting values, given in Table 7.2, indicate that the algorithm and image formation model are consistent and correspond well to the observed measurements. The frames from this experiment are shown in Fig. 7.8.

The performance of the steerable filter-based estimation of orientation and position is illustrated in Fig. 7.9 for simulated data and in Fig. 7.10 for an experimental acquisition. The image generated using the estimated positions and orientations matches the experimental measurement well, despite some residual aberrations that slightly modify the observed diffraction patterns.

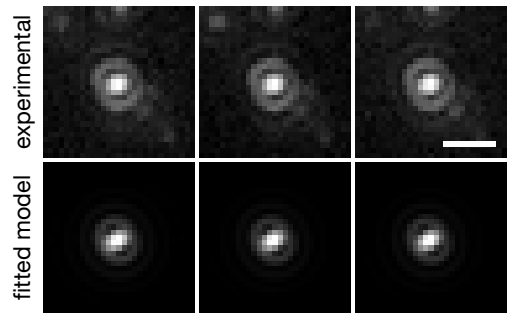


Figure 7.7 Frames from the experiment described in Table 7.1. Scale bar: 1 μm .

Table 7.1 Mean μ and standard deviation σ for position, orientation, and defocus, measured over 22 images of a single Cy5 molecule. Three of these frames are shown in Fig. 7.7, along with the fitted model.

	x_p	y_p	θ_p	ϕ_p	z
μ	$1.42 \mu\text{m}$	$1.37 \mu\text{m}$	85.45°	298.68°	214.53 nm
σ	3.00 nm	6.04 nm	1.05°	2.14°	10.72 nm

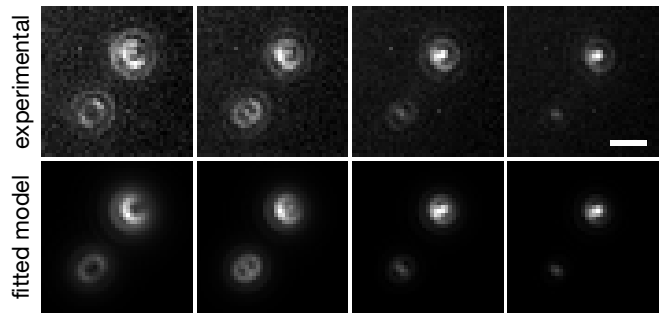


Figure 7.8 Frames from the experiment described in Table 7.2. Scale bar: 1 μm .

Table 7.2 Mean μ and standard deviation σ for position and orientation measured over 4 images of two Cy5 molecules. These frames are shown in Fig. 7.8, along with the fitted model.

	$x_p^{(1)}$	$y_p^{(1)}$	$\theta_p^{(1)}$	$\phi_p^{(1)}$
μ	$2.99 \mu\text{m}$	$1.38 \mu\text{m}$	86.46°	223.77°
σ	33.16 nm	28.62 nm	1.98°	5.30°
	$x_p^{(2)}$	$y_p^{(2)}$	$\theta_p^{(2)}$	$\phi_p^{(2)}$
μ	$1.40 \mu\text{m}$	$2.46 \mu\text{m}$	67.05°	293.26°
σ	21.48 nm	41.98 nm	4.45°	1.61°

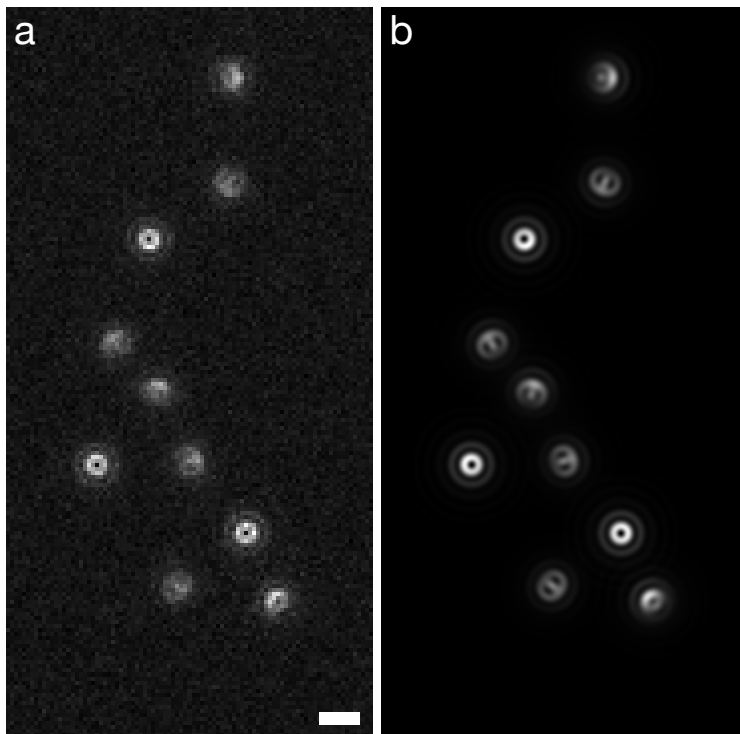


Figure 7.9 Detection of dipole orientations on simulated data, using the proposed steerable filters. (a) Dipole patterns at random, pixel-level positions and orientations. (b) High-resolution image generated using detected positions and orientations. Parameters: $NA = 1.45$, $n_i = 1.515$, $n_s = 1.00$, $z = 400$ nm, average PSNR = 25 dB, background intensity level 20%. Scale bar: $1 \mu m$.

7.6 Discussion

The method proposed in this paper should be of immediate benefit to optical imaging-based studies of molecular motors, as demonstrated in the DOPI paper by Toprak et al. [141]. These authors showed that the diffraction pattern of dipolar quantum dots [153] attached to myosin V can be clearly detected and tracked over time. Due to the computational cost of the matched filtering algorithm employed [143], the angular sampling of the templates was limited to 10° for ϕ_p and to 15° for θ_p , which also required the selection of dipoles oriented almost orthogonal to the optical axis for better accuracy (see supporting text of [141]). Due to a relatively small change in the observed diffraction pattern for values of θ_p between 0° and 45° , it was assumed that θ_p could only be determined with low accuracy using a matched filtering approach [143]. Our theoretical analysis shows that both angles in the parameterization of the dipole's orientation can be recovered with high

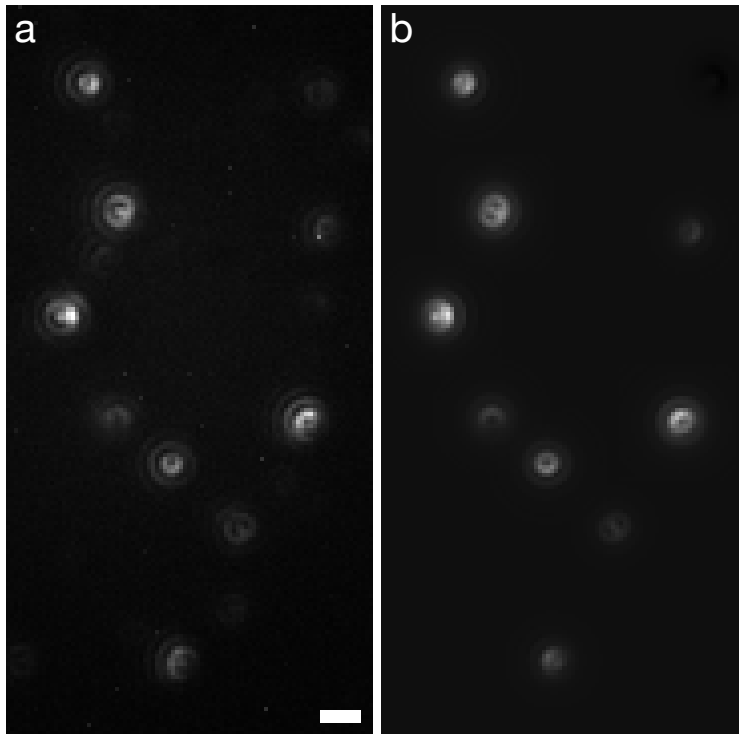


Figure 7.10 (a) Dipole diffraction patterns for ssDNA-bound Cy5 molecules at an air/glass interface. (b) Diffraction patterns rendered using the orientations and positions estimated from (a), using the proposed algorithm and image formation model. Scale bar: 1 μm .

accuracy.

DOPI requires acquisition of a pair of images: a defocused image for orientation estimation, and an in-focus image for Gaussian-based localization. As shown by Enderlein et al. [43], Gaussian-based localization applied to dipole diffraction patterns can introduce a significant bias in the estimated position, even for molecules that are imaged in focus. Our method removes these limitations: it performs well over a wide range of dipole orientations (only the estimation of ϕ_p for values of θ_p that are close to zero remains inherently inaccurate), and is relatively insensitive to the amount of defocus used, as shown in Fig. 7.5.

Recent advances in the development of FLM include expansions to 3-D, using either a combination of cylindrical optics and bivariate Gaussian fitting [26], or an interferometric estimation of fluorophore positions in direction of the optical axis [25], as well as orientation sensitive imaging using polarization-based techniques [39]. All of these approaches require some modification of the imaging system; the fitting algorithm described in this paper can be readily adapted to include 3-D localization, and is compatible

with standard TIRF setups.

7.7 Conclusion

We have introduced an efficient algorithmic framework based on 3-D steerable filters for the estimation of fluorescent dipole positions and orientations. Image formation for fluorescent dipoles can be expressed as a function of six templates weighted by functions of the dipole's orientation, leading to an effective filter-based estimation at the pixel-level, followed by an iterative refinement that yields super-resolved estimates. Experimental results on Cy5 dipoles demonstrate the potential of the proposed approach; estimation accuracies of the order of 5 nm for position and 2° for orientation are reported.

Chapter 8

Experimental calibration of an axially shift-variant point spread function model for fluorescence microscopy

8.1 Introduction

Deconvolution in fluorescence microscopy requires precise knowledge of the imaging system's 3-D point spread function (PSF) in order to yield meaningful results [7, 82, 154, 155]. The PSF can either be estimated based on a theoretical model, through experimental measurements, or by using a combination of both, where a model is computationally fitted to a measurement. The estimation is complicated by the fact that the PSF of the high-NA objectives used in fluorescence microscopy is shift-variant along the optical axis [156]. This is primarily the consequence of a mismatch between the refractive indices of the immersion and specimen media, which results in increasingly strong aberrations as the point source moves deeper into the specimen [71]. Other causes include mismatches between the refractive indices in the sample setup with respect to the objective's design values for these parameters. Even small mismatches are significant, and in addition to shift-variance, lead to a PSF that is characterized by a marked asymmetry with respect to the focal plane.

Several physically realistic PSF models described in the literature aim to accurately reproduce these aberrations (see Chapter 3); they take into ac-

This chapter is based on: F. Aguet et al., "An accurate PSF with few parameters for axially shift-variant deconvolution," in *Proc. 5th IEEE Int. Symp. Biomedical Imaging*, 2008, pp. 157–160, [46].

count the optical properties of the system, such as the refractive indices and thicknesses of the immersion, coverslip, and specimen layers in the sample setup [71, 113, 114]. In practice, some of these parameters are difficult to determine, which may lead to modeling errors. As a consequence, it is often more convenient to measure the PSF experimentally [81]. This can be achieved in multiple ways: by imaging fluorescent beads embedded in a mounting medium chosen to match the mean refractive index of the sample, by including such beads directly in the sample preparation [157], or by imaging isolated fluorescence-labeled point structures in the specimen [158]. Further possibilities include interferometric measurements of the amplitude PSF [159, 160].

There are two significant drawbacks to using an experimental PSF for deconvolution, however. First, the quality of measured PSFs rarely matches that of theoretical models, due to shot noise and the presence of background signals (e.g., due to autofluorescence). While it is possible to obtain a suitable experimental PSF through averaging of several measurements [161], the procedure can be tedious. Second, due to axial shift-variance, measured PSFs are rarely accurate over the complete sample space.

For this reason, a hybrid approach, where a theoretical model is matched to experimental measurements, is preferable. While it is clear that a diffraction limited model that matches experimental observations is advantageous for deconvolution [162], only a small number of methods that involve fitting a theoretical model to measurements have been proposed (usually in the context of parametric blind deconvolution). The most sophisticated of these methods is based on a polynomial parameterization of the phase [163]. While the number of degrees of freedom in that model is empirically chosen and comparable to state-of-the-art PSF formulations (see, e.g., [71, 109, 114]), the resulting PSF was shown to approximate the ground truth well. However, due to the absence of a depth-dependent term in the approximation of the phase, applications of this method are limited to shift-invariant deconvolution.

Pankajakshan et al. [164] proposed a similar approach for confocal fluorescence microscopy, where they assumed that the PSF can be approximated by a 3-D Gaussian function [165], which has the advantage of minimizing the degrees of freedom in the model. This approximation is also limiting, however, since it precludes the model from accurately reproducing a shift-variant PSF.

Haeblerlé et al. [166] showed that the parameters of a physically realistic scalar PSF can be estimated by fitting the model to an experimental PSF through correlation. Although this results in a diffraction-limited model suitable for deconvolution, the approach does not resolve potential ambiguities where different parameter combinations may result in near-identical

PSFs. As a consequence, the validity of the resulting model over the complete sample space is not guaranteed.

In this chapter, we present an estimation framework based on a slightly simplified version of a state-of-the-art model that resolves these ambiguities and results in a shift-variant PSF that accurately reproduces experimental observations. We first describe a vectorial model of image formation for optical microscopes that takes into account the optical properties of the immersion, glass, and specimen layers that constitute the sample setup. Subsequently, we proceed to show that different combinations of these parameters produce virtually identical PSFs and propose an approximation that reduces the parameter space of the model. In Section 8.6, we introduce a fitting algorithm based on this reduced model; the algorithm requires two experimental measurements at distinct depths in the specimen. Experimental results are presented in Section 8.7, and followed by a discussion of applications for the proposed framework in Section 8.8.

8.2 Image formation model

Some of the most accurate image formation models for microscopy are described by Hell et al. [114] and Török et al. [113], using vectorial theories of light propagation. Based on the analysis of Richards and Wolf [111], these equivalent calculations comprise propagation through the sample, glass (coverslip), and immersion layers of the setup, and incorporate aberrations arising from refractive index mismatches between these layers [133]. Microscope objectives are designed for use in a specific immersion medium; since the refractive index of the sample layer rarely matches that of the immersion layer, ideal imaging conditions are only met by sources located at the sample/coverslip interface. In their scalar formulation of image formation for fluorescence microscopes, Gibson and Lanni expressed aberrations in terms of the optical path difference (OPD) between the reference path corresponding to this design condition and the path corresponding to the actual experimental settings. Haeberlé showed that the aforementioned vectorial models can be formulated in terms of the OPD, which has the advantage of yielding expressions that depend entirely on known or sample-dependent parameters [109].

8.2.1 PSF model

The expression for the PSF resulting from the combination of these observations, formulated in object space, is given by

$$h(\mathbf{x}; \mathbf{x}_p, \boldsymbol{\tau}) = \frac{8\pi}{3} (|I_0|^2 + 2|I_1|^2 + |I_2|^2), \quad (8.1)$$

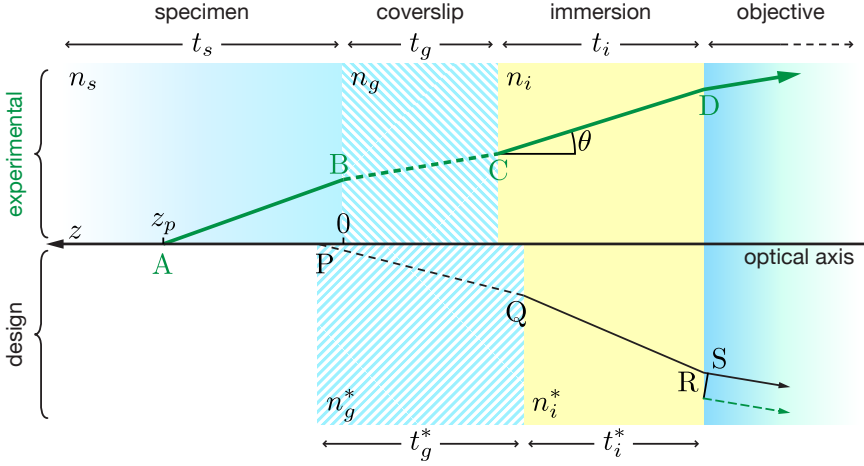


Figure 8.1 Schematic representation of the optical path difference. Design conditions are satisfied when the source is located at the specimen/coverslip interface, and no index mismatches occur. The green ray illustrates deviations from these conditions for a source located at an arbitrary depth z_p . Adapted from [71].

whose components are

$$\begin{aligned}
 I_0(\mathbf{x}; \mathbf{x}_p, \boldsymbol{\tau}) &= \int_0^\alpha B_0(\theta) \left(t_s^{(1)} t_s^{(2)} + t_p^{(1)} t_p^{(2)} \frac{1}{n_s} \sqrt{n_s^2 - n_i^2 \sin^2 \theta} \right) d\theta \\
 I_1(\mathbf{x}; \mathbf{x}_p, \boldsymbol{\tau}) &= \int_0^\alpha B_1(\theta) t_p^{(1)} t_p^{(2)} \frac{n_i}{n_s} \sin \theta d\theta \\
 I_2(\mathbf{x}; \mathbf{x}_p, \boldsymbol{\tau}) &= \int_0^\alpha B_2(\theta) \left(t_s^{(1)} t_s^{(2)} - t_p^{(1)} t_p^{(2)} \frac{1}{n_s} \sqrt{n_s^2 - n_i^2 \sin^2 \theta} \right) d\theta
 \end{aligned} \tag{8.2}$$

with

$$B_m(\theta) = \sqrt{\cos \theta} \sin \theta J_m(kr n_i \sin \theta) e^{ik\Lambda(\theta, z; z_p, \boldsymbol{\tau})}, \tag{8.3}$$

where $\mathbf{x} = (x, y, z)$ is a point on the image plane in object space (consisting of the detector coordinates (x, y) and defocus z), and \mathbf{x}_p is the position of the point source. The origin is located at the coverslip/sample layer interface. The parameter vector

$$\boldsymbol{\tau} = (n_i, n_i^*, n_g, n_g^*, n_s, t_i^*, t_g, t_g^*) \tag{8.4}$$

describes the optical properties of the sample setup, which is schematically represented in Fig. 8.1. The subscripts on the refractive indices n and thicknesses t indicate the respective layer; a parameter with an asterisk represents a design value. A is a constant amplitude, $r = \sqrt{(x - x_p)^2 + (y - y_p)^2}$, $k = 2\pi/\lambda$ is the vacuum wavenumber, where λ is the emission wavelength, and J_0 denotes the Bessel function of the first kind of order zero. The integrals are computed over the angular aperture $\alpha = \sin^{-1}(\text{NA}/n_i)$. For ease of

notation, all coordinates are expressed in object space, implying that we consider image space to be demagnified and projected into object space. The Fresnel transmission coefficients $t_p^{(l)}$ for p -polarized and $t_s^{(l)}$ for s -polarized light from layer l to layer $l + 1$, are given by

$$\begin{aligned} t_p^{(l)} &= \frac{2n_l \cos \theta_l}{n_{l+1} \cos \theta_l + n_l \cos \theta_{l+1}} \\ t_s^{(l)} &= \frac{2n_l \cos \theta_l}{n_l \cos \theta_l + n_{l+1} \cos \theta_{l+1}}, \end{aligned} \quad (8.5)$$

where $(n_1, n_2, n_3) = (n_s, n_g, n_i)$ for the three layers in the sample configuration. The angles θ_1 through $\theta_3 = \theta$ are expressed in function of the latter via the Snell-Descartes law (see Fig. 8.1).

The phase term $k\Lambda(\theta, \mathbf{x}; \mathbf{x}_p, \boldsymbol{\tau})$ is defined through the optical path difference $\overline{ABCD} - \overline{PQRS}$, i.e.,

$$\begin{aligned} \Lambda(\theta, z; z_p, \boldsymbol{\tau}) &= \left(z_p - z + n_i \left(-\frac{z_p}{n_s} - \frac{t_g}{n_g} + \frac{t_g^*}{n_g^*} + \frac{t_i^*}{n_i^*} \right) \right) n_i \cos \theta \\ &\quad + z_p \sqrt{n_s^2 - n_i^2 \sin^2 \theta} + t_g \sqrt{n_g^2 - n_i^2 \sin^2 \theta} \\ &\quad - t_g^* \sqrt{n_{g^*}^2 - n_i^2 \sin^2 \theta} - t_i^* \sqrt{n_{i^*}^2 - n_i^2 \sin^2 \theta}, \end{aligned} \quad (8.6)$$

and is computed according to the geometry of Fig. 8.1.

A detailed calculation of this model was provided in Chapter 7. For the sake of completeness, we note that the fitting algorithm described in the remainder of this chapter can also be implemented using the scalar formulation for the PSF by Gibson and Lanni [46], which, using the previously introduced conventions, is given by

$$h(\mathbf{x}; \mathbf{x}_p, \boldsymbol{\tau}) = \left| A \int_0^\alpha e^{ik\Lambda(\theta, z; z_p, \theta)} J_0(kr n_i \sin \theta) \sin \theta \cos \theta d\theta \right|^2. \quad (8.7)$$

8.3 Maximum-likelihood estimation framework

A maximum-likelihood estimation framework for the parameters in the PSF model is obtained analogously to the approaches formulated for localization (see, e.g., Chapter 5). Due to the similarities between the approaches, the formulation is omitted from this chapter.

8.4 Estimation of the model parameters

Fitting the PSF model $h(\mathbf{x}; \mathbf{x}_p, \boldsymbol{\tau})$ to an experimental measurement $s(\mathbf{x})$ entails the estimation of \mathbf{x}_p , the acquisition positions z , and the parameter vec-

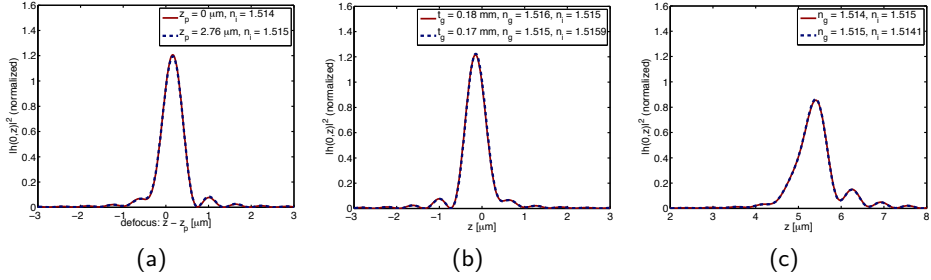


Figure 8.2 Illustration of near-identical PSFs resulting from significantly different parameter combinations. The red curves correspond to the axial intensity of the simulated measurement, and the blue dashed curve to the resulting model for a $63\times$, 1.4 NA oil immersion objective ($n_i^* = 1.515$). Unless indicated, the PSFs correspond to a source at $z_p = 0$. (a) Compensation for an immersion medium refractive index mismatch by the source position in the model. (b) Coverslip mismatch compensated by the estimated refractive index of the immersion medium. (c) Mismatch in the refractive index of the coverslip is compensated in the estimated refractive index of the immersion medium.

tor τ , as well as the amplitude A . The design values for the coverslip's refractive index n_g^* and thickness t_g^* , together with the working distance t_i^* and refractive index of the immersion medium n_i^* are part of the objective specifications and are assumed to be known. This leaves the parameters n_i , n_g , n_s , and t_g in τ to be estimated.

The degrees of freedom in the OPD render the estimation problem ill-posed, in the sense that combinations of significantly different parameter values generate virtually identical models. And while it is possible to obtain a good fit with such a model, there is no guarantee that the resulting parameters are consistent with the true experimental values. As a consequence, the model is not guaranteed to be consistent with measurements at source depths other than the one involved in the fitting process. The fitting results for some parameter combinations that illustrate this problem are given in Fig. 8.2. Note that the fitted models are highly similar to the original intensity profiles but not identical to them.

8.5 Simplified OPD model

In order to reduce the degrees of freedom in (8.6), we propose to neglect the contribution of the coverslip properties to the OPD, under the assumption that they are compensated by changes in the remaining parameters. Accord-

ingly, we replace the expression for the OPD with

$$\begin{aligned} \Lambda(\theta, z; z_p, \tau) \approx & \left(z_p - z + n_i \left(-\frac{z_p}{n_s} + \frac{t_i^*}{n_i^*} \right) \right) n_i \cos \theta \\ & + z_p \sqrt{n_s^2 - n_i^2 \sin^2 \theta} - t_i^* \sqrt{n_{i^*}^2 - n_i^2 \sin^2 \theta}. \end{aligned} \quad (8.8)$$

Some high-NA objectives are equipped with a corrective ring designed to compensate for aberrations induced by a mismatched coverslip, which further justifies the omission of the coverslip-related terms in the OPD. The result is different from a standard two-layer model (see, e.g., [114]) in the sense that it maintains the dependence on the working distance t_i^* of the objective and incorporates the effects of focusing on the immersion layer thickness [71]. The inclusion of these terms partially compensates for the shift that is observed between the true position of the fluorescent source z_p and the position where the observed intensity is maximal. This focal shift is non-negligible and highly non-linear for high-NA objectives.

8.6 Estimation algorithm

We now present an estimation algorithm for fitting the reduced OPD-based model to experimental measurements. To motivate the proposed approach, we first consider fitting the model to a PSF measured at the coverslip/sample layer interface. In this case, the set of unknown parameters is reduced to the acquisition positions $\{z_n\}$, the refractive index of the immersion medium n_i , as well as the amplitude A and the lateral position of the source (x_p, y_p) . Due to the non-convexity of the optimization criterion in terms of n_i and $\{z_n\}$, we propose to estimate the latter based on the maximum intensity position of the PSF. However, for values of $n_i \neq n_i^*$, a noticeable focal shift occurs.

8.6.1 Focal shift compensation

The dominant factor behind the focal shift is the mismatch between the refractive indices of the immersion and sample media. This depth-dependent shift is linear for low-NA objectives [114], but becomes highly nonlinear for high-NA objectives [167]. A similarly nonlinear shift occurs as a result of an index-mismatched immersion medium. Both sources of focal shift are illustrated in Fig 8.3. No closed-form expression for the maximum intensity position of the PSF can be obtained, and the focal shift for each set of parameters must be determined numerically by maximizing the on-axis intensity $h(z_p, z, \tau)$.

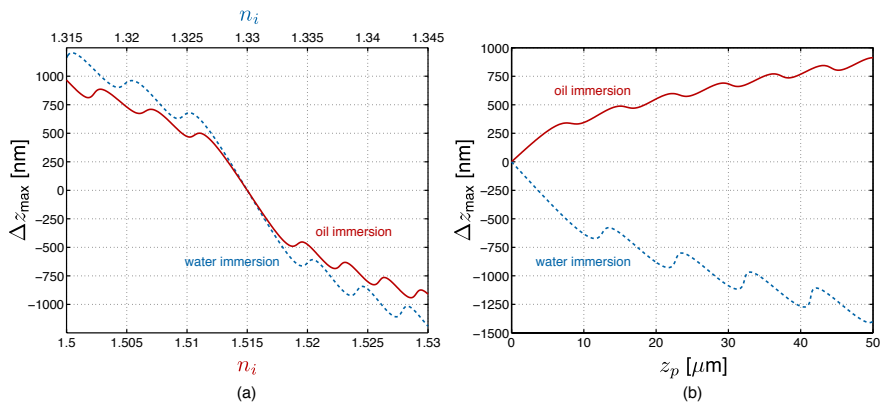


Figure 8.3 Shift Δz_{\max} of the PSF intensity maximum with respect to the source position z_p , as a function of refractive indices and source depth. (a) Shift for a source located at $z_p = 0$ as a function of immersion index variation for a $63\times$, 1.4 NA oil immersion objective and for a $63\times$, 1.2 NA water immersion objective. (b) Shift as a function of the source depth z_p in a medium with index $n_s = 1.46$, for the same objectives.

In the earlier example, the acquisition positions $\{z_n\}$ are thus adjusted for every update of the estimated immersion index \hat{n}_i by computing the corresponding focal shift (a curve analogous to those of Fig. 8.3(a) can be pre-computed and interpolated to speed up the algorithm).

8.6.2 Iterative approach based on two measurements

A complete fit of the PSF model is obtained by extending the approach introduced in the above example to two measurements. The first measurement is used to estimate the index of the immersion medium \hat{n}_i , as well as the acquisition positions $\{\hat{z}_n\}$, and is thus assumed to correspond to a fluorescent source located at the coverslip/specimen interface. This is straightforward to achieve in practice (details are given in Section 8.7.1), although we will later show that the algorithm converges to a correct solution even when the first source is not located at $z_p = 0$.

A second measurement corresponding to a source at an arbitrary depth in the specimen (preferably at the other extremity of the sample space with respect to the depth of the object of interest) is used to estimate \hat{n}_s . As part of this estimation, the source position x_p , as well as the amplitude A of the source need to be estimated. As mentioned at the beginning of this section, these parameters are also part of the estimation for the first measurement.

The complete fitting algorithm is schematically represented in Fig. 8.4. The two sources are denoted $z_p^{(a)}$ and $z_p^{(b)}$, respectively, and it is assumed that $z_p^{(a)} = 0$. The full algorithm is an iterative procedure that alternates between

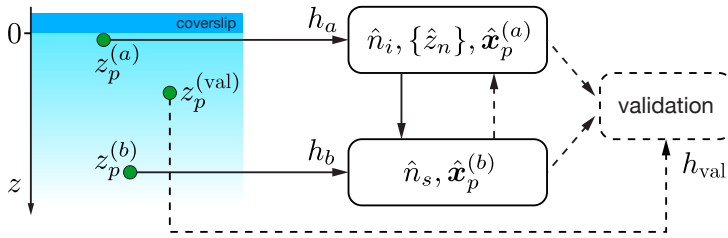


Figure 8.4 Illustration of the PSF calibration algorithm. The PSF h_a generated by a point source at the coverslip/sample interface is used to estimate the refractive index n_i of the immersion medium, as well as the positions of the acquisitions $\{z_n\}$. In the optimization, it is assumed that $z_p^{(a)} = 0$. A second PSF h_b corresponding to a source deep within the sample is used to estimate the refractive index n_s of the sample. The proposed model, parameterized by the estimates \hat{n}_i , \hat{n}_s , and $\{\hat{z}_n\}$ can then be validated against further PSF measurements h_{val} through 3-D localization.

the two previously described estimation methods. For the estimation of n_s and $\hat{x}_p^{(b)}$, the acquisition positions are computed based on the estimates of $\{z_n\}$ for the first measurement.

As indicated in Fig. 8.4, the model generated by the estimated parameters \hat{n}_i , \hat{n}_s , and $\{\hat{z}_n\}$ can be validated against other measurements in the sample through localization, i.e., through the estimation of the source position $x_p^{(\text{val})}$.

8.7 Results

Initial validation of the proposed model and algorithm was performed on shift-variant PSFs generated with the exact model (8.6). In results similar to the comparisons of Fig. 8.2, the fitted model was always equivalent to the simulated measurements in noise-free cases. Experimental validation was performed on fluorescent beads (170 nm PS-speck microspheres from Invitrogen) distributed over a thick layer ($> 20 \mu\text{m}$) of mounting medium.

8.7.1 Experimental setup

A diluted solution of beads was dried onto a coverslip and embedded in a solid mounting medium (Dako GlycerGel, refractive index $n_s = 1.46$), which resulted in a homogeneous distribution of beads throughout the sample. Imaging was performed using a $63\times$, 1.4 NA oil immersion objective and a $63\times$, 1.2 NA water immersion objective on a Leica DM 5500B widefield epifluorescence microscope (HCX PL APO objectives). The correction rings on the objectives were calibrated on a Leica TCS-SP2 AOBS confocal microscope, in order to minimize coverslip-induced aberrations. Complete stacks

	n_i	n_i^*	n_s	n_s^*	$z_p^{(b)} [\mu\text{m}]$	$z_{\text{val}} [\mu\text{m}]$
Oil immersion	1.5145	1.515	1.4598	1.460	17.945	9.052
Water immersion	1.3360	1.330	1.4603	1.460	28.936	13.189

Table 8.1 Estimated parameter values for the calibration experiments of Fig. 8.5.

of the sample were acquired; PSFs were manually chosen and segmented from these data sets. Beads that are bound to the coverslip lie in the same imaging plane and easily be detected.

8.7.2 Calibration results

The fitting results for selected PSFs are shown in Fig. 8.5. For the oil immersion objective, the PSF at the coverslip/sample interface presents a slight but noticeable asymmetry, which illustrates the likelihood of unexpected aberrations even in an ideal configuration where the system was carefully calibrated and the sample is the simplest possible, i.e. a point source bound to the coverslip. Fitting the proposed model to this measurement together with a PSF deep within the sample layer (see Fig. 8.5(a,c)) yields a model that fits the experimental PSF well over the complete sample space. This is illustrated in Fig. 8.5(b,e), where the measurement is localized (i.e., only x_p is estimated) using the calibrated PSF model. Axial intensity profiles, shown in Fig. 8.6 further emphasize the correspondence between the measurements and model; the discrepancies in the secondary oscillations can be attributed to noise and are much less obvious in the xz -section comparisons of Fig. 8.5. The values of the estimated parameters are reported in Table 8.1. It should be noted that the PSF corresponding to the design values of these parameters (i.e., assuming that $n_i = n_i^*$ and $n_s = n_s^*$) is significantly different from the model obtained through the proposed fitting algorithm.

For the water immersion objective, the PSFs (measured using the same sample) exhibit stronger aberrations. The PSF at the coverslip interface is shown in Fig. 8.5(g); a PSF at the opposite extremity of the sample space in Fig. 8.5(i). The model closely replicates the measurements, despite a slight axial tilt in some of the experimental PSFs. Due to the tilt, the secondary oscillations are also less pronounced in the axial profile comparison of Fig. 8.7. A measurement at an intermediary position (Fig. 8.5(h)) is again used to illustrate the validity of the calibrated model at intermediary positions, and the parameter values resulting from the fitting are reported in Table 8.1. For this example, a standard PSF obtained through the design values of the system is drastically different from the experiment and would be useless in de-

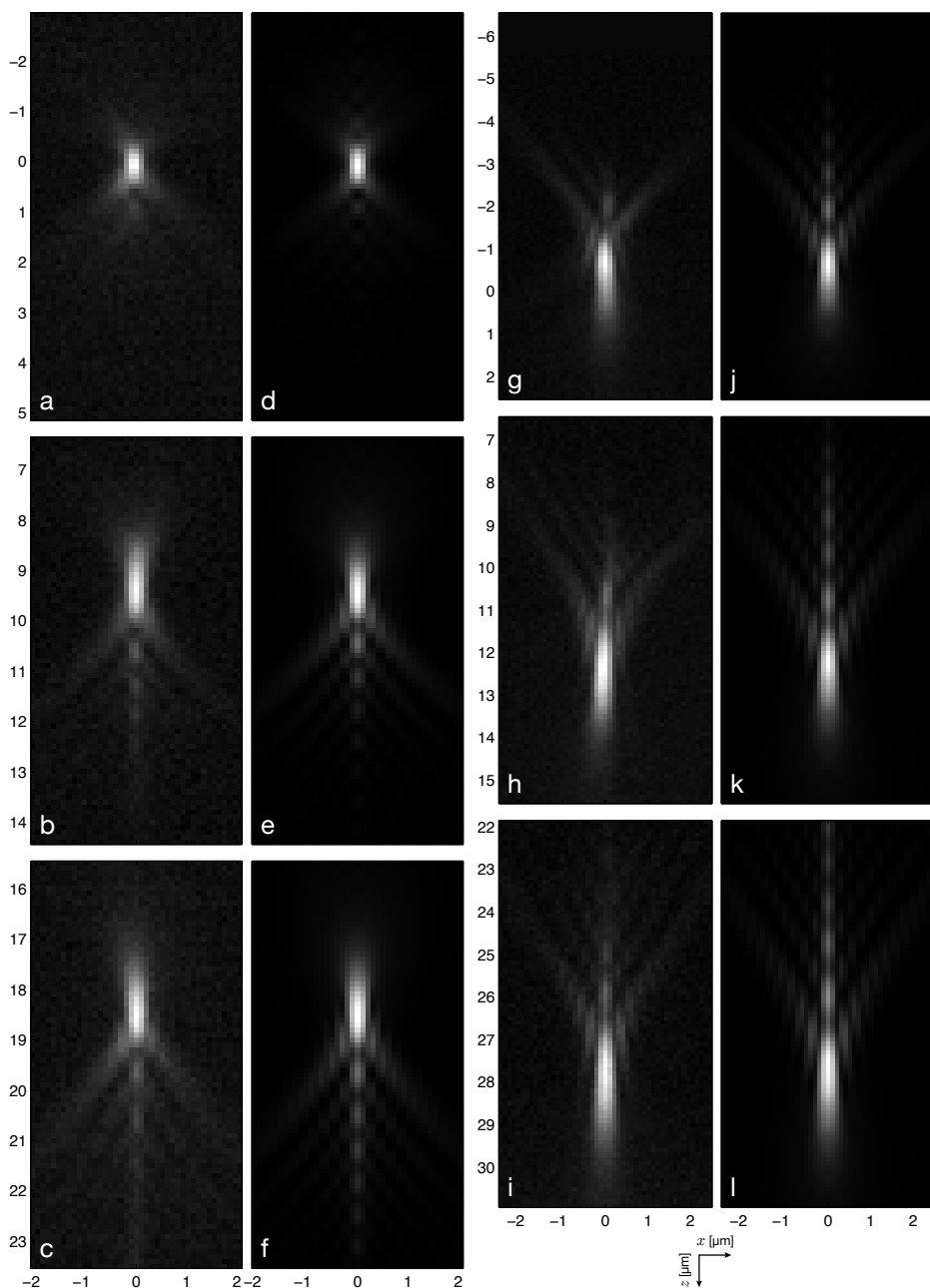


Figure 8.5 Fitting results. (a-c) Measurements with a Leica HCX PL APO CS 63 \times , 1.4 NA oil immersion objective. (d-f) PSF model calibrated to (a) and (c). (e) Validation of the model against (b). (g-i) Measurements with a Leica HCX PL APO 63 \times , 1.2 NA water immersion objective. (j-l) PSF model calibrated to (g) and (i). (k) Validation of the model against (h). See text for details.

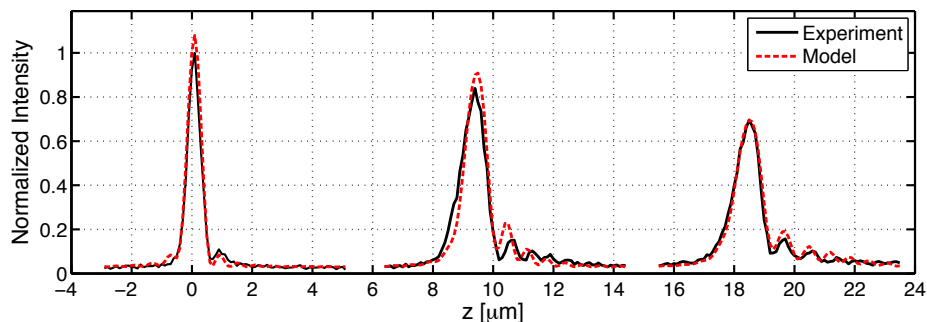


Figure 8.6 Axial intensity profiles for the $63\times$, 1.4 NA oil immersion objective results shown in Fig. 8.5. The black curve corresponds to measurements (a-c); the dashed red curve to the fitted model (d-f). Discrepancies between the curves are likely to be due to noise.

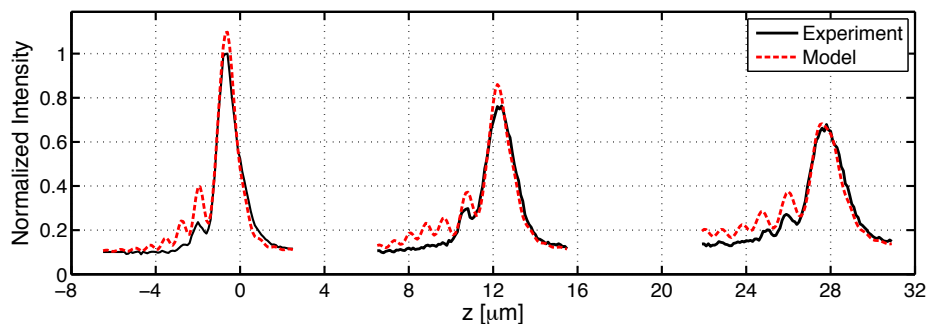


Figure 8.7 Axial intensity profiles for the $63\times$, 1.2 NA water immersion objective results shown in Fig. 8.5. The black curve corresponds to measurements (g-i); the dashed red curve to the fitted model (j-l). Discrepancies between the curves are due to a minor tilt in the axis of the measurements, as well as noise.

convolution applications.

As the estimated parameters values in Table 8.1 show, the difference between the estimations and design values are relatively small. The refractive index of the immersion medium clearly compensates for aberration sources that are not modeled in the OPD. On the other hand, the estimated values for the sample layer's refractive index remain very close to the expected index.

Computationally, the algorithm is very efficient; in our implementation, the evaluation of a PSF on 10^6 points, together with the relevant derivatives required for the parameter estimation, is achieved in less than 1.3 seconds (on a 2.66 Ghz Intel Xeon CPU). The complete fit of the model generally requires less than 2 minutes.

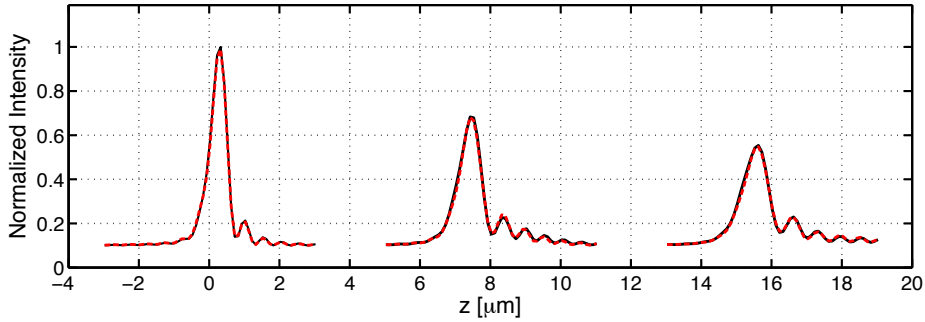


Figure 8.8 Axial intensity profiles for a fit to simulations lacking a measurement at the coverslip/specimen interface. The sources were positioned at $z_p = 5 \mu\text{m}$, $z_p = 12 \mu\text{m}$, and $z_p = 20 \mu\text{m}$; the axial intensity of the corresponding PSFs is shown in black. The dashed red curve corresponds to the intensity of the model fitted under the assumption that $z_p = 0 \mu\text{m}$ for the PSF located in $z_p = 5 \mu\text{m}$. Although the curves are not identical, the discrepancies between them are not significant.

8.7.3 Validity of the method for arbitrary measurements

In some experiments, it might not always be possible to measure the PSF at the coverslip/sample interface, especially when intrinsic point sources [158] or an aqueous mounting medium are used (in which case it can be difficult to bind fluorescent beads to the coverslip). The simplified OPD model is sufficiently general and can incorporate a depth-dependent aberration component into the index mismatch between n_i and n_s . In other words, the model can also be calibrated with two PSFs measured at arbitrary depths within the specimen; in the estimation algorithm, it is still assumed that $z_p^{(a)} = 0$. An example for such measurements is illustrated in Fig. 8.8, where measurements were generated for point sources located at 5, 12, and 20 μm into the specimen. The setup parameters correspond to the oil immersion experiments described earlier, i.e., with $n_i = 1.515$ and $n_s = 1.46$. The PSFs corresponding to $z_p = 5 \mu\text{m}$ and $z_p = 20 \mu\text{m}$ are used to calibrate the model, and the PSF at $z_p = 12 \mu\text{m}$ is used for validation, as in the previous experimental comparisons. In this noise-free example, the correspondence between the fitted model and the simulated measurements is optimal.

8.8 Discussion

The quality of the experimental results described in the previous section is highly promising for the application of the proposed model to deconvolution. In the case of shift-invariant deconvolution, the reduced number of parameters in the PSF combined with the fitting approach are an efficient

means of obtaining a diffraction-limited, noise-free model that matches experimental conditions. It is well established that such combinations outperform other solution in terms of deconvolution quality [162]. Calibrating the model by means of isolated point source measurements in the sample is feasible to implement in practice; a similar sample preparation to the one described can be used to include fluorescent beads in a biological specimen.

The main strength of the proposed approach is its suitability for shift-variant deconvolution problems. Although relatively few results have so far been published on this topic due to its computational and algorithmic challenges, axially shift-variant deconvolution has been shown to greatly improve upon shift-invariant deconvolution for thick specimens [156], where depth-dependent aberrations have a particularly strong effect on the PSF (see, e.g., Preza et al. [83] and Shaevitz et al. [168]).

Although the description of the model and fitting algorithm focused on widefield microscopy, the proposed framework is easily extensible to other modalities, such as confocal microscopy and 2-photon microscopy. For the former, this simply involves replacing the expression for the PSF with $|h_{\lambda_{\text{ex}}}(\mathbf{x}; \mathbf{x}_p, \boldsymbol{\tau})|^2 |h_{\lambda_{\text{em}}}(\mathbf{x}; \mathbf{x}_p, \boldsymbol{\tau})|^2$, where λ_{ex} and λ_{em} are the excitation and emission wavelengths, respectively. In addition to deconvolution, the algorithm can also be used in other applications where an exact model of the PSF is critical, such as single molecule localization approaches that are based on a PSF model, or for the quality assessment of microscope objectives.

Possible extensions of this work include, foremost, the application and evaluation of the calibrated model both in shift-invariant and shift-variant deconvolution. For shift-variant deconvolution, the model might be particularly useful in blind parametric approaches. Due to the minimal number of parameters, it should provide a significant advantage over methods that rely on more complex models (see, e.g. [163]).

Chapter 9

Model-based 2.5-D deconvolution for extended depth of field in brightfield microscopy

9.1 Introduction

The limited depth of field of conventional brightfield microscopes is a significant shortcoming when imaging specimens whose thickness and surface profile extend beyond the system's focal range. It is impossible to image such samples entirely in focus with a single acquisition; only those portions that lie within the depth of field appear in focus and sharp, whereas the remaining regions are blurred by the system's point spread function (PSF). A common way around this limitation consists in acquiring a series of optical sections of the sample by gradually moving it through the focal plane. This results in a "z-stack" of images that collectively contains all available in-focus information of the specimen. Such z-stacks can be difficult to interpret, and the success of an automated analysis essentially depends on its ability to correctly identify in-focus information. Many methods have been proposed for extending the depth of field of microscopes, either by optical means [169] or through image processing [170–172], and sometimes via a combination of both [173]. In practice, it is often achieved via the fusion of images by means of extended-depth-of-field (EDF) algorithms [174]. In this chapter, we propose a new model-based alternative to these approaches which combines

This chapter is based on: F. Aguet et al., "Model-based 2.5-D deconvolution for extended depth of field in brightfield microscopy," *IEEE Trans. Image Process.*, vol. 17, no. 7, pp. 1144–1153, 2008, [47].

the recovery of both the texture and the topography of the specimen in a single, global optimization process.

9.1.1 Review of previous work

Optical techniques

The first type of solution relies on modified microscope optics along with non-standard acquisition schemes. McLachlan described a system for illuminating the focal plane with a sheet of light that permits integration by axially scanning over the desired range of the specimen, and thus avoids collecting out-of-focus information [175]. Similarly, Sheppard et al. later proposed confocal microscopy as a means of scanning and integrating the sample along the axial direction [169]. An acquisition scheme using structured illumination was presented by Burke et al. [176]. A further approach consists in using pupil masks [177]; wave-front coding to increase the depth-of-field has been demonstrated in [178,179]. It is also worth noting that promising results have been achieved via annular illumination in the case of two-photon fluorescence microscopy [180].

Computational techniques

None of the above methods are practical or possible to implement for conventional brightfield microscopy, and thus image processing was exploited early on to propose alternate solutions. Regrouped under the denomination of EDF algorithms, this second type of solution facilitates the visualization and interpretation of z-stack acquisitions by combining the in-focus information from multiple images into a single fusion image that depicts the specimen entirely in focus. Due to the thickness and staining of samples prepared for brightfield microscopy, it is generally assumed that the information that appears in focus lies on the surface of the specimen (we shall refer to this information as the specimen's texture). Given a z-stack acquisition, the goal of EDF algorithms thus lies in determining the in-focus position z that corresponds to the surface of the specimen for every point (x, y) in the image plane. Almost all existing EDF methods are variations of the following scheme:

1. Slice-by-slice application of a high-pass criterion.
2. Energy measurement in a local neighborhood around each pixel (x, y) in every slice z .
3. Construction of an in-focus map by selection of the slice index z with maximal energy at every position (x, y) .

4. Generation of the EDF image based on the in-focus index map.

A notable byproduct of the above is the topographical information obtained in the form of the in-focus index map.

One of the earliest descriptions of EDF algorithms can be traced back to Pieper and Korpel; these authors discussed the use of pointwise criteria based on intensity, as well as nondirectional finite difference filtering to discriminate for in-focus regions [170]. Subsequently, Sugimoto and Ichioka suggested using the variance within fixed windows of the acquired z-stack as a possible sharpness criterion [181]. They also showed that the texture and topography can be used to generate a stereoscopic representation of the sample. Itoh et al. adapted this approach to account for possible intensity variations in reflected light microscopy by introducing a cylindrical lens into the system and evaluating the local variance according to the resulting astigmatic aberrations [182]. Other proposals include high-pass filtering [183], and gradient-based approaches, where the presence of sharp edges is used to detect in-focus areas [184].

To date, the most successful approaches rely on some form of multiresolution analysis; e.g., steerable pyramids [185–187] and wavelet decompositions [84, 171, 188–191]. By applying a wavelet transform to every slice, one automatically performs high-pass filtering at different resolutions. This approach avoids the choice of a fixed-size filter. The selection of the in-focus slice is performed in the wavelet domain too; i.e., at every resolution level. For a state-of-the-art wavelet approach, we refer to [174]; this work also includes a comparative evaluation of the primary EDF methods.

9.1.2 Towards a new model-based approach

The primary goal of all methods outlined above is to yield an accurate rendition of the sample's texture. Although the map of selected in-focus slice positions for every pixel yields some topographical information, this distance map is noisy and coarsely discretized, and is ill-suited for accurate 3-D reconstruction and texture mapping. Some approaches (see, e.g., [84]) use local consistency checks and smoothing to improve the appearance of the topography, but they do not guarantee an accurate interpretation of the specimen's surface profile, nor do they suppress the inherent "staircase" effects.

In this chapter, we propose a new algorithm for EDF that uses a parametric model of image formation to recover the specimen's texture and topography through an optimization process. Specifically, we assume that image formation is the result of a 3-D convolution between the PSF of the system and the sample, where the latter is modeled as a texture mapped onto a thin surface, which is described by a topography map [192]. We then formulate

the EDF reconstruction as a least-squares estimation problem, and propose a solution by alternate optimization of the texture and the topography. Compared to the previously discussed EDF techniques, the topography is not limited to discretized values anymore, since it can change in a continuous way to maximally match the measurements. A further advantage is that the texture estimation process is capable of acting as a deconvolution in cases where a residual blur remains at the in-focus position, or when the true in-focus position falls in between two slices. Compared to classical deconvolution, the texture estimation is much better conditioned since the whole z-stack contributes to its estimation — hence this process can be interpreted as a 2.5-D deconvolution operation.

9.1.3 Organization of the chapter

In the next section, we introduce our image formation model. After this, in Sect. 9.3, we formulate the least-squares estimation problem, along with its iterative, gradient-based solution. Subsequently, we present a simple, computationally efficient Gaussian PSF model and compare it to accurate optical models (Sect. 9.4). The proposed algorithm is then demonstrated in Sect. 9.5, where simulations and experimental results are shown. Finally, there are a number of practical issues raised by our technique that are investigated in Sect. 9.6, where we also discuss the influence of the PSF model's accuracy on the estimation results.

9.2 Image formation in brightfield microscopy

Brightfield microscopes can be configured to use either transmitted or reflected light (called diascope or episcopic configurations, respectively), depending on the specimen's optical properties. The transmission mode is appropriate for samples that are sufficiently transparent, whereas the reflection mode makes it possible to image opaque specimens. Consequently, we propose an image formation model that applies to both modalities. For an opaque specimen imaged in reflection, the object can be modeled as a 3-D surface, which leaves image formation unchanged. It turns out that this thin surface model is a valid approximation for the diascope configuration as well, under the condition that the specimen is sufficiently thick, such that its surface alone appears in focus. It should be noted that in the latter case, this is a somewhat idealized representation that ignores potential out-of-focus contributions from beneath the surface of the specimen (note, furthermore, that these contributions vary depending the local thickness and density of the specimen). However, it is a necessary simplification to make our ap-

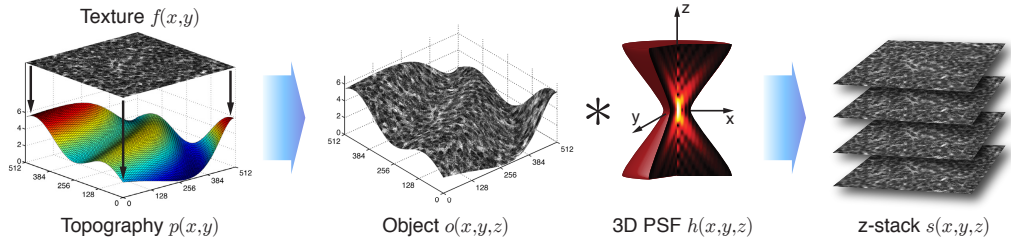


Figure 9.1 Image formation: illustration of the forward model. A texture mapped surface constitutes the object, which is convolved with the 3-D PSF of the system and sampled to obtain a z-stack acquisition. Phantom data for use in simulations was generated using this model.

proach feasible, and our experiments indicate that it does not ensue in a loss of precision in the estimation results (see Sect. 9.5). For this approximation to apply, transparent specimens should be significantly thicker than the system's depth of field, which is defined as

$$d = \frac{\lambda n_i}{\text{NA}^2}, \quad (9.1)$$

where λ is the illumination wavelength, n_i is the refractive index of the immersion medium, and NA designates the numerical aperture of the objective.

The theoretical developments below and in the following sections are stated for grayscale or single-channel data. The extension of these results as well as other issues pertaining to multi-channel data are presented in Sect. 9.3.5.

As mentioned, we express the sample $o(x, y, z)$ as a 3-D surface, described by a topography $p(x, y)$ onto which a texture $f(x, y)$ is mapped:

$$o(x, y, z) = f(x, y)\delta(z - p(x, y)), \quad (9.2)$$

where the Dirac distribution represents the surface. The image formation and acquisition process is modeled as a convolution between the object and the microscope's 3-D PSF $h(x, y, z)$, yielding the volume of acquisitions $\tilde{s}(x, y, z)$:

$$\tilde{s}(x, y, z) = \int_{\mathbb{R}^2} f(u, v)h(x - u, y - v, z - p(u, v)) \, du \, dv. \quad (9.3)$$

In practice, this is followed by sampling to generate discrete data.

9.3 Joint texture and topography estimation

We propose to recover the topography and texture based on the quadratic cost function

$$J(f, p) = \int_{\mathbb{R}^3} (s(x, y, z) - \tilde{s}(x, y, z))^2 dx dy dz, \quad (9.4)$$

where s is the measured image stack. Given this formulation, it is easy to see that an estimate of the topography will depend on the texture, and vice-versa. Therefore, we resort to an iterative two-phase optimization method that alternately updates the texture and the topography, where the texture and the topography at the τ th iteration are denoted as $f^{(\tau)}$ and $p^{(\tau)}$, respectively.

Note that this solution can be interpreted in the context of maximum likelihood. Under the hypothesis of an additive white Gaussian noise component on the image formation model described by Eq. (9.3), the minimization of (9.4) is equivalent to maximizing the corresponding likelihood function. In that setting, the estimation is performed using the expectation-maximization algorithm (EM) [193], where the texture represents the quantity to be estimated, and the topography corresponds to the hidden state. Specifically, the E-step performs the update of the texture given the current estimate of the topography (i.e., the hidden state), whereas the M-step updates the topography. This noise model is a valid assumption in the context of brightfield microscopy, where Gaussian-distributed read-out noise is the primary source. Nonetheless, in state-of-the-art cameras, read-out noise can usually be deemed negligible when compared to signal intensity.

In the following sections, we present the texture and topography estimation phases of the algorithm, and discuss some implementation issues. Two methods for texture estimation are described: a general one based on a non-separable PSF model, and a computationally more efficient one based on a simplified, separable PSF model.

9.3.1 Texture estimation

Exact model

Given an initial or current estimation $p^{(\tau)}$ of the topography, we estimate the texture by minimizing the cost function (9.4) with respect to f :

$$f^{(\tau+1)} = \arg \min_f J(f, p^{(\tau)}). \quad (9.5)$$

This minimization cannot be obtained in closed form, and is achieved by performing a steepest descent on J with respect to the texture $f(x, y)$. The

partial derivatives, easily obtained by applying the chain rule, are given by

$$\begin{aligned} \frac{\partial J}{\partial f(x, y)} &= \\ &-2 \int_{\mathbb{R}^3} e(x, y, z) h(x - u, y - v, z - p^{(\tau)}(u, v)) \, dx \, dy \, dz \Bigg|_{u=x, v=y} \\ &= -2(e * h^T)(x, y, p^{(\tau)}(x, y)), \end{aligned} \quad (9.6)$$

where \cdot^T stands for the spatial transpose; i.e., $h^T(x, y, z) = h(-x, -y, -z)$, and where $e(x, y, z) = s(x, y, z) - \tilde{s}(x, y, z)$. The gradient descent update step then consists of

$$f_{i+1}^{(\tau+1)}(x, y) = f_i^{(\tau+1)}(x, y) - \alpha \frac{\partial J}{\partial f(x, y)}, \quad (9.7)$$

where $f_{i=0}^{(\tau+1)}(x, y)$ is initialized with $f^{(\tau)}(x, y)$. The factor $\alpha > 0$ controls the strength of the update; its optimal value is obtained by performing a line search, which leads to

$$\alpha_{\text{opt}} = - \frac{\int_{\mathbb{R}^3} e(x, y, z) \omega(x, y, z) \, dx \, dy \, dz}{\int_{\mathbb{R}^3} \omega(x, y, z)^2 \, dx \, dy \, dz}, \quad (9.8)$$

where

$$\omega(x, y, z) = \int_{\mathbb{R}^2} \frac{\partial J}{\partial f(u, v)} h(x - u, y - v, z - p(u, v)) \, du \, dv. \quad (9.9)$$

Starting from $f^{(\tau)}$, several subiterations (index i) defined by Eq. (9.7) are performed to finally obtain a new estimate of the texture $f^{(\tau+1)}$.

Simplified, separable model

We now consider the above developments in conjunction with the simplest PSF model satisfactory for our image formation model, and show how this leads to an efficient and practical algorithm. The model

$$h(x, y, z) = \delta(x) \delta(y) h(z) \quad (9.10)$$

can be related to the hypothesis of in-focus information being correlated with intensity extrema along z [170]. Applying this, the forward model of (9.3) becomes

$$\begin{aligned} \tilde{s}(x, y, z) &= \int_{\mathbb{R}^2} f(u, v) \delta(x - u) \delta(y - v) h(z - p(u, v)) \, du \, dv \\ &= f(x, y) h(z - p(x, y)), \end{aligned} \quad (9.11)$$

and the cost function accordingly simplifies to

$$J(f, p) = \int_{\mathbb{R}^3} \left(s(\mathbf{x}) - f(x, y)h(z - p(x, y)) \right)^2 d\mathbf{x}, \quad (9.12)$$

where $\mathbf{x} = (x, y, z)$. The main point is that the global cost function can now be decomposed as

$$J(f, p) = \int_{\mathbb{R}^2} J(f, p)(x, y) dx dy, \quad (9.13)$$

where

$$J(f, p)(x, y) = \int_{\mathbb{R}} \left(s(x, y, z) - f(x, y)h(z - p(x, y)) \right)^2 dz, \quad (9.14)$$

and, consequently, the minimization can be performed in a decoupled fashion around the current point (x, y) . Specifically, the minimization of $J(f, p)(x, y)$ with respect to $f(x, y)$ yields

$$f(x, y) = \frac{\int_{\mathbb{R}} s(x, y, z)h(z - p(x, y)) dz}{\int_{\mathbb{R}} h(z - p(x, y))^2 dz}. \quad (9.15)$$

This expression is essentially a weighted interpolation among the slices of the z -stack around the position indicated by the topography. The above development can also be considered in the context of nearest-neighbor deconvolution, where analogous assumptions concerning the decoupling of the image formation model are made [194]. The key advantage of this simplified algorithm is the stability it lends to the overall estimation when used in conjunction with the topography estimation algorithm discussed below. This aspect, together with the use of the gradient-based estimation algorithm to perform deconvolution of the texture, is detailed at the end of this section and in the discussion (Section 9.6).

9.3.2 Topography estimation

In similar fashion, the topography can be updated using the latest texture estimate $f^{(\tau+1)}$. To this end, we minimize the cost function with respect to the topography:

$$p^{(\tau+1)} = \arg \min_p J(f^{(\tau+1)}, p). \quad (9.16)$$

The partial derivatives are also obtained using the chain rule as

$$\begin{aligned} \frac{\partial J}{\partial p(x, y)} &= 2f^{(\tau+1)}(u, v) \\ &\times \int_{\mathbb{R}^3} e(x, y, z) h_z(x - u, y - v, z - p(u, v)) \, dx \, dy \, dz \Big|_{u=x, v=y} \\ &= 2f^{(\tau+1)}(x, y) (e * h_z^T)(x, y, p(x, y)), \end{aligned} \quad (9.17)$$

where h_z stands for the partial derivative of the PSF with respect to z . Then, the gradient descent update step for the topography is

$$p_{i+1}^{(\tau+1)}(x, y) = p_i^{(\tau+1)}(x, y) - \alpha \frac{\partial J}{\partial p(x, y)}. \quad (9.18)$$

9.3.3 Coarse-to-fine optimization

The direct dependence of the topography update upon the current texture estimate $f^{(\tau+1)}$ can perturb the algorithm in its initial stages when strong global adjustments are being made, and make it converge towards an erroneous local optimum. To deal with this potential instability, we propose to perform the topography estimation in a coarse-to-fine framework, which has the effect of imposing regularity and robustness to the topography update, as the following development will show (see also Fig. 9.3). In our implementation, we have chosen to represent the topography at resolution m in a shift-invariant basis generated by symmetric B-splines of order n dilated by $m \in \mathbb{N}^+$:

$$p_m(\mathbf{x}) = \sum_{\mathbf{k} \in \mathbb{Z}^2} c_m[\mathbf{k}] \beta^n\left(\frac{\mathbf{x}}{m} - \mathbf{k}\right), \quad (9.19)$$

with $\mathbf{x} = (x, y)$ [195], and where the 2-D basis functions are formed from the tensor product of their 1-D counterparts. The minimization problem (9.16) then amounts to finding the “optimal” B-spline coefficients $c_m[\mathbf{k}]$. The corresponding partial derivatives of the criterion are

$$\begin{aligned} \frac{\partial J}{\partial c_m[k, l]} &= 2 \int_{\mathbb{R}^2} \beta^n\left(\frac{u}{m} - k, \frac{v}{m} - l\right) f(u, v) \\ &\times \left(\int_{\mathbb{R}^3} e(x, y, z) h_z(x - u, y - v, z - p_m(u, v)) \, dx \, dy \, dz \right) du \, dv \\ &= ((\beta_m^n)^T * \frac{\partial J}{\partial p})(mk, ml) \\ &= (\beta_m^n * \frac{\partial J}{\partial p})(mk, ml), \end{aligned} \quad (9.20)$$

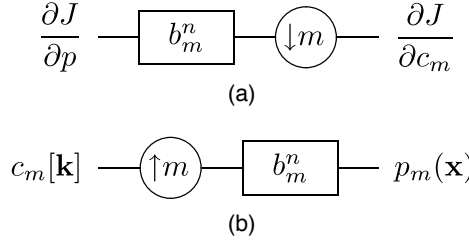


Figure 9.2 Downsampling and upsampling steps in the coarse-to-fine topography estimation algorithm. (a) B-spline gradient coarsening. (b) Fine-scale interpolation of the B-spline topography model.

where $\beta_m^n(x) = \beta^n(\frac{x}{m})$. Thus the gradient on the coefficients is essentially a smoothed and downsampled version of $\frac{\partial J}{\partial p}$, which can be implemented according to the block diagram shown in Fig. 9.2(a), where the smoothing filter $b_m^n[\mathbf{k}] = \beta^n(\frac{\mathbf{k}}{m})$ is the sampled version of the basis function in (9.20). Accordingly, the coefficient update at scale m becomes

$$c_m^{(i+1)}[k, l] = c_m^{(i)}[k, l] - \alpha \frac{\partial J}{\partial c_m}. \quad (9.21)$$

The fine scale sampling of the topography (required at each iteration) is finally obtained by upsampling c_m and post-filtering the result, as summarized in Fig. 9.2(b).

Due to the dependence of h on p in Eq. (7.22), the line search in Eq. (9.20) cannot be achieved in closed form. Here it is desirable to apply an iterative minimization scheme that does not depend on a parameter regulating the update step. Unfortunately, $J(f, p - \alpha J_p)$ is not necessarily convex, and thus a bounded optimization approach (i.e., via a quadratic upper bound) cannot be deployed. Instead, we resort to inverse parabolic interpolation, which converges reasonably fast and can be easily controlled via Brent's algorithm [196]. In practice $J(f, p - \alpha J_p)$ is smooth and has a unique minimum, and thus this scheme proves to be very efficient, requiring only a minimal number of iterations.

9.3.4 Implementation

The joint estimation of the texture and topography from a volume of acquisitions is achieved by alternating iterations of the methods outlined above. Starting from an initialization of the texture, we iterate between estimating the topography at scale m and refining the texture. Upon convergence at that scale, the algorithm switches to a finer scale ($m' = m/2$ in the dyadic case) and replicates this process. This is repeated until convergence at scale $m = 1$

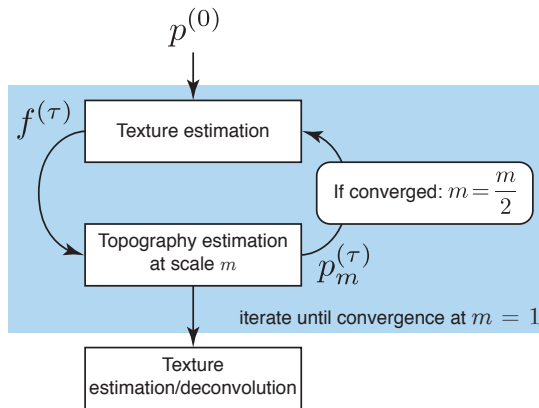


Figure 9.3 Schematic representation of the optimization algorithm. Starting from an estimate of the topography $p_m^{(\tau)}$ at scale m , the method alternates between texture and topography estimation until convergence at that scale, after which the process is repeated at successively finer scales.

is reached (see Fig. 9.3). In order to make this procedure as computationally efficient as possible, the texture estimation is performed using the simplified model at all scales except $m = 1$. At that stage, the higher precision and especially the deconvolution capabilities of the exact, gradient-based method are applied to generate the final fusion image. For the description of the topography, we used cubic B-splines ($n = 3$).

9.3.5 Refinements for processing color data

We propose to process multi-channel data sets via a straightforward extension of the algorithm above. While it would be possible to formulate our method to simultaneously operate on multiple channels, we believe that doing so during the estimation of the topography does not provide sufficient advantages when weighted against the resulting increase in computational cost, and, to a lesser degree, the influence of further degrees of freedom in the PSF model on the estimation result. Consequently, we chose to perform the estimation on grayscale data, appropriately converted from the color input. Dyes binding to a particular structure such as cell membranes or nuclei are frequently employed in biology; as a result, large specimens tend to exhibit a strongly dominant color after preparation. Taking this bias into account by performing the grayscale conversion using appropriate weights (obtained, for example, using principal component analysis) can lead to markedly improved results, as shown in [84].

The only modification to the single-channel algorithm then consists of extending the last texture estimation step (after the topography has con-

verged at scale $m = 1$) to operate on all channels in parallel, i.e., by applying each step of Eq. (9.7) individually to each channel.

9.4 Theoretical PSF model

The gradient-based algorithms presented above are not bound to any particular PSF model. In principle, it is therefore possible to use a highly accurate theoretical model that is potentially axially shift-variant and takes into account spherical aberrations, such as the scalar model proposed by Gibson and Lanni [71]. However, given that the problem is reasonably well-posed, and for the sake of decreasing computational complexity, we argue for the use of a Gaussian approximation of the microscope's PSF. Since PSF models are usually formulated for a single wavelength, they should be integrated over the spectrum of the light source used. In modern brightfield microscopes, the light source is well balanced over the visible spectrum, which means that the PSF needs to be uniformly integrated over the interval of visible wavelengths. The result of this integration is essentially a smoothing effect; in fact, the xy-sections of a white-light PSF for a low magnification objective closely resemble Gaussians.

At each iteration of the topography estimation, the PSF needs to be sampled over a given support for each point of the topography. It is therefore highly advantageous to use a Gaussian PSF model that is computationally much less complex to evaluate than an optically accurate PSF that involves numerical integration. As illustrated in Fig. 9.4, a good estimate of the PSF can be obtained by fitting a model of the form

$$h(x, y, z) = \frac{1}{2\pi(\eta_0 + \eta_1|z|)^2} \exp\left(-\frac{(x^2 + y^2)}{2(\eta_0 + \eta_1|z|)^2}\right) \quad (9.22)$$

to a theoretical PSF evaluated according to the optical properties of the microscope used, or to an experimentally measured PSF.

A key property of brightfield microscopes consists in Köhler illumination, which is designed to uniformly illuminate the sample independently of the position of the focus [197]. To account for this, the PSF needs to be normalized such that the intensity within each xy-section is equal to unity. This is not necessarily the case when the Gaussian PSF model is sampled over the integers. In particular, when $\sigma = \eta_0 + \eta_1|z|$ tends towards zero, $\sum_{i,j \in \Omega_2} h(i, j, k_0)$ goes to infinity, which is physically non-plausible. In order to avoid numerical blow up when $\sigma < 0.8$, we further normalize h by

$$\frac{1}{2\pi\sigma^2} \left(1 + 2e^{\frac{-1}{2\sigma^2}} (1 + e^{\frac{-3}{2\sigma^2}})\right)^2, \quad (9.23)$$

which is the sum over the essential support of the Gaussian.

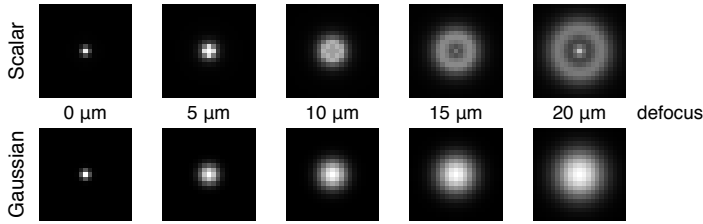


Figure 9.4 Comparison between a scalar PSF model [71] and its Gaussian approximation for a $10\times$, 0.3 NA objective for a CCD with $6.7 \times 6.7 \mu\text{m}^2$ pixels. Different focal settings are shown. For a given amount of defocus, the same dynamic range is used for illustration purposes. The corresponding parameters of the Gaussian model (Eq. (9.22)) are $\eta_0 = 0.670$, and $\eta_1 = 0.734$. A $5 \mu\text{m}$ increase in defocus corresponds to a unitary increase in z .

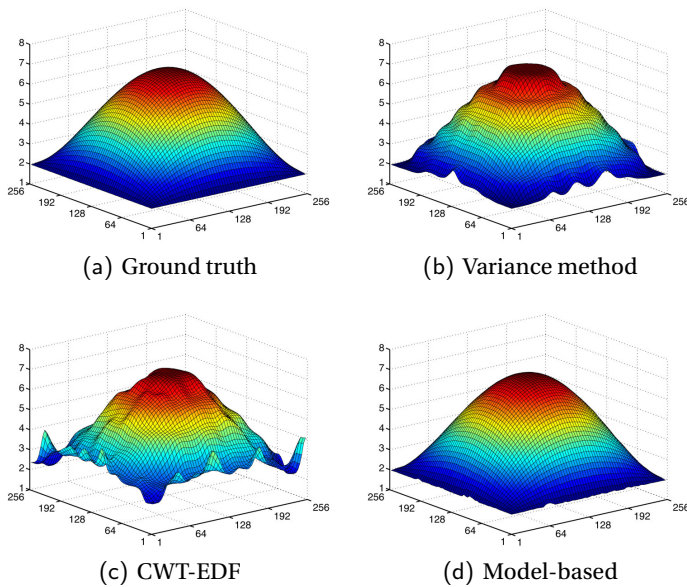


Figure 9.5 Simulation results for topography estimation using the variance-based, CWT-based, and model-based algorithms.

9.5 Results

We now present estimation results obtained from several data sets, first in simulation and then on acquisitions of biological specimens. Where appropriate, we compare our results to two reference methods for validation: one based on a local variance criterion and the other on a wavelet transform. As mentioned earlier, the former constitutes the classical approach to EDF. It has a low computational complexity and generally yields results of reasonable quality, which explains its ongoing popularity. Specifically, we compute the variance in a 5×5 window, and filter the resulting topography using

Method	Texture SNR	Topography SNR
Variance	32.07 dB	26.94 dB
CWT-EDF	32.41 dB	35.89 dB
Model-based	54.22 dB	53.36 dB

Table 9.1 Quantitative performance comparison for topography and texture estimation for various EDF methods

a Gaussian kernel with $\sigma = 2$ to enforce local smoothness.

Among state-of-the-art wavelet-based methods, we chose the complex wavelet-based EDF algorithm of [84], co-developed by two of us (from this point on, we will refer to it as the CWT-EDF method), which was shown to outperform competing methods in many instances. This choice is further justified by it being the only recent method that aims at providing a coherent estimate of the topography by imposing local smoothness and consistency constraints.

9.5.1 Performance comparison in simulation

In order to have a ground truth at our disposal for the comparison and qualitative assessment of the results produced by the above cited methods, we performed a first series of experiments using a simulated set of acquisitions. A z-stack of images was generated from a given topography and texture using the object and image formation model, i.e., by applying the non-stationary convolution of (9.9) (see Fig. 9.1).

In Fig. 9.5, we compare the topography estimation results obtained on a simulated stack containing eight images of a dome-shaped object onto which a 256×256 texture was mapped. The latter was derived from a brightfield image of a histological slide containing murine liver tissue. Our implementation of the CWT-EDF method permits to control the smoothness of the estimated topography; here we empirically optimize this step to maximize the quality of the topography. As expected, the model-based algorithm correctly recovers the topography, while the two reference methods only approximately approach the correct shape. The quality of the estimation results, in terms of the signal-to-noise ratio $\text{SNR} = 10 \log_{10}(|\text{signal}|^2/|\text{noise}|^2)$, is documented in Table 9.1. The continuous-domain formulation of the object model in our approach not only leads to a better estimation of the topography, but also deconvolves the texture at locations between slices, which accounts for the gain in estimation quality

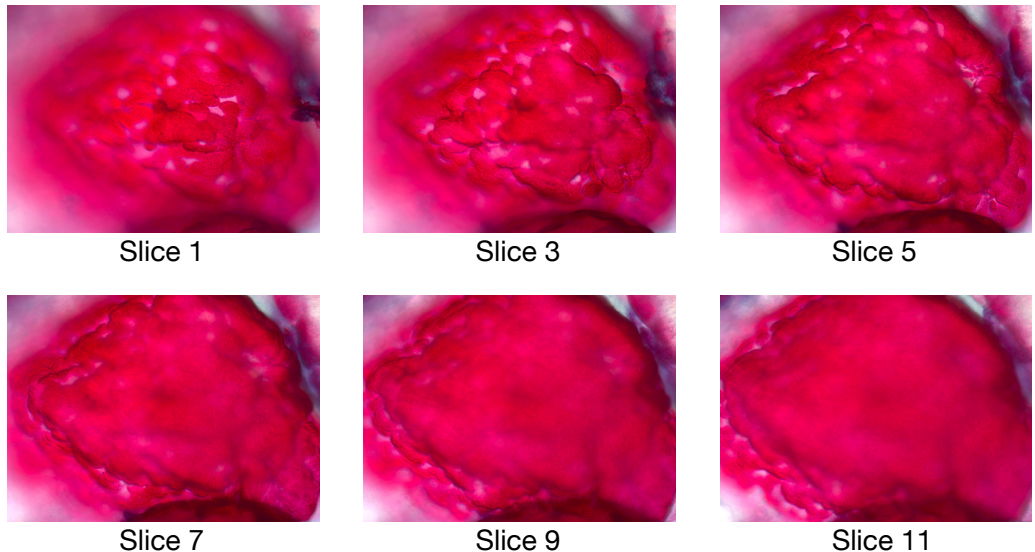


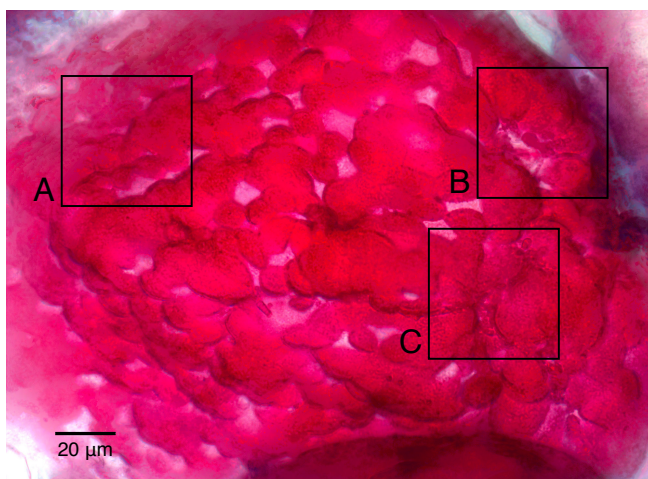
Figure 9.6 Individual image slices from the Peyer's patches stack. Distinct in-focus areas are clearly visible.

of both signals. Care was taken to generate phantom data containing in-focus information for all (x, y) -positions; this explains the relatively good quality of the texture estimation results for all methods. We initialized our method with a flat topography, and performed iterations at the scales $m = \{8, 4, 2, 1\}$. In general (also for the results on experimental data) the topography estimation typically requires around five subiterations, whereas the texture requires only 2-3 steps of the gradient update to reach convergence.

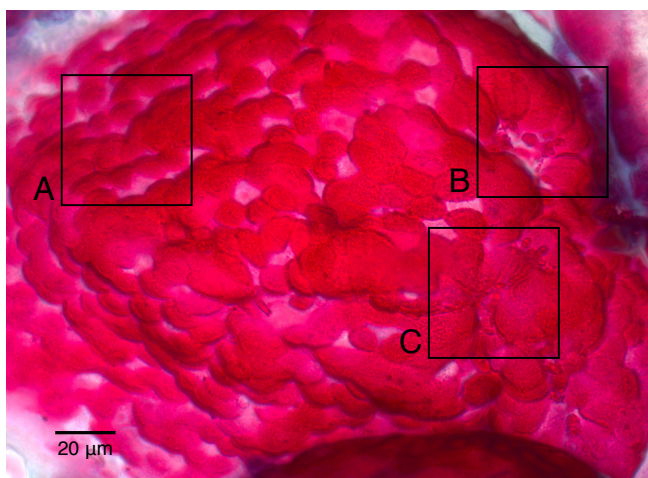
9.5.2 Results on experimental data

We now demonstrate the potential of our method on two sets of experimental acquisitions, one for a transmission setup and the other for a configuration using reflected light. The first specimen consists of a section of mouse intestine containing Peyer's patches, stained using a membrane-labeling dye. The sample was imaged using a Zeiss Plan-Neofluar $40\times$, 0.75 NA objective in air immersion, with a Jenoptik ProgRes CCD camera with $4.3\times 4.3\ \mu\text{m}^2$ pixels. 16 optical sections in steps of $3\ \mu\text{m}$ were acquired. The acquisitions have a resolution of 1996×1450 pixels, several of which are shown in Fig. 9.6.

The topography resulting from the joint estimation, shown in Fig. 9.9, clearly reveals the heap-like structure of the sample. This result was obtained by initializing the algorithm with the variance method, and by performing



(a)



(b)

Figure 9.7 Comparison of texture estimation against a wavelet-based method. The specimen is a sample of Peyer's patches in the mouse intestine. (a) Texture obtained using the complex wavelet-based algorithm described in [84], with maximal quality settings. (b) Texture resulting from our joint estimation algorithm. The coarse-to-fine estimation approach ensures local smoothness, which prevents mis-selection artifacts that are typical of approaches that rely on a high-frequency criterion.

iterations at the scales $m = \{16, 8, 4, 2, 1\}$. In Fig. 9.7 we compare the texture obtained with CWT-EDF and our method. At a first glance the results look similar, but the inspection of some details (see highlights of Fig. 9.7 in Fig. 9.8) reveals a marked improvement with our method. Notably, there is a complete absence of color artifacts typical of wavelet-based methods. Also,

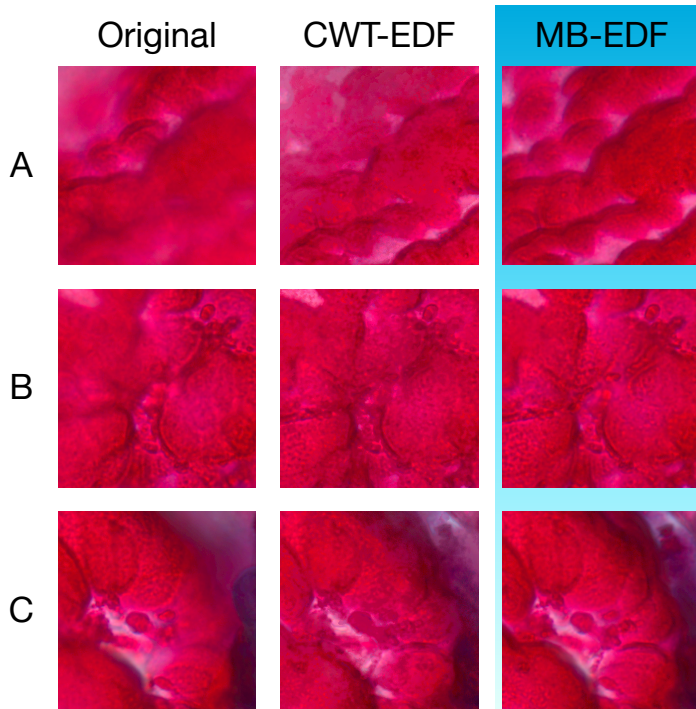


Figure 9.8 Details of the texture estimation comparison from Fig. 9.7.

the deconvolving action of the texture estimation restitutes several in-focus regions missing from the acquisitions. This is most noticeable around the cell boundaries, which appear much sharper (compare also with [191]).

Some artifacts are present in the topography, especially around the borders where structures are visible but out of focus in the acquisitions. These artifacts are direct effects of the convolution between the topography gradient and the basis functions during the coarse-scale iterations. As the algorithm moves to finer scales, a lack of in-focus information prevents further adjustments in the concerned regions.

Our second test specimen consisted of a common house fly imaged in reflection using a Zeiss Achroplan $4\times$, 0.1 NA objective in air immersion, with a QImaging Retiga CCD camera with $6.45\times 6.45\ \mu\text{m}^2$ pixels. The acquisitions were cropped to a 1000×1000 pixel region around the fly's eye. The z-stack consists of 32 images with a z-step of $20\ \mu\text{m}$.

The topography resulting from the joint estimation, shown in Fig. 9.11, reveals the homogeneous structure of the eye. The peaks present in the topography correspond to small hairs, which are also visible in the texture (Fig. 9.12). This result was obtained by initializing the algorithm with the variance method, and by performing iterations at the scales $m = \{32, 16, 8, 4, 2, 1\}$.

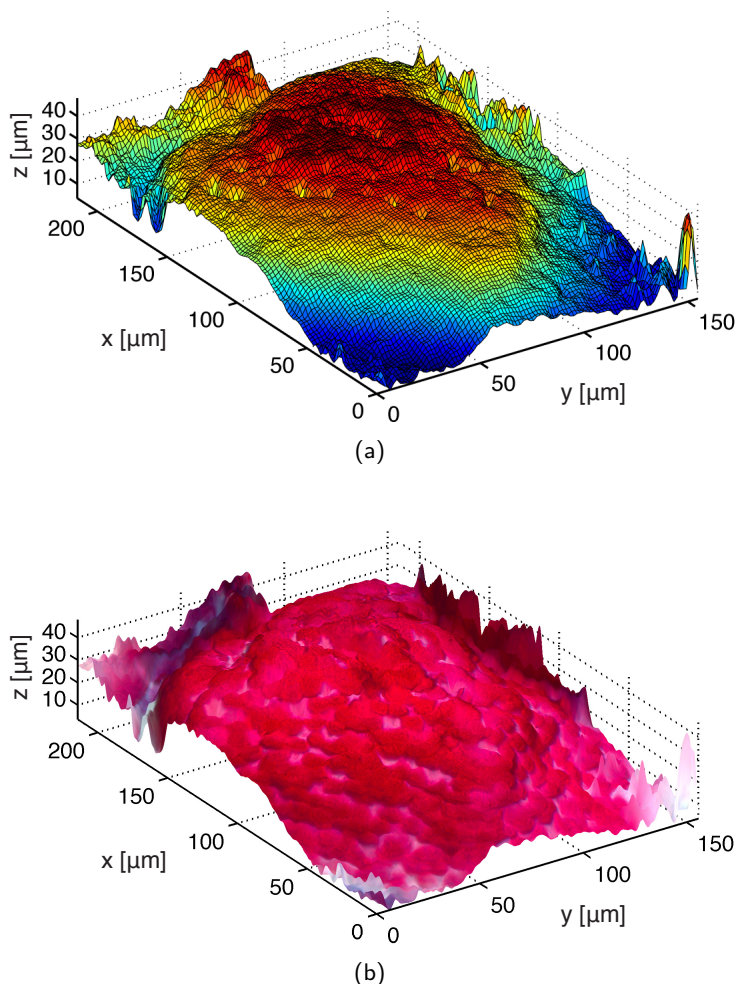


Figure 9.9 Texture mapping of the estimated texture from the Peyer's patches stack onto the corresponding estimated topography.

As these results attest to, recovering an accurate representation of the topography not only facilitates the analysis of thick specimens, but also leads to marked improvements in the estimated texture. Furthermore, the experiments confirm that the 2.5-D deconvolution leads to a sharp estimate of the texture when in-focus information is missing from the acquired data, or when it falls between acquisitions.

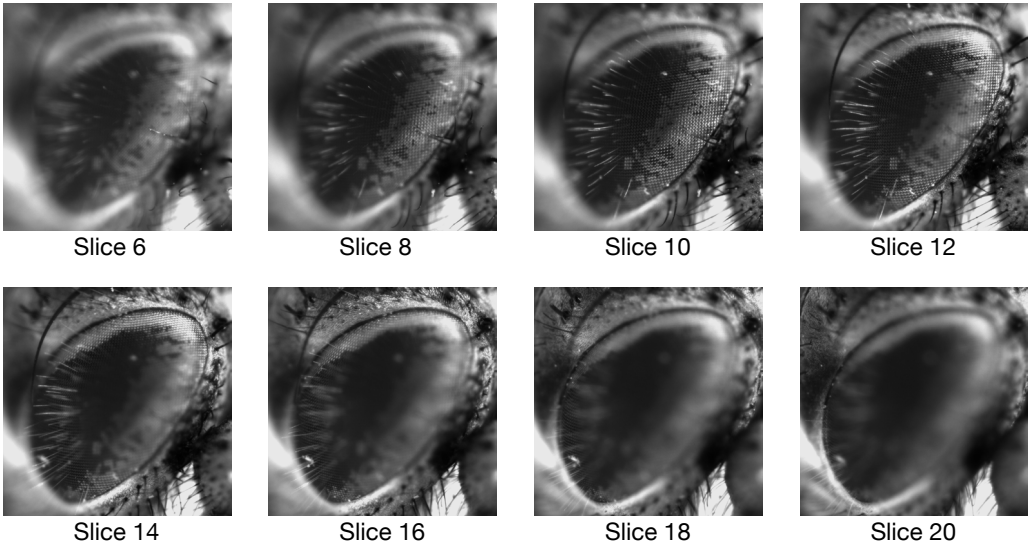


Figure 9.10 Individual images from the fly eye stack. Distinct in-focus areas are clearly visible.

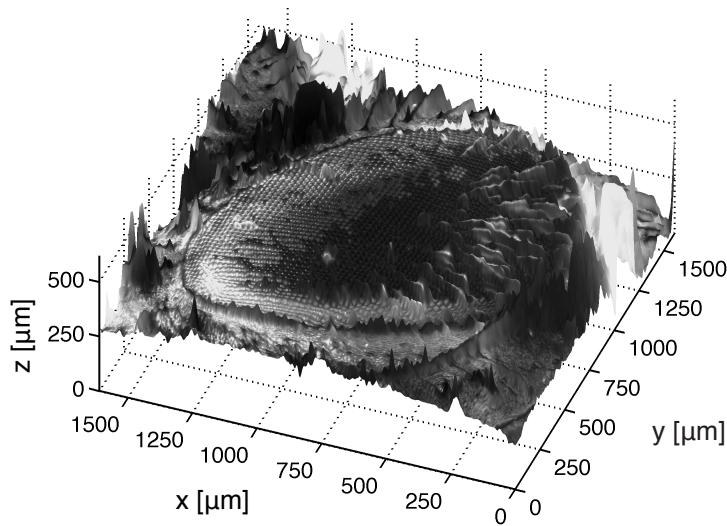


Figure 9.11 Texture mapping of the estimated texture from the fly stack onto the corresponding estimated topography.

9.6 Discussion

There are two key factors that can strongly impact on the performance of our method. We begin this section by examining the influence of the parameters

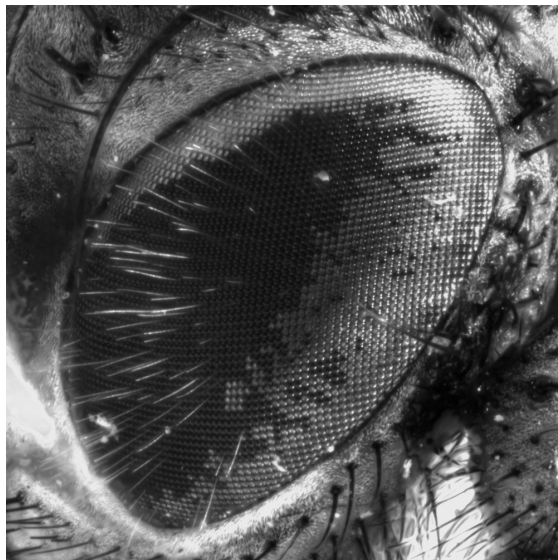


Figure 9.12 Fusion image estimated from a z-stack of a fly's eye.

controlling our Gaussian PSF model on the quality of the results, and subsequently discuss the computational performance of our approach in comparison to competing methods, in connection to which we briefly comment on possible initializations of the algorithm.

9.6.1 Sensitivity to the PSF model parameters

When dealing with experimental acquisitions, it frequently occurs that the PSF can only be approximately determined or measured. However, since the optimization of the texture and topography is generally well-posed (this is largely dependent upon the number of acquisitions in the z-stack), the reconstruction algorithm can be expected to be relatively insensitive to the parameterization of the PSF. This is indeed the case; to a certain extent, only the in-focus PSF $h(x, y, 0)$ needs to be precise. Otherwise, due to our assumptions on the specimen, the deconvolution of the fusion image is either too weak, or results in out-of-focus information being falsely reallocated to the texture. The Gaussian PSF approximation holds very well at the in-focus position, and consequently does not significantly affect the results.

In theory, an erroneous PSF can have an effect on the gain of the texture, i.e., lead to a scaling in intensity. This can in turn affect the topography estimation, and is especially problematic when operating on color data, where it can lead to false color artifacts. In our algorithm, however, due to the use of the separable texture estimation step throughout the joint estimation, this

effect is avoided altogether. Indeed, when considering the texture estimation as an interpolation, the possible values for the texture are constrained to the dynamic range of the input volume.

Simulations using data generated from the model showed that an error up to 30% on the η_1 parameter in the PSF model (9.22) leads to the recovery of the topography without any significant loss in accuracy.

9.6.2 Computational aspects

Although, due to its sophistication, our approach incurs a higher computational cost than wavelet-based EDF methods (which require a forward and inverse transform in combination with what are essentially point-wise operations), this cost is largely compensated for by the increased quality of the results. Nevertheless, the cost can be minimized by employing the separable texture estimation step whenever deconvolution of the texture isn't necessary (note that it cannot be diminished for the topography estimation). In practice, it therefore makes sense to reduce the total number of iterations by computing an initial estimate of the topography via the variance-based method. Given such an initialization, many coarse-scale iterations can be avoided. Using this scenario, our algorithm requires 64 s on a $512 \times 512 \times 10$ stack, whereas the CWT-EDF algorithm requires 16 s. Further means of acceleration could be a topic for future research.

9.7 Conclusion

We have presented a new approach to extended depth of field that constitutes a significant improvement over current methods in terms of the quality of the results. By stating the problem as a joint estimation of the sample's texture and topography, we are able to successfully recover a continuous and characteristic representation of the topography, devoid of the discretization artifacts present in existing methods. Additionally, the joint estimation model acts as a 2.5-D deconvolution operation for the resulting fusion image, which yields sharper textures, especially when the true in-focus information lies between acquisition planes. We demonstrated the validity of the approach on simulated data sets that were generated with a known topography, and obtained promising results on experimental acquisitions; improvements due to the continuous topography and texture deconvolution are clearly visible.

Since the recovered topography is continuous, it would be feasible to reconstruct a stereoscopic representation to further enhance the 3-D visualization of the specimen, as was suggested in [181]. While we presented our

method in the context of brightfield microscopy where it is likely to find its most immediate application, it is clear that, due to the relatively low sensitivity to accuracy of the PSF, the method is applicable to a wider range of optical systems with a limited depth of field. For example, a 3-D vision system combining shallow depth of field optics with the proposed method could be envisaged. In microscopy still, the method raises the possibility of performing profilometry, where it should be interesting to see with what accuracy the surface profile of an object can be quantitatively determined.

Foremost, our results illustrate the potential of a model-based approach in the context of EDF. Our solution has no pretense of optimality but should rather be viewed as a proof of concept. There likely is room for exploration and improvement, i.e., by applying a different regularization criterion, or by devising other algorithms that optimize the proposed cost function. A Java implementation (ImageJ plugin) of this work is available at

<http://bigwww.epfl.ch/demo/edf/>

Chapter 10

Conclusion

In this thesis, we introduced a framework for super-resolution fluorescence localization microscopy based on physically realistic PSF models. Specifically, we described algorithms for 3-D localization and orientation estimation of single fluorophores. Validation results indicate the potential of these methods to improve upon and outperform state-of-the-art super-resolution microscopy techniques. The principal results and contributions are summarized in the next section.

10.1 Summary of results

- **Super-resolved single molecule localization in 3-D** A framework for super-resolution localization of single fluorescent molecules based on a physically accurate image formation model was described. Experimental results for the proposed maximum-likelihood 3-D localization algorithm demonstrate accuracies at the nanometer scale in the acquisition plane and at the 10-nanometer scale along the optical axis; these values are in agreement with the theoretical limits on localization accuracy that were established using Cramér-Rao bounds [44].
- **Super-resolved dipole orientation estimation in 3-D** A method for the joint orientation and position estimation for fluorescent dipoles based on a 3-D steerable filter was introduced. In addition to nanometer-scale accuracies for lateral localization, orientation accuracies of the order of one degree are reported [45]. These results demonstrate the feasibility of super-resolved 3-D single molecule position and orientation estimation based on a physically realistic PSF model for the first time.

- **Physically realistic PSF models** The proposed localization algorithms rely on a physically accurate, axially shift-variant PSF model, which was described using state-of-the-art results from the literature. This model was extended for fluorescent dipoles and formulated as a steerable decomposition based on six basis functions, rendering the calculation of dipole diffraction patterns highly efficient [45]. Furthermore, a maximum-likelihood algorithm for the estimation of unknown parameters in these PSFs was proposed; results show an excellent agreement between the model and experimentally measured shift-variant PSFs. A fast numerical implementation of these models that accelerates computation by at least an order of magnitude with respect to competing approaches was described.
- **Extended-depth-of-field imaging** An extended-depth-of-field algorithm for the extraction of in-focus information from brightfield microscopy z-stacks was described. The fusion of in-focus information and estimation of the associated continuous topography is formulated as a 2.5-D deconvolution problem in a setting that extends the previously introduced localization methods to more complex object models, such as 3-D surfaces [47]. It is the first extended-depth-of-field method to estimate a continuous and super-resolved topography of specimens, enabling their 3-D visualization and facilitating their analysis.

10.2 Outlook for future research

The super-resolution localization methods presented in this thesis were validated either on single fluorophores or on fluorescent microspheres acting as point sources, which demonstrated their applicability to FLM. In addition to implementing the 3-D localization and orientation estimation algorithms in FLM and further validating them on a biological specimen, several extensions of these results are worth investigating.

- **3-D localization in FLM** The experiments described in Chapter 7 demonstrate that off-focus images of single Cy5 molecules with clearly visible diffraction rings and relatively high SNRs can be obtained in practice. These experiments were performed on molecules at an air/glass interface; nevertheless, similar observations were made for Cy5 molecules in water, where the SNR was diminished due to a stronger background signal. Thus, there exist no significant obstacles to implementing the proposed PSF-based 3-D localization method in FLM.

- **Super-resolved single molecule FRET** The single molecule orientation estimation accuracies reported in Chapter 7 are based on multiple images of the same molecule, and consequently lack validation against an absolute reference. We are currently investigating orientations in single molecule FRET experiments [198], where the transfer efficiency is correlated with the relative orientation between the donor and acceptor [199]. Using the setup described in Appendix D, it is possible to simultaneously record donor and acceptor fluorescence, and consequently to perform orientation estimation and FRET analysis. By labeling the 5' ends of double-stranded DNA fragments with a FRET pair such as Cy3-Cy5, the relative orientation between the two molecules can be precisely defined as a function of the number of base pairs in the fragment [200]. In addition to validating the proposed algorithm and PSF model, this method would also constitute a novel, high-precision approach to single-molecule FRET.
- **Rotational freedom in dipole orientation imaging** Single molecule orientations can be successfully measured as long as the molecule remains immobile during image acquisition. Although there exist processes where this constraint is satisfied (see, e.g., [141]), it is frequently not the case. Fluorophores typically have some rotational freedom, in which case the observed diffraction pattern only partially satisfies the dipole model. For experiments where this is observed, the steerable filter optimization could be generalized to take integration over the appropriate angles into account.
- **Sampling in FLM** Most of the signal processing efforts in FLM have so far concentrated on the localization problem, whereas the sampling aspects associated with the labeling, stochastic excitation, and imaging of fluorophores are still largely unexplored. While it can be argued that these aspects were of minor importance in early proof-of-concept experiments, where entire fluorophores populations in fixed samples were recorded, they become significant for live-cell imaging experiments [29]. It would therefore be appropriate to establish a rigorous theoretical framework for the derivation of optimal acquisition conditions in FLM that takes both localization and sampling aspects into account.
- **Parametric blind deconvolution** The reduced number of parameters in the PSF model described in Chapter 8 make it ideally suited for blind parametric deconvolution. In this context, it would be interesting to compare the performance of an approach based on this model with the formulation described in [163].

- **Shift-variant deconvolution** While the PSF model described in Chapter 8 reproduces axially shift-variant experimental measurements with high accuracy, it has not yet been implemented in a deconvolution algorithm. Few methods for shift-variant deconvolution have been proposed to date, essentially due to the high computational complexity associated with the problem. A notable approach relies on subdividing the sample space into layers within which shift-invariance is assumed, deconvolving each layer with a locally invariant PSF, and interpolating between the results [83]. This interpolation (which essentially amounts to projecting the PSF onto a fixed number of basis functions) is not exact, however, and could be a subject of further investigation for the proposed model.

Appendix A

Derivatives of the PSF models

A.1 Scalar model

In order to facilitate the notation of the derivative expressions, the PSF is rewritten as

$$h(\mathbf{x}; \mathbf{x}_p, \tau) = |I_0(\mathbf{x}; \mathbf{x}_p, \tau)|^2, \quad (\text{A.1})$$

where

$$I_0(\mathbf{x}; \mathbf{x}_p, \tau) = \int_0^\alpha B_0(\theta, \mathbf{x}; \mathbf{x}_p, \tau) d\theta, \quad (\text{A.2})$$

with

$$B_m(\theta, \mathbf{x}; \mathbf{x}_p, \tau) = e^{ik\Lambda(\theta, z; z_p, \tau)} J_m(kr n_i \sin \theta) \sin \theta \cos \theta. \quad (\text{A.3})$$

The derivatives with respect to the in-plane position x_p of the source are given by

$$\begin{aligned} \frac{\partial h}{\partial x_p} &= 2\Re\left\{ I_0^* \frac{\partial I_0}{\partial x_p} \right\} \\ \frac{\partial^2 h}{\partial x_p^2} &= 2\Re\left\{ \frac{\partial I_0^*}{\partial x_p} \frac{\partial I_0}{\partial x_p} + I_0^* \frac{\partial^2 I_0}{\partial x_p^2} \right\}, \end{aligned} \quad (\text{A.4})$$

where

$$\frac{\partial I_0}{\partial x_p} = kn_i \frac{x - x_p}{r} \int_0^\alpha B_1(\theta, \mathbf{x}; \mathbf{x}_p, \tau) \sin \theta d\theta, \quad (\text{A.5})$$

and where

$$\begin{aligned} \frac{\partial^2 I_0}{\partial x_p^2} &= kn_i \left(\frac{(x - x_p)^2}{r^3} - \frac{1}{r} \right) \int_0^\alpha B_1(\theta, \mathbf{x}; \mathbf{x}_p, \tau) \sin \theta d\theta \\ &\quad + \frac{1}{2} k^2 n_i^2 \frac{(x - x_p)^2}{r^2} \int_0^\alpha \left(B_2(\theta, \mathbf{x}; \mathbf{x}_p, \tau) - B_0(\theta, \mathbf{x}; \mathbf{x}_p, \tau) \right) \sin^2 \theta d\theta, \end{aligned} \quad (\text{A.6})$$

with analogous expressions for y_p . The partial derivatives of the phase term with respect to a component $\vartheta \in (z, z_p, \tau)$ are given by

$$\begin{aligned}\frac{\partial I_0}{\partial \vartheta} &= ik \int_0^\alpha \frac{\partial \Lambda}{\partial \vartheta} B_0(\theta, \mathbf{x}; \mathbf{x}_p, \tau) d\theta \\ \frac{\partial^2 I_0}{\partial \vartheta^2} &= ik \int_0^\alpha \left(\frac{\partial^2 \Lambda}{\partial \vartheta^2} + ik \frac{\partial \Lambda}{\partial \vartheta} \right) B_0(\theta, \mathbf{x}; \mathbf{x}_p, \tau) d\theta.\end{aligned}\tag{A.7}$$

The definition of the OPD is restated as:

$$\begin{aligned}\Lambda(\theta, z_n; z_p, \tau) &= \left(z_p - z_n + n_i \left(-\frac{z_p}{n_s} - \frac{t_g}{n_g} + \frac{t_g^*}{n_g^*} + \frac{t_i^*}{n_i^*} \right) \right) n_i \cos \theta \\ &\quad + z_p w(n_s) + t_g w(n_g) - t_g^* w(n_{g^*}) - t_i^* w(n_{i^*}),\end{aligned}\tag{A.8}$$

where

$$w(n) = \sqrt{n^2 - n_i^2 \sin^2 \theta}.\tag{A.9}$$

Its first derivatives are

$$\begin{aligned}\frac{\partial \Lambda}{\partial z_p} &= n_i \left(1 - \frac{n_i}{n_s} \right) \cos \theta + w(n_s) \\ \frac{\partial \Lambda}{\partial z_n} &= -n_i \cos \theta \\ \frac{\partial \Lambda}{\partial n_i} &= \left(z_p - z_n + 2n_i \left(-\frac{z_p}{n_s} - \frac{t_g}{n_g} + \frac{t_g^*}{n_g^*} + \frac{t_i^*}{n_i^*} \right) \right) \cos \theta \\ &\quad + n_i \sin^2 \theta \left(-\frac{z_p}{w(n_s)} - \frac{t_g}{w(n_g)} + \frac{t_g^*}{w(n_{g^*})} + \frac{t_i^*}{w(n_{i^*})} \right) \\ \frac{\partial \Lambda}{\partial n_g} &= t_g \left(\frac{n_i^2}{n_g^2} \cos \theta + \frac{n_g}{w(n_g)} \right) \\ \frac{\partial \Lambda}{\partial n_s} &= z_p \left(\frac{n_i^2}{n_s^2} \cos \theta + \frac{n_s}{w(n_s)} \right) \\ \frac{\partial \Lambda}{\partial t_g} &= -\frac{n_i^2}{n_g} \cos \theta + w(n_g),\end{aligned}\tag{A.10}$$

and the second derivatives are given by

$$\begin{aligned}
\frac{\partial^2 \Lambda}{\partial z_p^2} &= 0 \\
\frac{\partial^2 \Lambda}{\partial z_n^2} &= 0 \\
\frac{\partial^2 \Lambda}{\partial n_i^2} &= 2 \left(-\frac{z_p}{n_s} - \frac{t_g}{n_g} + \frac{t_g^*}{n_g^*} + \frac{t_i^*}{n_i^*} \right) \cos \theta \\
&\quad + \sin^2 \theta \left(-\frac{z_p}{w(n_s)} - \frac{t_g}{w(n_g)} + \frac{t_g^*}{w(n_{g^*})} + \frac{t_i^*}{w(n_{i^*})} \right) \\
&\quad + n_i^2 \sin^2 \theta \left(-\frac{z_p}{w(n_s)^3} - \frac{t_g}{w(n_g)^3} + \frac{t_g^*}{w(n_{g^*})^3} + \frac{t_i^*}{w(n_{i^*})^3} \right) \\
\frac{\partial^2 \Lambda}{\partial n_g^2} &= -t_g n_i^2 \left(\frac{2 \cos \theta}{n_g^3} + \frac{\sin^2 \theta}{w(n_g)^3} \right) \\
\frac{\partial^2 \Lambda}{\partial n_s^2} &= -z_p n_i^2 \left(\frac{2 \cos \theta}{n_s^3} + \frac{\sin^2 \theta}{w(n_s)^3} \right) \\
\frac{\partial^2 \Lambda}{\partial t_g^2} &= 0.
\end{aligned} \tag{A.11}$$

A.2 Vectorial model

The integrals involved in the calculation of the vectorial PSF model are rewritten as

$$\begin{aligned} I_0(\mathbf{x}; \mathbf{x}_p, \tau) &= \int_0^\alpha B_0(\theta, \mathbf{x}; \mathbf{x}_p, \tau) T_0(\theta; \tau) d\theta \\ I_1(\mathbf{x}; \mathbf{x}_p, \tau) &= \int_0^\alpha B_1(\theta, \mathbf{x}; \mathbf{x}_p, \tau) T_1(\theta; \tau) d\theta \\ I_2(\mathbf{x}; \mathbf{x}_p, \tau) &= \int_0^\alpha B_2(\theta, \mathbf{x}; \mathbf{x}_p, \tau) T_2(\theta; \tau) d\theta, \end{aligned} \quad (\text{A.12})$$

where

$$B_m(\theta, \mathbf{x}; \mathbf{x}_p, \tau) = \sqrt{\cos \theta} \sin \theta J_m(kr n_i \sin \theta) e^{ik\Lambda(\theta, z; z_p, \tau)}, \quad (\text{A.13})$$

and where

$$\begin{aligned} T_0(\theta; \tau) &= t_s^{(1)} t_s^{(2)} + t_p^{(1)} t_p^{(2)} \frac{1}{n_s} \sqrt{n_s^2 - n_i^2} \sin^2 \theta \\ T_1(\theta; \tau) &= t_p^{(1)} t_p^{(2)} \frac{n_i}{n_s} \sin \theta \\ T_2(\theta; \tau) &= t_s^{(1)} t_s^{(2)} - t_p^{(1)} t_p^{(2)} \frac{1}{n_s} \sqrt{n_s^2 - n_i^2} \sin^2 \theta. \end{aligned} \quad (\text{A.14})$$

The derivatives with respect to the in-plane position x_p are then accordingly given by

$$\begin{aligned} \frac{\partial I_0}{\partial x_p} &= kn_i \frac{x - x_p}{r} \int_0^\alpha B_1(\theta, \mathbf{x}; \mathbf{x}_p, \tau) T_0(\theta; \tau) \sin \theta d\theta \\ \frac{\partial I_1}{\partial x_p} &= kn_i \frac{x - x_p}{2r} \int_0^\alpha D_0(\theta, \mathbf{x}; \mathbf{x}_p, \tau) T_1(\theta; \tau) \sin \theta d\theta \\ \frac{\partial I_2}{\partial x_p} &= kn_i \frac{x - x_p}{2r} \int_0^\alpha D_1(\theta, \mathbf{x}; \mathbf{x}_p, \tau) T_2(\theta; \tau) \sin \theta d\theta, \end{aligned} \quad (\text{A.15})$$

where

$$D_m(\theta, \mathbf{x}; \mathbf{x}_p, \tau) = B_{m+2}(\theta, \mathbf{x}; \mathbf{x}_p, \tau) - B_m(\theta, \mathbf{x}; \mathbf{x}_p, \tau), \quad (\text{A.16})$$

with analogous expressions for y_p . The derivatives with respect to the axial position z_p are given by

$$\begin{aligned} \frac{\partial I_0}{\partial z_p} &= ik \int_0^\alpha \frac{\partial \Lambda(\theta, z; z_p, \tau)}{\partial z_p} B_0(\theta, \mathbf{x}; \mathbf{x}_p, \tau) T_0(\theta; \tau) d\theta \\ \frac{\partial I_1}{\partial z_p} &= ik \int_0^\alpha \frac{\partial \Lambda(\theta, z; z_p, \tau)}{\partial z_p} B_1(\theta, \mathbf{x}; \mathbf{x}_p, \tau) T_1(\theta; \tau) d\theta \\ \frac{\partial I_2}{\partial z_p} &= ik \int_0^\alpha \frac{\partial \Lambda(\theta, z; z_p, \tau)}{\partial z_p} B_2(\theta, \mathbf{x}; \mathbf{x}_p, \tau) T_2(\theta; \tau) d\theta. \end{aligned} \quad (\text{A.17})$$

Appendix B

Bessel functions

The Bessel functions of the first kind of order n can be defined through an integral representation, either as

$$J_n(z) = \frac{i^{-n}}{\pi} \int_0^\pi e^{iz \cos \phi} \cos(n\phi) d\phi, \quad (\text{B.1})$$

or as

$$J_n(z) = \frac{1}{2\pi i^n} \int_0^{2\pi} e^{iz \cos \phi} e^{in\phi} d\phi. \quad (\text{B.2})$$

These functions satisfy the following recursion properties:

$$\frac{\partial}{\partial z} J_n(z) = \frac{1}{2} (J_{n-1}(z) - J_{n+1}(z)) \quad (\text{B.3})$$

$$J_n(z) = \frac{z}{2n} (J_{n-1}(z) + J_{n+1}(z)) \quad (\text{B.4})$$

$$\frac{\partial}{\partial z} (z^{n+1} J_{n+1}(z)) = z^{n+1} J_n(z), \quad (\text{B.5})$$

which are used in the calculation of PSF derivatives. For the calculation of the Richard-Wolf integrals, the following equivalences are used:

$$\int_0^{2\pi} \cos(n\phi) e^{iz \cos(\phi-\phi_d)} d\phi = 2\pi i^n J_n(z) \cos(n\phi_d) \quad (\text{B.6})$$

$$\int_0^{2\pi} \sin(n\phi) e^{iz \cos(\phi-\phi_d)} d\phi = 2\pi i^n J_n(z) \sin(n\phi_d). \quad (\text{B.7})$$

The particular cases of these expressions involved in the formulation of PSF models are given by

$$\begin{aligned}
 \int_0^{2\pi} e^{iz \cos(\phi - \phi_p)} d\phi &= 2\pi J_0(z) \\
 \int_0^{2\pi} \sin(\phi) e^{iz \cos(\phi - \phi_d)} d\phi &= 2\pi i J_1(z) \sin(\phi_d) \\
 \int_0^{2\pi} \cos(\phi) e^{iz \cos(\phi - \phi_d)} d\phi &= 2\pi i J_1(z) \cos(\phi_d) \\
 \int_0^{2\pi} \sin(2\phi) e^{iz \cos(\phi - \phi_d)} d\phi &= -2\pi J_2(z) \sin(2\phi_d) \\
 \int_0^{2\pi} \cos(2\phi) e^{iz \cos(\phi - \phi_d)} d\phi &= -2\pi J_2(z) \cos(2\phi_d) \\
 \int_0^{2\pi} \sin^2(\phi) e^{iz \cos(\phi - \phi_d)} d\phi &= \pi (J_0(z) + \cos(2\phi_d) J_2(z)) \\
 \int_0^{2\pi} \cos^2(\phi) e^{iz \cos(\phi - \phi_d)} d\phi &= \pi (J_0(z) - \cos(2\phi_d) J_2(z)).
 \end{aligned} \tag{B.8}$$

Appendix C

Dipole model

C.1 Quartic equations for orientation estimation

The orientation parameters θ_p and ϕ_p are estimated by iteratively solving the two sets of quartic equations given below. The solution for θ_p is obtained by solving

$$\begin{aligned}
 & \tan^4 \theta_p (f_{13} \cos(\phi_p) + f_{23} \sin(\phi_p) - Ae_{12}) \\
 & + \tan^3 \theta_p (f_{33} - (f_{11} \cos(\phi_p)^2 + f_{12} \sin(2\phi_p) + f_{22} \sin(\phi_p)^2) \\
 & \quad + A(e_{11} - e_{13} - 2e_{22})) \\
 & + 3 \tan^2 \theta_p A(e_{12} - e_{23}) \\
 & + \tan \theta_p (f_{33} - (f_{11} \cos(\phi_p)^2 + f_{12} \sin(2\phi_p) + f_{22} \sin(\phi_p)^2) \\
 & \quad + A(e_{13} - e_{33} + 2e_{22})) \\
 & - (f_{13} \cos(\phi_p) + f_{23} \sin(\phi_p) - Ae_{23}) \\
 & = 0
 \end{aligned} \tag{C.1}$$

for $\tan \theta_p$, where $[\mathbf{E}]_{ij} = e_{ij}$. Similarly, the solution for ϕ_p is obtained by solving

$$\begin{aligned}
 & \tan^4 \phi_p (f_{12}^2 \sin^2 \theta_p - f_{13}^2 \cos^2 \theta_p) \\
 & + \tan^3 \phi_p (f_{13} f_{23} \cos^2 \theta_p + f_{12} (m_{11} - f_{22}) \sin^2 \theta_p) \\
 & + \tan^2 \phi_p (((f_{11} - f_{22})^2 - 2f_{12}^2) \sin^2 \theta_p - (f_{13}^2 + f_{23}^2) \cos^2 \theta_p) \\
 & + \tan \phi_p (f_{13} f_{23} \cos^2 \theta_p - f_{12} (f_{11} - f_{22}) \sin^2 \theta_p) \\
 & + f_{12}^2 \sin^2 \theta_p - f_{23}^2 \cos^2 \theta_p \\
 & = 0
 \end{aligned} \tag{C.2}$$

for $\tan \phi_p$, where $[\mathbf{M}_f]_{ij} = f_{ij}$.

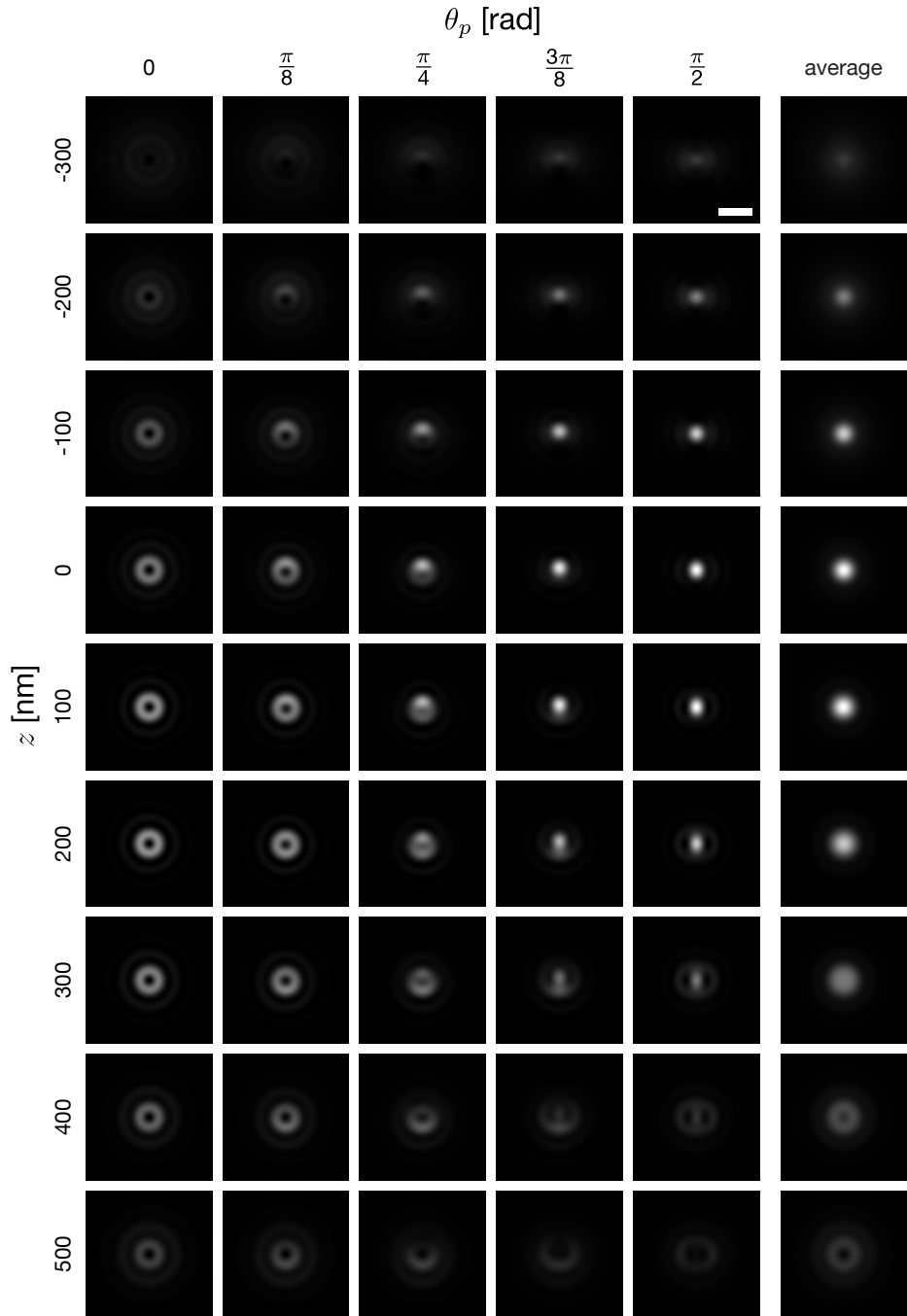


Figure C.1 Intensity distribution generated by a Cy3 dipole ($\lambda = 565$ nm) at an air/glass interface for different values of θ_p and z , imaged with a $100\times$, 1.45 NA objective. The radial angle is fixed at $\phi_p = 0$. The intensities are normalized across every focus value z . Every row, as well as planar rotations of each pattern, can be generated using six unique templates. Scale bar: 500 nm.

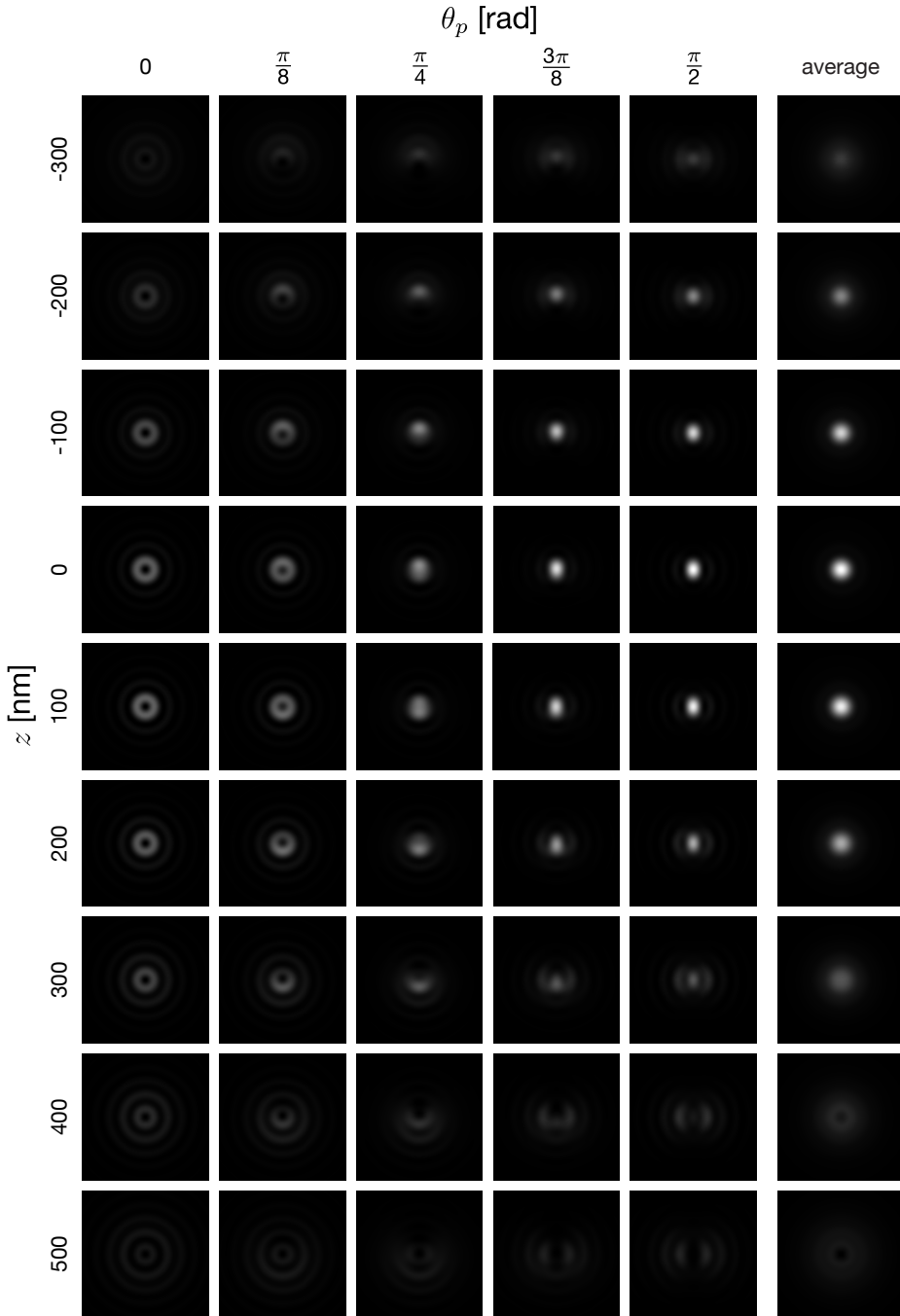


Figure C.2 Intensity distribution generated by a Cy3 dipole ($\lambda = 565$ nm) at a water/glass interface for different values of θ_p and z , imaged with a $100\times$, 1.45 NA objective. The radial angle is fixed at $\phi_p = 0$. The intensities are normalized across every focus value z . Every row, as well as planar rotations of each pattern, can be generated using six unique templates. Scale bar: 500 nm.

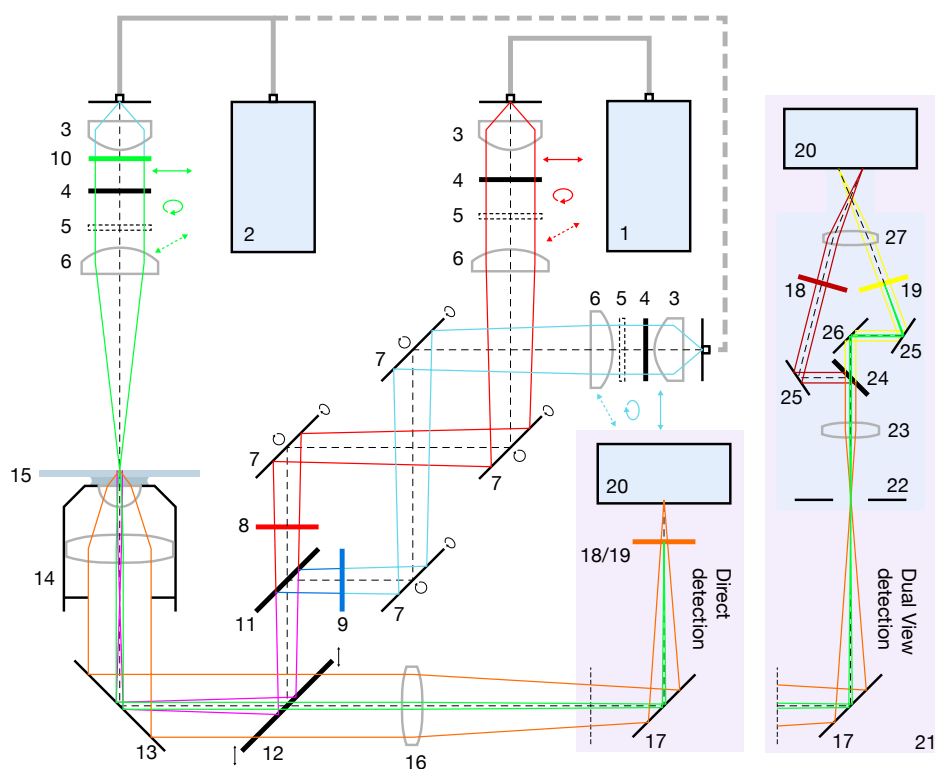
C.2 Derivatives of the dipole model

The partial derivatives involved in the evaluation of the Fisher information matrix and in the localization algorithm are

$$\begin{aligned}
 \frac{\partial h_{\theta_p, \phi_p}}{\partial x_p} &= \sin^2 \theta_p \left(2\Re\left\{ I_0^* \frac{\partial I_0}{\partial x_p} + I_2^* \frac{\partial I_2}{\partial x_p} \right\} \right. \\
 &\quad \left. + 2 \cos(2\phi_p - 2\phi_d) \Re\left\{ I_0^* \frac{\partial I_2}{\partial x_p} + I_2^* \frac{\partial I_0}{\partial x_p} \right\} \right) \\
 &\quad - 2 \sin(2\theta_p) \cos(\phi_p - \phi_d) \Im\left\{ I_1^* \left(\frac{\partial I_0}{\partial x_p} + \frac{\partial I_2}{\partial x_p} \right) - \frac{\partial I_1}{\partial x_p} (I_0^* + I_2^*) \right\} \\
 &\quad + 8 \cos^2 \theta_p \Re\left\{ I_1^* \frac{\partial I_1}{\partial x_p} \right\} \\
 \frac{\partial h_{\theta_p, \phi_p}}{\partial \theta_p} &= \sin 2\theta_p \left(|I_0|^2 + |I_2|^2 + 2 \cos(2\phi_p - 2\phi_d) \Re\{ I_0^* I_2 \} - 4 |I_1|^2 \right) \\
 &\quad - 4 \cos(2\theta_p) \cos(\phi_p - \phi_d) \Im\{ I_1^* (I_0 + I_2) \} \\
 \frac{\partial h_{\theta_p, \phi_p}}{\partial \phi_p} &= -4 \sin^2 \theta_p \sin(2\phi_p - 2\phi_d) \Re\{ I_0^* I_2 \} \\
 &\quad + 2 \sin(2\theta_p) \sin(\phi_p - \phi_d) \Im\{ I_1^* (I_0 + I_2) \}.
 \end{aligned} \tag{C.3}$$

Appendix D

Dipole imaging setup



- | | | |
|--------------------------------|-------------------------------------|--------------------------------|
| 1. Sepia II ps Laser, 635 nm | 10. Excitation filter, 515FS10-25mm | 19. Emission filter, HQ585/40m |
| 2. Ar+ Laser, 514/488 nm | 11. Combiner, z488bcm | 20. Andor Luca EMCCD |
| 3. Collimation lens | 12. Dichroic mirror, z470/635rpc | 21. Optical Insights Dual-View |
| 4. Quarter-wave plate | 13. Fixed mirror | 22. Adjustable aperture |
| 5. Optional polarizer | 14. Objective, 100x 1.45NA oil | 23. Collimation lens |
| 6. Focusing lens | 15. Sample | 24. Dichroic mirror, 585lp |
| 7. Adjustable mirror | 16. Tube lens | 25. Adjustable mirror |
| 8. Excitation filter, z635/20x | 17. Fixed mirror | 26. Fixed mirror |
| 9. Excitation filter, z488/20x | 18. Emission filter, HHQ710/100m | 27. Imaging lens |

Acknowledgements

This thesis would not have been possible without the help and input of many people. To begin, I would like to thank my thesis advisor, Prof. Michael Unser, for having convinced me to join his group and stay at EPFL, for the research topics he proposed to me and the freedom he has given me in exploring them, and for his many insights at crucial moments.

Likewise, this work could not have started without the help of Prof. Dimitri Van De Ville, who assisted me in exploring the intricacies of microscopy and optics at the beginning of the project. I thank him for his dedication and constant willingness to help.

The work on dipole imaging is the result of a fruitful collaboration with the group of Prof. Theo Lasser, whom I thank for his interest and many insightful discussions. I would like to thank Stefan, who worked with me during his semester and MSc projects, for his commitment, as well as other members of the Biomedical Optics Group with whom I've had the pleasure to collaborate: Iwan, Noelia, Claudio, and Marcel.

I thank Nathalie Garin and Floyd at the BioImaging and Optics platform who were of great help with the preparation of samples, and also extend my thanks to Boris Zarda, who helped me with the acquisition of PSF measurements. I am also grateful to Dr. Rainer Heintzmann and Prof. Christian Depeursinge for their insights.

I thank Prof. René Salathé, Dr. Suliana Manley, and Prof. Jean-Christophe Olivo-Marin for accepting to be on my thesis committee, and for their pertinent comments and feedback.

My years at BIG would never have been the same without my fellow PhD students: my office mates, Kunal and Ricard (and former office mates Amardeep, Vijay, and Rajesh), Matthieu, Djano, Jean-Charles, Pouya, Florian, Sathish, Cédric, Ildar, Aurélien, and former PhD students Michael and Mathews, as well as other fellow lab members: Chandra, Kai, Daniel, Philippe, Thierry, and Manuelle.

Finally, my deep gratitude goes to my family, who were always very supportive and enthusiastic. I thank them for everything.

Bibliography

- [1] E. Abbe, "Beiträge zur Theorie des Mikroskops und der mikroskopischen Wahrnehmung," *Arch. Mikr. Anat.*, vol. 9, pp. 413–468, 1873.
- [2] M. Minsky, "U.S. Patent no. 3013467. Microscopy apparatus," dec. 19, 1961 (Filed Nov. 7, 1957).
- [3] W. Denk, J. H. Strickler, and W. W. Webb, "Two-photon laser scanning fluorescence microscopy," *Science*, vol. 248, no. 4951, pp. 73–76, April 1990.
- [4] S. W. Hell and E. H. K. Stelzer, "Fundamental improvement of resolution with a 4pi-confocal fluorescence microscope using two-photon excitation," *Opt. Commun.*, vol. 93, pp. 277–282, 1992.
- [5] S. W. Hell and J. Wichmann, "Breaking the diffraction resolution limit by stimulated emission: stimulated-emission-depletion fluorescence microscopy," *Opt. Lett.*, vol. 19, no. 11, pp. 780–782, 1994.
- [6] R. Schmidt, C. A. Wurm, S. Jakobs, E. J., A. Egner, and S. W. Hell, "Spherical nanosized focal spot unravels the interior of cells," *Nat. Methods*, vol. 5, no. 6, pp. 529–544, 2008.
- [7] D. A. Agard and J. W. Sedat, "Three-dimensional architecture of a polytene nucleus," *Nature*, vol. 302, no. 5910, pp. 676–681, April 1983.
- [8] R. Heintzmann and C. Cremer, "Laterally modulated excitation microscopy: improvement of resolution by using a diffraction grating," in *Proc. SPIE*, vol. 3568, 1999, pp. 185–196.
- [9] M. G. L. Gustafsson, D. A. Agard, and J. W. Sedat, "T⁵M: 3D widefield light microscopy with better than 100nm axial resolution," *J. Microsc.*, vol. 195, pp. 10–16, 1999.
- [10] L. Shao, B. Isaac, S. Uzawa, D. A. Agard, J. W. Sedat, and M. G. L. Gustafsson, "T⁵S: Wide-field light microscopy with 100-nm-scale resolution in three dimensions," *Biophys. J.*, vol. 94, no. 12, pp. 4971–4983, 2008.
- [11] L. Schermelleh, P. M. Carlton, S. Haase, L. Shao, L. Winoto, P. Kner, B. Burke, M. C. Cardoso, D. A. Agard, M. G. L. Gustafsson, H. Leonhardt, and J. W. Sedat, "Subdiffraction multicolor imaging of the nuclear periphery with 3D structured illumination microscopy," *Science*, vol. 320, pp. 1332–1336, 2008.
- [12] N. Bobroff, "Position measurement with a resolution and noise-limited instrument," *Rev. Sci. Instrum.*, vol. 57, pp. 1152–1157, 1986.
- [13] M. K. Cheezum, W. F. Walker, and W. H. Guilford, "Quantitative comparison of algorithms for tracking single fluorescent particles," *Biophys. J.*, vol. 81, no. 4, pp. 2378–2388, 2001.
- [14] D. Thomann, D. R. Rines, P. K. Sorger, and G. Danuser, "Automatic fluorescent tag detection in 3D with super-resolution: application to the analysis of chromosome movement," *J. Microsc.*, vol. 208, no. 1, pp. 49–64, 2002.
- [15] E. Meijering, I. Smal, and G. Danuser, "Tracking in molecular bioimaging," *IEEE Signal Processing Magazine*, vol. 23, no. 3, pp. 46–53, 2006.

- [16] A. Yildiz, J. N. Forkey, S. A. McKinney, H. Taekjip, Y. E. Goldman, and P. R. Selvin, "Myosin V walks hand-over-hand: Single fluorophore imaging with 1.5-nm localization," *Science*, vol. 300, pp. 2061–2065, 2003.
- [17] R. E. Thompson, D. R. Larson, and W. W. Webb, "Precise nanometer localization analysis for individual fluorescent probes," *Biophys. J.*, vol. 82, no. 5, pp. 2775–2783, 2002.
- [18] R. J. Ober, S. Ram, and S. Ward, "Localization accuracy in single-molecule microscopy," *Biophys. J.*, vol. 86, pp. 1185–1200, 2004.
- [19] G. H. Patterson and J. Lippincott-Schwartz, "A photoactivatable GFP for selective photolabeling of proteins and cells," *Science*, vol. 297, no. 5588, pp. 1873–1877, September 2002.
- [20] M. Bates, T. R. Blosser, and X. Zhuang, "Short-range spectroscopic ruler based on a single-molecule optical switch," *Phys. Rev. Lett.*, vol. 94, no. 10, pp. 108 101(1–4), 2005.
- [21] E. Betzig, G. H. Patterson, R. Sougrat, O. W. Lindwasser, S. Olenych, J. S. Bonifacio, M. W. Davidson, J. Lippincott-Schwartz, and H. F. Hess, "Imaging intracellular fluorescent proteins at nanometer resolution," *Science*, vol. 313, pp. 1642–1645, 2006.
- [22] S. T. Hess, T. P. K. Girirajan, and M. D. Mason, "Ultra-high resolution imaging by fluorescence photoactivation localization microscopy," *Biophys. J.*, vol. 91, no. 11, pp. 4258–4272, 2006.
- [23] M. J. Rust, M. Bates, and X. Zhuang, "Sub-diffraction-limit imaging by stochastic optical reconstruction microscopy (STORM)," *Nat. Methods*, vol. 3, no. 10, pp. 793–795, 2006.
- [24] K. A. Lidke, B. Rieger, T. M. Jovin, and R. Heintzmann, "Superresolution by localization of quantum dots using blinking statistics," *Opt. Express*, vol. 13, no. 18, pp. 7052–7062, 2005.
- [25] G. Shtengel, J. A. Galbraith, C. G. Galbraith, J. Lippincott-Schwartz, J. M. Gillette, S. Manley, R. Sougrat, C. M. Waterman, P. Kanchanawong, M. W. Davidson, R. D. Fetter, and H. F. Hess, "Interferometric fluorescent super-resolution microscopy resolves 3D cellular ultrastructure," *Proc. Natl. Acad. Sci. USA*, vol. 106, no. 9, pp. 3125–3130, 2009.
- [26] B. Huang, W. Wang, M. Bates, and X. Zhuang, "Three-dimensional super-resolution imaging by stochastic optical reconstruction microscopy," *Science*, vol. 319, pp. 810–813, 2008.
- [27] M. F. Juetten, T. J. Gould, M. D. Lessard, M. J. Mlodzianoski, B. S. Nagpure, B. T. Bennett, S. T. Hess, and J. Bewersdorf, "Three-dimensional sub-100 nm resolution fluorescence microscopy of thick samples," *Nat. Methods*, vol. 5, no. 6, pp. 527–529, 2008.
- [28] G. Geisler, A. Schönle, C. von Middendorff, H. Bock, E. C., A. Egner, and S. W. Hell, "Resolution of $\lambda/10$ in fluorescence microscopy using fast single molecule photo-switching," *Appl. Phys. A*, vol. 88, pp. 223–226, 2007.
- [29] H. Shroff, C. G. Galbraith, J. A. Galbraith, and E. Betzig, "Live-cell photoactivated localization microscopy of nanoscale adhesions," *Nat. Methods*, vol. 5, no. 5, pp. 417–423, 2008.
- [30] S. W. Hell, "European patent no. EP0491289. Double-confocal scanning microscope," June 24, 1992 (Filed December 18, 1990).
- [31] Lord Rayleigh, "On the theory of optical images, with special reference to the microscope," *Philos. Mag.*, vol. 42, pp. 167–195, 1896.
- [32] A. C. Stiel, M. Andresen, H. Bock, M. Hilbert, J. Schilde, A. Schönle, C. Eggeling, A. Egner, S. W. Hell, and S. Jakobs, "Generation of monomeric reversibly switchable red fluorescent proteins for far-field fluorescence nanoscopy," *Biophys. J.*, vol. 95, no. 6, pp. 2989–2997, 2008.
- [33] F. V. Subach, G. H. Patterson, S. Manley, J. M. Gillette, J. Lippincott-Schwartz, and V. V. Verkhusha, "Photoactivatable mCherry for high-resolution two-color fluorescence microscopy," *Nat. Methods*, vol. 6, no. 2, pp. 153–159, 2009.

- [34] M. Heilemann, S. van de Linde, M. Schüttelpelz, R. Kasper, B. Seefeldt, A. Mukherjee, P. Tinnefeld, and M. Sauer, "Subdiffraction-resolution fluorescence imaging with conventional fluorescent probes," *Angew. Chem.*, vol. 47, pp. 6172–6176, 2008.
- [35] M. Bates, B. Huang, G. T. Dempsey, and X. Zhuang, "Multicolor super-resolution imaging with photo-switchable probes," *Science*, vol. 317, pp. 1749–1753, 2007.
- [36] H. Bock, G. Geisler, C. A. Wurm, C. von Middendorff, S. Jakobs, A. Schönle, A. Egner, S. W. Hell, and C. Eggeling, "Two-color far-field fluorescence nanoscopy based on photo-switchable emitters," *Appl. Phys. B*, vol. 88, pp. 161–165, 2007.
- [37] H. Shroff, C. G. Galbraith, J. A. Galbraith, H. White, J. Gillette, S. Olenych, M. W. Davidson, and E. Betzig, "Dual-color superresolution imaging of genetically expressed probes within individual adhesion complexes," *Proc. Natl. Acad. Sci. USA*, vol. 104, no. 51, pp. 20 308–20 313, 2007.
- [38] H. P. Kao and A. S. Verkman, "Tracking of single fluorescent particles in three dimensions: Use of cylindrical optics to encode particle position," *Biophys. J.*, vol. 67, pp. 1291–1300, 1994.
- [39] T. J. Gould, M. S. Gunewardene, M. V. Gudheti, V. V. Verkhusha, S.-R. Yin, J. A. Gosse, and S. T. Hess, "Nanoscale imaging of molecular positions and anisotropies," *Nat. Methods*, vol. 5, no. 12, pp. 1027–1030, 2008.
- [40] S. Manley, J. M. Gillette, G. H. Patterson, H. Shroff, H. F. Hess, E. Betzig, and J. Lippincott-Schwartz, "High-density mapping of single-molecule trajectories with photoactivated localization microscopy," *Nat. Methods*, vol. 5, no. 2, pp. 155–157, 2008.
- [41] J. S. Biteen, M. A. Thompson, N. K. Tselentis, G. R. Bowman, L. Shapiro, and W. E. Moerner, "Super-resolution imaging in live *Caulobacter crescentus* cells using photo-switchable EYFP," *Nat. Methods*, vol. 5, no. 11, pp. 947–949, 2008.
- [42] M. Speidel and E.-L. Jonas, A. and Florin, "Three-dimensional tracking of fluorescent nanoparticles with subnanometer precision by use of off-focus imaging," *Opt. Lett.*, vol. 28, no. 2, pp. 69–71, 2003.
- [43] J. Enderlein, E. Toprak, and P. R. Selvin, "Polarization effect on position accuracy of fluorophore localization," *Opt. Express*, vol. 14, no. 18, pp. 8111–8120, 2006.
- [44] F. Aguet, D. Van De Ville, and M. Unser, "A maximum-likelihood formalism for sub-resolution axial localization of fluorescent nanoparticles," *Opt. Express*, vol. 13, no. 26, pp. 10 503–10 522, 2005.
- [45] F. Aguet, S. Geissbühler, I. Märki, T. Lasser, and M. Unser, "Super-resolution orientation estimation and localization of fluorescent dipoles using 3-D steerable filters," *Opt. Express*, vol. 17, no. 8, pp. 6829–6848, 2009.
- [46] F. Aguet, D. Van De Ville, and M. Unser, "An accurate PSF with few parameters for axially shift-variant deconvolution," in *Proc. 5th IEEE Int. Symp. Biomedical Imaging*, 2008, pp. 157–160.
- [47] —, "Model-based 2.5-D deconvolution for extended depth of field in brightfield microscopy," *IEEE Trans. Image Process.*, vol. 17, no. 7, pp. 1144–1153, 2008.
- [48] F. Aguet, C. Vonesch, J.-L. Vonesch, and M. Unser, "An introduction to fluorescence microscopy: basic principles, challenges, and opportunities," in *Microscopic Image Analysis for Life Science Applications*, J. Rittscher, R. Machiraju, and S. T. C. Wong, Eds. Artech House, 2008, ch. 4, pp. 85–114.
- [49] C. Vonesch, F. Aguet, J.-L. Vonesch, and M. Unser, "The colored revolution of bioimaging," *IEEE Sig. Proc. Mag.*, vol. 23, no. 3, pp. 20–31, 2006.
- [50] A. H. Coons and M. H. Kaplan, "Localization of antigen in tissue cells. II. Improvements in a method for the detection of antigen by means of fluorescent antibody," *Journal of Experimental Medicine*, vol. 91, no. 1, pp. 1–13, 1950.
- [51] M. Chalfie, Y. Tu, G. Euskirchen, W. Ward, and D. C. Prasher, "Green fluorescent protein as a marker for gene expression," *Science*, vol. 263, no. 5148, pp. 802–805, February 1994.

- [52] A. Einstein, "Über einen die Erzeugung und Verwandlung des Lichtes betreffenden heuristischen Gesichtspunkt," *Annalen der Physik*, vol. 17, pp. 132-148, 1905.
- [53] P. Ellinger and A. Hirt, "Eine methode zur beobachtung lebender organe mit stärkster vergrößerung im fluoreszenzlicht," *Handbuch der biologischen Arbeitsmethoden*, vol. 5, no. 2, pp. 1754-1764, 1929.
- [54] H. Iams and B. Salzberg, "The secondary emission phototube," *Proceedings of the IRE*, vol. 23, no. 1, pp. 55-64, January 1935.
- [55] T. Förster, "Zwischenmolekulare energiewanderung und fluoreszenz," *Annalen der Physik*, vol. 6, no. 2, pp. 55-75, 1948.
- [56] A. L. Schawlow and C. H. Townes, "Infrared and optical masers," *Phys. Rev.*, vol. 112, no. 6, pp. 1940-1949, 1958.
- [57] T. H. Maiman, "Stimulated optical radiation in ruby," *Nature*, vol. 187, no. 4736, pp. 493-494, August 1960.
- [58] O. Shimomura, F. H. Johnson, and Y. Saiga, "Extraction, purification and properties of aequorin, a bioluminescent protein from the luminous hydromedusa, *aequorea*," *J. Cell. Comp. Physiol.*, vol. 59, pp. 223-239, 1962.
- [59] C. J. R. Sheppard and R. Kompfner, "Resonant scanning optical microscope," *Appl. Opt.*, vol. 17, no. 18, pp. 2879-2882, September 1978.
- [60] J. G. J. Baumann, J. Wiegant, P. Borst, and P. van Duijn, "A new method for fluorescence microscopical localization of specific dna sequences by in situ hybridization of fluorochrome-labelled rna," *Experimental Cell Research*, vol. 128, no. 2, pp. 485-490, August 1980.
- [61] J. R. Lakowicz, H. Szmajda, K. Nowaczyk, K. W. Berndt, and M. Johnson, "Fluorescence lifetime imaging," *Analytical Biochemistry*, vol. 202, no. 2, pp. 316-330, May 1992.
- [62] S. Inoué and F. I. Tsuji, "Aequorea green fluorescent protein. Expression of the gene and fluorescence characteristics of the recombinant protein," *FEBS Letters*, vol. 341, no. 2-3, pp. 277-280, March 1994.
- [63] T. Stearns, "Green fluorescent protein. the green revolution," *Current Biology*, vol. 5, no. 3, pp. 262-264, March 1995.
- [64] O. Shimomura, "The discovery of aequorin and green fluorescent protein," *J. Microsc.*, vol. 217, no. 1, pp. 3-15, January 2005.
- [65] D. C. Prasher, V. K. Eckenrode, W. W. Ward, F. G. Prendergast, and M. J. Cormier, "Primary structure of the Aequorea victoria green-fluorescent protein," *Gene*, vol. 111, no. 2, pp. 229-233, February 1992.
- [66] J. Zhang, R. E. Campbell, A. Y. Ting, and R. Y. Tsien, "Creating new fluorescent probes for cell biology," *Nature Reviews Molecular Cell Biology*, vol. 3, no. 12, pp. 906-918, December 2002.
- [67] J. Lippincott-Schwartz and G. H. Patterson, "Development and use of fluorescent protein markers in living cells," *Science*, vol. 300, no. 5616, pp. 87-91, April 2003.
- [68] A. Miyawaki, A. Sawano, and T. Kogure, "Lighting up cells: labelling proteins with fluorophores," *Nature Cell Biology*, vol. 5 (supplement), pp. S1-S7, September 2003.
- [69] M. Minsky, "Memoir on inventing the confocal scanning microscope," *Scanning*, vol. 10, no. 4, pp. 128-138, August 1988.
- [70] P. R. Norton, *Handbook of Optics*. McGraw-Hill, 1995, vol. 1, ch. Photodetectors, pp. 15.3-15.100.
- [71] S. F. Gibson and F. Lanni, "Experimental test of an analytical model of aberration in an oil-immersion objective lens used in three-dimensional light microscopy," *J. Opt. Soc. Am. A*, vol. 8, no. 10, pp. 1601-1613, 1991.
- [72] W. S. Boyle and G. E. Smith, "Charge coupled semiconductor devices," *Bell System Technical Journal*, vol. 49, no. 4, pp. 587-593, April 1970.
- [73] J. E. Wampler and K. Kutz, "Quantitative fluorescence microscopy using photomultiplier tubes and imaging detectors," *Methods Cell Biol.*, vol. 29, pp. 239-67, 1989.

- [74] J. Lippincott-Schwartz, A.-B. Nihal, and G. H. Patterson, "Photobleaching and photoactivation: following protein dynamics in living cells," *Nature Cell Biology*, vol. 5, no. 9, pp. Suppl:S7–S14, September 2003.
- [75] P. Selvin, "The renaissance of fluorescence resonance energy transfer," *Nature Structural Biology*, vol. 7, no. 9, pp. 730–734, 2000.
- [76] L. McMahon, R. Legouis, J.-L. Vonesch, and M. Labouesse, "Assembly of *C. elegans* apical junctions involves positioning and compaction by LET-413 and protein aggregation by the MAGUK protein DLG-1," *Journal of Cell Science*, vol. 114, no. 12, pp. 2265–2277, June 2001.
- [77] M. Jacob and M. Unser, "Design of steerable filters for feature detection using Canny-like criteria," *IEEE Trans. Pattern Anal. Mach. Intell.*, vol. 26, no. 8, pp. 1007–1019, August 2004.
- [78] D. Sage, F. R. Neumann, F. Hediger, S. M. Gasser, and M. Unser, "Automatic tracking of individual fluorescence particles: Application to the study of chromosome dynamics," *IEEE Transactions on Image Processing*, vol. 14, no. 9, pp. 1372–1383, 2005.
- [79] J.-C. Olivo-Marin, "Extraction of spots in biological images using multiscale products," *Pattern Recognition*, vol. 35, no. 9, pp. 1989–1996, September 2002.
- [80] J. Boutet de Monvel, S. Le Calvez, and M. Ulfendahl, "Image restoration for confocal microscopy: Improving the limits of deconvolution, with application to the visualization of the mammalian hearing organ," *Biophys. J.*, vol. 80, no. 5, pp. 2455–2470, May 2001.
- [81] J.-B. Sibarita, "Deconvolution microscopy," *Advances in Biochemical Engineering/Biotechnology*, vol. 95, pp. 201–243, May 2005.
- [82] W. Wallace, L. H. Schaefer, and J. R. Swedlow, "A workingperson's guide to deconvolution in light microscopy," *Biotechniques*, vol. 31, no. 5, pp. 1076–1097, November 2001.
- [83] C. Preza and J.-A. Conchello, "Depth-variant maximum-likelihood restoration for three-dimensional fluorescence microscopy," *J. Opt. Soc. Am. A*, vol. 21, no. 9, pp. 1593–1601, 2004.
- [84] B. Forster, D. Van De Ville, J. Berent, D. Sage, and M. Unser, "Complex wavelets for extended depth-of-field: A new method for the fusion of multichannel microscopy images," *Microsc. Res. Tech.*, vol. 65, pp. 33–42, 2004.
- [85] D. Thomann, J. Dorn, P. K. Sorger, and G. Danuser, "Automatic fluorescent tag localization II: Improvement in super-resolution by relative tracking," *J. Microsc.*, vol. 211, no. 3, pp. 230–248, September 2003.
- [86] L. G. Brown, "A survey of image registration techniques," *ACM Comput. Surv.*, vol. 24, pp. 325–376, 1992.
- [87] P. Thévenaz and M. Unser, "User-friendly semiautomated assembly of accurate image mosaics in microscopy," *Microscopy Research and Technique*, vol. 70, no. 2, pp. 135–146, 2007.
- [88] C. Ó. Sánchez Sorzano, P. Thévenaz, and M. Unser, "Elastic registration of biological images using vector-spline regularization," *IEEE Transactions on Biomedical Engineering*, vol. 52, no. 4, pp. 652–663, April 2005.
- [89] M. Liebling, A. S. Forouhar, M. Gharib, S. E. Fraser, and M. E. Dickinson, "Four-dimensional cardiac imaging in living embryos via postacquisition synchronization of nongated slice sequences," *J. Biomed. Opt.*, vol. 10, no. 5, pp. 054 001–(1–10), 2005.
- [90] C. Zimmer, E. Labruyere, V. Meas-Yedid, N. Guillen, and J.-C. Olivo-Marin, "Segmentation and tracking of migrating cells in videomicroscopy with parametric active contours: a tool for cell-based drug testing," *IEEE Transactions on Medical Imaging*, vol. 21, no. 10, pp. 1212–1221, October 2002.
- [91] E. Meijering, M. Jacob, J.-C. F. Sarria, P. Steiner, H. Hirling, and M. Unser, "Design and validation of a tool for neurite tracing and analysis in fluorescence microscopy images," *Cytometry A*, vol. 58A, no. 2, pp. 167–176, April 2004.

- [92] T. Zimmermann, J. Rietdorf, and R. Pepperkok, "Spectral imaging and its applications in live cell microscopy," *FEBS Letters*, vol. 546, no. 1, pp. 87–92, July 2003.
- [93] H. Tsurui, H. Nishimura, S. Hattori, S. Hirose, K. Okumura, and T. Shirai, "Seven-color fluorescence imaging of tissue samples based on Fourier spectroscopy and singular value decomposition," *Journal of Histochemistry and Cytochemistry*, vol. 48, no. 5, pp. 653–662, May 2000.
- [94] G. Carrero, D. McDonald, E. Crawford, G. de Vries, and M. J. Hendzel, "Using FRAP and mathematical modeling to determine the in vivo kinetics of nuclear proteins," *Methods*, vol. 29, no. 1, pp. 14–28, January 2003.
- [95] C. Zimmer, B. Zhang, A. Dufour, A. Thébaud, S. Berlemont, V. Meas-Yedid, and J.-C. Olivo-Marin, "On the digital trail of mobile cells," *IEEE Signal Processing Magazine*, vol. 23, no. 3, pp. 54–62, 2006.
- [96] X. Zhou and S. T. C. Wong, "Informatics challenges of high-throughput microscopy," *IEEE Signal Processing Magazine*, vol. 23, no. 3, pp. 63–72, 2006.
- [97] X. Michalet, F. F. Pinaud, L. A. Bentolila, J. M. Tsay, S. Doose, J. J. Li, G. Sundaresan, A. M. Wu, S. S. Gambhir, and S. Weiss, "Quantum dots for live cells, in vivo imaging, and diagnostics," *Science*, vol. 307, no. 5709, pp. 538–544, January 2005.
- [98] B. Dubertret, P. Skourides, D. J. Norris, V. Noireaux, A. H. Brivanlou, and A. Libchaber, "In vivo imaging of quantum dots encapsulated in phospholipid micelles," *Science*, vol. 298, pp. 1759–1762, 2002.
- [99] B. A. Griffin, S. R. Adams, and R. Y. Tsien, "Specific covalent labeling of recombinant protein molecules inside live cells," *Science*, vol. 281, no. 5374, pp. 269–272, July 1998.
- [100] J. S. Marchant, G. E. Stutzmann, M. A. Leissring, F. M. LaFerla, and I. Parker, "Multiphoton-evoked color change of DsRed as an optical highlighter for cellular and subcellular labeling," *Nat. Biotechnol.*, vol. 19, no. 7, pp. 645–649, July 2001.
- [101] R. Ando, H. Hama, M. Yamamoto-Hino, H. Mizuno, and A. Miyawaki, "An optical marker based on the UV-induced green-to-red photoconversion of a fluorescent protein," *Proceedings of the National Academy of Sciences*, vol. 99, no. 20, pp. 12 657–12 662, October 2002.
- [102] D. M. Chudakov, V. V. Verkhusha, D. B. Staroverov, E. A. Souslova, S. Lukyanov, and K. A. Lukyanov, "Photoswitchable cyan fluorescent protein for protein tracking," *Nat. Biotechnol.*, vol. 22, no. 11, pp. 1435–1439, November 2004.
- [103] M. Petráň, M. Hadravský, M. Egger, and R. Galambos, "Tandem-scanning reflected-light microscope," *J. Opt. Soc. Am. A*, vol. 58, no. 5, pp. 661–664, 1968.
- [104] D. Axelrod, "Cell-substrate contacts illuminated by total internal reflection fluorescence," *J. Cell Biol.*, vol. 89, no. 1, pp. 141–145, 1981.
- [105] —, "Total internal reflection fluorescence microscopy in cell biology," *Traffic*, vol. 2, no. 11, pp. 764–774, 2001.
- [106] R. Heintzmann, T. M. Jovin, and C. Cremer, "Saturated patterned excitation microscopy (SPEM) - a novel concept for optical resolution improvement," *Journal of the Optical Society of America A*, vol. 19, no. 8, pp. 1599–1609, August 2002.
- [107] J. Mitic, T. Anhut, M. Meier, M. Ducros, A. Serov, and T. Lasser, "Optical sectioning in wide-field microscopy obtained by dynamic structured light illumination and detection based on a smart pixel detector array," *Optics Letters*, vol. 28, no. 9, pp. 698–700, May 2003.
- [108] J. Huisken, J. Swoger, F. Del Bene, J. Wittbrodt, and E. H. Stelzer, "Optical sectioning deep inside live embryos by selective plane illumination microscopy," *Science*, vol. 305, no. 5686, pp. 1007–1009, August 2004.
- [109] O. Haeberlé, "Focusing of light through a stratified medium: a practical approach for computing microscope point spread functions. Part I: Conventional microscopy," *Opt. Commun.*, vol. 216, pp. 55–63, 2003.

- [110] E. Wolf, "Electromagnetic diffraction in optical systems. I. an integral representation of the image field," *Proc. R. Soc. London A*, vol. 253, no. 1274, pp. 349–357, 1959.
- [111] B. Richards and E. Wolf, "Electromagnetic diffraction in optical systems. II. structure of the image field in an aplanatic system," *Proc. R. Soc. London A*, vol. 253, no. 1274, pp. 358–379, 1959.
- [112] P. Debye, "Das Verhalten von Lichtwellen in der Nähe eines Brennpunktes oder einer Brennpunktlinie," *Annalen der Physik*, vol. 30, no. 14, pp. 755–776, 1909.
- [113] P. Török and R. Varga, "Electromagnetic diffraction of light focused through a stratified medium," *Appl. Opt.*, vol. 36, no. 11, pp. 2305–2312, 1997.
- [114] S. W. Hell, G. Reiner, C. Cremer, and E. H. K. Stelzer, "Aberrations in confocal fluorescence microscopy induced by mismatches in refractive index," *J. Microsc.*, vol. 169, pp. 391–405, 1993.
- [115] M. Born and E. Wolf, *Principles of Optics*, 7th ed. Cambridge University Press, 1959.
- [116] H. H. Hopkins, "The frequency response of a defocused optical system," *Proc. R. Soc. London A*, vol. 231, no. 1184, pp. 91–103, 1955.
- [117] —, "The concept of partial coherence in optics," *Proc. R. Soc. London A*, vol. 208, no. 1093, pp. 263–277, 1951.
- [118] J. W. Goodman, *Introduction to Fourier optics*. McGraw-Hill, 1968.
- [119] S. F. Gibson and F. Lanni, "Diffraction by a circular aperture as a model for three-dimensional optical microscopy," *J. Opt. Soc. Am. A*, vol. 6, no. 9, pp. 1357–1367, 1989.
- [120] G. B. Airy, "On the diffraction of an object-glass with circular aperture," *Trans. Camb. Phil. Soc.*, vol. 5, no. 3, pp. 283–291, 1835.
- [121] V. N. Mahajan, *Aberration Theory Made Simple*. SPIE, 1991.
- [122] H. H. Hopkins and M. J. Yzuel, "The computation of diffraction patterns in the presence of aberrations," *Acta Optica*, vol. 17, no. 3, pp. 157–182, 1970.
- [123] V. N. Mahajan, *Optical Imaging and Aberrations - Part II Wave Diffraction Optics*. SPIE, 2001.
- [124] S. F. Gibson, "Modeling the 3-D imaging properties of the fluorescence light microscope," Ph.D. dissertation, Carnegie Mellon University, 1990.
- [125] M. Leutenegger, R. Rao, R. A. Leitgeb, and T. Lasser, "Fast focus field calculations," *Opt. Express*, vol. 14, no. 23, pp. 11 277–11 291, 2006.
- [126] U. Kubitscheck, O. Kückmann, T. Kues, and R. Peters, "Imaging and tracking of single gfp molecules in solution," *Biophys. J.*, vol. 78, no. 4, pp. 2170–2179, 2000.
- [127] K. A. Winick, "Cramér-Rao lower bounds on the performance of charge-coupled-device optical position estimators," *J. Opt. Soc. Am. A*, vol. 3, no. 11, pp. 1809–1815, 1986.
- [128] D. L. Snyder and M. I. Miller, *Random Point Processes in Time and Space*, 2nd ed. Springer, 1991.
- [129] U. Kubitscheck, "Single protein molecules visualized and tracked in the interior of eukaryotic cells," *Single Molecules*, vol. 3, pp. 267–274, 2002.
- [130] A. Van Oijen, J. Köhler, J. Schmidt, M. Müller, and G. Brakenhoff, "3-dimensional super-resolution by spectrally selective imaging," *Chem. Phys. Lett.*, vol. 292, pp. 183–187, 1998.
- [131] N. Subotic, D. Van De Ville, and M. Unser, "On the feasibility of axial tracking of a fluorescent nano-particle using a defocusing model," in *Proc. 2nd IEEE Int Symp. Biomedical Imaging*, Arlington VA, USA, April 15–18 2004, pp. 1231–1234.
- [132] P. Török, R. Varga, Z. Laczik, and R. Booker, "Electromagnetic diffraction of light focused through a planar interface between materials of mismatched refractive indices: an integral representation," *J. Opt. Soc. Am. A*, vol. 12, no. 2, pp. 325–332, 1995.
- [133] A. Egner and S. W. Hell, "Equivalence of the Huygens-Fresnel and Debye approach for the calculation of high aperture point-spread functions in the presence of refractive index mismatch," *J. Microsc.*, vol. 193, no. 3, pp. 244–249, 1999.

- [134] M. Gu, *Advanced Optical Imaging Theory*. Springer, 2000.
- [135] V. Levi, Q. Ruan, and E. Gratton, "3-D particle tracking in a two-photon microscope: Application to the study of molecular dynamics in cells," *Biophys. J.*, vol. 88, pp. 2919–2928, 2005.
- [136] A. S. Marathay and J. F. McCalmont, "On the usual approximation used in the rayleigh-sommerfeld diffraction theory," *J. Opt. Soc. Am. A*, vol. 21, no. 4, pp. 510–516, 2004.
- [137] F. Aguet, D. Van De Ville, and M. Unser, "Sub-resolution maximum-likelihood based localization of fluorescent nanoparticles in three dimensions," in *Proc. 4th IEEE Int. Symp. Biomedical Imaging*, 2007, pp. 932–935.
- [138] S. W. Hell, "Microscopy and its focal switch," *Nat. Methods*, vol. 6, no. 1, pp. 24–32, 2009.
- [139] A. P. Bartko and R. M. Dickson, "Imaging three-dimensional single molecule orientations," *J. Phys. Chem. B*, vol. 103, no. 51, pp. 11 237–11 241, 1999.
- [140] R. Schuster, M. Barth, A. Gruber, and F. Cichos, "Defocused wide field fluorescence imaging of single CdSe/ZnS quantum dots," *Chem. Phys. Lett.*, vol. 413, pp. 280–283, 2005.
- [141] E. Toprak, J. Enderlein, S. Syed, S. A. McKinney, R. G. Petschek, T. Ha, Y. E. Goldman, and P. R. Selvin, "Defocused orientation and position imaging (DOPI) of myosin V," *Proc. Natl. Acad. Sci. USA*, vol. 103, no. 17, pp. 6495–6499, 2006.
- [142] M. Böhmer and J. Enderlein, "Orientation imaging of single molecules by wide-field epifluorescence microscopy," *J. Opt. Soc. Am. A*, vol. 20, no. 3, pp. 554–559, 2003.
- [143] D. P. Patra, I. Gregor, and J. Enderlein, "Image analysis of defocused single-molecule images for three-dimensional molecule orientation studies," *J. Phys. Chem. A*, vol. 108, pp. 6836–6841, 2004.
- [144] M. A. Lieb, J. M. Zavislan, and L. Novotny, "Single-molecule orientations determined by emission pattern imaging," *J. Opt. Soc. Am. B*, vol. 21, no. 6, pp. 1210–1215, 2004.
- [145] Z. Sikorski and L. M. Davis, "Engineering the collected field for single-molecule orientation determination," *Opt. Express*, vol. 16, no. 6, pp. 3660–3673, 2008.
- [146] M. R. Foreman, C. M. Romero, and P. Török, "Determination of the three-dimensional orientation of single molecules," *Opt. Lett.*, vol. 33, no. 9, pp. 1020–1022, 2008.
- [147] B. Sick, B. Hecht, and L. Novotny, "Orientational imaging of single molecules by annular illumination," *Phys. Rev. Lett.*, vol. 85, no. 21, pp. 4482–4485, 2000.
- [148] W. T. Freeman and E. H. Adelson, "The design and use of steerable filters," *IEEE Trans. Pattern Anal. Mach. Intell.*, vol. 13, no. 9, pp. 891–906, 1991.
- [149] E. H. Hellen and D. Axelrod, "Fluorescence emission at dielectric and metal-film interfaces," *J. Opt. Soc. Am. B*, vol. 4, no. 3, pp. 337–350, 1987.
- [150] G. W. Ford and W. H. Weber, "Electromagnetic interactions of molecules with metal surfaces," *Phys. Rep.*, vol. 113, no. 4, pp. 195–287, 1984.
- [151] M. Leutenegger, H. Blom, J. Widengren, C. Eggeling, M. Gösch, R. A. Leitgeb, and T. Lasser, "Dual-color total internal reflection fluorescence cross-correlation spectroscopy," *J. Biomed. Opt.*, vol. 11, no. 4, pp. 040 502–(1–3), 2006.
- [152] M. S. Robbins and B. J. Hadwen, "The noise performance of electron multiplying charge-coupled devices," *IEEE Trans. Electron Devices*, vol. 50, no. 5, pp. 1227–1232, 2003.
- [153] J. Hu, L.-s. Li, W. Yang, L. Manna, L.-w. Wang, and A. P. Alivisatos, "Linearly polarized emission from colloidal semiconductor quantum rods," *Science*, vol. 292, pp. 2060–2063, 2001.
- [154] J. G. McNally, T. Karpova, J. Cooper, and J.-A. Conchello, "Three-dimensional imaging by deconvolution microscopy," *Methods*, vol. 19, no. 3, pp. 373–385, November 1999.
- [155] P. Sarder and A. Nehorai, "Deconvolution methods for 3-d fluorescence microscopy images," *IEEE Sig. Proc. Mag.*, vol. 23, no. 3, pp. 32–45, 2006.

- [156] B. A. Scalettar, J. R. Swedlow, J. W. Sedat, and D. A. Agard, "Dispersion, aberration and deconvolution in multi-wavelength fluorescence images," *J. Microsc.*, vol. 182, no. 1, pp. 50–60, 1996.
- [157] A. Diaspro, S. Annunziata, and M. Robello, "Single-pinhole confocal imaging of sub-resolution sparse objects using experimental point spread function and image restoration," *Microsc. Res. Tech.*, vol. 51, no. 5, pp. 464–468, 2000.
- [158] J. Boutet de Monvel, E. Scarfone, S. Le Calvez, and M. Ulfendahl, "Image-adaptive deconvolution for three-dimensional deep biological imaging," *Biophys. J.*, vol. 85, no. 6, pp. 3991–4001, 2003.
- [159] R. Juškaitis and T. Wilson, "The measurement of the amplitude point spread function of microscope objective lenses," *J. Microsc.*, vol. 189, no. 1, pp. 8–11, 1998.
- [160] F. Charrière, A. Marian, T. Colomb, P. Marquet, and C. Depeursinge, "Amplitude point-spread function measurement of high-na microscope objectives by digital holographic microscopy," *Opt. Lett.*, vol. 32, no. 16, pp. 2456–2458, 2007.
- [161] Y. Hiraoka, J. W. Sedat, and D. A. Agard, "The use of a charge-coupled device for quantitative optical microscopy of biological structures," *Science*, vol. 238, pp. 36–41, 1987.
- [162] J. G. McNally, C. Preza, J.-A. Conchello, and L. J. Thomas, "Artifacts in computational optical-sectioning microscopy," *J. Opt. Soc. Am. A*, vol. 11, no. 3, pp. 1056–1067, 1994.
- [163] J. Markham and J.-A. Conchello, "Parametric blind deconvolution: a robust method for the simultaneous estimation of image and blur," *J. Opt. Soc. Am. A*, vol. 16, no. 10, pp. 2377–2391, 1999.
- [164] P. Pankajakshan, B. Zhang, L. Blanc-Feraud, Z. Kam, J.-C. Olivo-Marin, and J. Zerubia, "Blind deconvolution for diffraction-limited fluorescence microscopy," in *Proc. 5th IEEE Int. Symp. Biomedical Imaging*, 2008, pp. 740–743.
- [165] B. Zhang, J. Zerubia, and J.-C. Olivo-Marin, "Gaussian approximations of fluorescence microscope point-spread function models," *Appl. Opt.*, vol. 46, no. 10, pp. 1819–1829, 2007.
- [166] O. Haerberlé, F. Bicha, C. Simler, A. Dieterlen, C. Xu, B. Colicchio, S. Jacquy, and M.-P. Gramain, "Identification of acquisition parameters from the point spread function of a fluorescence microscope," *Opt. Commun.*, vol. 196, pp. 109–117, 2001.
- [167] A. Egner and S. W. Hell, "Aberrations in confocal and multi-photon fluorescence microscopy induced by refractive index mismatches," in *Handbook of confocal microscopy*, 3rd ed., J. B. Pawley, Ed. Springer, 2006, ch. 20, pp. 404–413.
- [168] J. W. Shaevitz and D. A. Fletcher, "Enhanced three-dimensional deconvolution microscopy using a measured depth-varying point spread function," *J. Opt. Soc. Am. A*, vol. 24, no. 9, pp. 2622–2627, 2007.
- [169] C. J. R. Sheppard, D. K. Hamilton, and I. J. Cox, "Optical microscopy with extended depth of field," *Proc. R. Soc. London A*, vol. 387, pp. 171–186, 1983.
- [170] R. J. Pieper and A. Korpel, "Image processing for extended depth of field," *Appl. Opt.*, vol. 22, no. 10, pp. 1449–1453, 1983.
- [171] H. Li, B. S. Manjunath, and S. K. Mitra, "Multisensor image fusion using the wavelet transform," *Graph. Models Image Process.*, vol. 57, no. 3, pp. 235–245, 1995.
- [172] V. S. Petrovic and C. S. Xydeas, "Gradient-based multiresolution image fusion," *IEEE Trans. Image Process.*, vol. 13, no. 2, pp. 228–237, 2004.
- [173] S. C. Tucker, W. T. Cathey, and E. R. Dowski, "Extended depth of field and aberration control for inexpensive digital microscope systems," *Opt. Express*, vol. 4, no. 11, pp. 467–474, 1999.
- [174] A. G. Valdecasas, D. Marshall, J. M. Becerra, and J. J. Terrero, "On the extended depth of focus algorithms for bright field microscopy," *Micron*, vol. 32, pp. 559–569, 2001.
- [175] D. McLachlan, "Extreme focal depth in microscopy," *Appl. Opt.*, vol. 3, no. 9, pp. 1009–1013, 1964.

- [176] J. F. Burke, G. Indebetouw, G. Nomarski, and G. W. Stroke, "White-light three dimensional microscopy using multiple-image storing and decoding," *Nature*, vol. 231, pp. 303–306, 1971.
- [177] G. Indebetouw and H. Bai, "Imaging with Fresnel zone pupil masks: extended depth of field," *Appl. Opt.*, vol. 23, no. 23, pp. 4299–4302, 1984.
- [178] E. R. Dowski and W. T. Cathey, "Extended depth of field through wave-front coding," *Appl. Opt.*, vol. 34, no. 11, pp. 1859–1866, 1995.
- [179] A. Castro and J. Ojeda-Castañeda, "Asymmetric phase masks for extended depth of field," *Appl. Opt.*, vol. 43, no. 17, pp. 3474–3479, 2004.
- [180] E. J. Botcherby, R. Juškaitis, and T. Wilson, "Scanning two photon fluorescence microscopy with extended depth of field," *Opt. Commun.*, vol. 268, pp. 253–260, 2006.
- [181] S. A. Sugimoto and Y. Ichioka, "Digital composition of images with increased depth of focus considering depth information," *Appl. Opt.*, vol. 24, no. 14, pp. 2076–2080, 1985.
- [182] K. Itoh, A. Hayashi, and Y. Ichioka, "Digitized optical microscopy with extended depth of field," *Appl. Opt.*, vol. 28, no. 15, pp. 3487–3493, 1989.
- [183] K. Kaneda, S. Ishida, A. Ishida, and E. Nakamae, "Image processing and synthesis for extended depth of field of optical microscopes," *Vis. Comput.*, vol. 8, no. 5–6, pp. 351–360, 1992.
- [184] M. Antunes, M. Trachtenberg, G. Thomas, and T. Shoa, *All-in-Focus Imaging Using a Series of Images on Different Focal Planes*, ser. Lecture Notes in Computer Science. Springer, 2005, vol. 3656, pp. 174–181.
- [185] E. H. Adelson, "Depth-of-focus imaging process," U.S. patent 4 661 986, 1987.
- [186] P. J. Burt and R. J. Kolczynski, "Enhanced image capture through fusion," in *Proc. 4th IEEE Int. Conf. Computer Vision*, 1993, pp. 173–182.
- [187] Z. Liu, K. Tsukada, K. Hanasaki, Y. K. Ho, and Y. P. Dai, "Image fusion by using steerable pyramid," *Pattern Recognit. Lett.*, vol. 22, pp. 929–939, 2001.
- [188] A. P. Bradley and P. C. Bamford, "A one-pass extended depth of field algorithm based on the over-complete discrete wavelet transform," in *Image and Vision Computing '04 New Zealand (IVCNZ'04)*, 2004, pp. 279–284.
- [189] S. Li, J. T. Kwok, I. W. Tsang, and Y. Wang, "Fusing images with different focuses using support vector machines," *IEEE Trans. Neural Netw.*, vol. 15, no. 6, pp. 1555–1561, 2004.
- [190] P. R. Hill, D. R. Bull, and C. N. Canagarajah, "Image fusion using a new framework for complex wavelet transforms," in *Proc. IEEE Int. Conf. Image Processing*, 2005, pp. 1338–1341.
- [191] L. Tessens, A. Ledda, A. Pižurica, and W. Philips, "Extending the depth of field in microscopy through curvelet-based frequency-adaptive image fusion," in *Proc. IEEE Int. Conf. Acoustics, Speech and Signal Processing*, 2007, pp. 1861–1864.
- [192] F. Aguet, D. Van De Ville, and M. Unser, "Joint texture and topography estimation for extended depth of field in brightfield microscopy," in *Proc. 3rd IEEE Int. Symp. Biomedical Imaging*, 2006, pp. 778–781.
- [193] A. P. Dempster, N. M. Laird, and D. B. Rubin, "Maximum likelihood from incomplete data via the EM algorithm," *J. Roy. Statist. Soc. B*, vol. 39, no. 1, pp. 1–38, 1977.
- [194] D. A. Agard, Y. Hiraoka, P. Shaw, and J. W. Sedat, "Fluorescence microscopy in three dimensions," *Methods Cell Biol.*, vol. 30, pp. 353–377, 1989.
- [195] M. Unser, A. Aldroubi, and M. Eden, "B-Spline signal processing: Part I - Theory," *IEEE Trans. Signal Proc.*, vol. 41, no. 2, pp. 821–833, 1993.
- [196] R. P. Brent, *Algorithms for Minimization without Derivatives*. Prentice Hall, 1973.
- [197] A. Köhler, "Ein neues Beleuchtungsverfahren für mikrophotographische Zwecke," *Zeitschrift für wissenschaftliche Mikroskopie*, vol. 10, pp. 433–440, 1893.
- [198] R. Roy, S. Hohng, and T. Ha, "A practical guide to single-molecule FRET," *Nat. Methods*, vol. 5, no. 6, pp. 507–516, 2008.

-
- [199] R. E. Dale, J. Eisinger, and W. E. Blumberg, "The orientational freedom of molecular probes—the orientation factor in intramolecular energy transfer," *Biophys. J.*, vol. 26, no. 2, pp. 161–193, 1979.
- [200] A. Iqbal, S. Arslan, B. Okumus, T. J. Wilson, G. Giraud, D. G. Norman, T. Ha, and D. M. Lilley, "Orientation dependence in fluorescent energy transfer between Cy3 and Cy5 terminally attached to double-stranded nucleic acids," *Proc. Natl. Acad. Sci. USA*, vol. 105, no. 32, pp. 11 176–11 181, 2008.

Curriculum Vitæ

EPFL / STI / IMT / LIB
BM 4.141 Station 17
Tel.: +41 21 693 41 53
Fax: +41 21 693 37 01

François Aguet

francois.aguet@epfl.ch
<http://bigwww.epfl.ch/aguets/>

Date of birth: October 1, 1980
Nationality: Swiss
Marital status: single

Education

2004-2009	Ph.D. thesis in biomedical imaging, Group of Prof. Michael Unser, Swiss Federal Institute of Technology, Lausanne (EPFL)
1999-2004	M.Sc. in computer science Swiss Federal Institute of Technology, Lausanne (EPFL)
1996-1999	Swiss Matura Exam, type C (scientific) Gymnase du Bugnon, Lausanne
1994-1996	Henry M. Gunn High School, Palo Alto, California
1993	Gymnasium Rämibühl, Zürich

Awards

Max Anliker Memorial Best Poster Award
(Swiss Society of Biomedical Engineering Annual Meeting, 2007)

Grants

Postdoctoral fellowship, Swiss National Science Foundation, grant for prospective researchers (18 months)

Teaching

Teaching assistant for “Image Processing I & II,” Prof. Michael Unser. Supervision of the image processing laboratories (2004-present)

Supervision of image processing semester research projects for Masters students

Lecturer for the doctoral school course “Biomicroscopy,” Prof. Theo Lasser, EPFL (subject: matrix optics)

Oral examination expert for “Applied photonics I & II,” Prof. Theo Lasser, EPFL

Professional activities

Reviewer: IEEE Trans. Image Processing, IEEE Trans. Medical Imaging, Proceedings of the IEEE, Optics Express, J. Opt. Soc. Am. A, IEEE International Symposium on Biomedical Imaging (2007-present)

Memberships: IEEE, BMES, SSBE

BMES EPFL student chapter: committee member & treasurer. Co-organized annual conference (2006 & 2007).

Technical Skills

Programming: Java, Matlab, C/C++, OpenGL, Mathematica

OS: Mac Os X, Windows XP

Graphics: Illustrator, Photoshop

Publishing: LaTeX, InDesign, iWork, Office, HTML/XML

Languages

Trilingual: French and German as mother tongues,
English acquired while living in the U.S.A.

Extracurricular

Classical music advanced piano classes at the Lausanne Conservatory,
previously cello, since the age of 7

Publications

Journal papers

F. Aguet, S. Geissbühler, I. Märki, T. Lasser, and M. Unser, "Super-resolution orientation estimation and localization of fluorescent dipoles using 3-D steerable filters," *Opt. Express* **17**(8), pp. 6829-6848, 2009.

F. Aguet, D. Van De Ville, and M. Unser "Model-based 2.5-D deconvolution for extended depth-of-field in brightfield microscopy," *IEEE Trans. Image Process.*, **17**(7), pp. 1144-1153, 2008.

F. Aguet, D. Van De Ville, and M. Unser, "A maximum-likelihood formalism for sub-resolution axial localization of fluorescent nanoparticles," *Opt. Express* **13**(26), pp. 10503-10522, 2005.

Reviews and Book chapters

F. Aguet, C. Vonesch, J.-L. Vonesch, and M. Unser, "An introduction to fluorescence microscopy: basic principles, challenges and opportunities," *Microscopic image analysis for the life sciences, Artech House* (Eds. J. Rittscher, S. T. C. Wong, R. Machiraju), pp. 85-114, 2008.

C. Vonesch, F. Aguet, J.-L. Vonesch, and M. Unser, "The colored revolution of bioimaging," *IEEE Signal Processing Magazine* **23**(3), pp. 20-31, 2006.

International conference proceedings (peer-reviewed)

F. Aguet, S. Geissbühler, I. Märki, T. Lasser, and M. Unser, "Steerable filters for orientation estimation and localization of fluorescent dipoles," *Proc. 6th IEEE International Symposium on Biomedical Imaging, ISBI 2009 (June 28-July 1)*, pp. 1166-1169, 2009.

F. Aguet, S. Geissbühler, I. Märki, T. Lasser, and M. Unser, "Super-resolved position and orientation of fluorescent dipoles," *European Conference on Biomedical Optics, ECBO 2009 (June 14-18)*, *Proc. SPIE 7367 (73670Y)*, 2009.

S. C. Sekhar, F. Aguet, S. Romain, P. Thévenaz, and M. Unser, "Parametric B-spline snakes on distance maps—application to segmentation of histology images," *Proc. 16th European Signal Processing Conference, EUSIPCO 2008 (August 25-29)*, 2008.

F. Aguet, D. Van De Ville, and M. Unser, "An accurate PSF model with few parameters for axially shift-variant deconvolution," *Proc. 5th IEEE International Symposium on Biomedical Imaging, ISBI 2008 (May 14-17)*, pp. 157-160, 2008.

F. Aguet, D. Van De Ville, and M. Unser, "Sub-resolution maximum-likelihood based localization of fluorescent nanoparticles in three dimensions," *Proc. 4th IEEE International Symposium on Biomedical Imaging, ISBI 2007 (April 12-15)*, pp. 932-935, 2007. **Invited paper.**

F. Aguet, D. Van De Ville, and M. Unser, "Joint texture and topography estimation for extended depth of field in brightfield microscopy," *Proc. 3rd IEEE International Symposium on Biomedical Imaging, ISBI 2006 (April 6-9)*, pp. 778-781, 2006.

F. Aguet, M. Jacob, and M. Unser, "Three-dimensional feature detection using optimal steerable filters," *Proc. 12th IEEE International Conference on Image Processing, ICIP 2005 (September 11-14)*, vol. 2, pp. 1158-61, 2005.

F. Aguet, D. Van De Ville, M. Unser, "Sub-resolution axial localization of nanoparticles in fluorescence microscopy," *European Conference on Biomedical Optics, ECBO 2005 (June 12-16)*, *Proc. SPIE 5860 (58600P)*, 2005.

Conference abstracts

F. Aguet, D. Van De Ville, M. Unser, "A model-based approach to extended depth of field for brightfield microscopy," *Swiss Society of Biomedical Engineering 2007 Meeting SSBE'07 (Neuchâtel, Switzerland)*, September 13-14, 2007. This work received the Max Anliker Memorial Poster Award.

F. Aguet, D. Van De Ville, M. Unser, "Extended depth of field and specimen topography estimation in brightfield microscopy," *CHUV Research Day, poster ODE-35, p. 226, (Lausanne, Switzerland)*, February 1, 2007.

F. Aguet, D. Van De Ville, M. Unser, "Maximum likelihood based tracking of fluorescent nanoparticles," *Swiss Society for Biomedical Engineering 2005 Annual Meeting SSBE'05 (Lausanne, Switzerland)*, September 1-2, 2005.

F. Aguet, D. Van De Ville, M. Unser, "On the fundamental limits of nano-particle tracking along the optical axis," *Swiss Society of Biomedical Engineering 2004 Annual Meeting SSBE'04 (Zürich, Switzerland)*, September 2-3, 2004.